

# UC Berkeley

## UC Berkeley Electronic Theses and Dissertations

### Title

Isolated Photon Cross Sections and Nuclear Modification Factor in  $\sqrt{s_{NN}} = 5.02$  TeV pp and p-Pb with ALICE

### Permalink

<https://escholarship.org/uc/item/2cd3m5m9>

### Author

Dixit, Dhruv

### Publication Date

2023

Peer reviewed|Thesis/dissertation

Isolated Photon Cross Sections and Nuclear Modification Factor in  $\sqrt{s_{\text{NN}}} = 5.02$  TeV pp  
and p-Pb with ALICE

by

Dhruv Dixit

A dissertation submitted in partial satisfaction of the  
requirements for the degree of

Doctor of Philosophy

in

Physics

in the

Graduate Division

of the

University of California, Berkeley

Committee in charge:

Professor Barbara Jacak, Chair

Professor Ori Ganor

Professor Jasmina Vujic

Spring 2023

Isolated Photon Cross Sections and Nuclear Modification Factor in  $\sqrt{s_{\text{NN}}} = 5.02$  TeV pp  
and p-Pb with ALICE

Copyright 2023  
by  
Dhruv Dixit

## Abstract

Isolated Photon Cross Sections and Nuclear Modification Factor in  $\sqrt{s_{\text{NN}}} = 5.02$  TeV pp  
and p-Pb with ALICE

by

Dhruv Dixit

Doctor of Philosophy in Physics

University of California, Berkeley

Professor Barbara Jacak, Chair

Prompt photons, produced via QCD Compton scattering or quark and anti-quark annihilation at leading order, are unique probes to study QCD processes since they do not interact strongly and therefore allow to control the dynamics of the initial hard parton scattering. Isolated photon production in pp collisions is one of the most clear tests of perturbative QCD processes and parton distribution functions. Photon measurement in p-A collisions provides the opportunity to measure possible modifications of the nucleon structure function in nuclei. ALICE has measured isolated photons at low  $p_{\text{T}}$ , thus extending previous measurements down to small  $x$ . In this thesis, the cross section of isolated photons for the range  $12 \text{ GeV}/c < p_{\text{T}} < 60 \text{ GeV}/c$  is presented in pp and p-Pb collisions at  $\sqrt{s_{\text{NN}}} = 5.02$  TeV along with photon nuclear modification factor ( $R_{p\text{Pb}}$ ).

# Contents

<b>Contents</b>	<b>i</b>
<b>List of Figures</b>	<b>iii</b>
<b>List of Tables</b>	<b>ix</b>
<b>1 Introduction</b>	<b>1</b>
1.1 The Standard model . . . . .	1
1.2 Quantum chromodynamics (QCD) . . . . .	3
1.2.1 Quarks and gluons . . . . .	3
1.2.2 Methods for QCD calculations . . . . .	7
1.3 Hot nuclear matter . . . . .	9
1.3.1 Heavy-ion collisions . . . . .	10
1.3.2 Anisotropic collective flow . . . . .	13
1.4 Cold nuclear matter effects . . . . .	16
1.4.1 Deep inelastic scattering . . . . .	17
1.4.2 Parton distribution functions (PDFs) . . . . .	20
1.5 Photons . . . . .	26
<b>2 ALICE: A Large Ion Collider Experiment</b>	<b>29</b>
2.1 The Large Hadron Collider . . . . .	29
2.2 The ALICE experiment . . . . .	31
2.2.1 Triggering in ALICE . . . . .	35
2.2.2 VZERO (V0) . . . . .	36
2.2.3 Inner Tracking System (ITS) . . . . .	39
2.2.4 Time Projection Chamber (TPC) . . . . .	45
2.2.5 ElectroMagnetic Calorimeter (EMCal) . . . . .	49
<b>3 Analysis</b>	<b>57</b>
3.1 Analysis summary . . . . .	57
3.2 Datasets . . . . .	59
3.3 Monte Carlo simulations . . . . .	61

3.4	Event selection . . . . .	62
3.4.1	Trigger Selection . . . . .	62
3.5	Calorimeter cluster reconstruction . . . . .	64
3.5.1	Definition . . . . .	64
3.5.2	Corrections . . . . .	65
3.5.3	Selection . . . . .	65
3.6	Photon Identification . . . . .	69
3.7	Isolation . . . . .	71
3.7.1	Underlying Event estimation . . . . .	71
3.7.2	UE correction to isolation variable . . . . .	73
3.8	Purity Measurement . . . . .	75
3.8.1	Template fit method . . . . .	75
3.8.2	Systematic uncertainties of the purity measurement . . . . .	81
3.8.3	Summary of systematic uncertainties of purity measurement . . . . .	87
3.9	Efficiency . . . . .	88
3.10	Luminosity . . . . .	91
3.11	Data driven trigger acceptance correction . . . . .	96
3.11.1	Correction procedure . . . . .	96
3.11.2	Systematic uncertainty for the trigger acceptance correction . . . . .	98
3.12	Systematic uncertainties . . . . .	105
<b>4</b>	<b>Results and Discussion</b>	<b>111</b>
4.1	Isolated Photon Cross Section . . . . .	111
4.2	Theory comparison . . . . .	112
4.3	The isolated photon nuclear modification factor ( $R_{pPb}$ ) . . . . .	113
<b>5</b>	<b>Conclusions</b>	<b>117</b>
	<b>Bibliography</b>	<b>120</b>

# List of Figures

1.2	Various measurements of $\alpha_s$ as a function of $Q$ along with a fit function. Image from ref [11] . . . . .	5
1.4	A slice of the lattice comprised of discretized space-time with lattice spacing $a$ . Quark fields are placed on the vertices, while the gluon fields ( $U_i$ , where $i = \mu$ or $\nu$ ) are placed between the vertices. Image from ref [11] . . . . .	9
1.6	The production of quark gluon plasma in space-time plane with the color indicating the temperature of the plasma (left). The process of Lorentz contracted heavy-ion discs colliding to create QGP at different times (right). Hadrons are represented by the blue and grey spheres, while the QGP is represented by red spheres. Images from ref [16]. The $y$ in this figure is rapidity, the measure of relativistic velocity. . . . .	11
1.7	Images from ref [18] . . . . .	12
1.8	Panel (a) presents schematically the collision zone between two incoming nuclei. Panel (b) illustrates initial-state anisotropy in the collision zone converting into final-state elliptic flow, and panel (c) measured as anisotropy in particle momentum. Image from ref [19] . . . . .	14
1.9	Panel (a) shows the collision and isotropy (red curve) and anisotropy (blue curve) in case of a weakly interacting gas or a liquid being formed. Panel (b) shows ALICE measured of $v_n$ with $n = 2,3$ and 4 from top to bottom. Panel (c) shows comparisons of ATLAS's $v_2$ measured event-by-event. Image from ref [16] . . . . .	15
1.10	The image is a cartoon illustrating elliptic flow ( $v_2$ ) and triangular flow ( $v_3$ ). Image from ref [14] . . . . .	16
1.11	) Lattice QCD calculations (colored bands) of the pressure $P$ , energy density $\epsilon$ , and entropy density $s$ of hot QCD matter in thermal equilibrium at temperature $T$ . There is a continuous crossover from hadron gas (colored lines) to QGP at higher temperatures. This crossover phase transition is expected in the low baryon density region of the QCD phase diagram as seen in figure 1.5a by the dashed red lines. Image from ref [16] . . . . .	17

1.12	The kinematic quantities for deep inelastic scattering. The quantities $p_1$ and $p_3$ are the four-momenta of the incoming and outgoing electron, $p_2$ is the four-momentum of the proton, and $W$ is the mass of the recoiling system $X$ . The exchanged particle is a photon which transfers four-momentum $q^2 = (p_1 - p_3)^2$ to the proton. Image from ref [1]	18
1.13	Examples of different quark PDFs: (i) a single point-like particle, (ii), three quarks, each having 1/3 of the proton's momentum, (iii) three quarks exchanging momentum via gluons, (iv) same as (iii), but with higher order interactions. Image from ref [1]	20
1.14	A sketch depicting the behavior of the nuclear structure function ratio as a function of $x$ , for a fixed $Q^2$ . The magnitude of the deviation from unity is not to scale. Image from ref [24]	22
1.15	Images from ref [25]	23
1.16	Top: An illustration of the EPPS16 fitting function $R_i^A$ . Bottom: Comparisons of nuclear modification factors for u, d, s quarks and gluon between EPPS16 and nCTEQ15 at $Q^2 = 10\text{GeV}$ . Image from ref [29]	25
1.17	The various sources of photon production in heavy ion collisions The collisions occurs around the z-axis and colors describe the state of the medium at time t. Image from ref [30]	26
1.18	Leading order Feynman diagrams for direct photon production: (a) and (c) are Compton scattering, (b) and (d) are quark-antiquark annihilation. Image from ref [31]	27
1.19	Parton distribution functions for unpolarized protons (a), polarized protons (b), and lead nucleic (c). Image from [32]	28
2.1	CERN accelerator complex. Image from ref [36].	30
2.2	LHC interaction points. Image from ref [37].	32
2.3	ALICE schematics with the subsystems labeled. Image from ref [42].	33
2.4	Cartesian and spherical coordinates, and pseudorapidity orientations	34
2.5	Layout of the ALICE CTP in the experimental cavern. Image from ref [47].	35
2.6	The V0 highlighted in red within a schematic of the ALICE central barrel.	37
2.8	Schematic design of the V0A (left) and V0C (right). Image from ref [39].	38
2.9	The entire ITS and three different style of silicon detector layers highlighted in red within a schematic of the ALICE central barrel region near the beam pipe. Images from ref [54].	40
2.10	Particle identification in the ITS using $dE/dx$ . Image from ref [55].	41
2.11	An SPD layer around the beam pipe. Image from ref [56].	42
2.12	A module of the SDD. Image from ref [57].	43
2.14	A schematic of the ALICE detector with the TPC highlighted in red. Images from ref [54].	46
2.15	The $dE/dx$ of the TPC. Plot from ref [62]	47
2.16	Schematics of the TPC. Images from ref [62].	47



2.17	A schematic of the ALICE detector with the EMCAL and the DCal highlighted in red. Image from ref [54]	48
2.18	The acceptance of all the ALICE calorimeters in the $\eta - \varphi$ plane in terms of the different super modules (SM). The EMCAL is on the left, while the DCal+PHOS is on the right. Image from ref [64].	49
2.19	A picture of an EMCAL module along with a schematic. Image from [64].	51
2.20	Comparing the dimensions of the different components of the EMCAL in $\eta - \varpi$ for one super module.	52
2.21	Diagram showing the shower shape of a cluster in the EMCAL, long with the major and minor axis of the ellipse drawn around the shower shape using equation 3.4. The colors indicate the energy deposited in the cell, with darker cells indicating larger energy deposition. Image from [64]	54
2.22	Right: Cell energy spectra for all cells compared to good cells. Left: Map of good, bad, and dead cells in the EMCAL and DCal. Image from [64].	55
2.23	Images from [64]	56
3.1	Distribution of variables used in the cluster selection of p-Pb data. The red vertical lines represent the cuts used. The cluster cuts get applied sequentially, i.e. the clusters cut with a given variable do not appear in the next.	67
3.2	Distribution of variables used in the cluster selection in pp data. The red vertical lines represent the cuts used. The cluster cuts get applied sequentially, i.e. the clusters cut with a given variable do not appear in the next.	68
3.3	Two shower shape distributions - single photon (left) and decay photons (right)	69
3.4	Shower shape parameter $\sigma_{long}^2$ vs cluster $p_T$ as measured by ALICE for 7 TeV pp data. The solid black lines indicate bounds of the shower shape used in this thesis: $0.1 < \sigma_{long}^2 < 0.3$ . Image from [74]	70
3.5	The isolation cone of radius R around the photon $\gamma$ . The tracks within the cone are summed up according to equation 3.6.	72
3.6	Distribution of the median charged-particle transverse momentum density, $\rho$ , in pp and p-Pb data, for a minimum-bias selection (left panel) and in photon-triggered events (right panel).	73
3.7	Cluster isolation before and after underlying event subtraction in p-Pb (left panel) and pp (right panel) collisions.	74
3.8	Isolation distribution of clusters that pass our selection in p-Pb photon-jet and dijet simulations, and corresponding cumulative distribution. Two vertical lines at $ISO = 1.5 \text{ GeV}/c$ (green) and $ISO = 5.0 \text{ GeV}/c$ are shown in the right panel for reference.	74
3.9	Isolation variable distribution of clusters with $p_T$ between 12 and 16 $\text{GeV}/c$ in p-Pb data (left panel) and pp data (right panel). The green shaded are represents the signal region ( $ISO < 1.5 \text{ GeV}/c$ ); the red represent the sideband ( $5 < ISO < 10 \text{ GeV}/c$ ) used to estimate the background template.	76

3.10	Normalized signal (blue) and background (yellow) distributions used as input for the template fit. These distributions correspond to clusters with $p_T$ in the 15–20 GeV/ $c$ range. . . . .	77
3.11	An example of the template fit with and without the background template correction in p–Pb for clusters with $12 < p_T < 15$ GeV/ $c$ . The goodness of fit is better after the correction and the purity is significantly lower. . . . .	78
3.12	Template fit results in pp and p–Pb data. The stacked histograms (yellow for background, blue for signal) are the predicted counts given the best-fit value of the number of signal photons, $N_{\text{sig}}$ . The hatched gray area represents the interval considered for the purity estimate. The bottom panels show the normalized residuals of the fit, considering the statistical uncertainty on the isolated cluster data and the background template added in quadrature. . . . .	79
3.13	Purity of isolated-photon selection as a function of cluster $p_T$ . The error bar represents statistical uncertainty only. The error band represents the systematic uncertainty only. . . . .	80
3.14	Purity of isolated-photon selection as a function of cluster $p_T$ and the error function fit to the purity for pp (left) and p–Pb (right), . . . . .	80
3.15	Template fit results of background-only template method for pp and p–Pb data. The yellow histograms are the predicted counts given the best-fit value of the total number of clusters in the background dominated region. The hatched gray area represents the interval considered for the purity estimate. The bottom panels show the normalized residuals of the fit, considering the statistical uncertainty on the isolated data and the background template added in quadrature. . . . .	82
3.16	Template fit results (purity and $\chi^2/\text{dof}$ ) as a function of anti-isolation region for clusters with $15 < p_T < 20$ GeV/ $c$ in pp (top) and p–Pb (bottom). The green band shows the selected sideband region. The blue and red bands show the full extent of the purity within the selected sideband region. . . . .	84
3.17	Linear fits for the double ratio (as described in Equation 3.11) for the $\sigma_{\text{long}}^2$ variable in pp data. Included are the value and uncertainty of the fitted slope (in red). . . . .	85
3.18	Linear fits for the double ratio (as described in Equation 3.11) for the $\sigma_{\text{long}}^2$ variable in p–Pb data. Included are the value and uncertainty of the fitted slope (in red). . . . .	86
3.19	The isolated photon efficiency, along with the isolation, reconstruction and shower shape efficiencies for pp (top) and p–Pb(bottom). . . . .	89
3.20	The photon $p_T$ response matrix and the isolated photon bin migration pp (top) and p–Pb(bottom). . . . .	90
3.21	A comparison of the isolated photon efficiency between pp and p–Pb . . . . .	91
3.22	The EMCAL triggered and minimum bias cluster spectra for pp (top) and p–Pb(bottom). . . . .	92
3.23	The turn on curves and trigger rejection factor fits for pp (top) and p–Pb(bottom). A zero degree polynomial fit is applied to calculate the trigger rejection factor. The fit ranges are provided on the figures next to respective turn on curve. . . . .	93

3.24	Top: The trigger spectra is scaled by the trigger rejection factor and compares to the minimum bias spectra. Bottom: ratio of the scaled triggered spectra and the minimum bias spectra . . . . .	95
3.25	Cluster $\eta$ distributions for data and MC along with the data/MC ratio for p–Pb(top) and pp(bottom). . . . .	97
3.26	Cluster $\eta$ data/MC ratios broken down by period for p–Pb(top) and by run for pp(bottom). The "Good pp" list does not include runs 282440 and 282365. . . . .	99
3.27	Residuals of the cluster $\eta$ data/MC ratios broken down by period for p–Pb(top) and by run for pp(bottom) compared to the full dataset. The "Good pp" list does not include runs 282440 and 282365. . . . .	100
3.28	The data/MC ratio along with the average of the local maxima (dotted line) for pp and p–Pb. . . . .	101
3.29	The data/MC ratio along with the average of the local maxima (dotted line) for pp and p–Pb. . . . .	102
3.30	The data/MC ratio for the 2D- $\eta\varphi$ distribution along with bins used to calculate the average(dotted oval) for pp and p–Pb. . . . .	102
3.31	The map of the masked FastORs for the 17q 5.02 TeV pp period. . . . .	103
3.32	Comparison of the isolation photon cross section calculated five different ways: $\eta$ , $\varphi$ , and 2D $\eta\varphi$ -corrections and fastOR masking cluster and event rejection (top). The ratio of the different ways compared with the $\eta$ -correction method (bottom).Error bars only reflect the statistical uncertainty. . . . .	104
3.33	Relative change in the cross section as a result of turning the $\eta$ -correction on and off in p–Pb(left) and pp(right). . . . .	105
3.34	The purity fit functions for the purity central values as well as fits to adjusting the central values up or down one standard deviation systematic. The pp fits are shown on the top, while the p–Pb fits are shown on the bottom. . . . .	106
3.35	The systematic uncertainty due to each individual component of the purity systematic uncertainty propagated to the cross section for both pp(left) and p–Pb(right). The y-axis is the relative systematic uncertainty using half the difference in the cross section of changing the purity by $\pm 1\sigma$ . . . . .	107
3.36	Changes to the relative signal and background template uncertainties as a function for the anti-isolation cut . . . . .	108
3.37	Looking at the effect of the purity systematic uncertainty components on the pp cross section with the background template and anti-isolation selection correlation present(left) and removed(right). . . . .	109
3.38	A look at the percent contribution of the major sources of systematic uncertainty on cross section as a function of $E_T$ for pp and p–Pb. . . . .	110
4.1	Isolated photon cross section for pp (left) and p–Pb(right).The boxes represent the systematic uncertainty while the error bars represent the statistical uncertainty. All points have a statistical uncertainty, but it might be hard to see to the log scale. . . . .	111

4.2	Isolated photon cross section for pp (left) and p–Pb(right) compared with NLO JETPHOX and calculations provided by Werner Vogelsang. The boxes represent the systematic uncertainty while the error bars represent the statistical uncertainty. All points have a statistical uncertainty, but it might be hard to see to the log scale. . . . .	112
4.3	Isolated photon cross section data/JETPHOX ratio for pp (left) and p–Pb(right) compared with NLO JETPHOX and calculations provided by Werner Vogelsang. The boxes represent the systematic uncertainty while the error bars represent the statistical uncertainty. The green band is the scale uncertainty on JETPHOX . . . . .	113
4.4	Comparisons of the nuclear modification factor between different nPDFs at $Q = 10\text{GeV}$ : nNNPDF3.0, nCTEQ15, and EPPS16 in $(x, Q^2)$ space . . . . .	114
4.5	The $R_{p\text{Pb}}$ is shown using the ratio of pp cross section presented in this analysis and the p–Pb cross section presented in this analysis. . . . .	116
5.1	A comparison of isolated photon cross sections in $\sqrt{s_{\text{NN}}} = 5.02, 7, 8,$ and $13\text{ TeV}$ pp and $5.02\text{ TeV}$ p–Pb. Note that the isolation criteria have some differences between the different measurements. The cross sections are compared with JETPHOX. The figure was provided by Gustavo Conesa Balbastre, and created using ALICE preliminary cross-section measurements in $8\text{ TeV}$ pp by Florian Jonas and $13\text{ TeV}$ pp by Ran Xu. . . . .	119

# List of Tables

1.1	The eight types of gluons . . . . .	4
2.1	Summary of various parameters for the different silicon detectors . . . . .	41
3.1	ALICE Data Preparation Group run list classifications . . . . .	59
3.2	Datasets used in this analysis. The runs listed in the table corresponds to those that are in the good run list appropriate for analysis using the EMCal and ITS detectors. . . . .	60
3.3	EMCal triggers used in this analysis. . . . .	61
3.4	Monte Carlo simulations used in this analysis. . . . .	61
3.5	Number of events that passed our full event selection for each of data taking period used in this analysis. The numbers are also shown separately for MB, EG1 and EG2, and EG2calo triggers. . . . .	64
3.6	Median transverse momentum density mean and standard deviation in minimum-bias and and photon-triggered events in pp and p–Pb data. The statistical uncertainty in these numbers is negligible. . . . .	73
3.7	Summary of the systematic uncertainties on the purity as measured with $\sigma_{\text{long}}^2$ in p–Pb collisions. All values are in absolute percentage. “Stat.” refers to the statistical uncertainty; “Signal” refers to the signal template uncertainty; “Anti-iso” refers to the uncertainty due to the sideband selection; “Bkg” refers to the uncertainty due to the background template correction; “Total” is the sum of the previous three columns in quadrature. . . . .	87
3.8	Summary of the systematic uncertainties on the purity as measured with $\sigma_{\text{long}}^2$ in pp collisions. All values are in absolute percentage. “Stat.” refers to the statistical uncertainty; “Signal” refers to the signal template uncertainty; “Anti-iso” refers to the uncertainty due to the sideband selection; “Bkg” refers to the uncertainty due to the background template correction; “Total” is the sum of the previous three columns in quadrature. . . . .	87
3.9	The integrated luminosity measured for each trigger. . . . .	94
3.10	Summary of uncertainties in isolated photon cross section measurement in pp and p–Pb. . . . .	110

## Acknowledgments

During my doctorate journey, I have encountered innumerable people who have helped me along the way. Thank you to my village for believing in me and supporting me throughout this chapter of my life. First, I would like to thank my parents, grandparents, and my entire family who have been my foundation of love and support. I am extremely grateful to my parents for the sacrifices they have made which allowed me to pursue this journey of a doctorate degree.

I would like to express my deepest appreciation to my wife, Ruchi, for her love and constant support, for all the late nights and early mornings, and for keeping me sane over the past few months. Thank you for being my life coach, sounding board, co-scientist in the kitchen, and adventure co-pilot. And most of all, thank you for being my best friend.

Thank you to all my friends for laughing at my puns, indulging me in board game nights, and supporting my goals.

I had the pleasure of collaborating with my colleagues in ALICE. Thank you for including me in a large global community, expanding my horizons, and making my stays at CERN memorable. In particular, thank you to Constantin, Florain, Friederike, Gustavo, Marie, Markus, Martin, and Nico for lending me your help, feedback, and expertise in the development of the analysis and measurements in this thesis.

I'd like to acknowledge the members of the my qual committee Jasmina, Kam-Biu, and Ori for that difficult exam which pushed me to be a better physicist. I would be remiss not to mention the support from NSSC, especially Bethany, for providing me opportunities to share my work, and explore the scope and applications of nuclear physics. This material is based upon work supported by the Department of Energy National Nuclear Security Administration through the Nuclear Science and Security Consortium under Award Number DE-NA0003996.

This endeavor would not have been possible without the help and support from my colleagues at Berkeley. Special thanks to Alwina and Fernando who started this graduate school journey with me. Thank you for our office discussions on physics, life, pokemon, and more. I have learned so much from working together with you. I would like to extend my sincere thanks to the post-docs and scientists of the group: Miguel, for introducing me to the exciting physics of photon cross sections; Yue Shi, for always having answers to all my questions and helping me with my service work, Preeti and Minjung for showing me the ropes in ALICE, Nikki for teaching me about detector designs and hardware, and Rey for always going above and beyond in my times of need. Particular thanks to Wenqing for your expertise about photon measurements, and reading and providing detailed feedback on the early drafts of this thesis. Many thanks to Peter and Mateusz for helping me see the big picture. Anjali, Beatrice, Benjamen, Berenice, Charlie, Drew, Eliane, Emma, Erica, Ezra, Fernando, Ivan, Ivan, Jose, James, Kirill, Kyle, Michael, Raymond, Spencer, Stuti, Tucker, Winston, and Youqi thank you for all the discussions, conversations, and support in meetings.

Much credit for constantly showing me the light at the end of long dark tunnels, and guiding me ever-so-gently goes to my mentor and advisor, Barbara. I could not have undertaken this journey without all of her support. It was not always smooth sailing these seven years. During the turbulent times no one believed me in more than Barbara. Barbara has gone above and beyond to help me grow both professionally and personally. From the time when I was a fledgling graduate student, Barbara always advocated for me and taught me to advocate for myself. As my mentor, Barbara has molded me into a pragmatic and creative physicist with the skills to succeed in any path I choose. I would like to express my deepest appreciation to Barbara for shaping into the scientist and person I am today. Thank you.

# Chapter 1

## Introduction

What is physics? When searching for the definition of physics in a dictionary, on the internet, or asking someone, one will find answers that are similar to the quote below from Encyclopedia Britannica.

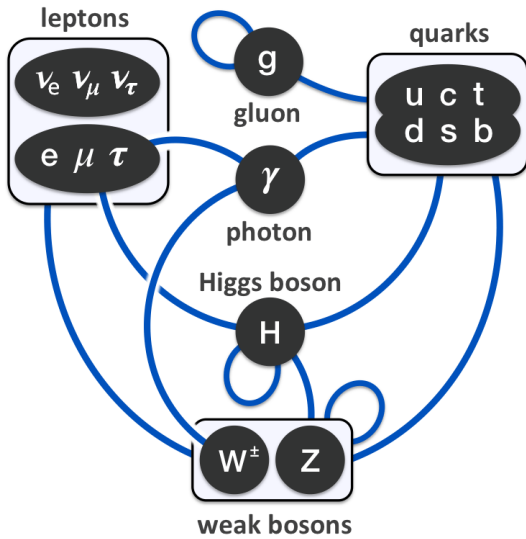
*Physics, science that deals with the structure of matter and the interactions between the fundamental constituents of the observable universe. In the broadest sense, physics is concerned with all aspects of nature on both the macroscopic and submicroscopic levels.*

The quote above showcases the grand scale of what is encompassed within the field of physics. There are physicists studying massive structures in the universe like stars, galaxies, and black holes. There are others who study matter on the smallest of scales such that they need a "microscope" that weighs approximately ten thousand tons and is the size of a five story building. In order to "see" particles, what is needed? Light. Photons. In this thesis, we will embark on a journey to measure the light produced as a result of the interactions of the most elementary particles. The rest of the introduction presents topics and concepts regarding the interaction of elementary particles. This is followed by a description of the experimental apparatus, the analysis procedure to make our photon measurement, presentation of the results, and a conclusion discussing on the results. Let us start with the most elementary particles and the physics which governs them.

### 1.1 The Standard model

The Standard Model is a theory of particle physics that describes the behavior of subatomic particles and the forces that govern their interactions. It is based on the principles of quantum mechanics and the theory of relativity. Three of the four fundamental forces of nature are described by the standard model: the strong force, the weak force, and the electromagnetic force [1]. It does not include gravity, which is described by the theory of general relativity. In the Standard Model, particles are divided into two basic categories:





(a) Elementary particles of the Standard Model and their interactions. The blue lines indicate which particles can interact with which bosons. Image from ref [2]

### Standard Model of Elementary Particles

	three generations of matter (fermions)			interactions / force carriers (bosons)	
	I	II	III		
mass	≈2.2 MeV/c <sup>2</sup>	≈1.28 GeV/c <sup>2</sup>	≈173.1 GeV/c <sup>2</sup>	0	≈124.97 GeV/c <sup>2</sup>
charge	2/3	2/3	2/3	0	0
spin	1/2	1/2	1/2	1	0
<b>QUARKS</b>	<b>u</b> up	<b>c</b> charm	<b>t</b> top	<b>g</b> gluon	<b>H</b> higgs
	4.7 MeV/c <sup>2</sup>	96 MeV/c <sup>2</sup>	4.18 GeV/c <sup>2</sup>	0	0
	-1/3	-1/3	-1/3	0	0
	1/2	1/2	1/2	1	0
	<b>d</b> down	<b>s</b> strange	<b>b</b> bottom	<b>γ</b> photon	
<b>LEPTONS</b>	0.511 MeV/c <sup>2</sup>	105.66 MeV/c <sup>2</sup>	1.7768 GeV/c <sup>2</sup>	≈91.19 GeV/c <sup>2</sup>	
	-1	-1	-1	0	
	1/2	1/2	1/2	1	
	<b>e</b> electron	<b>μ</b> muon	<b>τ</b> tau	<b>Z</b> Z boson	
	<1.0 eV/c <sup>2</sup>	<0.17 MeV/c <sup>2</sup>	≈18.2 MeV/c <sup>2</sup>	≈80.360 GeV/c <sup>2</sup>	
	0	0	0	±1	
	1/2	1/2	1/2	1	
	<b>ν<sub>e</sub></b> electron neutrino	<b>ν<sub>μ</sub></b> muon neutrino	<b>ν<sub>τ</sub></b> tau neutrino	<b>W</b> W boson	
					<b>SCALAR BOSONS</b>
					<b>VECTOR BOSONS</b>

(b) The properties of the elementary particles. Image from ref [3]

fermions and bosons. Fermions are particles which have 1/2 integer spin, and they make up matter, such as electrons and quarks. Bosons are particles which have integer spin and carry forces between fermions, such as photons (which carry the electromagnetic force) and gluons (which carry the strong force). The Standard Model describes the behavior of fermions in terms of their properties, such as their mass, spin, and electric charge. The numerical values for these properties can be seen in figure 1.1b. Each fermion has its own antiparticle which has the same mass, spin, and isospin as the particle, but with opposite charge. For example, a positron is identical to an electron but carries a positive charge. Fermions are divided into two categories: quarks and leptons. Quarks are the building blocks of protons and neutrons, and there are six types of quarks: up, down, charm, strange, top, and bottom. As seen in figure 1.1a, quarks interact with gluons, photons, weak bosons, and the Higgs boson. Leptons are particles that do not interact strongly with other particles, and there are six types of leptons: electrons, muons, taus, and their corresponding neutrinos.

Interactions between particles are described in terms of the exchange of bosons. The electromagnetic force is carried by photons, which are massless bosons that travel at the speed of light. The weak force is carried by three massive bosons: the  $W^+$ ,  $W^-$ , and  $Z$  bosons. The strong force is carried by eight massless gluons, which interact with quarks to hold them together in protons and neutrons. Quarks and gluons together are collectively called partons. Generally, particles comprised of quarks and gluons are called hadrons. Hadrons are divided into two classes: baryons, hadrons with three quarks such as protons and neutrons, and mesons, hadrons with two quarks or quark-antiquark such as pions( $u+\bar{d}$ ),

$J/\psi(c+\bar{c})$ .

The Standard Model is a quantum field theory, which means that it describes particles and their interactions in terms of fields that pervade space and time. These fields are represented by mathematical objects called quantum fields, which are used to calculate the probabilities of different particle interactions. There have been predictions from the Standard Model which have been confirmed by many experiments, including the discovery of the W [4, 5] and Z [6] bosons at CERN in 1983 and the discovery of the Higgs boson [7, 8] at CERN in 2012. However, the Standard Model is not a complete theory of particle physics, as it does not include gravity, explain the nature of dark matter and dark energy, or explain the quark or neutrino masses, but despite that it is the most successful theory of particle physics to date.

## 1.2 Quantum chromodynamics (QCD)

The strong force is one of the four fundamental forces of nature. It is a fundamental force because it cannot be explained in terms of other forces, such as the electromagnetic force or the weak force. Strong interactions bind quarks and gluons together to form protons and neutrons, which in turn make up atomic nuclei. Within a nucleus, protons with an electric charge of  $+1$  are expected to repel each other, but due to the strong interactions from exchanging pions and other neutral mesons the protons overcome the electromagnetic repulsion and stay bound in the nucleus. The strong force is a very short-range force, acting only over distances of about one femtometer, which is approximately the size of a nucleon. At one femtometer, if magnitude of the strong force was 1, the magnitudes of the electromagnetic force, weak force, and gravity would be  $10^{-3}$ ,  $10^{-8}$ , and  $10^{-37}$ , respectively. At longer distances, the strong force becomes weaker and is eventually overwhelmed by the electromagnetic force and gravity.

### 1.2.1 Quarks and gluons

The strong force is mediated by gluons, which are massless and carry a color charge. All particles which carry the color charge (quarks and gluons) can participate in strong interactions. In order to form a stable particle, quarks must combine to form a color-neutral state. The color charge comes in three colors: red, blue, and green, and their color opposites, or anticolors: antired, antiblue, and antigreen. In order to form a color-neutral state, either the color and anticolor combine to be cancelled or all three colors (or anticolors) have to be present in equal amount. Examples of color-neutral states are: (blue)+(antiblue), (red)+(blue)+(green), or (antired)+(antiblue)+(antigreen).

Gluons themselves carry a color charge, which allows them to interact with other gluons and with quarks. The strong force is a self-interacting force, which means that the force between two quarks is mediated by the exchange of multiple gluons. While quarks will have one of any color (or anticolor if it is an antiquark), gluons carry a color-anticolor

$(r\bar{b} + b\bar{r})/\sqrt{2}$	$(r\bar{g} + g\bar{r})/\sqrt{2}$	$(b\bar{g} + g\bar{b})/\sqrt{2}$
$-i(r\bar{b} - b\bar{r})/\sqrt{2}$	$-i(r\bar{g} - g\bar{r})/\sqrt{2}$	$-i(b\bar{g} - g\bar{b})/\sqrt{2}$
$(r\bar{r} - g\bar{g})/\sqrt{2}$	$(r\bar{r} + g\bar{g} - 2b\bar{b})/\sqrt{6}$	$(r\bar{r} + g\bar{g} + b\bar{b})/\sqrt{3}$

Table 1.1: The eight types of gluons

together. There would give nine gluons if the colors and anticolors are paired up in all possible combinations; however, red-antired, blue-antiblue, and green-antigreen are color neutral states, color neutral gluons don't exist, so these three are not possible. In quantum physics, there is superposition, mixing of particles with the same quantum states, which results in gluons which have a linear combination of two different color-anticolor pairs. For unlike color-anticolor pairs, there are six states given by the first two rows of table 1.1. Same color-anticolor pairs cannot be added together but they can be subtracted as in row 3, column 1. The example here uses red and green, but this can be done for any color pair. The only other linearly independent combination left given by  $(r\bar{r} - g\bar{g})\sqrt{2}$ . Note that choice of the two colors used in row 3, column 1 dictates the third used in  $(r\bar{r} + g\bar{g} - 2b\bar{b})\sqrt{6}$  in order for them to be independent of each other. The final linearly independent combination available will be the color singlet state -  $(r\bar{r} + g\bar{g} + b\bar{b})\sqrt{3}$ ; however, this state is not physically possible. There is no chargeless gluon which behave like a photon.

QCD has two interesting properties which were discovered experimentally, and predicted by theory. The first is asymptotic freedom [9, 10] - at very high energies or short distances, the strong force becomes weaker and particles can interact more freely. This phenomenon differs from the behavior of electromagnetism and the weak force. The reason for asymptotic freedom lies in the way that gluons interact with each other. As discussed previously, gluons carry color charge, which is a property of the strong force analogous to electric charge in electromagnetism. Unlike photons, which carry no electric charge and do not interact with each other, gluons can interact with each other through their color charge. This interaction causes the strong force to become weaker at short distances, because the gluons effectively screen each other's interactions. The second interesting QCD property is confinement - quarks and gluons cannot exist in isolation, but must exist in bound, color neutral states. While confinement is phenomenologically well-established, and consistent with everything observed so far experimentally, there is no analytical proof<sup>1</sup>. Both of these properties can be seen in the measurements of  $\alpha_s$ , the QCD coupling constant which describes the strength of the strong interaction as a function of  $Q^2$ , the energy scale. The relationship between

---

<sup>1</sup>In fact, it is one of the seven Millennium Prize Problems defined by the Clay Mathematics Institute, with a \$1,000,000 USD prize for its solution.

$\alpha_s$  and  $Q$  is shown in figure 1.2. At low  $Q$ , corresponding to large distances,  $\alpha_s$  appear to

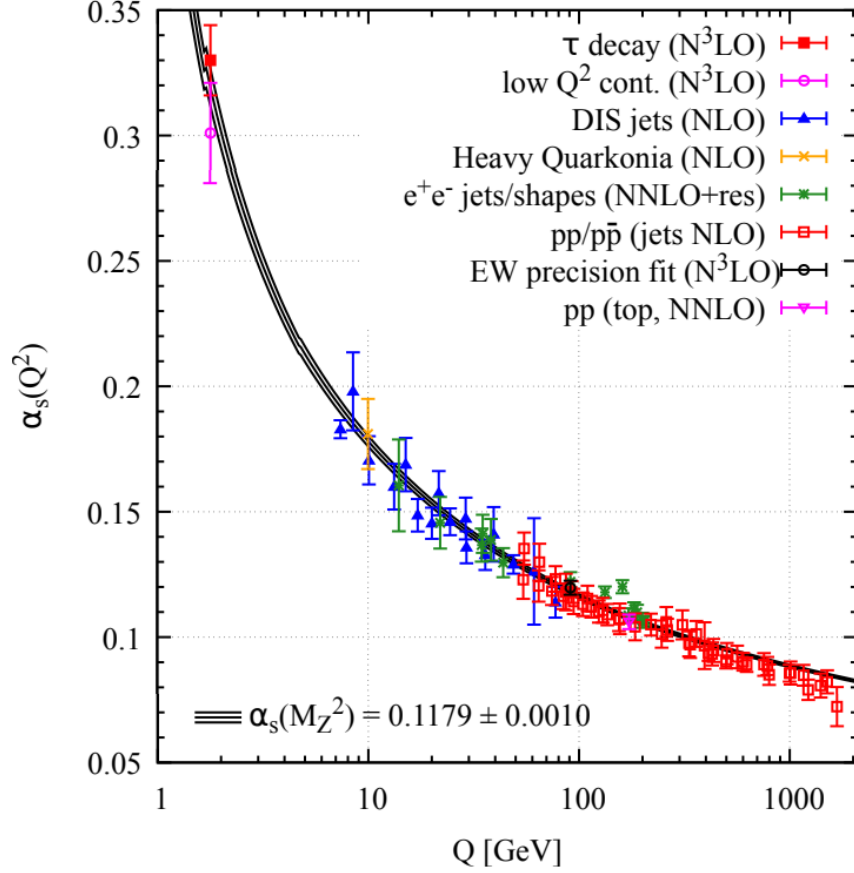


Figure 1.2: Various measurements of  $\alpha_s$  as a function of  $Q$  along with a fit function. Image from ref [11]

asymptotically approach infinity. If two partons were pulled apart, the  $\alpha_s$  will continue to increase with the distance until it is energetically more favorable for a quark-antiquark to be produced out of vacuum. On the other end, as  $Q$  increases and the distance between the partons shrinks, the strength of the strong force become weaker. This phenomena is exactly what was predicted to be asymptotic freedom. The coupling constant can be written as a function of the energy scale as

$$\alpha_s(Q^2) = \frac{4\pi}{(11 - \frac{2}{3}N_f) \ln \frac{Q^2}{\Lambda_{QCD}}} \quad (1.1)$$

where  $N_f$  is the number of quarks, and  $\Lambda_{QCD}$  is a constant which roughly indicates the scale at which the perturbatively defined coupling would diverge [11].

So far, our QCD discussion has been focused on intuitively understanding the strong interaction and exchange of color between quarks and gluons. Now, we bring in the mathematical foundation to have a more rigorous understanding of QCD. The starting point of understanding the behaviour of any system is by using a Lagrangian function. The QCD Lagrangian is the mathematical expression that describes the behavior of quarks and gluons (equation 1.2).

$$\mathcal{L}_{QCD} = \sum_q^{n_f=6} \bar{\psi}_{q,a} (i\gamma^\mu \partial_\mu - g_s \gamma^\mu t_{a,b}^c \mathcal{A}_\mu^c - m_q \delta_{a,b}) \psi_{q,b} - \frac{1}{4} F_{\mu\nu}^A F^{A\mu\nu} \quad (1.2)$$

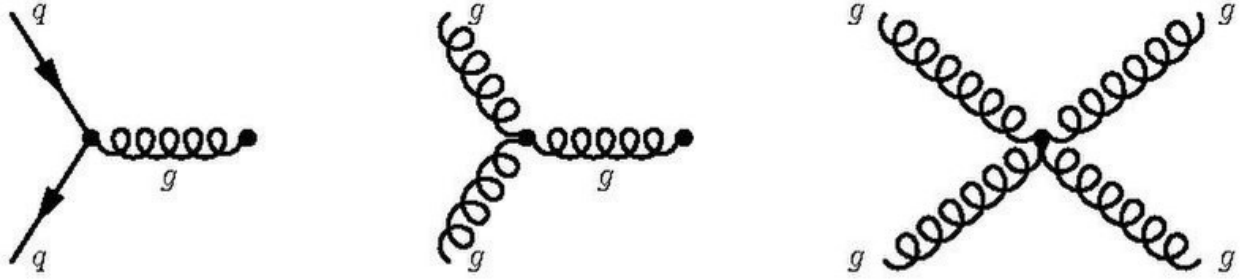
The Lagrangian contains the quark-field spinors ( $\psi_{q,a}$ ), which are four element column matrices which describe spin 1/2 particles with indices for  $n_f = 6$  quark flavor ( $q$ ) and  $n_c = 3$  quark colors ( $a$ ). The gluon fields are described by  $\mathcal{A}_\mu^c$ , where  $c$  is the 8 gluon colors [1]. There also needs to be a term which can describe the strong interaction performed by mediating gluons, essentially table 1.1, but now in matrix form:  $t_{a,b}^c$ , which are eight  $3 \times 3$  matrices (known as the Gell-Mann matrices) which generate the SU(3) group. The set of all unitary matrices with a determinant of 1 forms the SU(3) group under the group operation of matrix multiplication. SU(3) is the chosen group for QCD because gauge transformations are preserved, i.e. the color charge due to the gluon interactions is conserved.  $g_s$  is the QCD coupling constant. The coupling constant is sometimes written as  $\alpha_s = \frac{g_s}{4\pi}$ , where  $\alpha_s$  is the same coupling constant as mentioned previously in equation 1.1.  $\gamma^\mu$  are the Dirac  $\gamma$ -matrices.  $F_{\mu\nu}^A$  is the gluon field tensor with the full form

$$F_{\mu\nu}^A = \partial_\mu \mathcal{A}_\nu^A - \partial_\nu \mathcal{A}_\mu^A - g_s f_{ABC} \mathcal{A}_\mu^B \mathcal{A}_\nu^C, \quad (1.3)$$

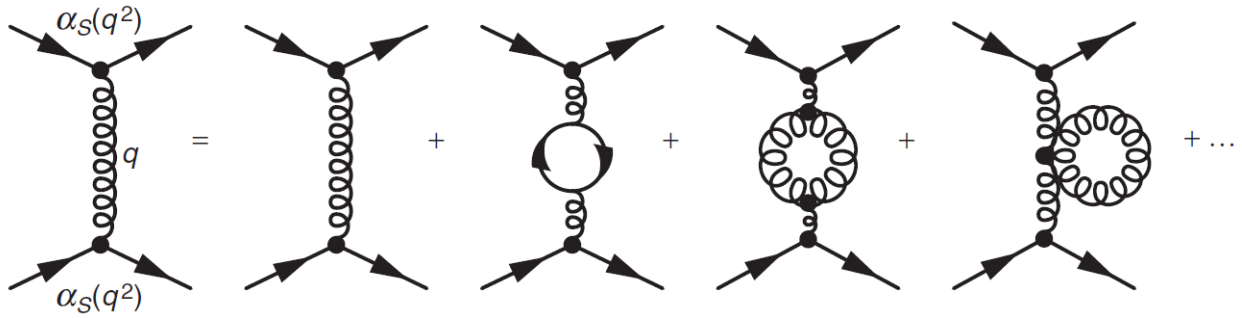
where  $f_{ABC}$  are the structure constants of the SU(3) group. Since SU(3) is a non-abelian group, the commutative property does not hold. The structure constants arise from the commutation relation between the Gell-Mann matrices and are defined as  $[t^A, t^B] = i f_{ABC} t^C$ .

Since gluons can interact with each other, there are additional vertices in the Feynman diagram. The vertex on the left in figure 1.3a is the quark-gluon vertex, analogous to a lepton-photon vertex for QED. Since gluons self-interact via their color, there are now three gluon and 4 gluon vertices as well. Similar to QED, gluons can also have loops in the Feynman diagram. Some examples of gluon loops are shown in figure 1.3b. Leading order calculations use Feynman diagrams without any loops, while next-to-leading order calculations start including loop diagrams as well. The more loops are in diagrams the higher the order. Gluon self-interaction lets the gluon densities within nucleons grow exponentially large at higher energies, potentially giving rise to new states of matter.

The existence and nature of strong interactions has been confirmed by many experiments, including scattering experiments and studies of nuclear decay. QCD is a very complex theory, and it is still an active area of research in particle physics with many open questions. One of the most active fields in studying QCD using heavy ion collisions to investigate hot and cold nuclear matter.



(a) QCD Feynman diagram vertices. Image from ref [12]



(b) QCD Feynman diagram gluon loops. Image from ref [1]

## 1.2.2 Methods for QCD calculations

QCD observables can be calculated using both perturbative and non-perturbative methods depending on the energy scale. QCD Feynman diagrams where the a gluon can be replaced with a photon can be calculated simply using QED Feynman rules, while including the color factors for quarks and gluons. For example, comparing the QED fermion-photon vertex ( $-ie\gamma^\mu$ ) to the QCD fermion-gluon vertex ( $-g_s\gamma^\mu t^c$ ) shows that only changes are a different coupling constant and the Gell-Mann matrices ( $t^A$ ) which act on the color part of the quark wave function. The comparison also holds for the propagators. The QCD gluon propagator ( $-\frac{ig_{\mu\nu}}{q^2}\delta^{ca}$ ) is similar to the QED photon propagator ( $-\frac{ig_{\mu\nu}}{q^2}$ ) with an added delta-function. The delta-function ensures that the gluon emitted at vertex  $\mu$  is the same as the gluon absorbed at vertex  $\nu$  [1]. Since gluons can interact with themselves, there are QCD Feynman diagrams where the gluon cannot be treated as a photon with a color factor correction. In these cases, perturbative QCD is used.

In perturbative QCD (pQCD), the strong coupling constant ( $\alpha_s$ ) is renormalized using some renormalization energy scale  $\mu_R$ . The renormalization group equation, also called beta-function, is used to encode the dependence of  $\alpha_s$  on  $\mu_R$  as seen in equation 1.4.

$$\mu_R^2 \frac{d\alpha_s}{d\mu_R^2} = \beta(\alpha_s) = -(b_0\alpha_s^2 + b_1\alpha_s^3 + \dots) \quad (1.4)$$

The beta function is expanded in terms of  $\alpha_s$  and the coefficients  $b_i$  are called loop corrections

of the beta function such that  $b_0$  is the 1-loop coefficient,  $b_1$  is the 2-loop coefficient, and so on. The negative sign of the beta function gives rise to asymptotic freedom. At next-to-leading order (NLO), the beta-function is  $-b_0\alpha_s^2$ , and substituting in the value of  $b_0 = (11n_c - 2n_f)/(12\pi)$ , where  $n_f$  is the number of quark flavours and  $n_c$  is the number color charges, results in equation 1.5 [11].

$$\mu_R^2 \frac{d\alpha_s}{d\mu_R^2} = [(11n_c - 2n_f)/(12\pi)]\alpha_s^2 \quad (1.5)$$

Solving the equation 1.5 for  $\alpha_s$  and evaluating  $\alpha_s$  at  $\mu_R = Q^2$  results exactly into equation 1.1. As mentioned previously,  $\Lambda_{QCD}$  defines where energy scale at which perturbation cannot be used since  $\alpha_s$  becomes to large and renormalization group equation diverges. Experimentally,  $\Lambda_{QCD}$  has been measured to be around 200 MeV [13]. To conclude, as seen in figure 1.2, as  $Q$  increases,  $\alpha_s$  decreases, and at small values of  $\alpha_s$  the strong interactions are weak making pQCD calculations are possible.

Unfortunately, pQCD is not applicable at all energies or in all collision systems. Cross sections are prominent observable for QCD. Fully inclusive cross sections, (e.g.  $e^+e^- \rightarrow$ ) hadrons can be calculated using pQCD, but pQCD breaks down for many deep inelastic scattering (DIS) (e.g.  $ep \rightarrow e + X$ ) cross sections with initial state hadrons [11]. This holds true even for high energy proton+proton collisions at the Relativistic Heavy Ion Collider (RHIC) and the Large Hadron Collider (LHC). In fact, most pp collisions are soft, i.e. the momentum transfer of the colliding partons is small. The soft collisions arise from the exchange of a low energy gluon even if the collision centre-of-mass energy is large (in the GeV or TeV ranges). A non-perturbative method called lattice QCD is needed to calculate QCD observables.

In lattice QCD, Euclidean space-time is discretized into a lattice as seen in figure 1.4. The points represent the vertices of the lattice, where quark fields are placed. The lattice spacing,  $a$ , is the distance between the vertices, where gluon fields are placed. Calculations can be performed for a continuum instead of a discrete lattice by taking the limit  $a \rightarrow 0$ . Lattice QCD calculations are executed by numerically computing path integrals between the vertices of the lattice. Unlike pQCD, where the gauge must be fixed, lattice QCD is gauge invariant. Gauge transformation of quarks and antiquarks are  $q(x) \rightarrow q(x)V(x)$  and  $\bar{q}(x) \rightarrow \bar{q}(x)V^\dagger(x)$ , where  $V(x)$  is an element of  $SU(3)$ , and  $x$  is space-time position on the lattice vertex. Two quarks, located at two adjacent vertices, can be connected using the gluon fields such as  $\bar{q}(x)U_\mu(x)q(x+a\hat{\mu})$ , where  $\hat{\mu}$  is the unit vector in same  $\mu$  direction as the gluon field as seen in figure 1.4. The gluon fields are responsible for connecting any quark vertex, located at  $x$ , with an adjacent quark, located at  $x+a\hat{\mu}$ . The full action around the square in figure 1.4 is given by

$$S_g = \beta \sum_{x,\mu,\nu} \left[ 1 - \frac{1}{3} \text{ReTr}[U_\mu(x)U_\nu(x+a\hat{\mu})U_\mu^\dagger(x+a\hat{\nu})U_\nu^\dagger(x)] \right], \quad (1.6)$$

where  $U_\mu$  and  $U_\nu$  are the gluon fields in the  $\mu$  and  $\nu$  directions, and  $\beta$  is lattice coupling [11]. Replacing the sum for an integral leads back to continuum QCD. Like pQCD, Lattice QCD

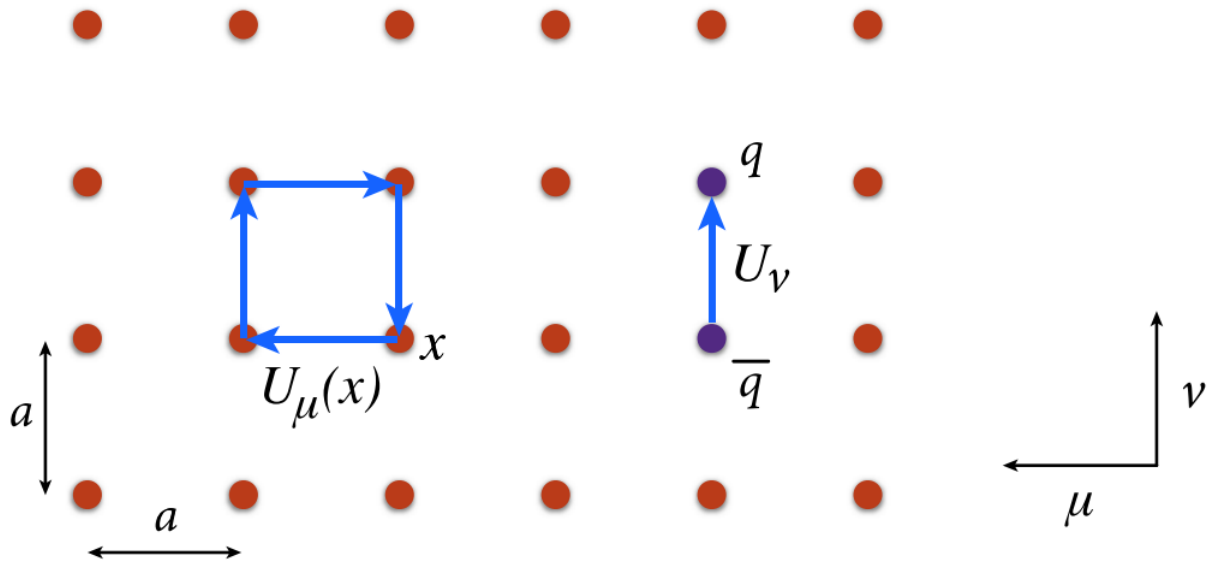


Figure 1.4: A slice of the lattice comprised of discretized space-time with lattice spacing  $a$ . Quark fields are placed on the vertices, while the gluon fields ( $U_i$ , where  $i = \mu$  or  $\nu$ ) are placed between the vertices. Image from ref [11]

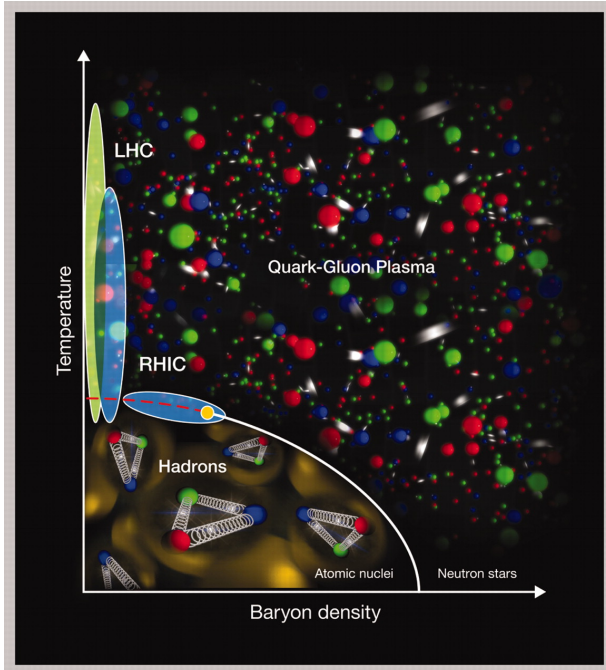
also has its limitations. Besides requiring large amounts of computational resources and efficiency algorithms, Lattice QCD is also limited by the discretization uncertainty due to the non-zero values of  $a$ .

### 1.3 Hot nuclear matter

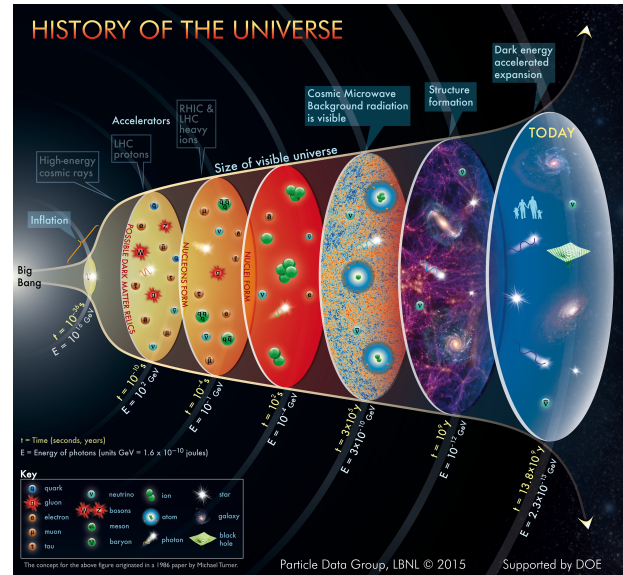
Hot nuclear matter refers to a state of nuclear matter that is at extremely high temperatures and/or densities. This can occur in various situations, such as in the early universe, and in heavy ion collisions at particle colliders. At high temperatures and densities, the individual nucleons that make up atomic nuclei can no longer be treated as individual particles, but instead become part of a collective system known as a quark-gluon plasma (QGP) [14]. In the extremely high density and pressure environment created during relativistic heavy ion collisions, the quarks and gluons are no longer bound within hadrons, but in a deconfined state. This makes the properties of the QGP very different from those of ordinary nuclear matter. As seen in figure 1.5a, QGP can be created as a result of high temperatures or high baryon densities. Hot QGP is created as a result of the high temperatures produced in heavy-ion collisions. The cores of neutron are predicted to contain QGP, but this QGP is supposed to be a result of high density, instead of high temperatures.

Quark-gluon-plasma existed roughly one microsecond ( $10^{-6}$  s) after the Big Bang. As





(a) A cartoon illustrating the QCD phase diagram. Image from ref [14].



(b) The history of the universe: from the big bang to now. Image from ref [15]

seen in figure 1.5b, between  $10^{-6}$  s to  $10^{-4}$  s after the Big Bang, as the universe expanded and the soup of quarks and gluons cooled, it condensed into the hadronic states seen today as seen in figure 1.5a.

### 1.3.1 Heavy-ion collisions

In order to study QGP, heavy ions are accelerated and collided at very high energies. At the RHIC and the LHC, gold and lead ions are collided respectively. Figure 1.6 shows the process of ions colliding, leading to the production of QGP. Due to Lorentz contraction, instead of colliding spheres, the ions are flattened into thin disks with a diameter of 14 fm, as seen at the time of  $-5 \text{ fm}/c$  [16]. Each dish is comprised of many quarks, antiquarks, and gluons with three more quarks compared to antiquarks per nucleon. The distribution of the partons is not uniform across each disk. These spatial variations occur due to the fluctuations in the instantaneous parton distributions within in each nucleon in the nuclei. As the color fields of the two discs collide, color charge is exchanged between the discs, and color fields are generated longitudinally, in the direction of the heavy-ion beams. While the discs are receding, the longitudinal color fields fill the space between the discs, reducing the energy in the discs. While most of the partons interactions involve little momentum transfer, a small fraction of the incident partons have hard interactions with large momentum transfers. These hard interactions produce high  $p_T$  particles, such as the photons measured in this thesis.

The collision of two highly Lorentz contracted nuclei results in the maximum energy density. The system is predicted to achieve equilibrium around  $1 \text{ fm}/c$  after the collision has occurred. At the thermal equilibrium temperature of QGP ( $300 \text{ MeV}$ ), lattice QCD calculates an energy density of  $12.7 \text{ GeV}/\text{fm}^3$  ( $\approx 12 T^4$ ), approximately 20 times larger than the energy density of  $500 \text{ MeV}/\text{fm}^3$  inside a hadron. Long with the increase in energy density, there is also an increase in the entropy. Before the collision, the initial state only has the two discs resulting in negligible entropy, but in the final state, after the collision, there can be  $\approx 30,000$  particles [16]. As seen in right cartoon of figure 1.6, there is staggering difference in the number free particles at time of  $-5 \text{ fm}/c$  and time of  $50 \text{ fm}/c$ .

As the discs recede from each other, the QGP expands and cools hydrodynamically as a relativistic fluid. The longitudinal color fields are still present and more quarks and gluons are being created. This results in new QGP forming in the wake of the discs as seen in figure 1.6. The right figure also shows the evolution of QGP in space-time indicating that the hottest QGP is at high rapidity ( $y$ ). Due to the small specific viscosity ( $\eta/s \approx 0.08 - 0.20$ ) [17] of QGP, the expansion and cooling process is isentropic. Once the QGP cools to  $155 \text{ MeV}$ , the QGP undergoes a phase transition to hadrons. Once inelastic scattering of the hadrons has stopped, the QGP is said to have undergone chemical freeze-out. The hadrons still scatter elastically until the temperature drops to  $95 \text{ MeV}$ , where thermal freeze out occurs [16]. After the thermal freeze out, the momentum of the hadrons is fixed and hadrons move freely.

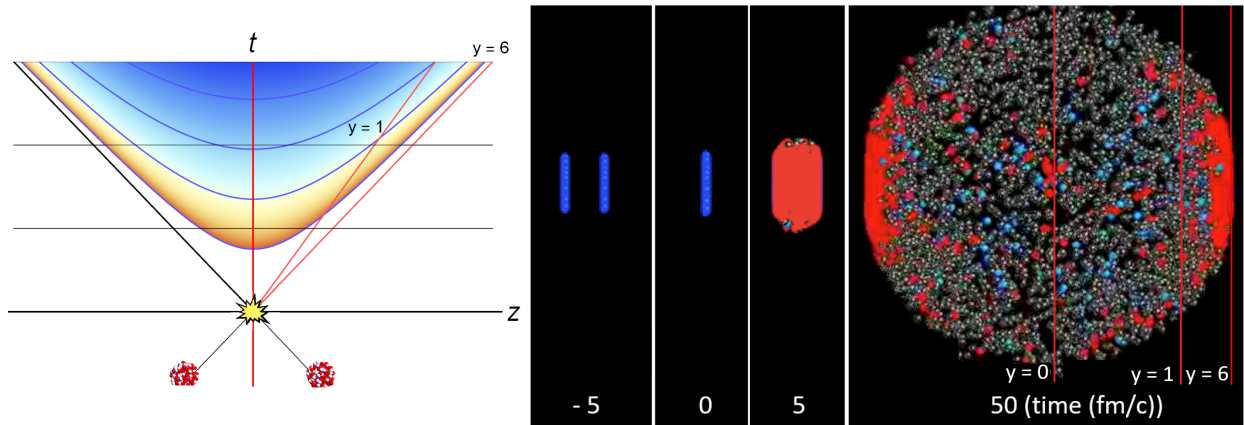
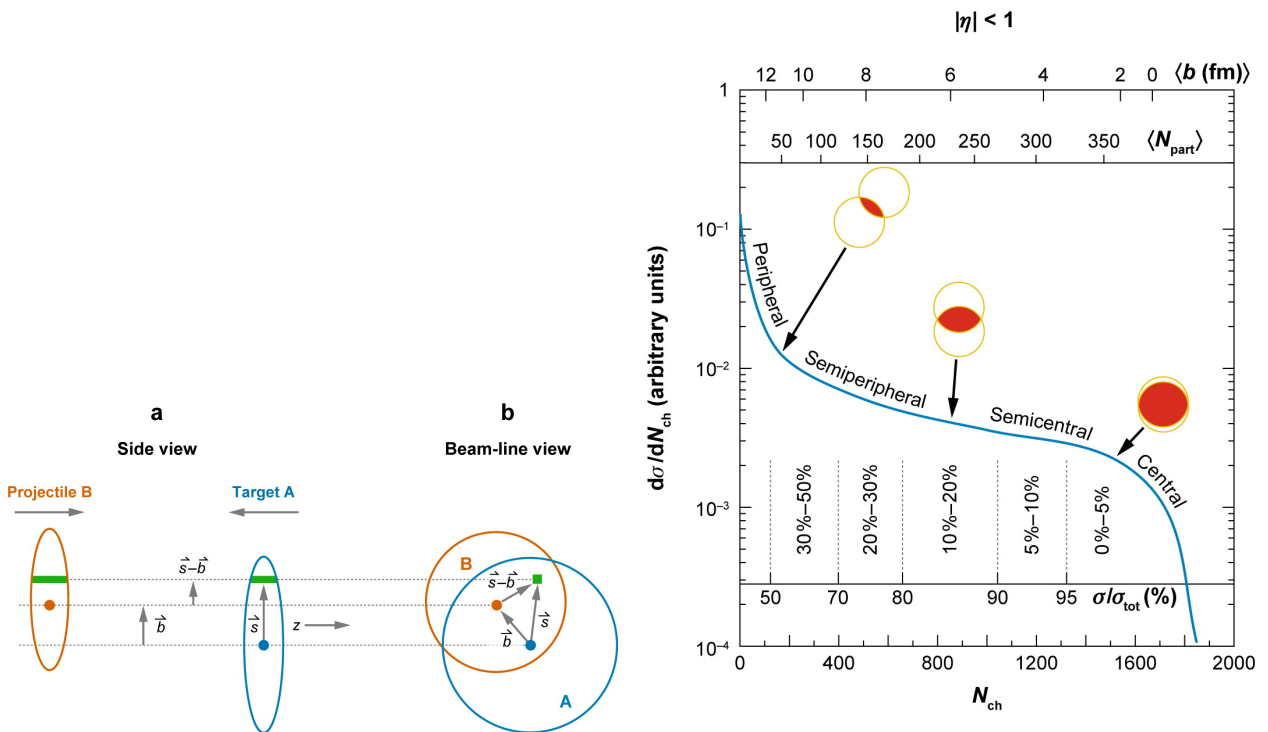


Figure 1.6: The production of quark gluon plasma in space-time plane with the color indicating the temperature of the plasma (left). The process of Lorentz contracted heavy-ion discs colliding to create QGP at different times (right). Hadrons are represented by the blue and grey spheres, while the QGP is represented by red spheres. Images from ref [16]. The  $y$  in this figure is rapidity, the measure of relativistic velocity.

### 1.3.1.1 Centrality

So far, the images in figure 1.6 used to describe the heavy-ion collisions indicate that two Lorentz contracted discs with colliding head-on. This is not always case. There will be collisions where two discs will collide only partially. In order to determine the initial geometry of the collision, centrality will be introduced.

Figure 1.7a shows two colliding nuclei from transverse and longitudinal views. For heavy-ion collider experiments, such as ALICE, the choice of target and projectile is arbitrary. The impact parameter ( $\vec{b}$ ) is the distance between the center of the masses between the two nuclei in the plane transverse to the direction of the beam. From the definition of  $\vec{b}$ , it follows that if the center of masses of the nuclei are closer to each other in the transverse direction, then the magnitude of  $\vec{b}$  would be smaller. Since the  $\vec{b}$  cannot be measured experimentally, it has been calculated from Monte Carlo simulation using a procedure called Glauber model calculation [18].



Miller ML, et al. 2007. Annu. Rev. Nucl. Part. Sci. 57:205–43

(a) The schematic of the Glauber model geometry of a heavy-ion collision with transverse (a) and longitudinal (b) perspectives.

Miller ML, et al. 2007. Annu. Rev. Nucl. Part. Sci. 57:205–43

(b) A cartoon correlating the final state observable  $N_{ch}$  with the impact parameter ( $\vec{b}$ ) and number of participating nucleons ( $N_{part}$ ).

Figure 1.7: Images from ref [18]

The Glauber model calculates the number of participating nucleons ( $N_{part}$ ) and the number of binary collisions ( $N_{coll}$ ) as a function of  $\vec{b}$ . Looking at the beam-line view in figure 1.7a, the overlap region is the area of target A intersected by the area of projectile B. The number of nucleons from A which will collide with nucleons from B are the number of participating nucleons. For example, in the overlap region, if A had five nucleons, and B had 9 nucleons, then  $N_{part}^A = 5$ , and  $N_{part}^B = 9$ . Since the nuclei will pass through each other, all 5 nucleons from A will collide with all 9 nucleons from B resulting in 45 ( $9 \times 5$ ) binary collisions - the  $N_{coll}$ . The Glauber model calculation generates many configurations of figure 1.7a with different  $\vec{b}$ , resulting in distributions of  $N_{part}$  and  $N_{coll}$ . There is an assumption that a monotonic relation exists between the number of the produced particles (multiplicity) and  $N_{part}$  [18]. This assumption is validated experimentally, as there is a history measuring multiplicity of proton-ion collisions using different ions (varying number of nucleons in the nuclei) which is proportional to calculations of  $N_{part}$  to a good approximation [16]. The multiplicity distribution is then divided into percentile classes which determine the centrality of a collision as seen in figure 1.7b<sup>2</sup>. To summarize, centrality is used to estimate the impact parameter and provides a picture of the initial geometry of a heavy-ion collisions. The initial geometry of the collision gives rise to final state momentum anisotropies in the QGP.

### 1.3.2 Anisotropic collective flow

Strong correlations have been observed between particles widely separated in rapidity with momenta in different direction. Azimuthal correlations have been extensively studied as a function of the centrality, particle type, rapidity,  $p_T$ , and fluctuations in the initial geometry of each collision. Azimuthal correlations are measured using the azimuthal angle ( $\varphi$ ) which is centered around the beam axis (z-axis), and defined in spherical coordinates as:  $\varphi = \arccos \frac{z}{\sqrt{x^2+y^2+z^2}}$ . Using the coordinate system shown in figure 1.8 panel (a),  $\varphi$  is the angle between z-axis and the magenta line from the origin. These azimuthal correlations can be well explained using relativistic hydrodynamics.

The collective behavior of QGP was very surprising. The initial expectations were that QGP was predicted to be a weakly coupled gas at equilibrium. It was possible that the interactions between partons were so weak that a thermal equilibrium would never be reached due to asymptotic freedom and the high energies probed at RHIC and LHC. Additionally, QCD is strongly coupled at the energy scales within an order of magnitude of the confinement/deconfinement scale. After the experiments at RHIC, it has been realized that this QCD temperature range describes a strongly coupled relativistic liquid, and a not weakly coupled gas of free particles [20, 21]. There must have been weak coupling at early times in

---

<sup>2</sup>The figure defines hard cut offs for the centrality bins (such as 0%-5% or 20%-30%) and labels the bins as central, semicentral, etc, but in reality, the centrality bins and labels are not that rigid. Some papers will define central 0%-5%, others define is as 0%-10%. There is even more variance in centrality percentiles for semicentral

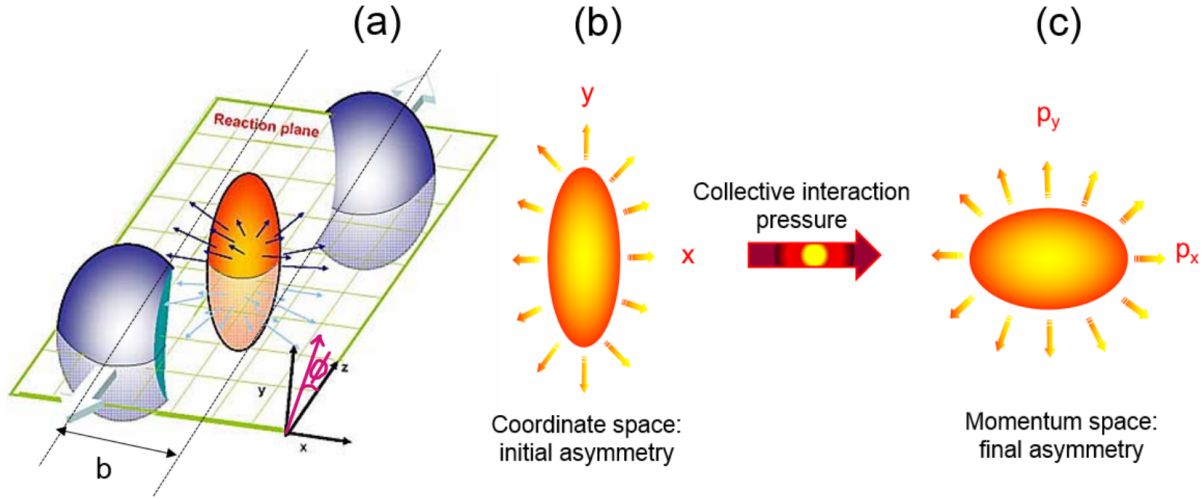
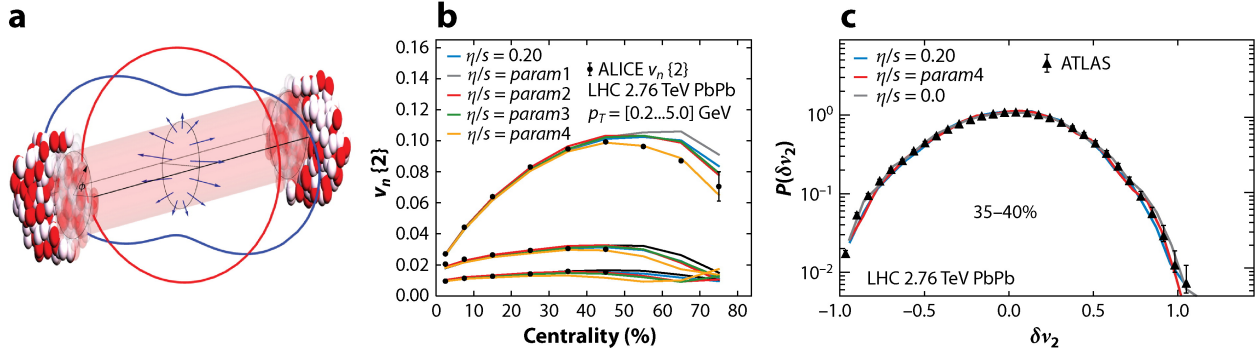


Figure 1.8: Panel (a) presents schematically the collision zone between two incoming nuclei. Panel (b) illustrates initial-state anisotropy in the collision zone converting into final-state elliptic flow, and panel (c) measured as anisotropy in particle momentum. Image from ref [19]

the collisions, but the duration of the weak coupling in the initial moments of a RHIC or LHC collision is an open question.

The anisotropy of the particles in heavy-ion collisions shows that QGP is a strongly coupled liquid, not a weakly coupled gas. As mentioned previously in section 1.3.1, the distribution of partons in the nucleons and nucleons in the nuclei is not uniform. This leads to initial state anisotropies. If the QGP was a gas of weakly interacting partons, then scatterings would be rare, expansion of QGP would be associated with random motion of the partons, and the azimuthal distribution of particles in the final state ends up close to isotropic. But, if the QGP was a strongly coupled liquid<sup>3</sup>, then hydrodynamics would convert the initial state anisotropies, which leads to pressure gradients, into the final state momentum anisotropies. For perfectly circular collisions (a central collision), the anisotropies would strictly arise from the non-uniform distributions of partons within the nuclei. However, for peripheral collisions, the overlap region of the two nuclei is asymmetric as seen figure 1.8 panel (a), where an elliptically shaped overlap region is produced. The asymmetry of the overlap region leads to pressure gradients which cause more particles to flow in the direction of the reaction plane (green grid). The reaction plane is defined by two vectors: the impact parameter ( $\vec{b}$ ) and beam direction ( $\vec{z}$ ). Panels (b) and (c) of figure 1.8 illustrate how the initial state asymmetry of the overlap region in position space is converted into final state asymmetry in momentum space via the pressure gradients. To quantify the azimuthal momentum anisotropy, a Fourier transformation is performed on the angular distribution of final state hadrons. The Fourier transformation results in anisotropic flow coefficients  $\bar{v}_n$ ,

<sup>3</sup>spoiler - it is



Busza W, et al. 2018.  
Annu. Rev. Nucl. Part. Sci. 68:339–76

Figure 1.9: Panel (a) shows the collision and isotropy (red curve) and anisotropy (blue curve) in case of a weakly interacting gas or a liquid being formed. Panel (b) shows ALICE measured of  $v_n$  with  $n = 2, 3$  and  $4$  from top to bottom. Panel (c) shows comparisons of ATLAS's  $v_2$  measured event-by-event. Image from ref [16]

defined as,

$$\frac{d\bar{N}}{d\varphi} = \frac{\bar{N}}{2\phi} \left( 1 + 2 \sum_{n=1}^{\infty} \bar{v}_n \cos n(\varphi - \bar{\Psi}_n) \right), \quad (1.7)$$

where  $\varphi$  is the azimuthal angle, defined previously, centered around the beam axis and in the transverse plane as seen panel (a) of figure 1.9.  $\bar{N}$  is the average number of particles in the event<sup>4</sup>.  $\bar{\Psi}_n$  are the event plane angles with respect to the beam direction. The event plane is an estimate of the reaction plane since the reaction plane cannot be measured experimentally as it defined using the impact parameter. Panel (b) of figure 1.9 shows the measurements of the flow coefficients  $v_2$ ,  $v_3$ , and  $v_4$  as a function of centrality. As the collisions become less central, there is an increasing  $v_2$ , indicating a hydrodynamical evolution. The amplitude of elliptic flow grows with as centrality percentiles increase because the overlap region of the incoming nuclei becomes more asymmetric. The higher Fourier components of the angular distribution arise from fluctuations in the initial positions of the nucleons inside the nuclei as seen in figure 1.10 [14]. The impact of the initial state is also seen in figure 1.9, panel (c) which shows the event-by-event distribution of  $v_2$  for semicentral collisions. These measurements serve as an excellent way to constrain the initial conditions of the hydrodynamical models.

Shear viscosity ( $\eta$ ) determines how easily momentum can be exchanged between distant particles in a fluid. Larger shear viscosity implies that gradients in the fluid velocity will dissipate into heat faster. The specific viscosity ( $\eta/s$ ), defined as the ratio of the shear viscosity to entropy density, measures the effects of the shear viscosity on the fluid. Smaller values of specific viscosity corresponds to the fluid have more "liquidness". This ratio is dimensionless in Planck units where  $\hbar$  and  $k_B$  are set to 1. The magnitude of the flow

<sup>4</sup>An event is the results after a collision or interaction occurs between particles

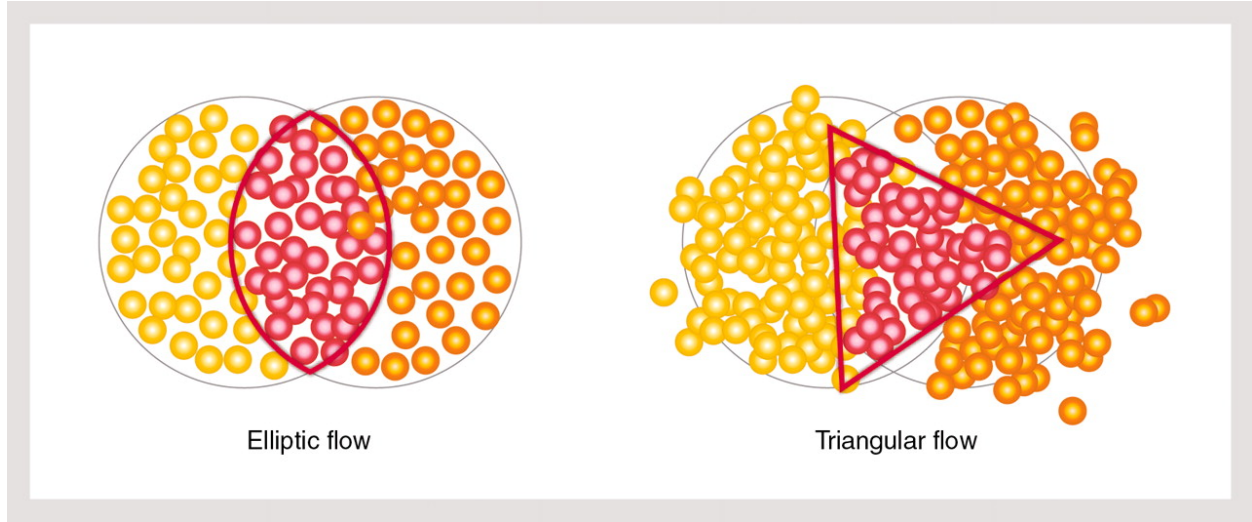


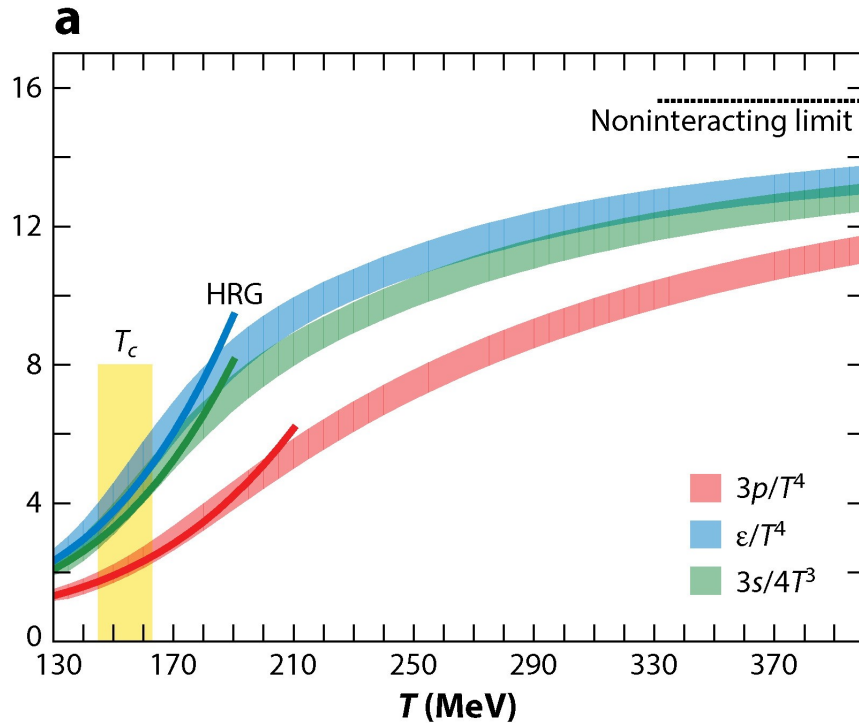
Figure 1.10: The image is a cartoon illustrating elliptic flow ( $v_2$ ) and triangular flow ( $v_3$ ). Image from ref [14]

coefficients,  $v_n$  should be sensitive to the viscosity of the plasma. Specific viscosity controls how rapidly gradients introduced in the initial conditions are dissipated into heat. This means that the comparisons of hydrodynamic calculations to data using different values for the specific viscosity in hydrodynamics (figure 1.9 panels b and c) can be used to constrain the value of specific viscosity. Lattice QCD calculations can be used to calculate initial condition values for parameters of the QCD equation of state such as pressure, energy density, and entropy density as seen in figure 1.11.

Simulation can be used along with the initial conditions to calculate the specific viscosity of QGP. The specific viscosity of QCD is estimated to be 0.08-0.20 [17], which is very close to the theoretical limit of  $\eta/s = 1/4\pi$ . Due to the very low specific viscosity, the quark-gluon-plasma is called the perfect liquid.

## 1.4 Cold nuclear matter effects

In heavy-ion collisions, the final state is effected by medium related effects due to the presence of QGP as well as initial state effects from the structure of the collision. These effects arising from the structure of the initial state of the collision are called cold nuclear matter effects. Understanding and separating cold nuclear matter effects from final state effects will lead to a better understanding of QGP effects.



Busza W, et al. 2018.  
*Annu. Rev. Nucl. Part. Sci.* 68:339–76

Figure 1.11: ) Lattice QCD calculations (colored bands) of the pressure  $P$ , energy density  $\epsilon$ , and entropy density  $s$  of hot QCD matter in thermal equilibrium at temperature  $T$ . There is a continuous crossover from hadron gas (colored lines) to QGP at higher temperatures. This crossover phase transition is expected in the low baryon density region of the QCD phase diagram as seen in figure 1.5a by the dashed red lines. Image from ref [16]

### 1.4.1 Deep inelastic scattering

Before studying initial state effects in a large, messy, system such as Pb–Pb, the initial state effects can be better studied in a small, clean system such as electron-proton collisions:  $e + p \rightarrow e + X$ . The leading order Feynman diagram of deep inelastic scattering is seen in figure 1.12. The differential cross section can be written in terms of a few invariant kinematic variables:

- $Q^2 = -q^2$
- $x \equiv \frac{Q^2}{2p_2 \cdot q}$  - this is also known as Bjorken  $x$ , the fraction of the proton momentum carried by the quark struck by the electron



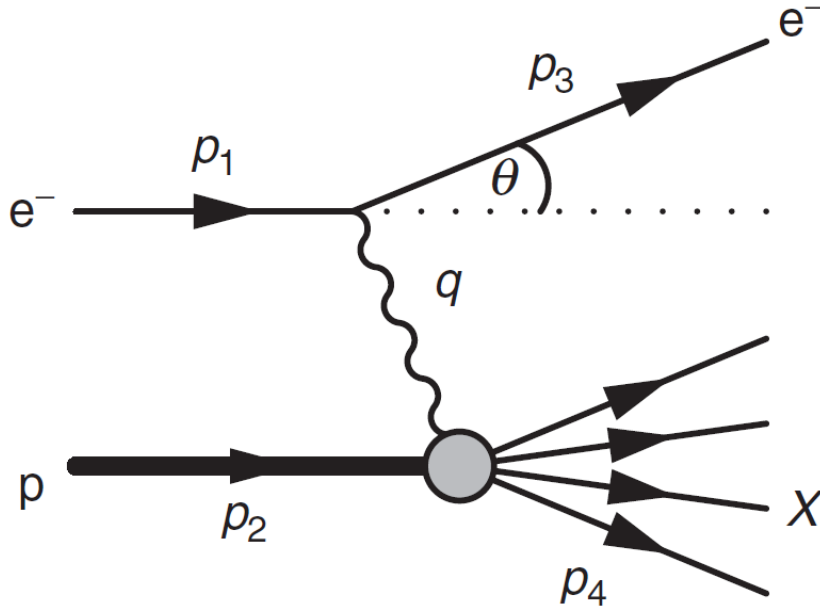


Figure 1.12: The kinematic quantities for deep inelastic scattering. The quantities  $p_1$  and  $p_3$  are the four-momenta of the incoming and outgoing electron,  $p_2$  is the four-momentum of the proton, and  $W$  is the mass of the recoiling system  $X$ . The exchanged particle is a photon which transfers four-momentum  $q^2 = (p_1 - p_3)^2$  to the proton. Image from ref [1]

- $y \equiv \frac{p_2 \cdot q}{p_2 \cdot p_1}$  - this is the inelasticity, the fractional energy lost by the electron in the proton rest frame, i.e.  $1 - \frac{E_3}{E_1}$
- $v \equiv \frac{p_2 \cdot q}{m_p}$  - this is the energy lost by the electron in the proton rest frame, i.e.  $E_1 - E_3$
- $W^2 = p_4^2 = (p_2 + q)^2$  - this is the invariant mass of the hadronic system  $X$

For a fixed center-of-mass energy ( $\sqrt{s}$ ), the kinematics of the inelastic scattering can be defined using two independent variables of the four invariant variables:  $Q^2, x, y, v$ , since  $x = \frac{Q^2}{2m_p v}$ ,  $Q^2 = (s - m_p^2)xy$ , and  $y = (\frac{2m_p}{s - m_p^2})v$ , where  $s = (p_1 + p_2)^2$ . Since  $y$  is proportional to  $v$ , they are not independent to each other and cannot be chosen as the pair to define the kinematics of the inelastic scattering. Since two independent variables are required, the cross section can be expressed in terms of these two variables. The cross section for  $ep \rightarrow eX$  inelastic scattering, mediated by one virtual photon is given by,

$$\frac{d^2\sigma}{dx dQ^2} = \frac{4\pi\alpha^2}{Q^4} \left[ \left(1 - y - \frac{m_p^2 y^2}{Q^2}\right) \frac{F_2(x, Q^2)}{x} + y^2 F_1(x, Q^2) \right], \quad (1.8)$$

where  $\alpha$  is the electromagnetic coupling and  $F_1(x, Q^2)$  and  $F_2(x, Q^2)$  are known as proton structure functions. The structure functions encode the interaction between the photon and

the proton. Structure functions are not calculable in pQCD. The cross section can be slightly simplified if the scattering has  $Q^2 \gg m_p^2 y^2$  into

$$\frac{d^2\sigma}{dx dQ^2} = \frac{4\pi\alpha^2}{Q^4} \left[ (1-y) \frac{F_2(x, Q^2)}{x} + y^2 F_1(x, Q^2) \right] \quad (1.9)$$

The first studies of the structure functions were performed at the Stanford Linear Accelerator Center using electron scattering inelastically off a liquid hydrogen target, and the differential cross section was measured over various ranges of electron energy [1]. The experimental results revealed that two interesting features. The first feature was that both  $F_1(x, Q^2)$  and  $F_2(x, Q^2)$  were almost independent of  $Q^2$ ,

$$F_1(x, Q^2) \rightarrow F_1(x) \text{ and } F_2(x, Q^2) \rightarrow F_2(x) \quad (1.10)$$

The lack of  $Q^2$  dependence indicates that electron is scattering of another a point-like particle in the proton. The dependence of the structure functions only on the momentum fraction is also referred to as Bjorken scaling. The second feature was that  $F_1$  and  $F_2$  are not independent of each other, but related as  $F_2(x) = 2xF_1(x)$ . The reasoning for this relation is explained using the idea that inelastic  $e + p$  scattering is actually elastic  $e + q$  scattering. The electron is probing the electric and magnetic contribution of the quark to the scattering mediated by a virtual photon.

Since the  $e + p$  inelastic scattering can now be treated as a QED scattering of two point-like particles, the Feynman rules can be used to compute the matrix element describing the transition from initial state to final state of the electron and quark scattering ( $e + q \rightarrow e + q$ ).

$$M_{fi} = \frac{Q_q e^2}{q^2} [\bar{u}(p_3) \gamma^\mu u(p_1)] g_{\mu\nu} [\bar{u}(p_4) \gamma^\nu u(p_2)] \quad (1.11)$$

$$\langle |M_{fi}|^2 \rangle = 2Q_q^2 e^4 \left( \frac{s^2 + u^2}{t^2} \right), \quad (1.12)$$

where  $s = p_1 + p_2$ ,  $t = p_1 - p_3$  and  $u = p_1 - p_4$  are the Mandelstam variables. The transition matrix can be related to the cross section using

$$\frac{d\sigma}{d\Omega^*} = \frac{1}{64\pi^2} \frac{p_f^*}{p_i^*} |M_{fi}|^2, \quad (1.13)$$

where  $p_i^*$  and  $p_f^*$  are initial and final state momenta in the center-of-mass frame. Combining equations 1.11-1.13 along with a variable change from  $\Omega^* \rightarrow dq^2 \rightarrow dQ^2$  results in

$$\frac{d\sigma}{dQ^2} = \frac{2\pi\alpha^2 Q_q^2}{Q^4} \left[ (1-y) + \frac{y^2}{2} \right], \quad (1.14)$$

which resembles cross section expressed using structure functions (equation 1.9). While equation 1.9 describes the cross section as an electron probing the electric and magnetic distributions within a proton, equation 1.14 describes the cross section in terms of the elastic scattering of an electron and a quark.

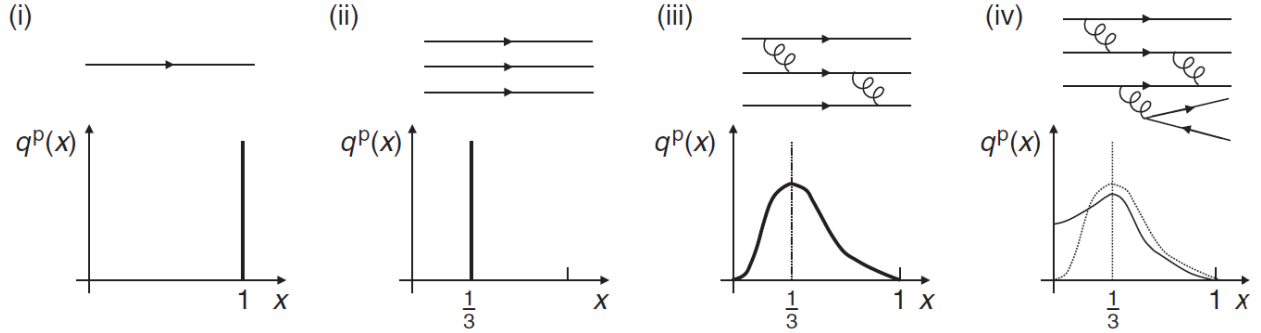


Figure 1.13: Examples of different quark PDFs: (i) a single point-like particle, (ii), three quarks, each having  $1/3$  of the proton's momentum, (iii) three quarks exchanging momentum via gluons, (iv) same as (iii), but with higher order interactions. Image from ref [1]

## 1.4.2 Parton distribution functions (PDFs)

### 1.4.2.1 Proton PDFs

In a relativistic nucleon, the quarks interact with each other via the exchange of gluon, creating more quarks and gluons. Thus, there is a distribution of quarks and gluons within the nucleon. These distributions are modelled using Parton Distribution Functions (PDFs). For example, the PDF of the down quark in a proton can be expressed as  $d^p(x)\delta x$ , which represents the number of down quarks within the proton with momentum fractions in the range  $x$  to  $x + \delta x$ . The quark and gluon PDFs are not calculated from first principles, but can be determined by analysing experimental DIS and hard scattering processes results. Figure 1.13 shows four example of potential quark PDFs within a proton. In the case (i), the PDF is simply a Dirac delta function centered at 1. Case (ii) is similar, but the PDF would be a delta function at  $1/3$ , but normalized for three quarks. Case (iii) would be similar to case (ii) with a delta function at  $1/3$ , but with smearing. Case (iv) starts to resemble the NLO quark PDFs which are currently used to describe the quark distributions within a proton.

The  $ep$  DIS cross section has been described using structure functions (equation 1.9) and using the parton model, the idea that a proton is a composite particle comprised of quarks and gluons, by treating the DIS cross section as an elastic  $e + q \rightarrow e + q$  cross section (equation 1.14). The final method to describe a DIS cross section will be using the parton distribution functions. Starting with equation 1.14, which is only a single differential cross section, the elastic scattering of an electron and a quark with a particular quark flavor  $i$ , charge  $Q_i$ , and momentum fraction in the range  $x$  to  $x + \delta x$  is given by,

$$\frac{d^2\sigma}{dQ^2} = \frac{4\pi\alpha^2}{Q^4} \left[ (1-y) + \frac{y^2}{2} \right] \times Q_i^2 q_i^p(x) \delta x, \quad (1.15)$$

where  $q_i^p$  is the PDF for the quark with flavor  $i$ . The double differential cross section is

obtained simply by dividing by  $\delta x$  and summing over all six the quark flavors, resulting in

$$\frac{d^2\sigma}{dx dQ^2} = \frac{4\pi\alpha^2}{Q^4} \left[ (1-y) + \frac{y^2}{2} \right] \sum_i^6 Q_i^2 q_i^p(x). \quad (1.16)$$

Comparing equation 1.9 with equation 1.16, the structure functions can now be defined in terms of the PDFs.

$$F_2(x, Q^2) = 2xF_1(x, Q^2) = x \sum_i^6 Q_i^2 q_i^p(x) \quad (1.17)$$

Looking at the right side of the equation 1.17, there is no  $Q^2$  dependence for the PDF. Using the parton model and PDFs to describe the structure functions naturally predicts Bjorken scaling because no strong  $Q^2$  dependence is expected for an elastic collision of point-like particles. Since PDFs are not calculable from first principles, the relation between the structure functions and PDFs helps extract PDF information from DIS experiments.

#### 1.4.2.2 Nuclear shadowing

Nuclear effects in DIS were thought to be negligible. Quarks were expected to be insensitive to the nuclear environment and the nucleus was viewed as collection of quasi-free nucleons [22]. In 1983, the European Muon Collaboration measured and published the structure functions of iron and deuterium which showed that the structure functions are modified in a larger nucleus [23]. The phenomenon quickly became a hot topic and has been extensively studied since then. To see if the structure function was sensitive to nuclear effects, a structure function of a nuclei was compared with that of a single nucleon scaled by the number of nucleons in the nuclei ( $A$ ) as seen in equation 1.18.

$$R_{F_2}^A(x, Q^2) = \frac{F_2^A(x, Q^2)}{AF_2^{\text{nucleon}}(x, Q^2)}, \quad (1.18)$$

In fact, ratios of the structure function  $F_2(x, Q^2)$  were measured over a large in range in  $x$  as seen by the sketch in figure 1.14. The structure function measured for a bound nucleon is different from the structure function measured of a free nucleon. The quark is somehow sensitive to the binding of its nucleon. The ratio of  $F_2$  is divided into four regions with the range of the region determined by the value of  $x$  when the ratio intersects unity. There are four regions:

- $x > 0.8$  - this region is known as Fermi motion because the behavior of  $R_{F_2}^A$  is attributed to the Fermi motion of nucleons in the nucleus
- $0.3 < x < 0.8$  - this is the EMC effect region named after European Muon Collaboration which experimentally discovered the phenomena
- $0.1 < x < 0.3$  - this region is known as "anti-shadowing" and there is enhancement a few percents above unity

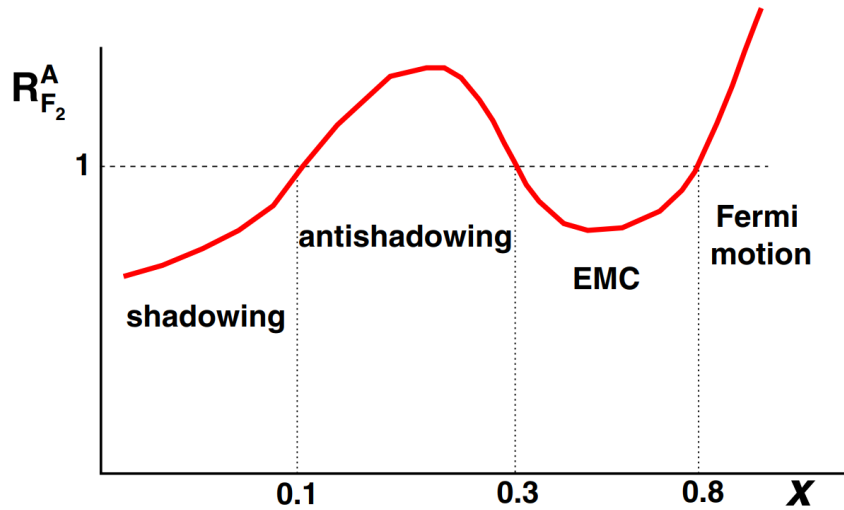


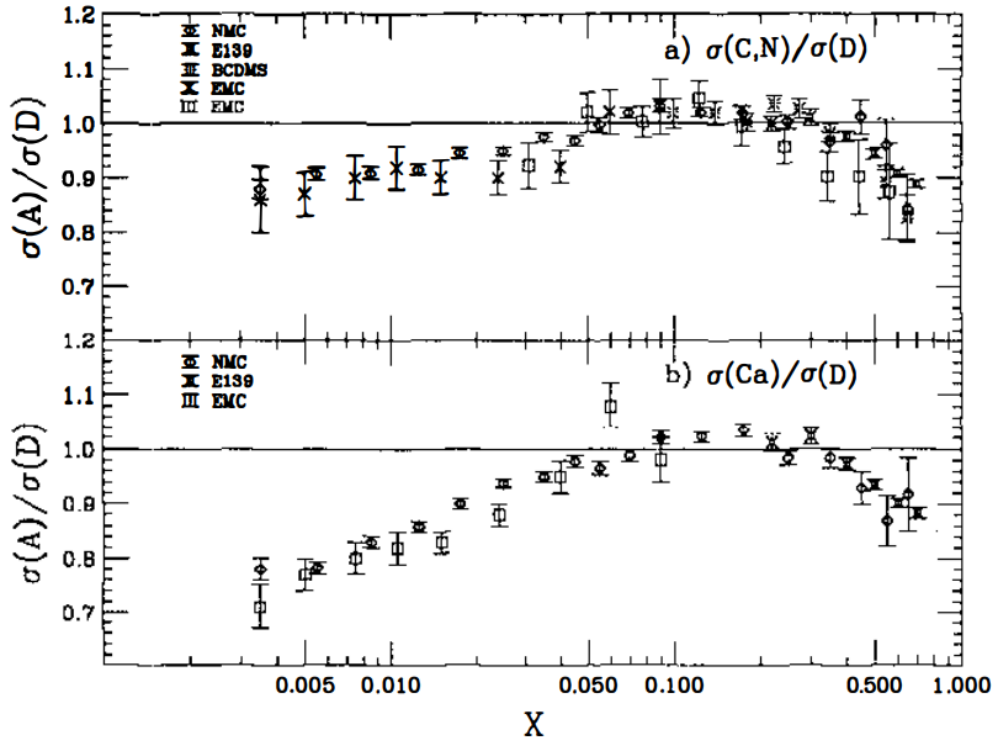
Figure 1.14: A sketch depicting the behavior of the nuclear structure function ratio as a function of  $x$ , for a fixed  $Q^2$ . The magnitude of the deviation from unity is not to scale. Image from ref [24]

- $x < 0.1$  - this region is known as "shadowing" and the ratio here is less than unity

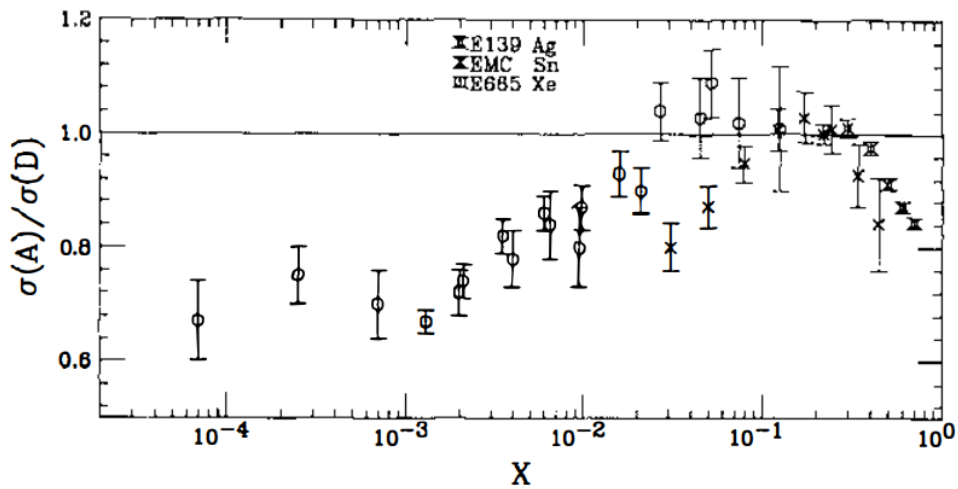
The following sentences will discuss the shadowing effect. The other three effects are not being discussed here since the kinematic reach (in terms of  $x$ ) of the LHC collisions is in the shadowing region [24]. Further details can be found on the other three effects in the references [22, 25] Initially, shadowing and antishadowing were predicted to occur due to the overlap of parton in different nucleons. In the parton model, shadowing is attributed to small- $x$  gluons from different nucleons overlapping in the longitudinal direction. The shadowing region begins when the gluons exceed a longitudinal size larger than the nucleon-nucleon distance, and continues to smaller  $x$  until it reaches a saturation value (not shown in the sketch in figure 1.15). Experimentally, it has been found that shadowing depends on the  $A$ , the number of nucleons in the nucleus as seen in figure 1.15. The mechanisms behind nuclear effects on the structure functions are still open question.

### 1.4.2.3 Nuclear PDFs

Since the structure functions of a bound nucleon are different from those of a free nucleon, the same must be true for PDFs based on 1.17. The nucleus cannot be treated as simple ensemble of  $Z$  protons and  $(A-Z)$  neutrons. Understanding parton distributions for nucleons bound within a nuclei uses nuclear parton distribution functions (nPDFs). Similar to proton PDFs, nPDFs have been determined by global fits to experimental data for hard processes such as deep inelastic scattering on nuclei and nuclear collision experiments. There are many generators for calculating PDFs and nuclear PDFs such as EPS09 [26], HKN07 [27],



(a) Ratios of deep inelastic cross section on targets of (a) carbon and nitrogen, and (b) calcium, compared to deuteron.



(b) Ratios of deep inelastic cross section on targets of tin, xenon, and silver, compared to deuteron.

Figure 1.15: Images from ref [25]

nCTEQ15 [28]. The following general discussion on nPDFs will try to remain as general as possible regarding any equations, but if any specific equations are needed, EPPS16 [29] will be used. The different nPDFs used in this thesis and difference between them will be discussed in chapter 4. The nPDF calculations are performed at NLO using pQCD. The nPDFs are also a function of  $A$ , the number of nucleons in the nucleus. The nPDFs are obtained via fits to experimental measurements such as deep inelastic scattering data, di-lepton and pion production from proton-nucleus collisions, and jet<sup>5</sup> and heavy flavor<sup>6</sup> production data. Most nPDFs relate a bound proton PDF to one free proton PDF using the nuclear modification factor, i.e.

$$f_i^{p/A}(x, Q^2) = R_i^A(x, Q^2) f_i^p(x, Q^2) \quad (1.19)$$

where  $f_i^{p/A}$  is the bound proton PDF for mass number  $A$ ,  $f_i^p$  is the free proton PDF, and  $R_i^A$  is the nuclear modification factor, which quantifies the difference between nuclear effects in a nucleus of mass number  $A$  compared to an ensemble of  $A$  free nucleons. For EPPS16,  $R_i^A$  is defined as piecewise function,

$$R_i^A(x, Q_0^2) = \begin{cases} lra_0 + a_1(x - x_a)^2 & x \leq x_a \\ b_0 + b_1x^\alpha + b_2x^{2\alpha} + b_3x^{3\alpha} & x_a \leq x \leq x_e \\ c_0 + (c_1c_2x)(1x)^{-\beta} & x_e \leq x \leq 1 \end{cases} \quad (1.20)$$

where  $Q_0^2$  is the parameterization scale, and  $\alpha = 10x_a$ . The coefficients  $a_i, b_i, c_i$ , are determined using the small- $x$  limit ( $x \rightarrow 0$ ), the antishadowing maximum at  $x = x_a$  and the EMC minimum at  $x = x_e$ . The bound neutron PDFs ( $f_i^{n/A}(x, Q^2)$ ) for each quark flavor are obtained from the bound proton PDFs. For  $Q^2 > Q_0^2$  the PDFs are obtained by solving the Dokshitzer–Gribov–Lipatov–Altarelli–Parisi (DGLAP) evolution equations. The DGLAP equations describe the variation in PDFs at varying energy scales ( $Q^2$ ), i.e. how the number of partons increase or decrease with time within the nucleon as result of  $(x, Q^2)$ . The structure function ratio of bound proton and neutron is parameterized using different experimental results. Figure 1.16 shows an illustration of the EPPS16 fitting function along with values of the bounds of the piecewise function  $R_i^A$ . It also shows the nuclear modification factors of u, d valence quarks, u, d, s sea quarks and the gluon. For all  $x < 0.05$ , the EPPS central values are all below unity, similar to the fitting function in the shadowing region. Both nCTEQ15 and EPPS15 seem to follow the same trend. The sea up and down quarks and the gluon nuclear modification factor have the smaller uncertainties compared to the valence quarks.

---

<sup>5</sup>a jet is a spray of hadrons created when one parton scatters or radiates other partons and then all the partons hadronize

<sup>6</sup>heavy flavor refers to the three heavier quarks: charm, bottom, and top

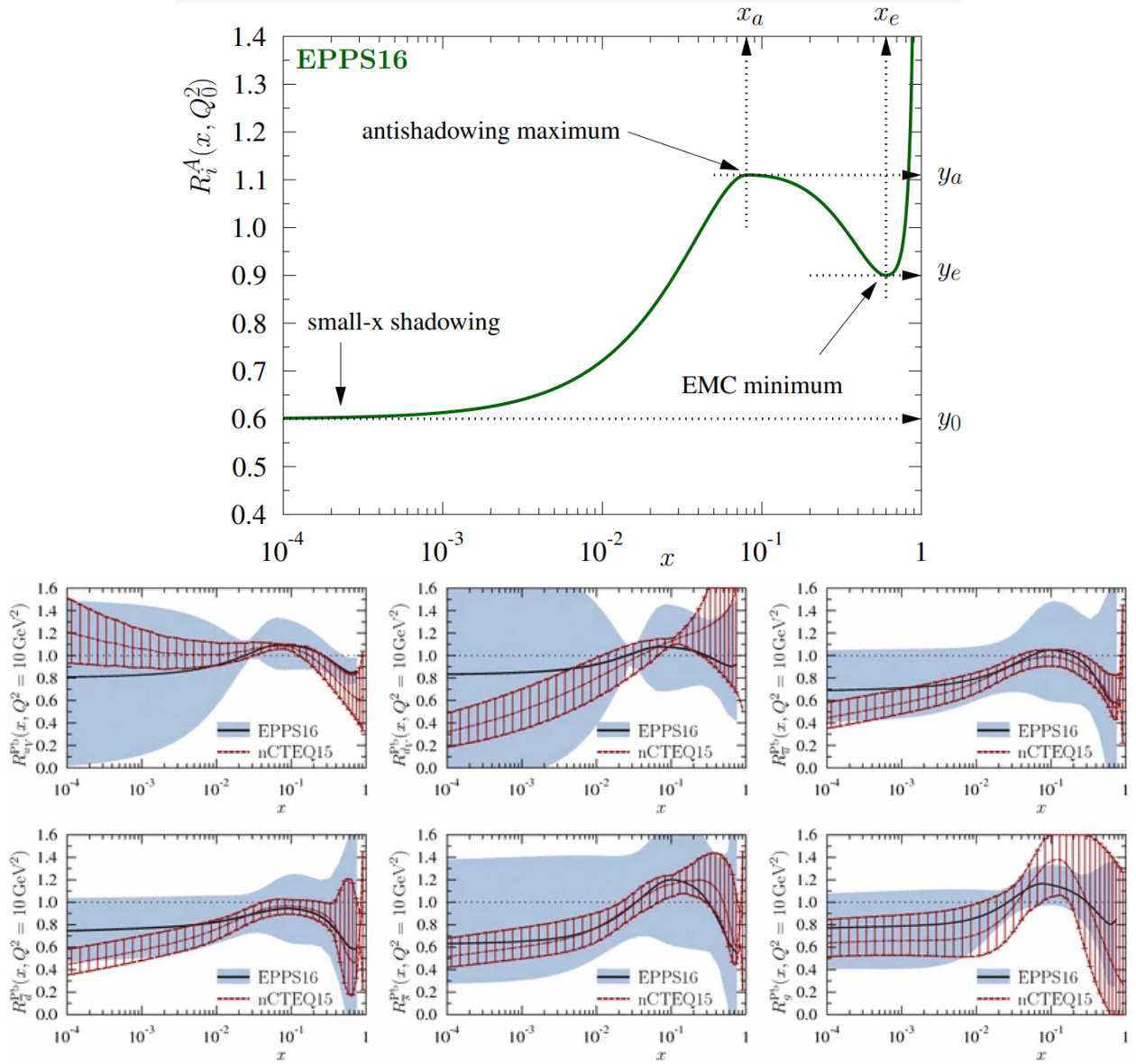


Figure 1.16: Top: An illustration of the EPPS16 fitting function  $R_i^A$ . Bottom: Comparisons of nuclear modification factors for u, d, s quarks and gluon between EPPS16 and nCTEQ15 at  $Q^2 = 10 \text{ GeV}^2$ . Image from ref [29]



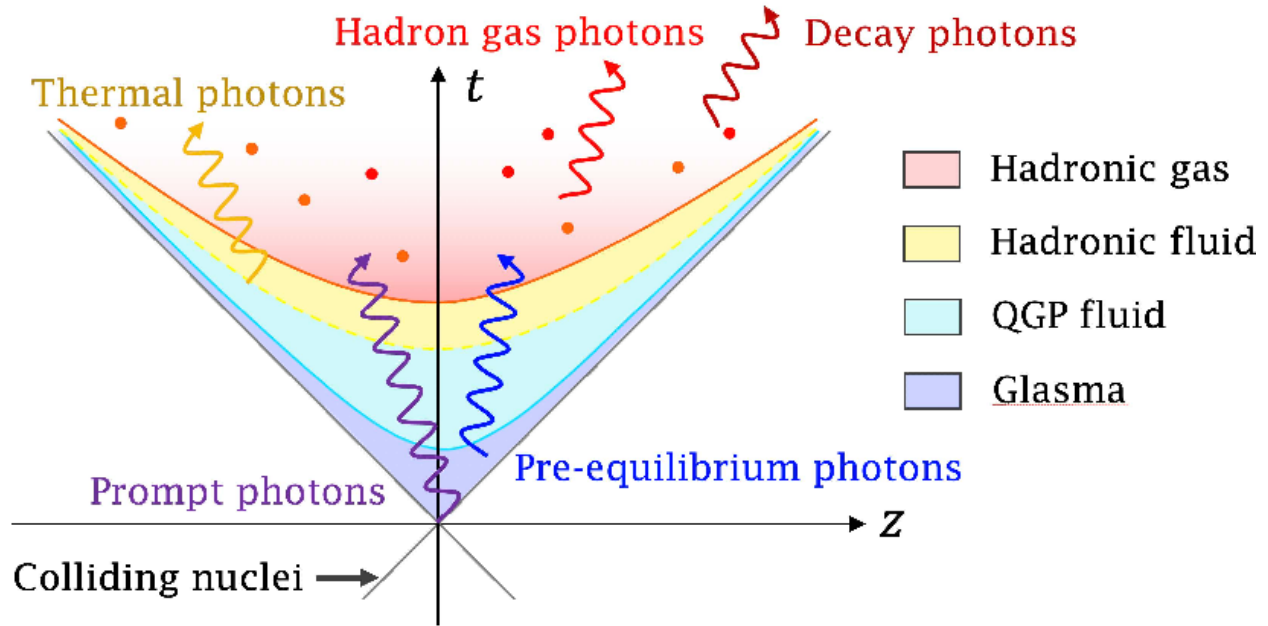


Figure 1.17: The various sources of photon production in heavy ion collisions. The collisions occur around the  $z$ -axis and colors describe the state of the medium at time  $t$ . Image from ref [30]

## 1.5 Photons

In high energy heavy ion collisions, photons can be produced in multiple ways at different stages of the collision. Since photons do not have color charge, they are a unique probe to study the initial state hard scattering as they can reach the detector without interacting in a QCD medium. There is, however, a large background of photons in addition to those produced in the initial hard scattering as seen in figure 1.17. The photons are classified in many different ways:

- prompt photons: these photons are produced at the start of the collisions from hard processes which large momentum transfers
- pre-equilibrium photons: these photons are semi-hard, produced in the initial stages of the QGP
- thermal photons: these are soft photons produced by the radiating QGP
- hadron gas photons: these photons are emitted while the hadrons are interacting with QGP
- decay photons: these photons are a result of hadrons, such as  $\pi^0$ , decaying into photons

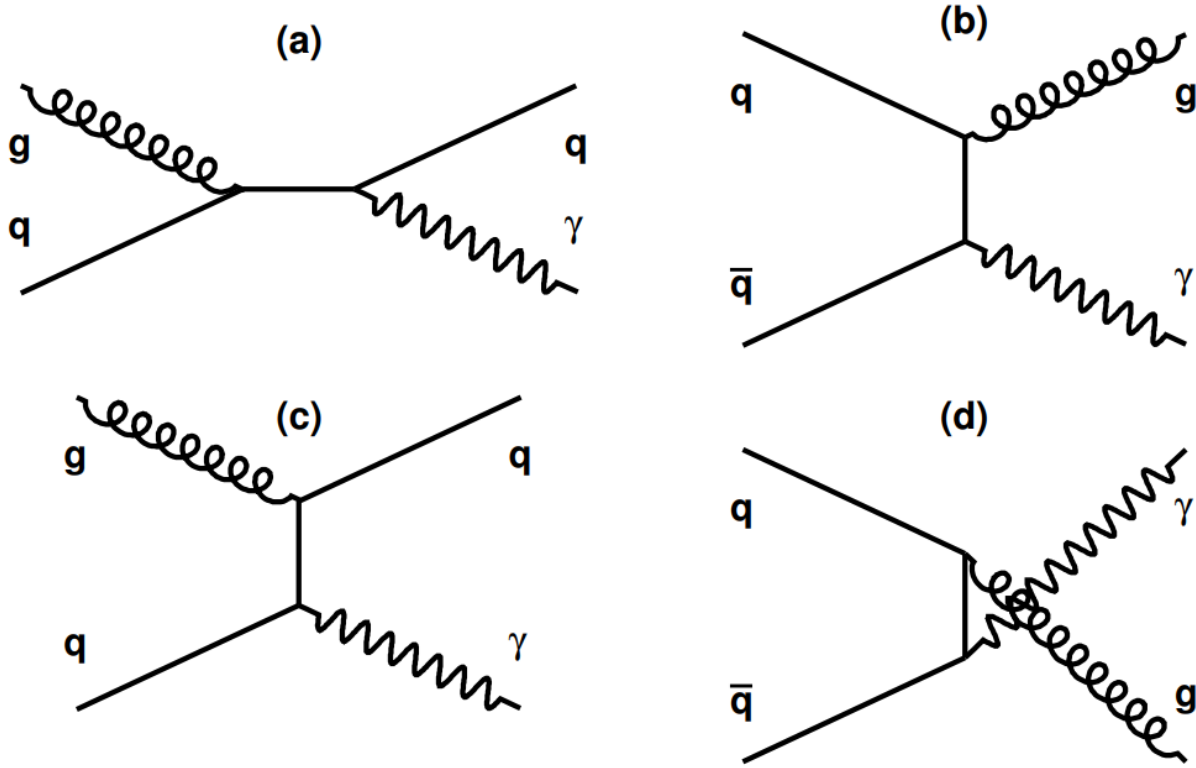
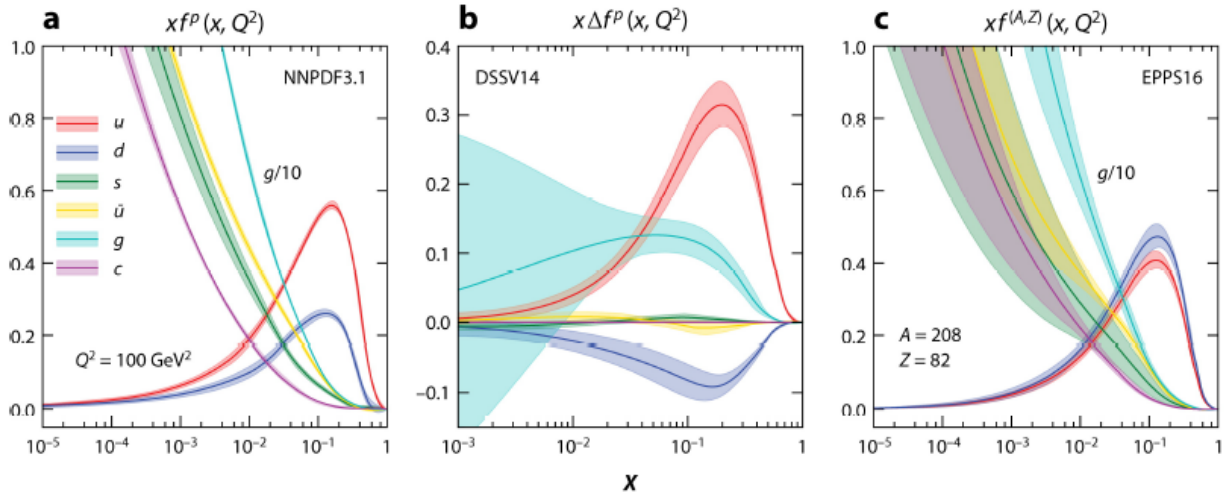


Figure 1.18: Leading order Feynman diagrams for direct photon production: (a) and (c) are Compton scattering, (b) and (d) are quark-antiquark annihilation. Image from ref [31]

The signal photons for this thesis are "direct photons" and "fragmentation photons". At leading order in perturbative QCD, the direct photons are produced in hard scattering processes such as quark-gluon Compton scattering ( $qg \rightarrow q\gamma$ ) (1.18a,c) or quark-antiquark annihilation ( $q\bar{q} \rightarrow g\gamma$ ) (1.18b,d), whereas the fragmentation photons are the product of the collinear fragmentation of a parton ( $q\bar{q}(gg) \rightarrow \gamma + X$ ).

Since there is parton opposite to the photon, that parton will fragment and start to hadronize which will result in spray of hadrons called a jet. Within the jet, there are likely to be neutral pions which will decay into two photons. Such decay photons are the background to the signal photons. Neutral pions produced in soft processes will also decay into double photons, adding to the background for this measurement. At LHC energies, Compton scattering and gluon fusion ( $gg \rightarrow q\bar{q}\gamma$ ) dominate due to the high-gluon density in the proton at small values of Bjorken- $x$ , as seen in figure 1.19 (a, c). At small values of Bjorken- $x$ , the gluon density within the nucleon increases very rapidly which means that QCD Compton scattering will be the dominate leading order photon production process.

Direct and fragmentation photons have no physical meaning beyond the leading order description and cannot be factorized; the sum of their cross sections is the physical observable.




 Ethier JJ, Nocera ER. 2020.  
Annu. Rev. Nucl. Part. Sci. 70:43–76

Figure 1.19: Parton distribution functions for unpolarized protons (a), polarized protons (b), and lead nucleic (c). Image from[32]

These photons serve as a control since they are not expected to interact with the medium. Hadrons will interact with the medium and any modification in hadron observables such as energy,  $p_T$ , angular distributions, etc can be identified by comparing the same observable with photons. For example, the photon cross section can be compared to the jet cross section to understand how the jets are affected by the QGP. The comparison between p–Pb and Pb–Pb data disentangles effects due to the quark-gluon plasma and “cold-nuclear matter” effects such as modification of parton distribution functions in nuclei, as well as elastic, inelastic and coherent multiple parton scattering processes inside a large nucleus. This is because final-state effects associated with the quark-gluon plasma are expected to be absent or suppressed in p–Pb collisions<sup>7</sup>.

<sup>7</sup>This statement is not 100% true. Recently, there has been measurements of QGP signatures, such as azimuthal anisotropy and  $J/\psi$  suppression, in small systems such as pp and p–Pb [33]. However, the presence of QGP in small systems is an open question and a hotly debated topic.

## Chapter 2

# ALICE: A Large Ion Collider Experiment

### 2.1 The Large Hadron Collider

The European Organization for Nuclear Research (CERN) is located at the border between France and Switzerland, near the Swiss city of Geneva. Founded in 1954, CERN has expanded our understanding of nature with many scientific breakthroughs in the fields of particle and nuclear physics such as the discovery of the W and Z bosons, and the Higgs boson [7, 8] just to name a few. CERN has built multiple research facilities and accelerators in order to advance the frontiers of the Standard Model such as the Large Electron-Positron collider and Super Proton–Antiproton Synchrotron which operated in the past, and the Large Hadron Collider which is currently operational.

The Large Hadron Collider (LHC) is largest and highest energy particle accelerator in the world. It is located in a tunnel 175 m underground mostly in France at the French-Swiss border. The tunnel has a circumference of 27 km, with a cross-sectional diameter of 3.8 m. Inside the tunnel, there are two beam pipes in which the proton or ion<sup>1</sup> beams travel in opposite direction and intersect that one of the four intersection points. The LHC uses more than 10,000 superconducting magnets to accelerate, shape, and focus the beams. There are more than 1200 dipole magnets and almost 400 quadrupole magnets which are kept at temperatures around 1.9 K. To maximize the chances for collisions, the LHC collides particles in bunches. In order to keep the particles bunched together, there are eight radio frequency cavities per beam. There are 2802 bunches per proton beam [34], and 733 bunches per ion beam [35]. The proton and ion beams are accelerated to a maximum energy of 6.5 TeV and 2.56 TeV/nucleon, respectively.

Before the particle beams enter the LHC, the particles are accelerated through a series of accelerators which gradually ramp up the energy of the beams as shown in figure 2.1.

---

<sup>1</sup>The LHC has collided lead ( $^{208}\text{Pb}^{82+}$ ) and xenon ( $^{129}\text{Xe}^{54+}$ ) ions, but in this thesis, ion(s) will be used to indicate lead ions

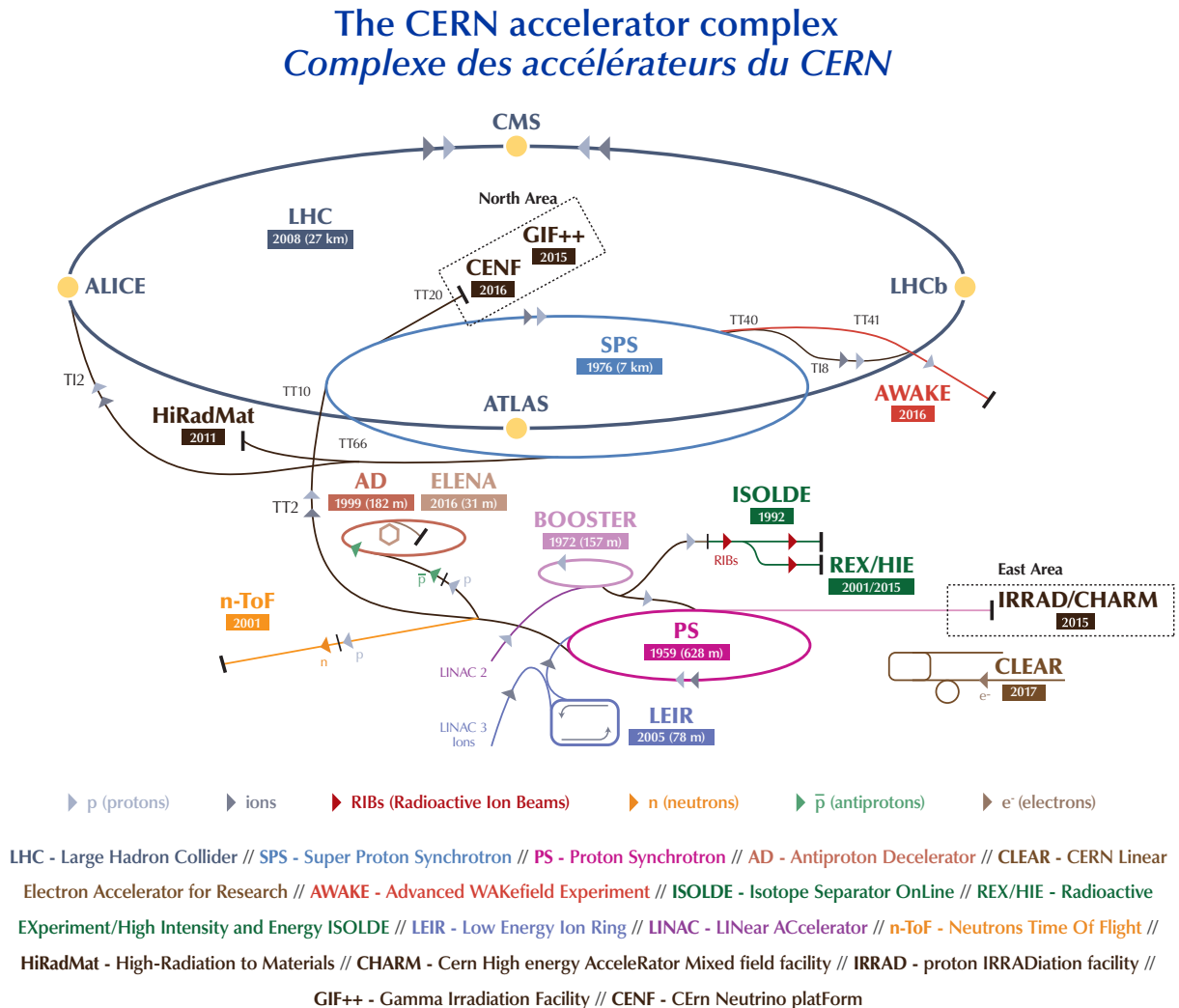


Figure 2.1: CERN accelerator complex. Image from ref [36].

The journey of the protons begins from a bottle of hydrogen gas where the hydrogen atoms are converted into  $H^-$  ions, stripped of their electrons by passing through a carbon foil, and accelerated to an energy of 50 MeV in the linear accelerator, Linac2. Next, the protons travel from Linac2 to the Proton Synchrotron Booster (Booster) where they reach an energy of 1.4 GeV, then to the Proton Synchrotron (PS) which accelerates the protons to 25 GeV. The penultimate accelerator in the chain is the Super Proton Synchrotron (SPS) which accelerates the protons to 450 GeV, and leads to the proton injection into the LHC. The ions have the same destination, but a different origin from the protons. Metallic lead is evaporated into a gas and moved into a plasma chamber. Some of the electrons are stripped

due to the interactions of the lead gas and the plasma. The lead ions accelerated to a starting energy of 4.2 MeV/nucleon in the linear accelerator, Linac3. The Low Energy Ion Ring (LIER) takes the ions from the Linac3 and accelerates them to the 72 MeV/nucleon. On the way from the Linac3 to the LIER, the lead ions pass through a stripper foil which removes more electrons, and the remaining electrons are removed in the PS. Now, the ions experience the same accelerator chain as the protons; they reach 5.9 GeV/nucleon in the PS, and 177 GeV/nucleon in the SPS before being injected into the LHC.

The proton and ion beams moving opposite directions in two separate rings inside the LHC. The two beams are kept separate while they move around the LHC, only to intersect and collide at specific points on the LHC called interaction points (IP). The LHC has eight interaction points as seen in figure 2.2. Four interaction points are currently used by the four large detectors. The four large detectors at each interaction are ATLAS [38] at IP1, ALICE [39] at IP2, CMS [40] at IP5, and LHCb [41] at IP8. Each of these detectors are operated by large, international collaborations, with same name as the detector, consisting of more than 100 different countries and 1000 scientists, engineers, and staff.

The operation of the LHC is separated in long term period knows as LHC Runs, and in-between the LHC Runs, there are Long Shutdown during with both the LHC as well as the different detectors upgrade, repair, and prepare the hardware for the upcoming LHC Run. LHC Run 1 started in 2009 and ended in 2013, followed up the Long Shutdown 1 which lasted for two year, until the start of LHC Run 2 in 2015. LHC Run 2 ended in 2018, followed by Long Shutdown 2 (2018-2022). The third operational run, LHC Run 3, just started this past year with higher proton energies and luminosity. The data used in this thesis are from LHC Run 1 and LHC Run 2.

## 2.2 The ALICE experiment

ALICE (A Large Ion Collider Experiment) is one of the four large detectors at the LHC, and it is operating at IP2. It is a general-purpose detector with a focus on understanding quantum chromodynamics (QCD), the physics of strong interactions, using heavy-ion collisions. ALICE is optimized to study quark-gluon-plasma (QGP), the strongly interacting matter created during heavy-ion collisions. The detector is designed with subsystems specialized for measuring different observables. A list and location of all the different subsystems of the ALICE detector is shown in figure 2.3. The scale of the detector can be estimated based on reference humans shown in the figure. The detector weighs approximately ten thousand tons with overall dimensions of  $16 \times 16 \times 26\text{m}^3$  [39].

The ALICE coordinate system is defined by setting the z-axis parallel to the beam pipe, the x-axis points towards the center of the circle created by the LHC rings, and y-axis points up, perpendicular to both the x-axis and z-axis, towards the sky. Since ALICE has a barrel design, it is more natural to use an altered spherical coordinates, where the radial axis ( $r$ ) and azimuthal angle ( $\varphi$ ) are the standard transformations of the Cartesian coordinates  $x$  and  $y$ , but instead of polar angle ( $\vartheta$ ), pseudorapidity is used instead. Pseudorapidity ( $\eta$ ) is

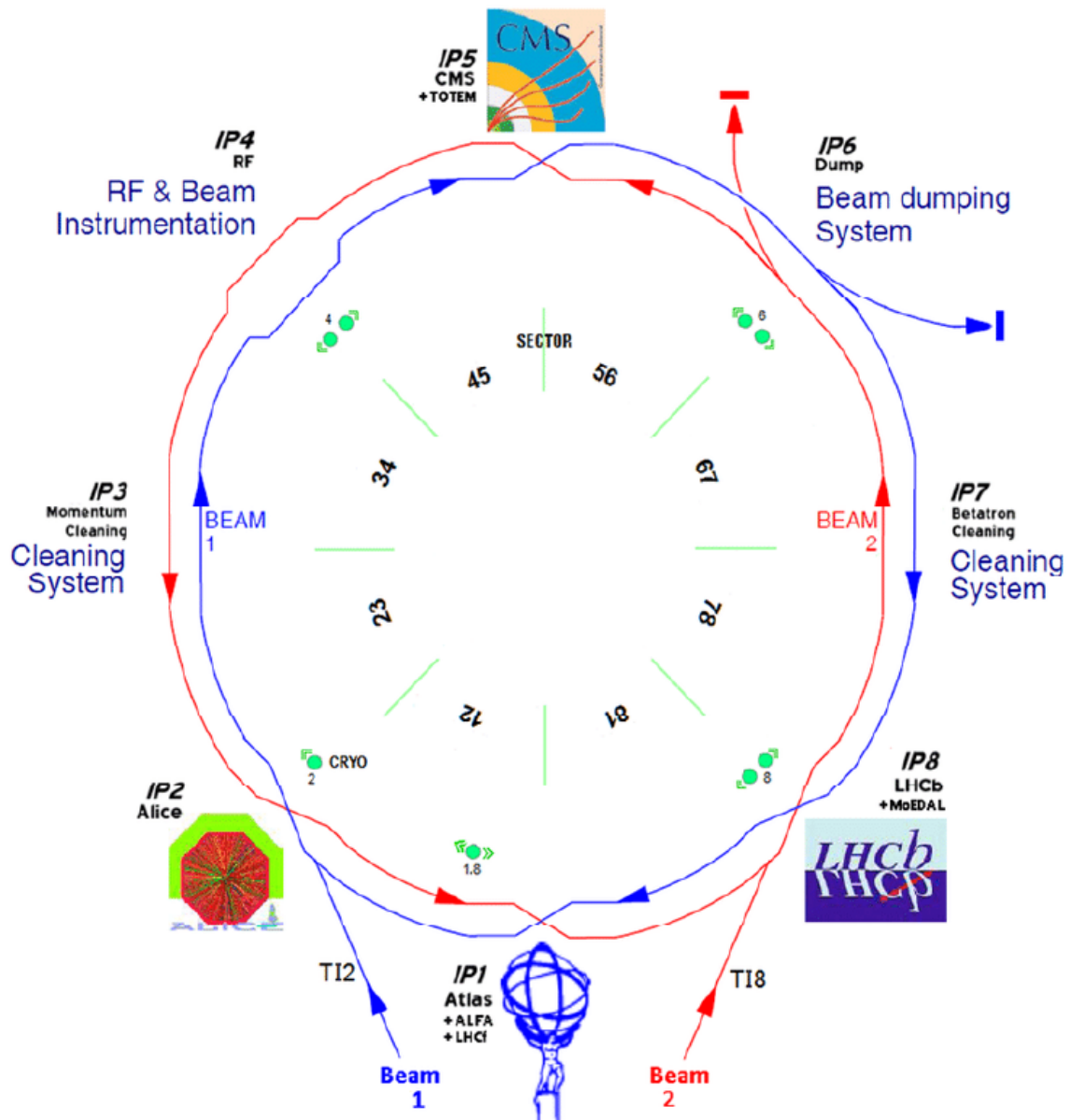


Figure 2.2: LHC interaction points. Image from ref [37].

## THE ALICE DETECTOR

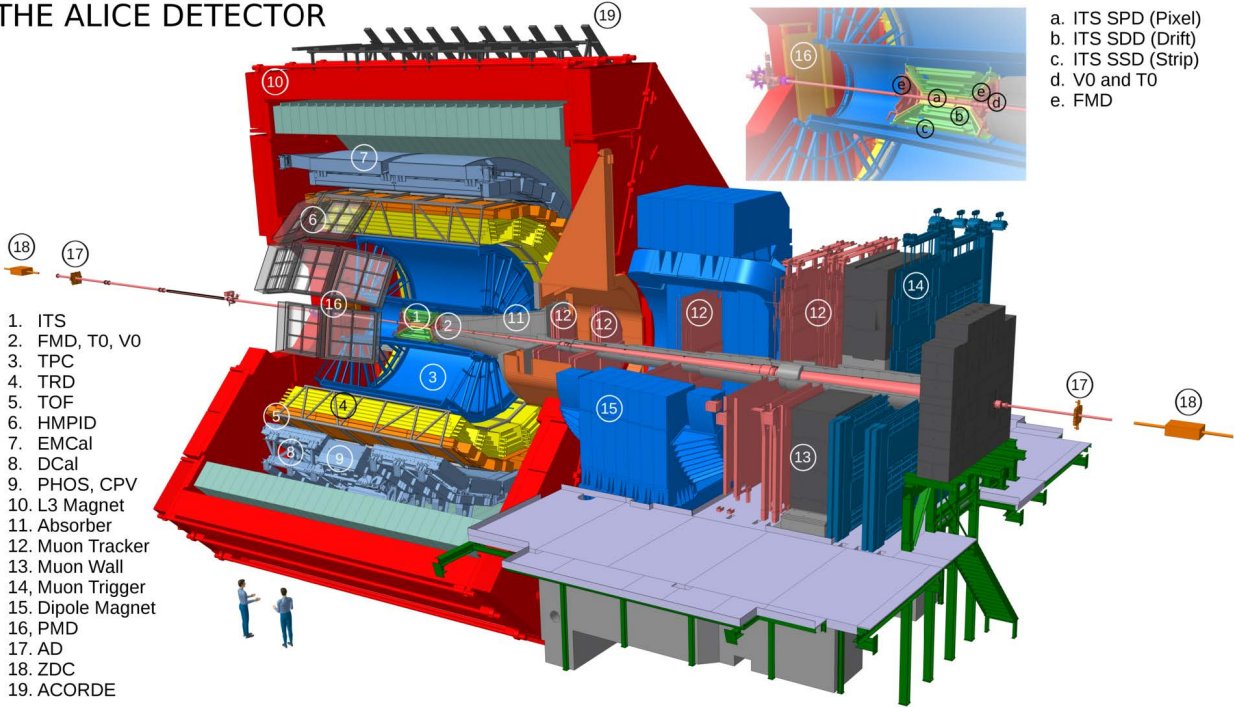


Figure 2.3: ALICE schematics with the subsystems labeled. Image from ref [42].

defined as a function of the polar angle as seen in equation 2.1.

$$\eta = -\ln\left(\tan \frac{\theta}{2}\right) \quad (2.1)$$

The orientation of the axis in Cartesian and spherical coordinates with respect to the ALICE detector is shown in figure 2.4a, while a cartoon indicating the position of a particle based on its pseudorapidity is shown in figure 2.4b.

The ALICE detector can be separated into three regions: forward, backward, and central barrel [45]. The L3 magnet, reused from L3 experiment at LEP, generates a 0.5 T magnetic field, and surrounds the entire ALICE central barrel. Particles traversing the central barrel will encounter the two layers of the silicon pixel (SPD), drift (SDD), and strip (SSD) each. All six silicon layers together form the Inner Tracking System (ITS). Next, the particles pass through the Time-Projection Chamber (TPC). The ITS and the TPC combined are responsible for particle tracking and momentum resolution. After the TPC, the particles encounter the Time-Of-Flight detector (TOF), the High Momentum Particle Identification Detector (HMPID), and the Transition Radiation Detector (TRD), which are the three particle identification subsystems. The final subsystems in the central barrel are the electromagnetic calorimeters: PHOS, EMCal, and DCal. Except for the calorimeters and the HMPID, the ALICE central barrel subsystems has full coverage in azimuth, and the entire central barrel



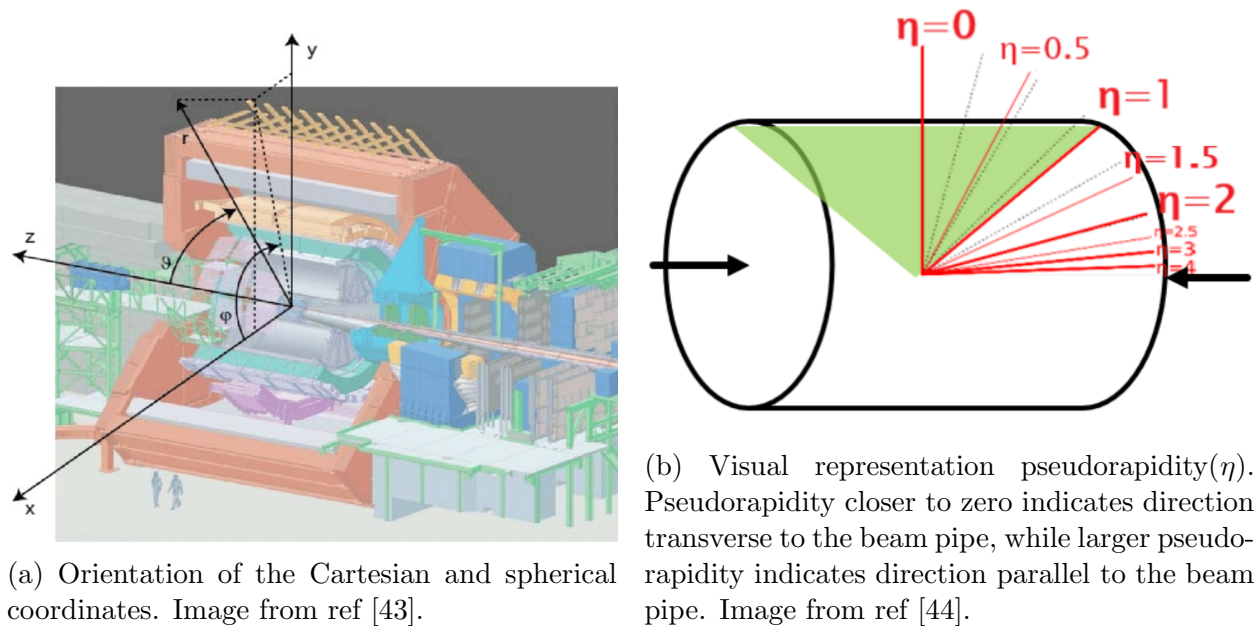


Figure 2.4: Cartesian and spherical coordinates, and pseudorapidity orientations

covers a range of  $|\eta| < 0.9$  in pseudorapidity. The forward and backward subsystems include the Zero Degree Calorimeter (ZDC), Photon Multiplicity Detector (PMD), Forward Multiplicity Detector (FMD), a muon spectrometer which contains the Muon Chambers (MCH) and Muon Triggers (MTR), and the triggering detectors TZero (TO) and VZero (V0) which cover a pseudorapidity range of  $|\eta| > 0.9$ .

While ALICE was designed as general-purpose detector, it is the only dedicated heavy-ion detector at the LHC. Due to the focus on measuring observables from heavy-ion collisions, ALICE needed to be able to detect and identify a wide range of particles produced in heavy-ion collisions. One of the primary design considerations for ALICE was its ability to handle the high particle multiplicities, the number of particles produced per unit of pseudorapidity, of heavy-ion collisions. Initial estimates of multiplicity density from charged particles at mid-rapidity in central Pb–Pb ranged from  $dN/d\eta$  of 2000 to 8000. The interaction rate of Pb–Pb collisions provided by the LHC was 3-4 kHz[45] for LHC Run 1 and 8 kHz[46] for LHC Run 2, both of which are below the ALICE threshold of avoiding pileup. Handling the high multiplicity central Pb–Pb events required detectors with a high granularity. The subsections 2.2.2-2.2.5 provide more details on the specific subsystems used for the isolated photon cross-section measurements: V0 for triggering, ITS and TPC for charged particle tracking used to isolate the photons, and EMCal and DCal for photon reconstruction and transverse energy measurement.

### 2.2.1 Triggering in ALICE

The ALICE detector, designed to cope with the high multiplicity conditions of Pb–Pb collisions, requires a complex trigger system. A trigger system allows ALICE to detect when an interesting collision occurred, serves as the starting point for data collection, filtering out pileup events, and accommodating the readout times of different subsystems. ALICE Central Trigger Processor (CTP) is one of the most complex among all the LHC experiments [47]. It is located in the ALICE experimental cavern and its layout is shown in figure 2.5. The

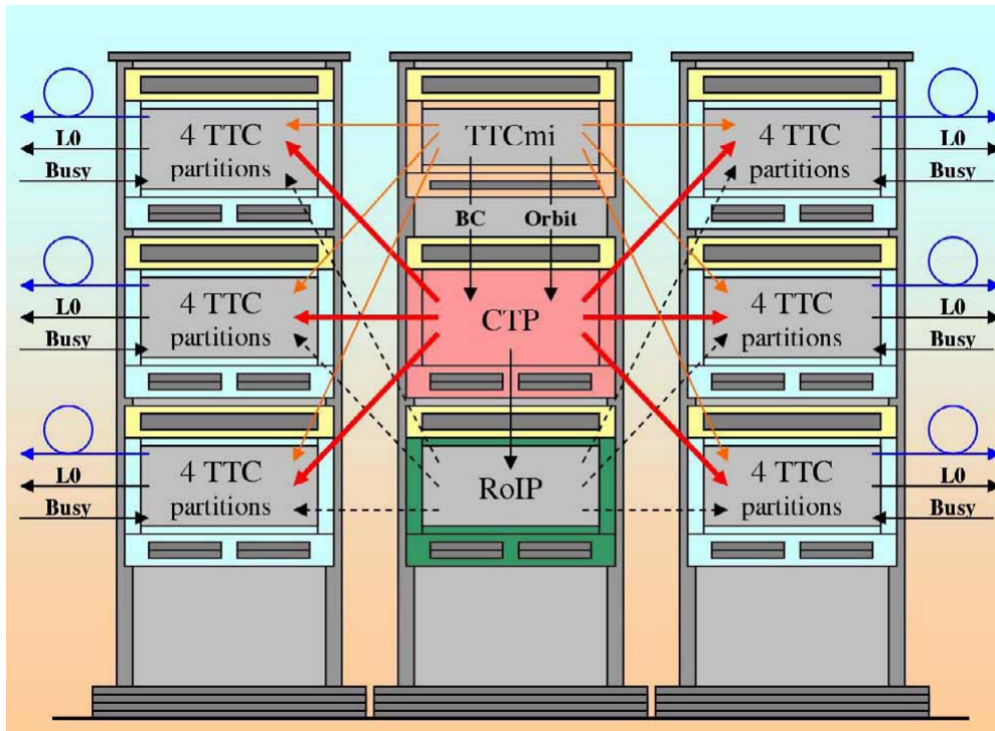


Figure 2.5: Layout of the ALICE CTP in the experimental cavern. Image from ref [47].

CTP is designed to handle 24 subsystems, which can be partitioned into up to six different groups known as trigger clusters. Each trigger cluster is independent of the others and can be triggered individually. Due to the different levels of latency from different detectors, there is a three level hierarchical hardware trigger structure in place: L0, L1, and L2. The L0 triggers are the fastest, with a latency of  $1.2 \mu\text{s}$ . The purpose of the L0 trigger is to start the busy signal for all detectors in the affected trigger cluster and send a signal to all detectors with fast sample-and-hold electronics. The next trigger level, L1, has a latency of  $6.5 \mu\text{s}$ . Most of the detector hardware trigger signals are included in the L1; however, the decisions to send the data to the data acquisition and the software trigger High Level Trigger (HLT) only occurs after the L2 signal. L2 has latency of  $88 \mu\text{s}$ , which is due to the long drift time of the TPC [48]. There are 24 L0 trigger inputs, 24 L1 trigger inputs, and 12 L2 trigger

inputs. All the inputs can be combined with AND logic, but a few can be combined with other logic functions. The varied ways in which the trigger inputs are combined allows the CTP to be robust in the different collision environments and beam species combinations.

In order to protect the detector from recording events which have significant levels of overlap from other interactions before or after the event selected by the trigger, a system of past-future protection is implemented as a way to combat pile-up. The past-future refers to time interval before and after the interaction. The past-future protection select events which either have no pileup in a given time interval before and after the interaction, or with a number of pile-up interactions up to a programmable limit. The past-future protection operates independently for each trigger cluster and is performed at all three trigger levels. Further details regarding ALICE CTP, the design of the past-future protection circuit, as well as block diagrams of the other circuits such as generation of L0 triggers, etc can be found in references [47] and [48].

The triggers mentioned so far have been hardware triggers, but ALICE also has HLT software trigger which comes into play during the data acquisition after the L2 trigger. The HLT is comprised of a computing farm of up to 1000 multiprocessor PCs which perform a detailed online analysis to mostly complete event. Besides event selection, the HLT works to reduce the event size by either compressing the event information or limiting the data processed during readout. A description of the HLT operation can be found in reference [49], and the performance of the HLT can be found be in reference [50].

### 2.2.2 VZERO (V0)

The V0 detector is one of the main L0 triggering detectors of ALICE, and is used to measure the energy of charged particles produced in the collisions of heavy ions. It is located at the forward and backward regions of the ALICE detector, as seen by the red regions in figure 2.6, and consists of two arrays of scintillators, V0A and V0C, on opposite sides of the interaction point. The V0A, positioned opposite to the muon spectrometer, and V0C, in front of the hadronic absorber, are located at distances of 3.3 meters and -0.9 meters from the interaction point, respectively [45]. This geometry allows the V0 detector to cover a wide range of pseudorapidities. The V0A scintillators cover the pseudo-rapidity range  $2.8 < \eta < 5.1$ , while the V0C scintillators cover the range  $-3.7 < \eta < -1.7$ . Both the V0 arrays have full coverage in azimuth. Each array contains 32 scintillators, providing a total of 64 scintillators for the detector. The 32 scintillators per array are distributed in four rings with 8 scintillator in each inner two rings and 16 scintillators in each outer two rings, as shown in the photo of the V0C array in figure 2.7a. Each ring is partitioned into eight  $45^\circ$  sectors, one of which can be seen glowing under ultraviolet light in figure 2.7b.

The scintillators are made of BC-404 plastic scintillating material and are designed to detect charged particles by measuring the light produced when particles pass through the material. The scintillating material is 2.5 and 2.0 cm thick in the V0A and V0C, respectively. The V0 detector works by measuring the time of flight of particles passing through the scintillator material. The light produced by the particles is detected by photomultiplier

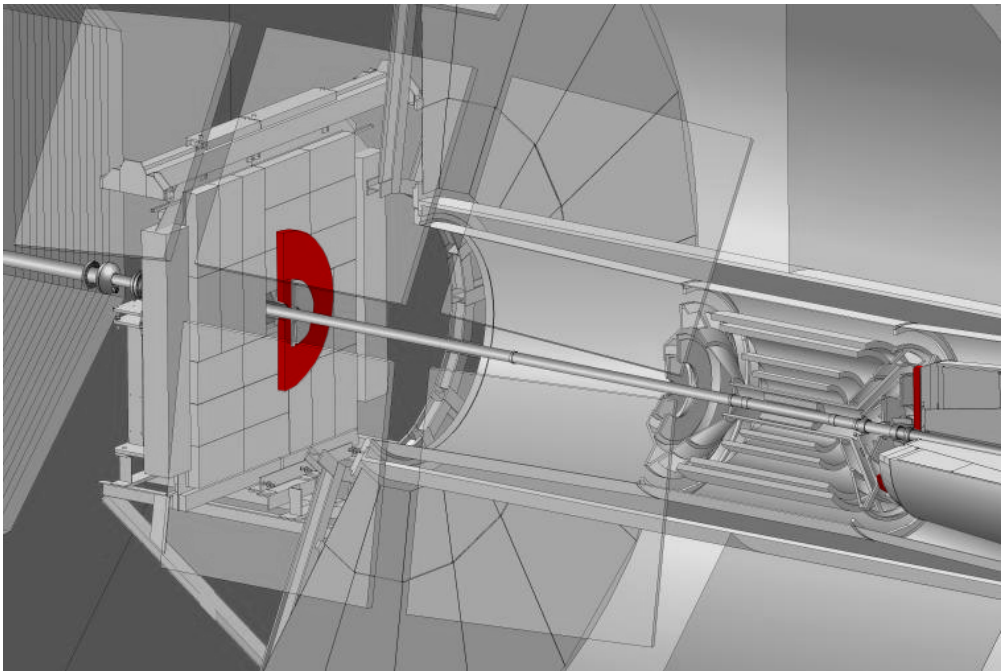
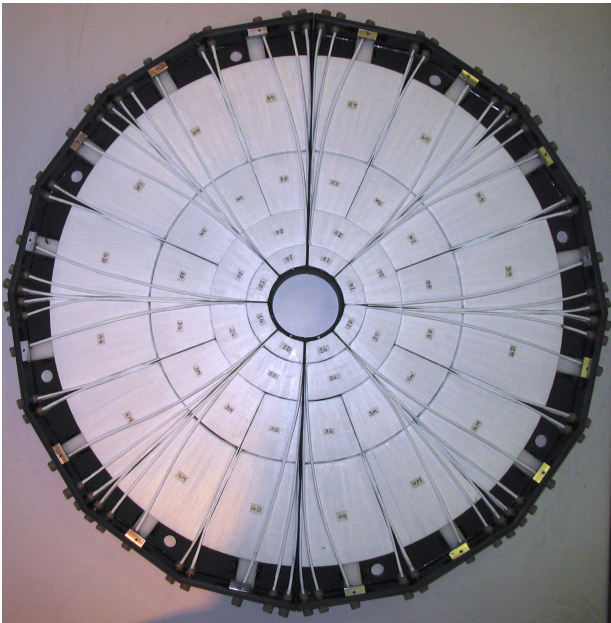
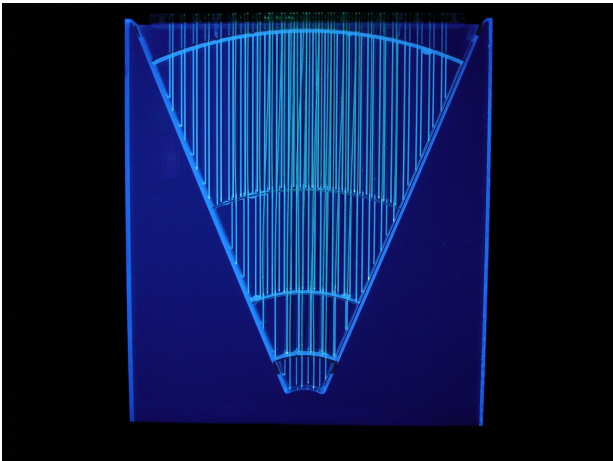


Figure 2.6: The V0 highlighted in red within a schematic of the ALICE central barrel.



(a) The V0C array. Image from ref [51]



(b) One of the 8 sectors from the V0A array illuminated under ultraviolet light. Image from ref [52].

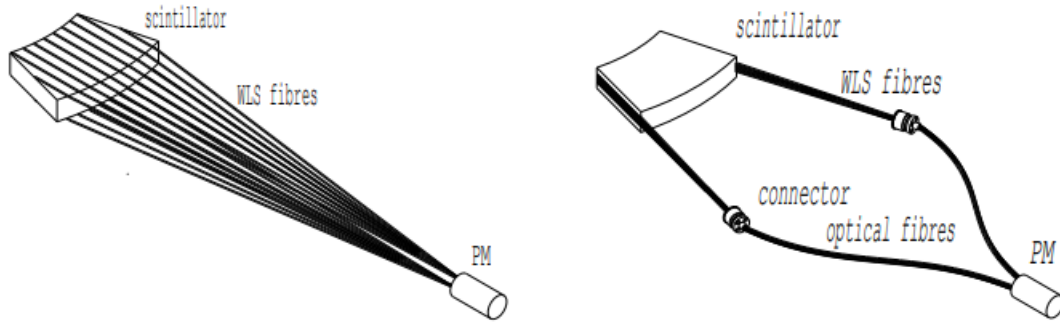


Figure 2.8: Schematic design of the V0A (left) and V0C (right). Image from ref [39].

tubes (PM), which are connected to the scintillator material with 1 mm diameter BCF9929A Wave-Length Shifting (WLS) fibres as seen in figure 2.8. The photomultiplier tubes convert the light into an electrical signal. The time difference between the signals from the two scintillators in each array is used to determine the direction of the particle and its energy. Pre-adjusted time windows in coincidence with the time signals from the scintillators are used for minimum bias, beam-gas and multiplicity triggers. A signal in both the V0A and the V0C, also known as V0AND, is used to define the minimum bias, a trigger with least amount of trigger conditions i.e. smallest bias, trigger condition for ALICE.

Besides the minimum bias trigger, the V0 is also used for centrality determination in Pb–Pb. It can be used to identify events with a small impact parameter, which correspond to central collisions. Due to the monotone relationship between the number of registered particles in the V0 arrays and the number of primary emitted particles, the V0 can be used to indicate the centrality of the collision via the multiplicity recorded in the event. Cuts on the number of fired scintillators and on the total charge can be applied to achieve rough centrality triggers. The centrality of the collision can then be determined by comparing the measured multiplicity with the multiplicity expected for a fully overlapping collision. This is done by using a Monte Carlo Glauber model [18], which simulates the collision process and predicts the multiplicity as a function of the impact parameter between the colliding nuclei. The measured multiplicity is compared with the model prediction, and the best fit percentile class is taken as the centrality of the collision as described previously in section 1.3.1.1.

The V0 detector is capable of detecting particles with energies in the range of a few hundred MeV to several GeV. It can identify particles such as protons, pions, kaons, and other mesons, as well as nuclei such as deuterons and tritons. The comprehensive technical report of the V0 detector can be read in reference [53].

### 2.2.3 Inner Tracking System (ITS)

The ALICE Inner Tracking System (ITS) is a silicon microstrip detector that is designed to track the trajectory of charged particles produced in heavy-ion collisions at the Large Hadron Collider (LHC). Its main tasks are to identify the position of the primary vertex with a resolution better than  $100 \mu\text{m}$ , secondary vertex reconstruction from B and D meson decays, track and identify particles with momentum below  $200 \text{ MeV}/c$ , and improve the momentum and tracking resolution of the TPC as well as cover the TPC's dead regions, which lack readout due to size and design constraints. The ITS is located very close to the interaction point, coaxial to the beam pipe, from 4 cm to 43 cm radially from the beam pipe. The inner and outer radius were determined based on the constraints given by the position of the beam pipe and the TPC, respectively. The ITS has full coverage in azimuth, with a coverage of  $|\eta| < 0.9$  in pseudorapidity, but the first layer has a larger coverage ( $|\eta| < 1.98$ ) so that there is continuous coverage of the charge multiplicity from the central region to the FMD [39].

Figure 2.9 shows the position of the ITS (fig 2.9a in the ALICE detector schematics along with the three different sub-detectors which compose the ITS: the Silicon Pixel Detector (SPD, fig 2.9b), the Silicon Drift Detector (SDD, fig 2.9c), the Silicon Strip Detector (SSD, fig 2.9d). The first two layers are the SPD, followed by the SDD, with the SSD for the outer two layers. The ordering was determined based on high particle multiplicity in heavy ion collisions. Table 2.1 details the values of the spatial precision, track resolution, cell size, distance from the beam pipe, and the total number of cells for the different layers of the ITS. The four inner most layers have better spatial precision and track resolution compared to the SSD. Since momentum resolution for low  $p_T$  particle is dominated by multiple scattering effects, the material budget is kept to a minimum. The SDD and SSD need a minimum thickness of  $300 \mu\text{m}$  for acceptable signal-to-noise ratio. There is overlap between the layers to fully cover the solid angle, thus the detectors effective thickness is  $0.4\%$  of the radiation length ( $0.004X_0$ ). Each sub-detector is designed to provide different levels of precision in tracking the charged particles produced in the collisions, and together they form a high-precision tracking system that can measure the positions and momenta of charged particles with very high accuracy. The four outer layers have analogue readout, as result, they are also used for particle identification using  $dE/dx$  measurement for highly ionizing particles at low-momentum as seen in figure 2.10. Thus, the ITS can act as a standalone low-momentum particle spectrometer.

#### 2.2.3.1 SPD

The SPD is composed of two barrel-shaped layers of silicon pixels arranged parallel to the beam pipe. The SPD covers the radial range from 16.4 cm to 23.9 cm and has a total of 240 modules, each containing  $260 \times 160$  pixels that are  $50 \mu\text{m}$  ( $r\varphi$ )  $\times$   $425 \mu\text{m}$  ( $z$ ) in size. The pixels are arranged in a grid pattern and are separated by a  $25 \mu\text{m}$  gap. Longer sensor cells are used near the readout chips to ensure coverage between readout chips. The sensor

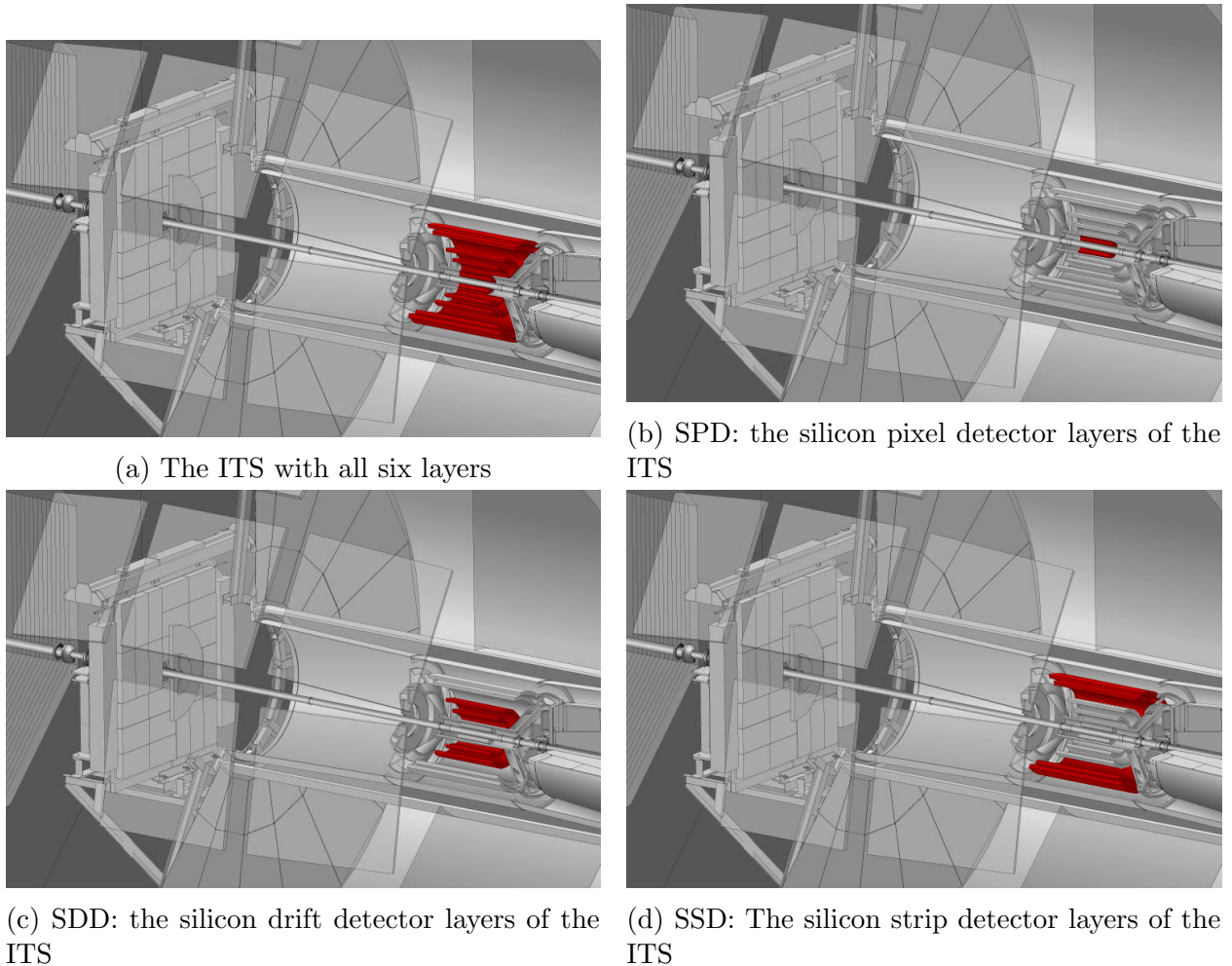


Figure 2.9: The entire ITS and three different style of silicon detector layers highlighted in red within a schematic of the ALICE central barrel region near the beam pipe. Images from ref [54].

matrix has an active area of  $12.8 \text{ mm } (r\varphi) \times 70.7 \text{ mm } (Z)$ . Each front-end chip reads out a sub-matrix of  $256 (r\varphi) \times 32 (z)$  detector cells.

The SPD is designed to provide high resolution tracking of the charged particles, with a spatial resolution of about  $12 \mu\text{m}$  in the transverse plane and  $100 \mu\text{m}$  in the longitudinal direction. The transverse resolution is set by the position accuracy in the plane perpendicular to the beam axis, while the longitudinal resolution is the position accuracy along the beam axis. The spatial resolution of the SPD is achieved by the small size of the pixels and the very thin readout electronics. The thickness of the sensor is  $200 \mu\text{m}$ , while the thickness of the readout chip is  $150 \mu\text{m}$ .

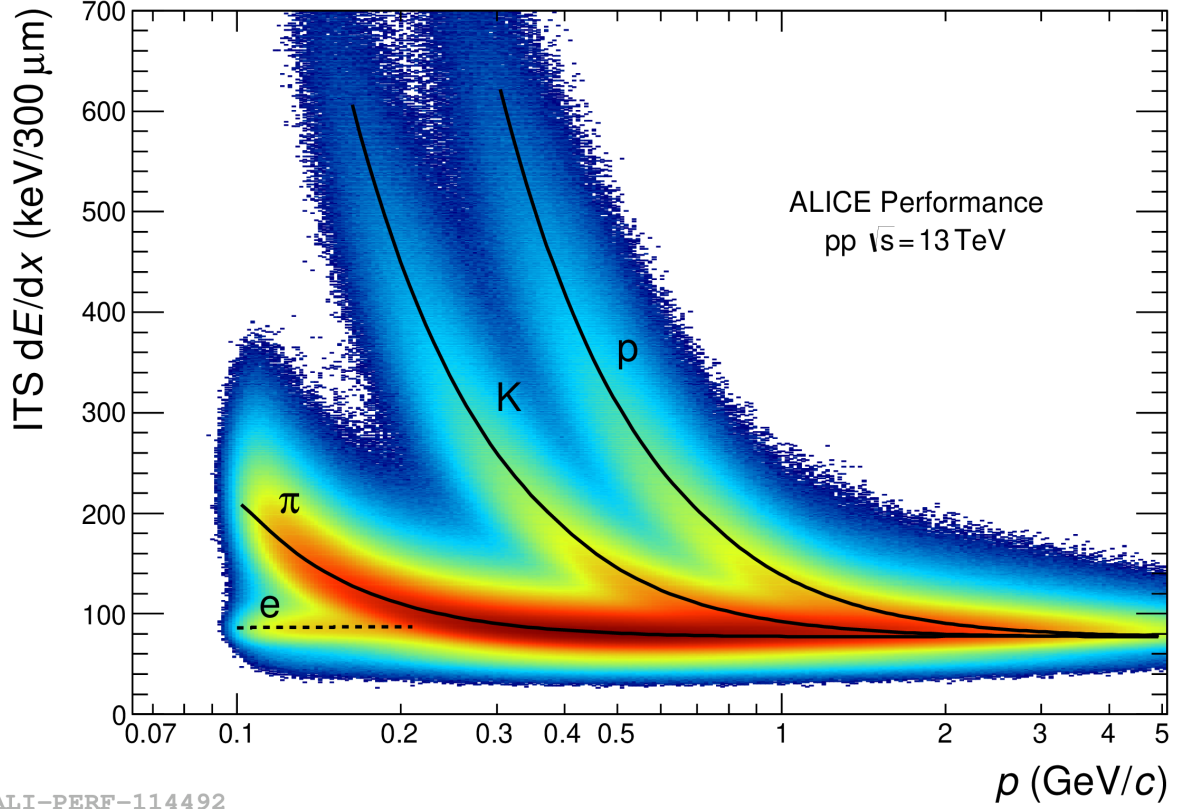


Figure 2.10: Particle identification in the ITS using  $dE/dx$ . Image from ref [55].

Parameter	SPD	SDD	SSD
Spatial precision $r\varphi$ ( $\mu\text{m}$ )	12	35	20
Spatial precision $z$ ( $\mu\text{m}$ )	100	25	830
Track resolution $r\varphi$ ( $\mu\text{m}$ )	100	200	300
Track resolution $z$ ( $\mu\text{m}$ )	850	600	2400
Cell size ( $\mu\text{m}^2$ )	$50 \times 425$	$202 \times 294$	$95 \times 40000$
Distance from the beam pipe (cm)	3.9-7.6	15.0-23.9	38.0-43.0
Total number of cells (M)	9.84	23	2.6

Table 2.1: Summary of various parameters for the different silicon detectors





Figure 2.11: An SPD layer around the beam pipe. Image from ref [56].

The SPD is operated at an average temperature of 25-30° C to reduce the rate of radiation-induced damage to the silicon sensors. The cooling system for the SPD is provided by perfluorobutane that circulates through a network of pipes that run through the detector. The SPD is also used for triggering and event selection in the ALICE experiment. Each pixel chip provides a Fast-OR digital pulse when one or more of the pixels in the matrix are hit. The Fast-OR signal reach the CTP within  $\sim 800$  ns of the interaction in order to meet the latency requirements of the L0-trigger.

### 2.2.3.2 SDD

The SDD is composed of two barrel-shaped layers of silicon drift detectors arranged parallel to the beam pipe. There is a bias voltage of -2.4 kV applied to cells to obtain a the drift velocity is  $8.1 \mu\text{m}/\text{ns}$ . The front-end electronics samples the signal of each collection anode at a frequency of 40.08 MHz and are readout by 512 electronic channels. The size of the cell is  $294 \times 202 \mu\text{m}^2$ , corresponding to  $89.1 \times 103$  cells per detector. The precision along the drift direction ( $r\phi$ ) is  $35 \mu\text{m}$ , and along the anode axis ( $z$ ) is better than  $30 \mu\text{m}$  over 94%

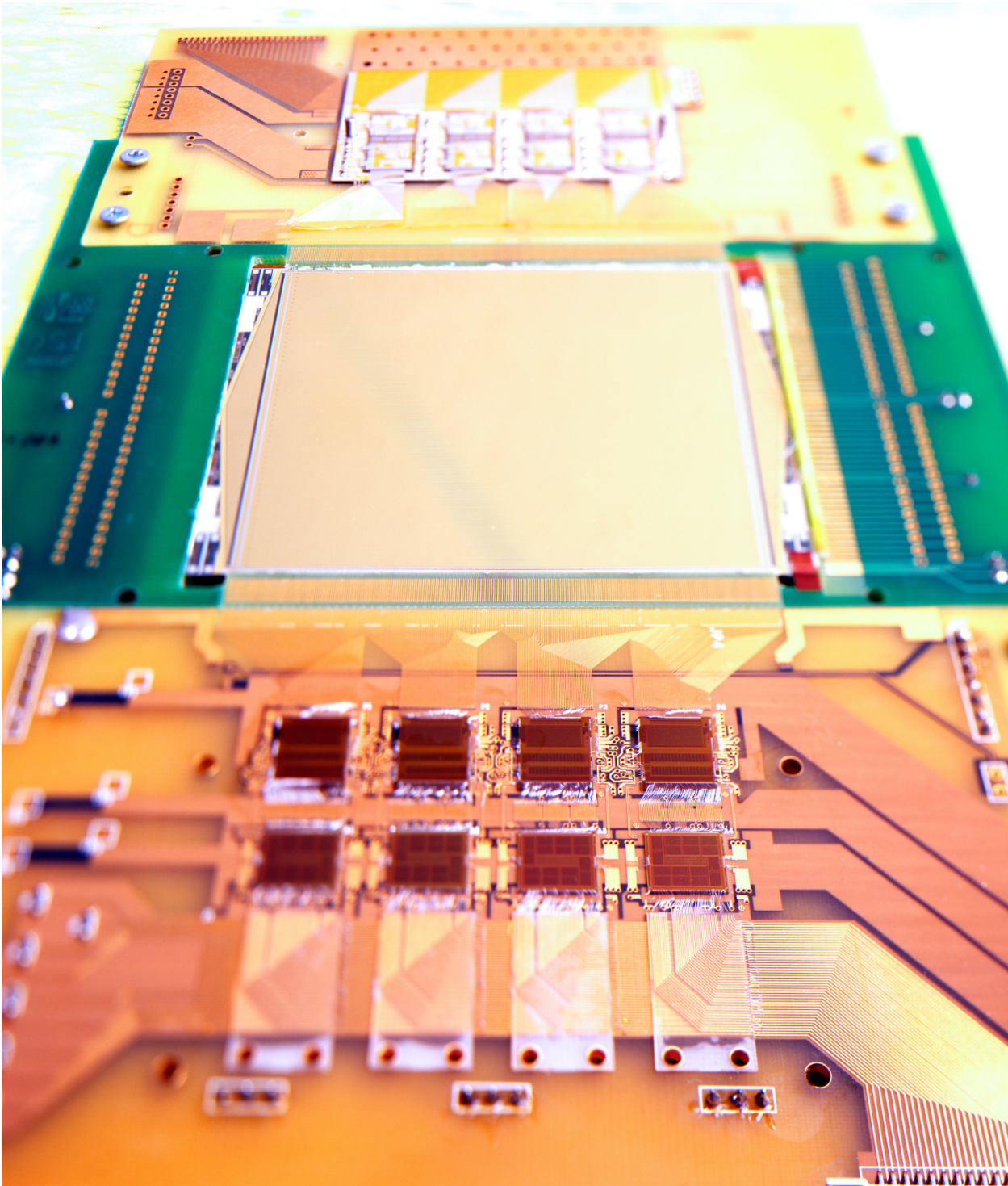
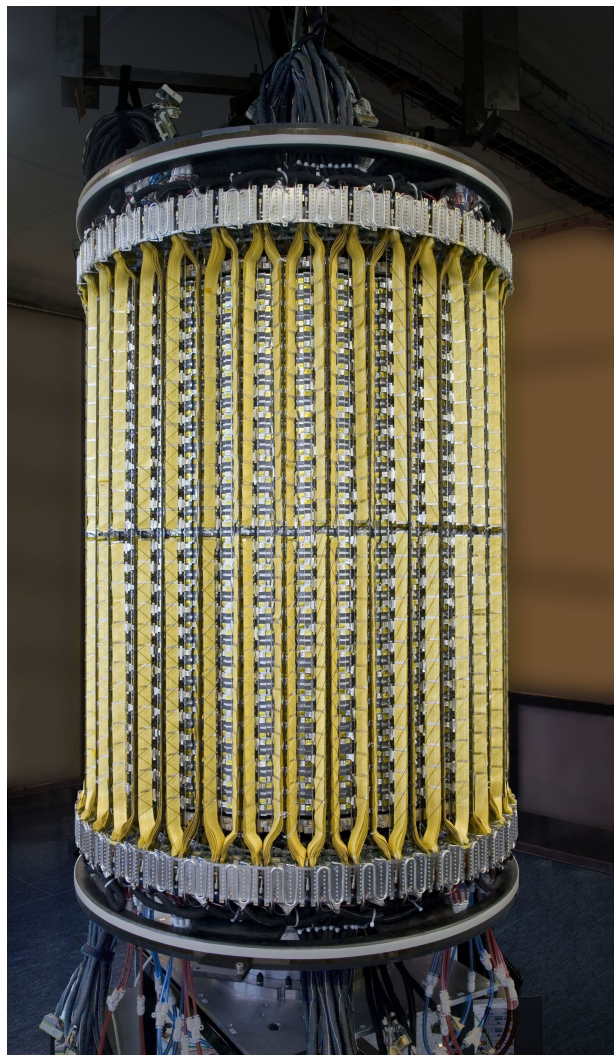
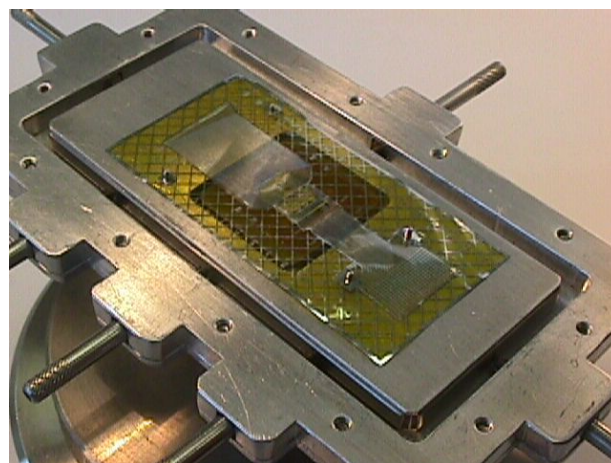


Figure 2.12: A module of the SDD. Image from ref [57].



(a) The SSD. Image from ref [59]



(b) The SSD front-end chip. Image from ref [60].

of the detector surface and reaches  $60 \mu\text{m}$  close to the anodes, where a fraction of clusters affects only one anode. The average values are  $35 \mu\text{m}$  and  $25 \mu\text{m}$  respectively. The detection efficiency is larger than 99.5% for amplitude thresholds as high as 10 times the electronic noise. A SDD module (figure 2.12) has one silicon drift detector and two front-end hybrids on it. The SDDs modules are then mounted on structures called ladders. The SDD is operated at an average temperature of  $25^\circ \text{C}$ . The cooling system for the SDD is provided by super thermoconductive carbon fiber thin plates. The thin plates are mounted on the front-end electronics; they serve as a heat bridge to the cooling tubes, and provide an efficiently heat sink [58].

### 2.2.3.3 SSD

The SSD is composed of two barrel-shaped layers of silicon strip detectors arranged parallel to the beam pipe. It is primarily used to match tracks from the ITS to the TPC. It is also used for low momentum particle identification using  $dE/dx$  measurement. The detector design was optimized to have minimal material budget in order to reduce the effects of multiple scattering. An SSD module is comprised of one sensor is connected to two hybrid integrated circuits with six front end chips [61]. The sensors on the module are  $300\ \mu\text{m}$  thick and they have 768 strips on each side. In order to keep the material budget low, the support structure, made of Carbon Fibre Composite, is also used as the thermal bridge. CFC stiffener is  $300\ \mu\text{m}$  thick, and connects the front-end chips to cooling tubes using aluminum clamps [58]. The SSD modules are assembled on ladders similar to those supporting the SDD. The size of these ladders is one module wide while being 25 modules long in the direction of beam. There are a total of 72 ladders, which combined carry 1698 modules, and are supported by CFC support cones. The ladders on each layer have shift in their position such that the radius of each ladder is slightly different in order to cover full azimuth. Additional cooling of the modules is done by water running through two,  $40\ \mu\text{m}$  wall thickness, phynox tubes along each ladder.

The SDD modules are connected to the Front-End ReadOut Module (FEROM) using endcap modules which are placed at both ends of each ladder. The SDD modules' front-end chips send 2.6 million analog samples to the FEROM, which digitizes them in order to keep up with the trigger rate in ALICE. The signals from all 1698 modules are digitized in parallel. The spatial resolution of the SSD is better than  $20\ \mu\text{m}$  in the  $r\varphi$  direction and is  $820\ \mu\text{m}$  in  $z$ . Due to the use of CFC, only half of the material budget comes from the support, while the other half is sensors on the SSD modules.

## 2.2.4 Time Projection Chamber (TPC)

The TPC is the main tracking detector in ALICE. It was designed and optimized to provide charged-particle momentum measurements with good two-track separation, particle identification, and vertex determination. The TPC has full azimuthal and  $|\eta| < 0.9$  coverage for tracks with full radial track length, matching that of the ITS. A large  $p_T$  range is covered from about  $0.1\ \text{GeV}/c$  up to  $100\ \text{GeV}/c$  with good momentum resolution. The spatial resolution in  $r\varphi$  is  $1100$  to  $800\ \mu\text{m}$  and in  $z$   $1250$  to  $1100\ \mu\text{m}$ . Figure 2.16b shows the TPC highlighted in red within a schematic of the ALICE detector.

The TPC is a cylindrical detector that surrounds the interaction region and covers the radial range from  $85\ \text{cm}$  to  $250\ \text{cm}$ , with a length of  $500\ \text{cm}$  in the beam direction. It is the largest of the ALICE detectors, with a length of  $5.6$  meters and a diameter of  $5$  meters. The detector is made of a large cylindrical field cage, with drift volume of  $90\ \text{m}^3$ , filled with  $90\%$  Ne and  $10\%$   $\text{CO}_2$  mixture, divided in two halves by the central cathode [62]. The drift gas was optimised for drift speed, low diffusion, low radiation length and hence low multiple scattering, small space-charge effect, and ageing and stability properties. However,

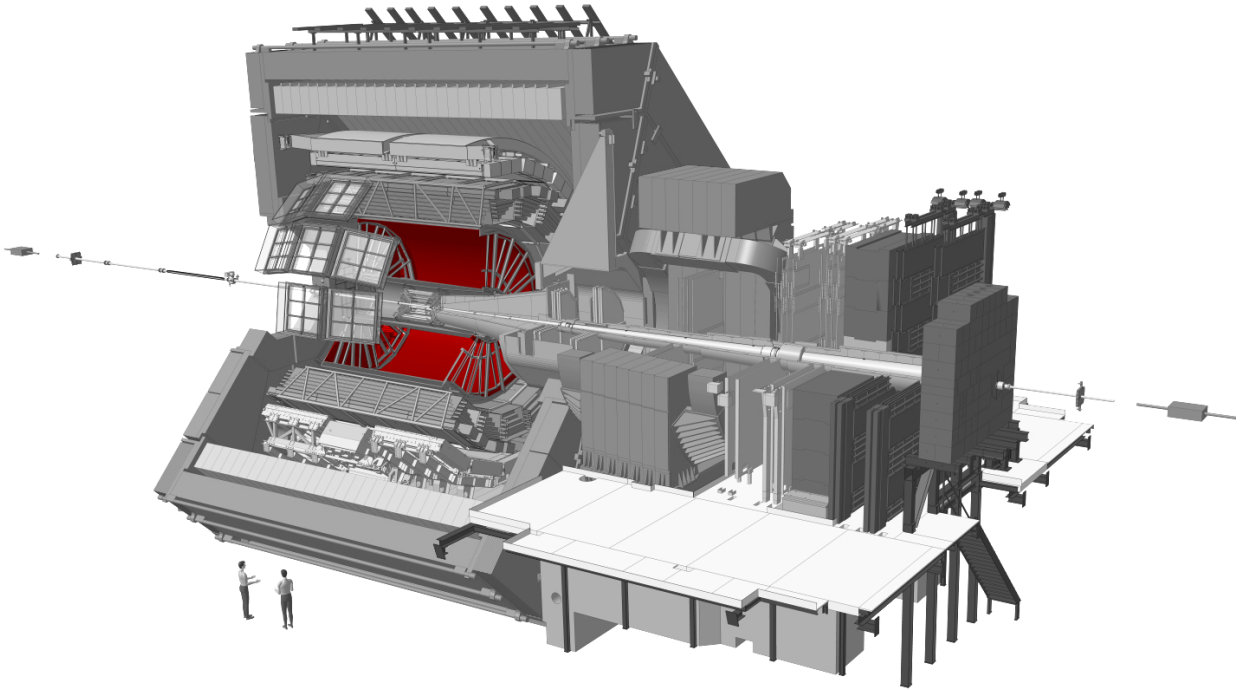


Figure 2.14: A schematic of the ALICE detector with the TPC highlighted in red. Images from ref [54].

the drift speed in Ne-CO<sub>2</sub> is very sensitive to temperature, requiring the TPC to maintain its temperature with  $\Delta T \leq 0.1$  K. The TPC drift length is  $2 \times 2500$  mm, drift field is 400 V/cm, drift speed is 2.7 cm/ms, and the maximum drift time is 92 ms. The cathode is kept at a voltage of -100 kV.

The TPC is a gaseous detector that relies on the ionization of a gas for the detection of charged particles. When a charged particle travels through gas, it create a trail of free electrons and ions. The longitudinal electric field in the TPC causes the electrons and ions to drift towards the anode and cathode respectively. Thin wires with an applied voltage serve as anodes, while the cathode is plane in the center of the TPC. Due to the applied voltage, there is strong magnetic field near the anode. The electrons accelerated in the magnetic field will give rise to secondary ionization and a subsequent chain reaction known as avalanche multiplication. At the endcap of the TPC are the anode wires. The electrons projected onto the endcaps give information about the  $(r, \varphi)$  coordinates of the charged particle trajectory. The drift velocity and the drift time of the electrons can be used to determine the  $z$  coordinate of the charge particle trajectory. The ions have a slower drift velocity compared to the electrons and take longer to reach the cathode, making the detector readout slow.

The energy deposited at the electrodes is proportional to the number of ionisation, which

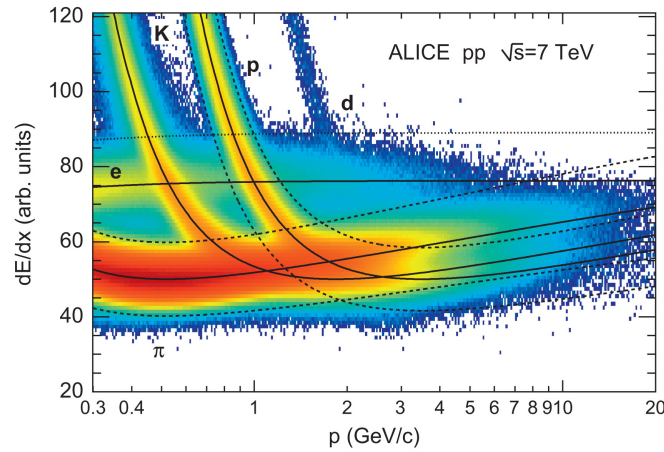


Figure 2.15: The  $dE/dx$  of the TPC. Plot from ref [62]

is proportional to the energy deposited per unit length,  $dE/dx$ . The  $dE/dx$  measurement for the TPC is shown in figure 2.15. A clear separation between different particle species at low momentum is apparent. The separation at high momenta is worse than the separation at low momenta [62]. The  $dE/dx$  resolution for isolated tracks in the TPC is 5.0%, while the multiplicity resolution of the TPC at  $dN/d\eta = 8000$  is 6.8% [63].

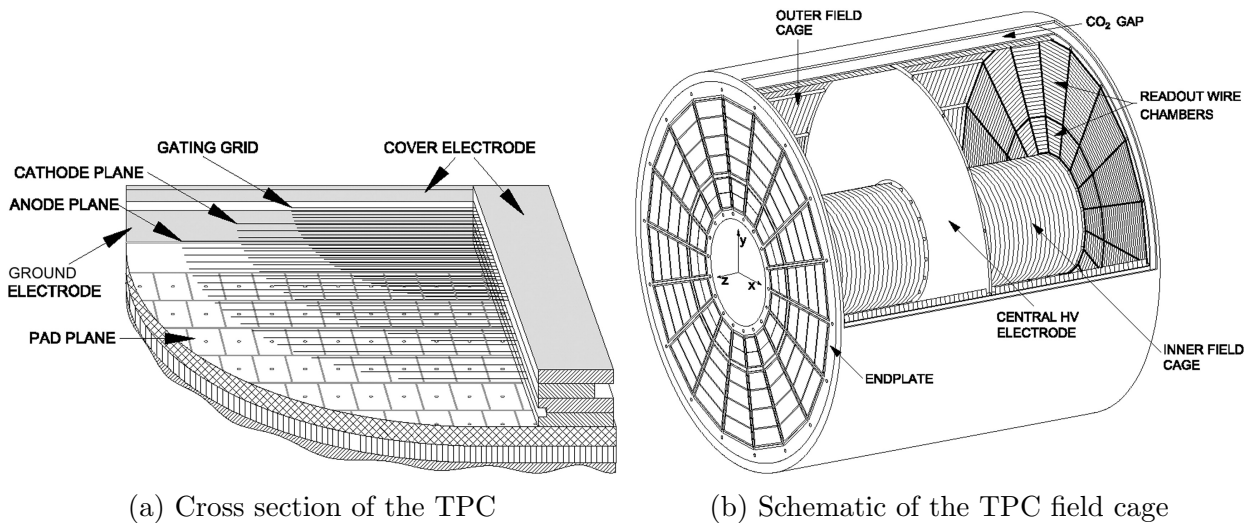


Figure 2.16: Schematics of the TPC. Images from ref [62].

Figure 2.16 shows a cross section view of the TPC and components of the TPC field cage. Multi-wire proportional chambers with readout pads are mounted at both ends of the barrel. Electrons from ionization caused by the incoming charged particles drift at constant velocity to the readout end plates, containing a total of 560,000 readout channels. The

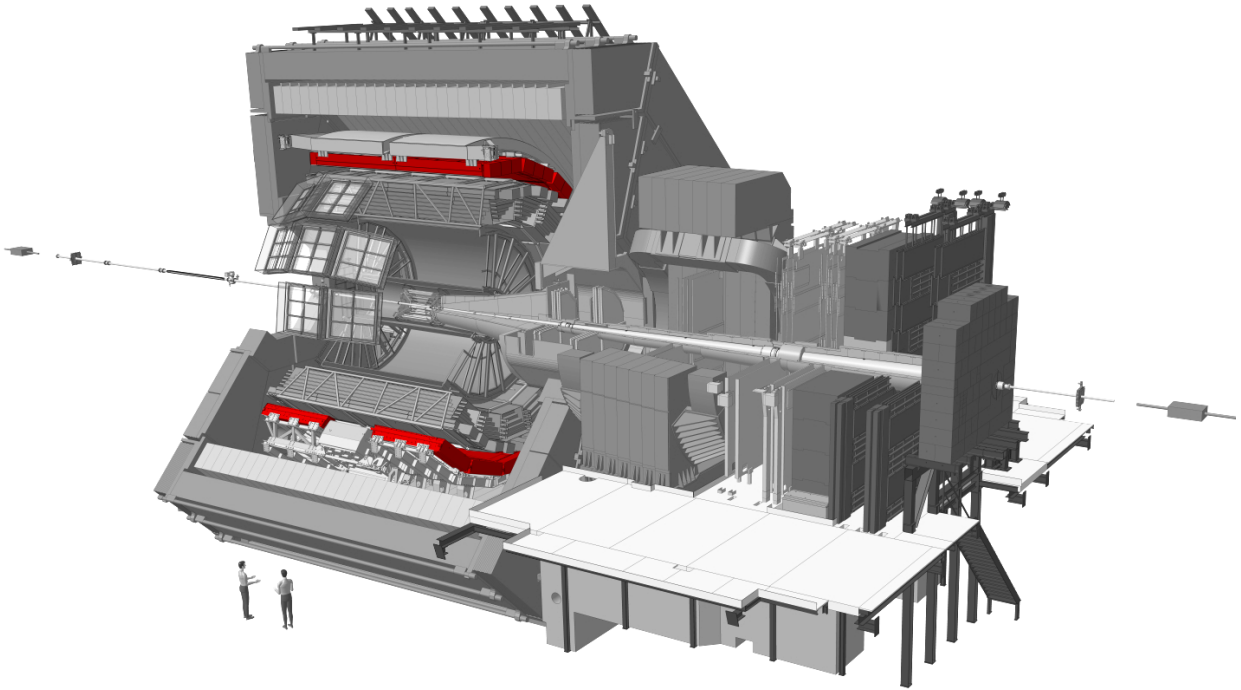


Figure 2.17: A schematic of the ALICE detector with the EMCal and the DCal highlighted in red. Image from ref [54]

readout chambers cover the two end plates of the TPC cylinder with an overall active area of  $32.5 \text{ m}^2$ . The radial range of the active area is from 84.8 cm to 132 cm and from 134.6 cm to 246.6 cm for the inner and outer chamber, respectively. In order to have the necessary  $dE/dx$ , position and track resolution, the readout pads come in three different sizes:  $4 \times 7.5 \text{ mm}^2$  in the inner chamber and  $6 \times 10 \text{ mm}^2$  and  $6 \times 15 \text{ mm}^2$  in the outer chamber.

The TPC requires a temperature variation of less 0.1 K uniformly across the entire drift volume. The thermal gradient inside the ALICE magnet is about 5 K, so multiple systems are used in order to keep the TPC cool. The first system is an elaborate set of heat screens: heat screens connecting the outer radius to the TRD, heat screens at the inner radius to screen heat from the ITS, heat screens in the readout chambers to protect the front-end electronics, and heat screens at the front-end electronics to shield from heat outside the TPC. There are also two cooling systems: one for the front-end electronics, and the second for cooling the potential dividers, which help create the uniform electrostatic field inside the TPC field cage.

## 2.2.5 ElectroMagnetic Calorimeter (EMCal)

ALICE has three separate electromagnetic calorimeters: ElectroMagnetic Calorimeter (EMCal), PHOTon Spectrometer (PHOS), and Dijet Calorimeter (DCal). The EMCal and DCal have the same design. The EMCal was installed half in 2009 and half in 2011, while the DCal was installed in 2014 [64]. All the photons used for the isolated photon cross-section measurement are only from the EMCal acceptance because for the p-Pb data taking period in 2013, there was no DCal present. In order to prevent unnecessary sources of systematic uncertainties, the photons in the DCal acceptance are not used from the 2017 pp data set. The PHOS has a different design requiring high granularity and high energy and position resolution, which comes at the cost of more expensive detector technology and limited acceptance. The EMCal was designed to measure electrons from heavy-flavor hadron decays, the electromagnetic component of jets, and direct photons and neutral mesons. The EMCal is the main detector photon reconstruction and photon energy measurement. Details on photon reconstruction are in section 3.5.

The EMCal has a larger acceptance, and less strict requirements regarding energy and position resolution than PHOS. In this thesis, all references to EMCal only refer to the EMCal installed 2008 and 2014, not any other electromagnetic calorimeter. The EMCal is the primary subsystem for photon reconstruction and photon energy measurement. The acceptance of the EMCal is  $|\eta| < 0.7$  and  $1.40 < \varphi < 3.26$  as seen in the figure 2.18.

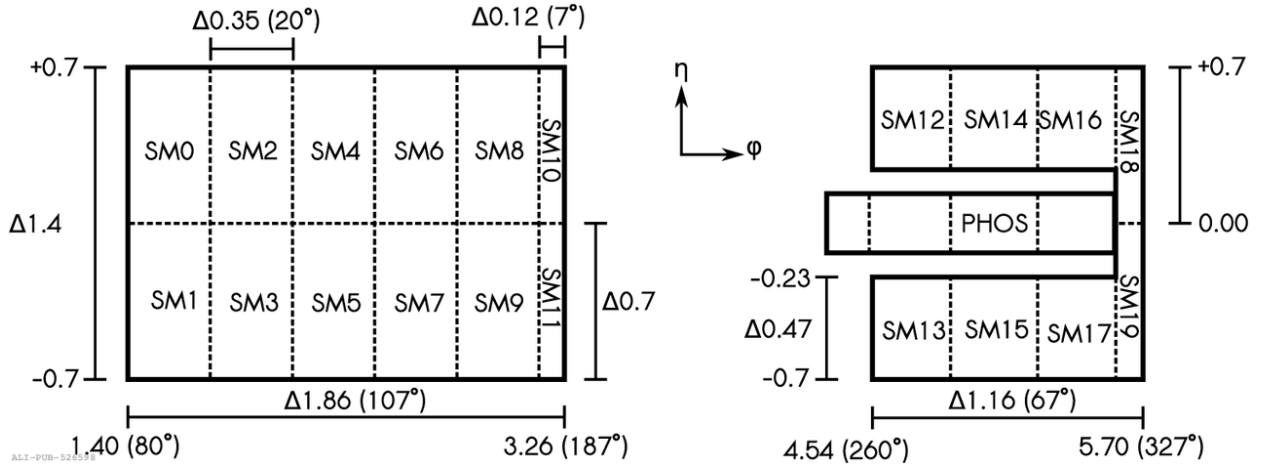


Figure 2.18: The acceptance of all the ALICE calorimeters in the  $\eta - \varphi$  plane in terms of the different super modules (SM). The EMCal is on the left, while the DCal+PHOS is on the right. Image from ref [64].



### 2.2.5.1 Design

The ALICE EMCAL is a sampling calorimeter. A sampling calorimeter is a type of particle detector that measures the energy of particles by sampling the electromagnetic shower resulting from their interactions with a high Z material. The basic design of a sampling calorimeter consists of alternating layers of absorber (a high Z material), which interacts with the particle and converts its energy into a cascade of secondary particles, and active material, which detects the resulting particle shower and produces a signal that is proportional to the energy of the original particle. These particles then traverse through the active material, and produce a detectable signal. The signal is proportional to the energy deposited by the original particle in the absorber material. By measuring the energy of the particle shower in the active material and knowing the thickness and composition of the absorber material, the energy of the original particle can be reconstructed. This is typically done by summing up the energy deposits in the different layers of the sampling calorimeter. For the EMCAL, the absorber layer is lead (Pb) and the active material is Polystyrene scintillator (Scint). The EMCAL has a longitudinal pitch of 1.44 mm Pb and 1.76 mm scintillator with longitudinal wavelength-shifting fiber which run through the layers of Pb-Scint providing light collection [39]. This layout of absorber-active material threaded with wavelength-shifting fiber is called Shashlik.

The smallest unit of the EMCAL is the tower (used interchangeably with cell). There are 12,288 towers in the EMCAL. The towers are approximately projective in  $\eta-\varphi$  plane, meaning that they provide uniform coverage of the solid angle around the collision point. The size of each tower is  $\delta\eta \times \Delta\varphi \simeq 0.0143 \times 0.0143$ , while the physics volume is  $6.0 \times 6.0 \times 20.6$  cm<sup>3</sup> [64]. The tower consists of 77 layers of scintillator and 76 layers of lead. The scintillator layer both starts and ends the array in the tower. Four towers, in a  $2 \times 2$  arrangement, create a module. The various components of modules including support material, cooling, readout and electronics are shown in figure 2.19. The modules are organized in an array of 12 modules in  $\varphi$  called EMCAL strips ( $2$  towers  $\times$   $24$  towers). Twenty-four EMCAL strips in  $\eta$  create a super module (SM). In terms of the building block, a full size EMCAL super module is 24 modules (48 towers) in  $\eta$  and 12 modules (24 towers) in  $\varphi$ . The effective radiation length ( $X_0$ ) is 12.3 mm, and the length of a module covers 20.1 radiation lengths. The effective Molière radius  $R_M$  is 3.20 cm. The sampling fraction, the ratio of the energy deposited in the active (dense) layer of the calorimeter to the total energy deposited by the particle in the calorimeter, is  $1/10.5$  [64]. The EMCAL has two different size super modules (given in the orientation  $\eta \times \varphi$  : full super modules ( $24 \times 12$  modules) and one-third super modules ( $24 \times 4$ ). Each full super module consists of 288 modules, while each one-third super module consists of 94 modules. As seen in figure 2.18, there are 10 full size super modules (numbered SM 0-9 inclusive), and two 1/3 size super modules (numbered SM 11 and 12). The front of the super modules are located 4.5 m away radially from the beam pipe.

## THE EMCAL Module Components

### Containment: 88 parts

- 1) Back (holes: 144 thru for fibers + springs + mech. support), 1
- 2) Compression (holes: 144 thru for fibers + springs), 1
- 3) Front Plate (holes: 144 thru for fibers + springs + mech. support), 1
- 4) 5) Plungers (10)
- 6) Bellville washers (75)

### Tensioning and Insulation:

#### 40 parts

- 7) Stainless steel straps (4)
- 8) Screws (24)
- 9) Flanges (8)
- 10) Light tight stickers (4)

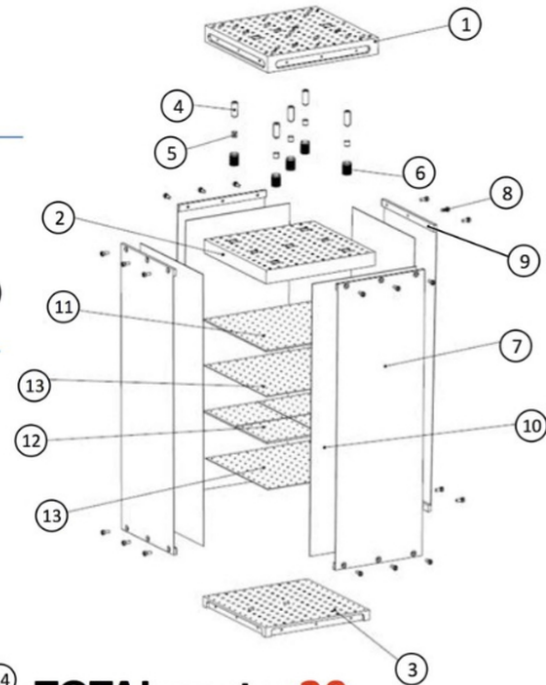
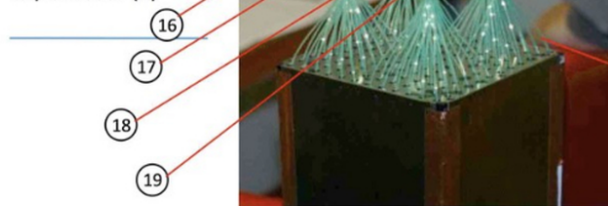
### Sandwich:

#### 538 parts

- 11) Lead tiles (76)
- 12) Scintillator tiles (308)
- 13) Bond paper sheets (154)

### Readout and Electronics: 165 parts

- 14) WLS fibers (144)
- 15) APD (4)
- 16) CSP (4)
- 17) Light guides (4)
- 18) Mount (4)
- 19) Collars (4)
- 20) Diffuser (1)



**TOTAL parts: 20**

**TOTAL components: 831**

Plus cabling, GMS and mech. supports

Figure 2.19: A picture of an EMCAL module along with a schematic. Image from [64].

### 2.2.5.2 Electronics and Readout

At the end of the tower, the wavelength shifting fibers are consolidated into groups of 36 fibers and connect to avalanche photo diodes (APD). The APDs are used as the photosensors, operated at moderate gain for low noise and at high gain to maximize the energy and timing resolution. The APDs are connected to a Charge Sensitive Preamplifier (CSP), which amplifies the electrical signal generated by the APDs. The amplitude of the signal is proportional to the number of integrated electrons from the APD, and thus proportional to the energy deposited in the tower. The CSPs of  $2 \times 8$  adjacent towers are connected to an adaptor called the T-Card, and signals from the two adjacent T-Card are then sent to the Front-End Electronic (FEE) card at the end of the SM. One T-card covers  $2 \times 8$  towers, while one FEE card covers  $4 \times 8$  towers. The high gain and low gain ranges of the FEE-card are 15.3 MeV to 15.6 GeV and 248 MeV to 250 GeV, respectively [64].

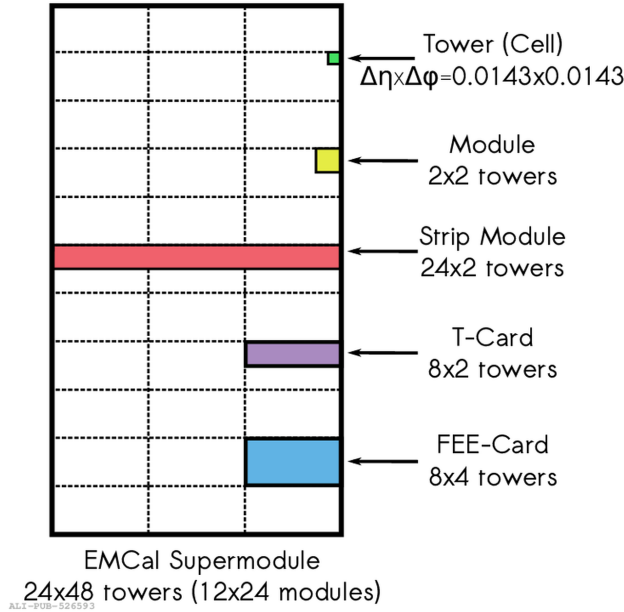


Figure 2.20: Comparing the dimensions of the different components of the EMCAL in  $\eta - \varphi$  for one super module.

### 2.2.5.3 Triggering

The EMCAL trigger system, designed into specific hardware boards, provides both L0 and L1 triggers to the ALICE CTP. The analog trigger signals of  $2 \times 2$  groups of adjacent towers are summed in the FEE cards. Summed signals from twelve FEE cards (each FEE card sums the signal from  $2 \times 2$  towers, 96 total sums) is sent to the Trigger Region Unit (TRU). Each TRU covers one-third super module. For the p-Pb data, the orientation of the TRU covered  $4 \times 3$  FEE-cards in the  $\eta \times \varphi$  plane in the super module. For the pp data, the orientation was changed and the one-third super module was covered as  $12 \times 1$  FEE-cards in  $\eta \times \varphi$  plane. The sums from the twelve FEE-cards are digitized at 40 MHz, the LHC clock frequency. The  $2 \times 2$  digitized sums are integrated using time samples, followed by a pedestal subtraction, and combined into  $4 \times 4$  sums known as trigger patches. These trigger patches are created in the TRU, and an algorithm is used to find the peak of the signal. The signal peak is compared to a pre-defined threshold to determine if there is a high energy shower in a particular TRU, and that a high energy particle was detected in that super module. A logical OR is performed between all the TRUs in the Summary Trigger Unit (STU), and a signal sent to the ALICE CTP for an L0 trigger if STU determines that there is at least one TRU where the summed signal peak was above the L0 threshold. The L0 signal from the STU to the CTP is sent within 800 ns after the collision occurs [64].

If the L0 trigger signal is accepted by the CTP, the process of going from the  $2 \times 2$  digitized sums to the trigger patches is performed again, but this time in the STU for the

EMCal as whole instead of at the TRU for a section of a super module. This process helps determine if there is high energy shower anywhere within the EMCal acceptance which would pass the EMCal L1- $\gamma$  trigger (the L1 electron/photon trigger) thresholds. For the L1-jet trigger, trigger patches are  $16 \times 16$  towers and  $32 \times 32$  towers large. For event selection, the EMCal L1 trigger, for both  $\gamma$  and jet, can have up two thresholds: high and low. An L1 trigger signal will be sent to the CTP if signal peak threshold in the STU is larger than L1 trigger threshold (high or low).

#### 2.2.5.4 Calibration

Calibration of the EMCal is an essential step to ensure accurate measurement of the energy deposited by these particles. There are different types of calibrations performed on the EMCal in order to obtain accurate measurements as summarised below.

##### Cell energy calibration

The goal of the cell (same as towers) energy calibration is to calculate a calibration coefficients for each cell such that all cells report the same energy when given the same input. The cell energy calibration for the ALICE EMCal is performed using  $\pi^0 \rightarrow \gamma\gamma$  decay. The invariant mass distribution of  $\pi^0$  candidates is measured using two decay photons, one of which has a cluster centroid located in the cell being calibrated. The cluster centroid is the central cell in the cluster based on the shape of the electromagnetic shower. The shower shape is defined and further discussed in section 3.6. The distribution of the  $\pi^0$  invariant mass is fitted with the sum of a Gaussian and a second-order polynomial. The Gaussian is used to describe the pion mass peak, and the polynomial is used to fit the combinatorial background. The calibration coefficient,  $c_i$  is calculated as the ratio of the pion PDG mass  $M_{\pi^0}^{PDG}$  and the pion mass obtained from the mean of the Gaussian fit to the invariant mass distribution ( $\mu_i^{\text{fit}}$ ):  $c_i = (M_{\pi^0}^{PDG}/\mu_i^{\text{fit}})^n$ , where  $n$  is chosen to be 1.5 [64]. Both decay photons were required to be within the same super module to avoid effects from the misalignment in the EMCal super modules in the  $z$  direction. The cluster seed cell must have minimum energy of 100 MeV and the rest of the cells must have 50 MeV, at least. The shower shape of the cluster was required to be  $< 0.5$  in order to selected circular cluster which did not have an associated track. The clusters must have a time difference less than 20 ns between them and be within 20 ns of the collision. Finally, the cluster energy was  $0.7 \text{ GeV} < E_{\text{cluster}} < 10 \text{ GeV}$  for the calibration. Because reconstructing the pions mass peak requires both decay photons to be present in the EMCal, cells at the edge of the super module cannot be calibrated this way since part of the electromagnetic shower is lost.

##### Bad channel map

There are some cells in the calorimeter which have a discontinuous energy response, are noisy, or give improper spectra. These cells are identified as bad cells and need to be masked. The behaviour of the bad cells can be seen in the right plot of figure 2.22 where the energy

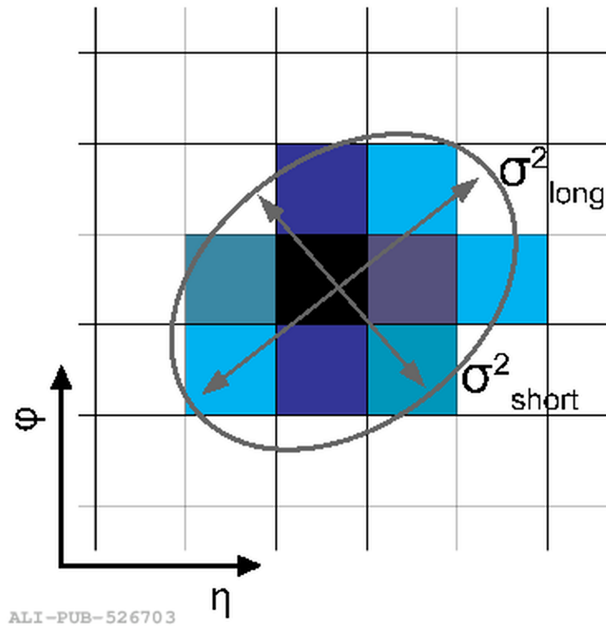


Figure 2.21: Diagram showing the shower shape of a cluster in the EMCAL, long with the major and minor axis of the ellipse drawn around the shower shape using equation 3.4. The colors indicate the energy deposited in the cell, with darker cells indicating larger energy deposition. Image from [64]

distribution for all cells has spikes not seen in the good cells. Two variables, the mean energy per cell and the number of hits recorded by a cell, are used to identify the bad cells. Certain cells might give a bad response only in certainty energy ranges so the two variables are evaluated independent of each other over various energy slices. The assumption that the number of hits per channel should only differ statically is used to weed out noisy, hot, cold, dead, or otherwise improper channels.

### Cell time calibration

The cell time calibration corrects for physical differences which can shift the cell time for each cell such as cable length, electronic response time, and time shifts due to clock phase difference. The cell time information is corrected by taking an average of the cell over a long period, which can be as long one data taking period or a whole year.

### Cell temperature calibration

The temperature calibration is necessary because the gain of the APD is linearly dependent on the temperature. Since the temperature can fluctuate during the runs, a correction to the gain is applied offline. There are LEDs and temperature sensors installed near the APDs

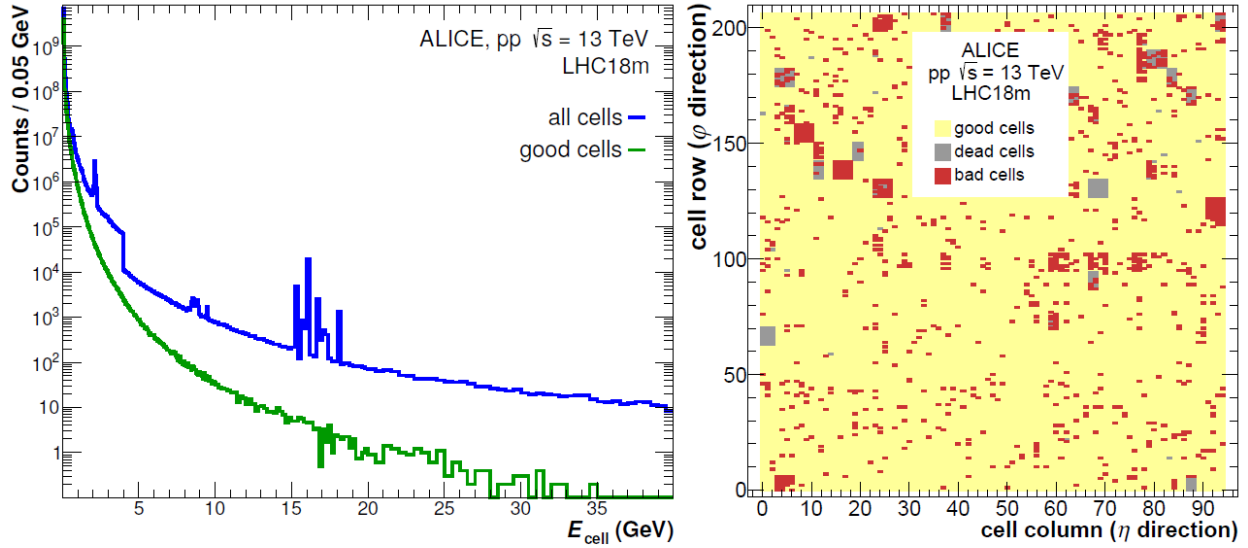
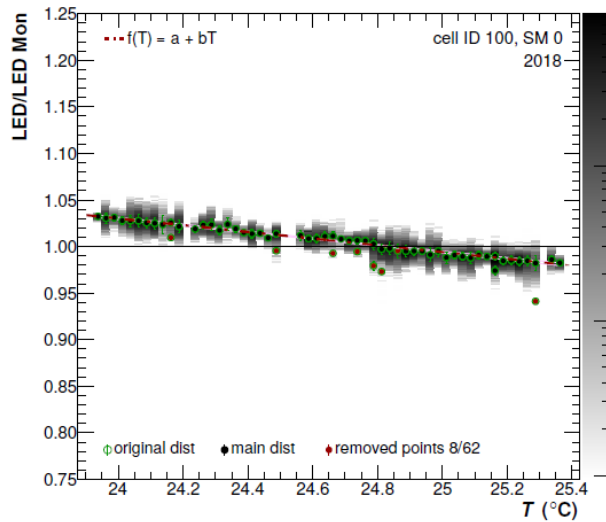


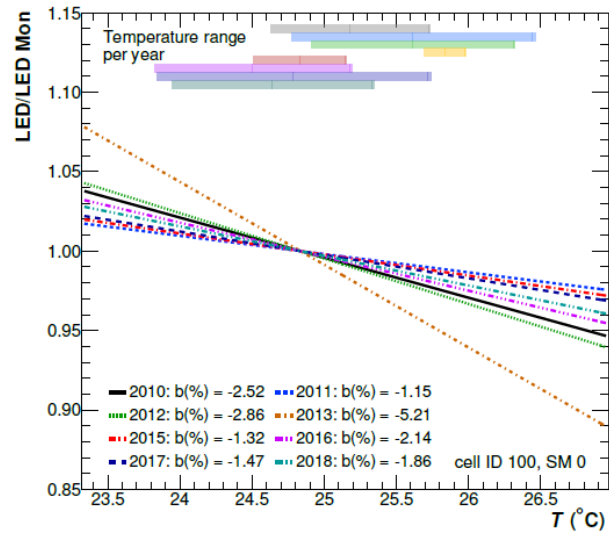
Figure 2.22: Right: Cell energy spectra for all cells compared to good cells. Left: Map of good, bad, and dead cells in the EMCal and DCal. Image from [64].

at various locations. The LED pulses are monitored throughout the runs as a function of time for the different EMCal strips. The average temperature from the temperature sensors was used to calibrate the data. The light yield from the LEDs is compared to the LED monitoring signal and a linear fit is performed for the ratio as seen for an example cell in figure 2.23a. For most cells, like the one in figure 2.23b, the slope parameter did not vary as function of time unless the gain of the APDs had changed. The most frequent value of the slope was around  $-1.8\%/^{\circ}\text{C}$  within the range  $-2.5\%/^{\circ}\text{C}$  to  $-1.2\%/^{\circ}\text{C}$ . For cells with slopes were below  $-7\%/^{\circ}\text{C}$  or greater than  $-1.2\%/^{\circ}\text{C}$ , the average slope of all cells for that year was set as the calibration coefficient.

Further technical or performance details regarding the ALICE EMCal can be found in the EMCal performance paper [64].



(a) The ratio of LED signal to the LED monitoring signal long with a linear fit. The full 2018 data sample is shown in gray. The green open circles indicate the maximum temperature for each temperature slice. The black points are dominant cluster in the temperature slice while the blue points show the shift after the offset is correction. The fit only performed for the black and blue points combined. Red points are outliers which were excluded from the fitting procedure.



(b) Comparison of the calibration coefficients for different years.

Figure 2.23: Images from [64]

# Chapter 3

## Analysis

### 3.1 Analysis summary

We use the data collected by the ALICE detector during 2013 for p–Pb collisions at  $\sqrt{s_{\text{NN}}} = 5.02$  TeV, and during 2017 for pp collisions at  $\sqrt{s_{\text{NN}}} = 5.02$  TeV. The EMCal triggers are used to select events with a high-momentum calorimeter cluster. The EMCal trigger thresholds were set to  $p_{\text{T}} = 7$  and  $11$  GeV/ $c$  for the p–Pb collisions and  $5$  GeV/ $c$  for the pp collisions. Photons with  $p_{\text{T}}$  of  $12$ – $40$  GeV/ $c$ , equivalent to  $x_{\text{T}} = 2p_{\text{T}}/\sqrt{s_{\text{NN}}}$  of  $0.006$ – $0.012$ , were analyzed.

The recipe for the photon production cross section is given by equation 3.1,

$$\frac{d^2\sigma}{dp_{\text{T}}d\eta} = \frac{N_{ev} \times P}{L_{int} \times \epsilon_{\gamma}^{iso}} \times \frac{d^2N}{N_{ev}dp_{\text{T}}d\eta} \quad (3.1)$$

where  $\frac{d^2N}{N_{ev}dp_{\text{T}}d\eta}$  is the event normalized differential photon spectrum. The  $d\eta$  is rapidity acceptance normalization defined as  $\frac{2\pi}{\Delta\varphi\Delta\eta}$ , where  $\Delta\varphi \times \Delta\eta$  is acceptance of the EMCal. Numerically,  $\Delta\varphi = 1.86$  rad and  $\Delta\eta = 1.4$  rad as seen in figure 2.18. The spectra are corrected using the isolated photon efficiency  $\epsilon_{\gamma}^{iso}$  and purity ( $P$ ).  $L_{int}$  is the integrated luminosity in the measurement, and  $N_{ev}$  (sec 3.4) is the number of events analyzed. The efficiency (sec 3.9) is a measure how many photons produced in the collision are detected by the EMCal. The purity (sec 3.8) measures the percent of true signal within our "signal" sample. The integrated luminosity (sec 3.10) relates the number of events provided by the LHC to the number of events triggered by the EMCal.

The difference between the electromagnetic shower profiles of single photons and decay photon pairs ( $\gamma^{\text{decay}}$ ) is used to distinguish between signal photons (direct and fragmentation photons) and background photons (decay photons from neutral hadrons). Clusters passing the isolation and shower shape selections are named isolated  $\gamma$  candidates or " $\gamma^{\text{iso}}$  candidates". The main background for  $\gamma^{\text{iso}}$  candidates arises from multi-jet events where one jet contains a  $\pi^0$  or  $\eta$  meson that carries most of the jet energy. These mesons can decay into collinear photon pairs which are close enough to deposit most of their energy in the same



cell, and thus appear to be a single photon cluster. These mesons can also decay asymmetrically such that most of the meson energy is one of the photons and the other photon is missed by the detector. Such  $\gamma^{\text{decay}}$ 's are misidentified as single photons in the EMCal due to the EMCal cell granularity ( $\Delta\eta \times \Delta\phi \approx 14.3 \times 14.3 \text{ mrad}^2$ ).

The signal purity in the  $\gamma^{\text{iso}}$  selection is measured using the “template-fit method”, in which the measured shower-shape distribution is fit with the sum of signal and background templates with the relative normalization as the single free parameter. The background template is data-driven, calculated with an anti-isolated side-band requirement. The anti-isolated side-band is the region where there are many particles around the photon, i.e. the photon is not isolated.

A Monte Carlo simulation based correction is applied to account for biases arising from signal shape - isolation criterion correlations. The signal template is obtained from photon-jet simulation. The parton opposite to the photon will fragment into a jet. This simulation mimics a photon-jet event in data. The purity of our  $\gamma^{\text{iso}}$  selection is measured to be around 20% at 12 GeV/ $c$  and increases to about 55% at 20 GeV/ $c$  and above. The purity measurements used in this analysis follow directly from [65].

One of the novel aspects of this analysis is the use of ITS standalone tracking for isolation cuts on the photon. The performance of the ITS-standalone tracking has been validated by measuring the charged particle spectrum and comparing it with published ALICE measurements at the same center-of-mass energy [65]. The ITS tracks are used to construct a charged particle isolation variable; omission of neutral particles from the isolation criterion reduces correlations between isolation and shower-shape variables, albeit at the expense of a slightly lower purity.

The template fit was checked independent of simulations, by fitting a purely data driven background outside of the signal region. This check shows that we are not sensitive to the detailed simulation of the shower-shape distributions [65].

The integrated luminosity is calculated using the trigger rejection factors in pp and p-Pb collisions. The trigger rejection factors are obtained from the ratio of the photon spectra created using photons from EMCal triggered events and comparing them to photons spectra created using the minimum bias trigger. The trigger rejection factors are multiplied by the number of events selected for that trigger and divided by the minimum bias cross section measured using van Der Meer scans [66] and [67]. This process is described in greater detail in section 3.10.

Finally, all the ingredients come together to give us the isolated photon cross sections in pp and p-Pb. We scale the pp cross section by the number of nucleons in a lead nucleus and take a ratio to obtain the nuclear modification factor -  $R_{p\text{Pb}}$ .

$$R_{p\text{Pb}} \equiv \frac{1}{A_{\text{Pb}}} \frac{(d^2\sigma^{p\text{Pb}}/dp_{\text{T}}d\eta)}{(d^2\sigma^{pp}/dp_{\text{T}}d\eta)} \quad (3.2)$$

where  $A_{\text{Pb}}$  is 208, the number of nucleons in a Pb nucleus, and the cross sections are the defined in equation 3.1.

## 3.2 Datasets

ALICE data collection is done in large time windows called periods, which are named with the last two digits of year along with a single letter, and can last from a few weeks to a couple of months. Within the periods, the smallest unit of data collection are runs. Each run is given a unique number. Runs can be as short as a few seconds or last multiple hours. An example would be Run 195872 from 13d, where 195872 is the run number and 13d is the period. The ALICE Data Preparation Group (DPG) determines good runs based on the status of the subsystems used during the data collection. There are five categories, shown in table 3.1, which require different subsystems to be in good condition while data taking. The DPG also process the raw data and performs event reconstruction for all the runs, in which all the tracks, vertices, cluster, etc. are identified, their observables (momentum, energy, position, etc.) are calculated and stored. The various iterations of data reconstruction are called passes.

Name	Detector requirement
Tracklet	SSD, SPD, SDD, V0
CentralBarrelTracking	SSD, SPD, SDD, V0, TPC
CentralBarrelTracking_calor	SSD, SPD, SDD, V0, TPC, EMC
CentralBarrelTracking_hadronPID	SSD SPD SDD V0 TPC TOF T0
CentralBarrelTracking_electronPID	SSD SPD SDD V0 TPC TOF TRD T0

Table 3.1: ALICE Data Preparation Group run list classifications

The data sets used in this analysis are shown in Table 3.2. We use the high-luminosity runs of the 2013 p–Pb run (13d,e,f) and the 2017 pp run (17q) that were collected with EMCal triggers. Additionally, we also use the minimum bias triggered p–Pb runs from 13c which are used to calculate the trigger rejection factor for p–Pb.

Photon events were selected by the ALICE EMCal trigger. The EMCal issues triggers at two different levels, Level 0 (L0 trigger) and Level 1 (L1 trigger). The events that pass L0 trigger selection are further processed at L1 trigger. The L0 trigger decision, issued at most  $1.2 \mu\text{s}$  after the collision, is based on the analog charge sum of  $2 \times 2$  adjacent cells evaluated with a sliding window algorithm within each physical Trigger Region Unit (TRU) spanning  $4 \times 24$  cells in coincidence with a minimum bias trigger. The L1 trigger decision, which must be taken within  $6.2 \mu\text{s}$  after the collision, can incorporate additional information from different TRUs, as well as other triggers or detectors [48]. Additionally, the L1 extends the  $2 \times 2$  sliding window search across neighboring TRUs, resulting in a  $\approx 30\%$  larger trigger area than the L0 trigger [68]. In 2013 for p–Pb collisions, one L0 and two L1 triggers with different thresholds were used. The L0 trigger threshold was 3 GeV, while the L1 trigger thresholds were 11 GeV and 7 GeV, well above the L0 trigger efficiency turn-on region. The pp collisions used an L0 and single L1 threshold, of 2.5 GeV and 4 GeV, respectively. Details of the trigger strings used for trigger selection in this analysis are mentioned in section 3.4.

Table 3.2: Datasets used in this analysis. The runs listed in the table corresponds to those that are in the good run list appropriate for analysis using the EMCal and ITS detectors.

Name	Config.	Run Number list	Pass
13c	p-Pb	195529, 195531, 195566, 195567, 195568, 195592, 195593, 195596, 195633, 195635, 195644, 195673, 195675, 195677.	pass4
13d	p-Pb	195872, 195871, 195867, 195831, 195829, 195787, 195783, 195767, 195760, 195724.	pass4
13e	p-Pb	196310, 196309, 196308, 196214, 196208, 196201, 196200, 196199, 196197, 196194, 196187, 196185, 196107, 196091, 196090, 196089, 196085, 195958, 195955, 195935.	pass4
13f	Pb-p	197342, 197341, 197302, 197300, 197299, 197298, 197297, 197296, 197260, 197258, 197256, 197255, 197254, 197248, 197247, 197189, 197153, 197152, 197138, 197092, 197091, 197027, 197015, 197012, 197011, 197003, 196974, 196973, 196972, 196967, 196965, 196721, 196720, 196714, 196706, 196703, 196702, 196701, 196648, 196646, 196608, 196535, 196528.	pass4
13f_new	Pb-p	196433, 196474, 196475, 196477, 196722. 196772, 196773, 196774, 196869, 196870, 196874, 196876, 197139, 197142, 197143, 197144, 197145, 197147, 197148, 197149, 197150, 197348, 197349, 197351, 197386 197387, 197388.	pass4
17q	pp	282440, 282437, 282415, 282411, 282402, 282399, 282398, 282393, 282392, 282391, 282367, 282366, 282365	muon_calor_pass1 pass1_wSDD

The average number of inelastic collisions per bunch crossing,  $\mu$ , is 0.020–0.060 for the 2013 p–Pb data set and in the range 0.015–0.045 for the 2017 pp dataset <sup>1</sup>.

<sup>1</sup>This information can be found in [http://aliquaevs.web.cern.ch/aliquaevs/data/2013/LHC13d/pass4/global\\_properties.pdf](http://aliquaevs.web.cern.ch/aliquaevs/data/2013/LHC13d/pass4/global_properties.pdf) and [http://aliquaevs.web.cern.ch/aliquaevs/data/2017/LHC17q/cpass1\\_pass1/global\\_properties.pdf](http://aliquaevs.web.cern.ch/aliquaevs/data/2017/LHC17q/cpass1_pass1/global_properties.pdf)

Table 3.3: EMCal triggers used in this analysis.

Dataset	Trigger Strings
p-Pb	CEMC7EG1-B-NOPF-CENTNOTRD, CEMC7EG2-B-NOPF-CENTNOTRD,
pp	CEMC7EG2-B-NOPF-CALO

### 3.3 Monte Carlo simulations

Monte Carlo (MC) simulations were used to obtain the signal shower-shape distributions for the template fits (section 3.8)

The simulations of hard processes with isolated photon production in inelastic pp collisions were based on the PYTHIA event generator [69]. In PYTHIA, the signal events are included via  $2 \rightarrow 2$  matrix elements with  $gq \rightarrow \gamma q$  and  $q\bar{q} \rightarrow \gamma g$  hard scatterings, defined at leading order, followed by the leading-logarithm approximation of the partonic shower. The soft underlying events in pp collisions as well as fragmentation are included with the default PYTHIA models.

For the simulation of p-Pb events, the pp samples were embedded into p-Pb inelastic events generated with DPMJET [70]. An appropriate rapidity boost of  $\Delta y = +0.465$  in the direction of the proton beam is added into the simulated events in order to mimic a p-Pb environment.

The simulation events were divided several different transverse momentum bins called  $p_T^{\text{hard}}$ -bins so that there are adequate statistics for rarer hard collisions producing particles at higher  $p_T$ . However, in order to compare to data, the  $p_T^{\text{hard}}$ -bins have to be weighted to provide a realistic description of photon production. The weights are calculated using

$$w_{p_T^{\text{hard}}} = \frac{\sigma_{\text{hard}}}{N_{\text{trials}} \times N_{\text{ev}}}, \quad (3.3)$$

where  $\sigma_{\text{hard}}$  is the average hard process cross section,  $N_{\text{trials}}$  is the number of trials needed to produce the hard process, and  $N_{\text{ev}}$  is the number of generated events [71]. Table 3.4 shows the MC simulations used in this analysis. Each sample is simulated with the detector configuration appropriate for the runs used in this analysis.

Table 3.4: Monte Carlo simulations used in this analysis.

Name	Configuration
17g6a1	p-Pb, 5 TeV, PYTHIA8 Gamma-Jet +DPMJET anchored to 13d/e/f
17g6a3	p-Pb, 5 TeV, PYTHIA8 Jet-Jet +DPMJET anchored to 13d/e/f
18b10a_calo	pp 5 TeV, PYTHIA8 Gamma-Jet anchored to 17p/q
18l2a	pp 5 TeV, PYTHIA8 Jet-Jet anchored to 17p/q

There are two types of simulation:  $\gamma$ -jet and dijet. In the  $\gamma$ -jet simulation, there are signal photon produced from the leading order hard processes mentioned in section 1.5:

QCD Compton scattering and quark-antiquark annihilation. In dijet simulation, back-to-back jets are produced with leading order processes such as two quark scattering mediated by a gluon or a Z boson. Since the final state is two jets, the photons in that simulation are going to be decay photons of the  $\pi^0$  within the jets.

## 3.4 Event selection

We use the following event selection criteria to ensure good event quality and uniform acceptance:

- Runs passing the quality assurance for EMCal and ITS in the Runs Conditions Table as well as approved by ALICE DPG (the selected runs are listed in Table 3.2).
- Selected at least one of the EMCal triggers (detailed below in sub section 3.4.1)
- Valid vertex ( $|z| \neq 0.0$ ) and  $|z| < 10$  cm
- Pileup rejection using information provided by the SPD.

### 3.4.1 Trigger Selection

The analysis was performed on ntuples which are resident on disk in Berkeley. The ntuples are a "tree" structure where all event information is stored on its "branches". Additionally, in the ntuples, the information is stored on an event-by-event (collisions-by-collision) basis. This is advantageous because we can keep track of the events and prevent any cross-event correlations. The ntuples stores the trigger information into trigger bits, two array of size 50:

$$\begin{aligned} \text{trigger\_mask}[0] &= \text{esd\_event} \rightarrow \text{GetTriggerMask}(), \text{ and} \\ \text{trigger\_mask}[1] &= \text{esd\_event} \rightarrow \text{GetTriggerMaskNext50}() \end{aligned}$$

These trigger bits are set to ones and zeros based which triggers were fired for the event. The trigger logbook identifies the trigger ID of each trigger string. For example, the EG2 triggered events recorded by the CALO trigger cluster during the 17q period has the following trigger string: CEMC7EG2-B-NOPF-CALO. As seen here, the trigger string has four components, separated by hyphens. The first part refers to the triggering detector and specific trigger for that detector. For example, CEMC7EG2 corresponds to one of the L1 trigger in the EMCal called EG2. The next component of the trigger refers to the type of collisions which occurred: beam-gas (A), beam-beam (B), or gas-gas(C). The last two parts refer to the past future protection (NOPF) and the trigger cluster (CALO is one such trigger cluster), both of which were previously discussed in section 2.2.1.

Each data taking run in ALICE uses multiples trigger strings. These strings were assigned a trigger ID. For each run, trigger ID is unique for each trigger string. While within one

period, the trigger strings and their corresponding trigger IDs are same for most runs, this not always case. There are some periods where the trigger strings have different trigger IDs in different runs. In order to check if the appropriate trigger was fired, bitwise AND comparisons between the trigger ID and the `trigger_mask` were performed. For example, the trigger string CEMC7EG2-B-NOPF-CALO had the trigger ID 27. In that, the bitwise AND selection would be

$$\text{trigger\_mask}[0] \& (1 \ll 27) \neq 0$$

If result of the left-hand side was not 0, then the event was selected using CEMC7EG2-B-NOPF-CALO trigger. Note: if the trigger ID was greater than 50, then we compared with `trigger_mask[1]`. In ALICE, the triggers have an abbreviated form starting with "k". For example, the minimum bias trigger is called `kINT7` which refers to an AND logic operation between the `V0A` and the `V0C`, also called `V0AND`. However, not all triggers with an `INT7`, the notation for a `V0AND`, are minimum bias triggers. The mapping of the k-names are obtained from an internal ALICE file which stores the k-names and maps them to the appropriate trigger string combinations. For example, for 17p/q, we have,

```
oadb_pp_17pq(AliVEvent :: kINT7,
             "+ CINT7 - B - NOPF[CENT | FAST]",
             "B", triggerCount);
```

which means that an event with `CINT7-B-NOPF-CENT` or `CINT7-B-NOPF-FAST` will be selected when using a `kINT7` flag. The following triggers strings are used in the analysis:

- `CINT7-B-NOPF-ALLNOTRD` (MB): p-Pb minimum bias trigger used for 13cdef
- `CEMC7EG1-B-NOPF-CENTNOTRD` (EG1): p-PbEMCal L1 high threshold trigger (11 GeV) used for 13def
- `CEMC7EG2-B-NOPF-CENTNOTRD` (EG2): p-PbEMCal L1 low threshold trigger (7 GeV) used for 13def
- `CINT7-B-NOPF-CENT` and `CINT7-B-NOPF-FAST` (MB): pp minimum bias trigger used for 17q runs 282367, 282366, 282365.
- `CEMC7EG2-B-NOPF-CALO` (EG2calo): pp EMCal L1 trigger (4 GeV) used for all 17q runs.

In this analysis, the photon spectra are created separately for each trigger, i.e. a cluster spectrum is filled with only clusters from events passing a particular EG trigger. However, there exist events where multiple triggers of interest have fired. In order to avoid double counting the same clusters for different cluster spectra if multiple triggers fire for the same event, the event is only counted for the lowest threshold trigger. For example, if an event

recorded for both EG1 and EG2, it would only be selected as an EG2 event since EG2 has a lower threshold.

The total number of events that pass the selection criteria in each sample is shown in Table 3.5.

Table 3.5: Number of events that passed our full event selection for each of data taking period used in this analysis. The numbers are also shown separately for MB, EG1 and EG2, and EG2calo triggers.

Dataset	$N^{\text{total}}$	$N^{\text{MB}}$	$N^{\text{EG1}}$	$N^{\text{EG2}}$
13c	46,711,817	40,532,292		
13d	16,103,992	819,062	280,764	106,349
13e	22,062,025	1,036,053	359,198	174,411
13f	57,457,480	2,041,251	821,225	389,011
13f_new	37,477,765	1,346,773	485,726	251,862
p–Pb Total	133,101,262	5,243,139	1,946,913	921,633

Dataset	$N^{\text{total}}$	$N^{\text{MB}}$	$N^{\text{EG2}}$
17q pass1_wsDD	61,928,961	41,994,137	2,740,605
17q muon_calor_pass1	33,520,820		6,456,795
pp Total	95,449,781	41,994,137	9,197,400

## 3.5 Calorimeter cluster reconstruction

### 3.5.1 Definition

EMCal clusters are formed by a clustering algorithm that combines signals from adjacent cells. We use calorimeter clusters defined with the “V1” clustering algorithm. The “V1” algorithm starts from a “seed” cell, found by performing a search for a cell which is a local-maximum, and adds “neighbor” cells to the cluster if they are above a given energy threshold. The cluster definition is exclusive, so once a cell is assigned to a cluster, it is not considered for other clusters. The minimum energy for the seed cell was set to 500 MeV, and the minimum energy for the neighbor cell was set to 100 MeV; these values are several times larger than the standard deviation of the electronic noise. The typical cluster was formed using around 10 cells. The distribution of the number of cells in a cluster is in figure 3.1 for p–Pband figure 3.2 for pp.

### 3.5.2 Corrections

We apply several corrections at the cell level, implemented within the “EMCal Correction Framework,”<sup>2</sup> before the clustering algorithm is run over the data and simulations. The following corrections are applied:

- “CELLENERGY”  
This performs an energy calibration of cells, with coefficients obtained with  $\pi^0 \rightarrow \gamma\gamma$  mass measurements. This calibration is applied for data.
- “CELLBADCHANNEL”  
This removes cells that have been declared hot or dead for a given run period. This calibration is applied for data and simulations.
- “CELLTIMECALIB”  
This correction applies constant offsets to the cell time measurements to minimize the spread among cells. This calibration is applied for data.
- “CELLEMULATECROSSTALK”  
This correction, described in detail in Ref [72], modifies the simulated cell energies to emulate the cell cross-talk that has been observed in data. This is applied to all the simulations described in Table 3.4.
- “CLUSTERNONLINEARITY”  
This performs a correction for cluster energy for cells which give a non-linear response. This calibration is applied for data and simulations.

For more details on the corrections, beyond those mentioned in section 2.2.5, please refer to the EMCAL performance paper [64].

### 3.5.3 Selection

The following selection is applied on the calibrated clusters. The cluster selection is identical to the cluster selection used in [73], with the addition of a azimuthal angle cut in order to exclusively select photons in EMCAL.

- Cluster pseudorapidity:  $|\eta| < 0.67$
- Cluster azimuthal angle:  $1.396 < \phi < 3.2$   
The acceptance cuts ensures that each photon was seen in the EMCAL acceptance.
- Number of cells cut:  $N_{\text{cell}} \geq 2$   
This requirement removes clusters that are likely dominated by noise.

---

<sup>2</sup>[http://alidoc.cern.ch/AlIPhysics/master/\\_r\\_e\\_a\\_d\\_m\\_eemc\\_corrections.html](http://alidoc.cern.ch/AlIPhysics/master/_r_e_a_d_m_eemc_corrections.html)



- Exoticity:  $E_{\text{cross}}/E_{\text{max}} > 5\%$   
We remove “exotic” or “spiky” clusters likely coming from slow neutrons or highly-ionizing particles hitting the avalanche photo-diode of a cell by a requirement on the ratio of the summed energy around the leading cell to the energy in the leading cell.
- Cluster time:  $|t| < 20$  [ns]  
We require a cluster time measurement of  $|t| < 20$  ns to remove out-of-bunch pileup.
- Number of local maxima:  $N_{LM} < 3$   
This cuts suppresses background and improves the MC simulation description of the background [74].
- Distance seed-cell to bad-channel  $\geq 1$  cells.
- Shower Shape:  $0.1 < \sigma_{\text{long}}^2 < 0.3$   
The shower shape cut helps separate single photon clusters from merged photon cluster
- Isolation:  $ISO < 1.5$  GeV/ $c$   
The isolation cut removes all photons which have more 1.5 GeV/ $c$  energy around them in a  $R = 0.4$  cone around them.

All cluster spectra presented in this analysis only contain photons which have passed through all the cuts listed above, except for the trigger rejection factor calculation where the isolation cut was not applied. Figures 3.1 and 3.2 show the distribution of the variables used in the cluster selection and the effect of sequential selection (“cut flow”) for the p–Pb and pp data respectively.

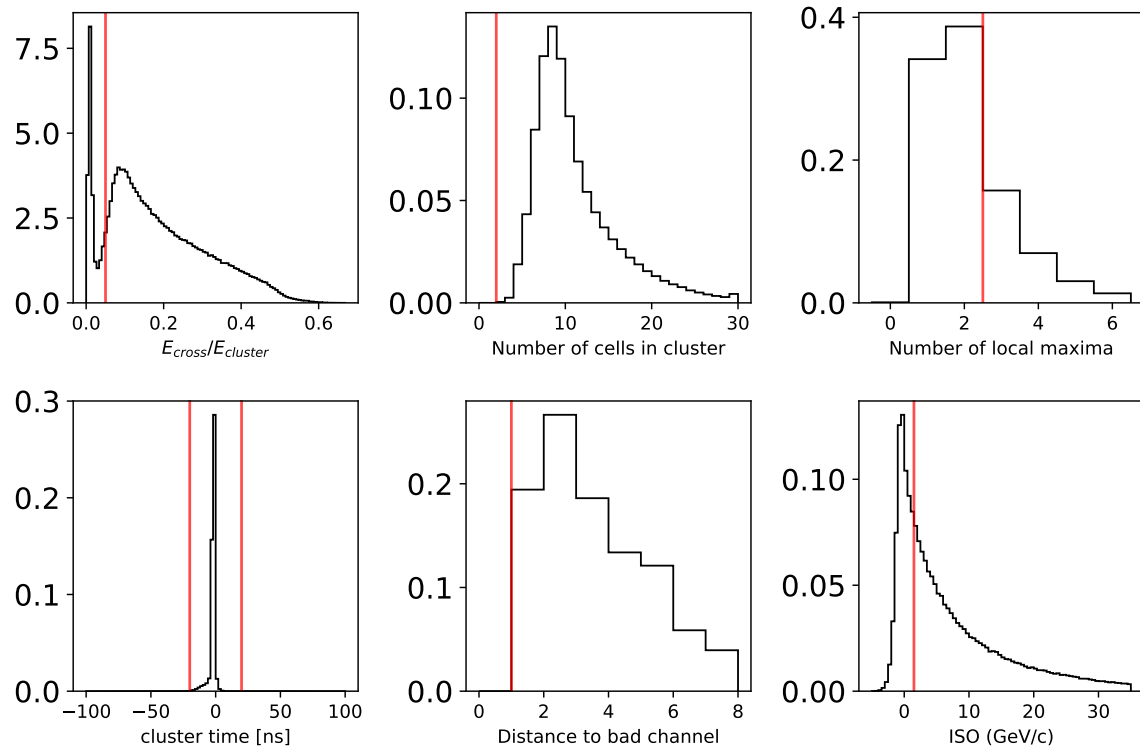


Figure 3.1: Distribution of variables used in the cluster selection of p-Pb data. The red vertical lines represent the cuts used. The cluster cuts get applied sequentially, i.e. the clusters cut with a given variable do not appear in the next.

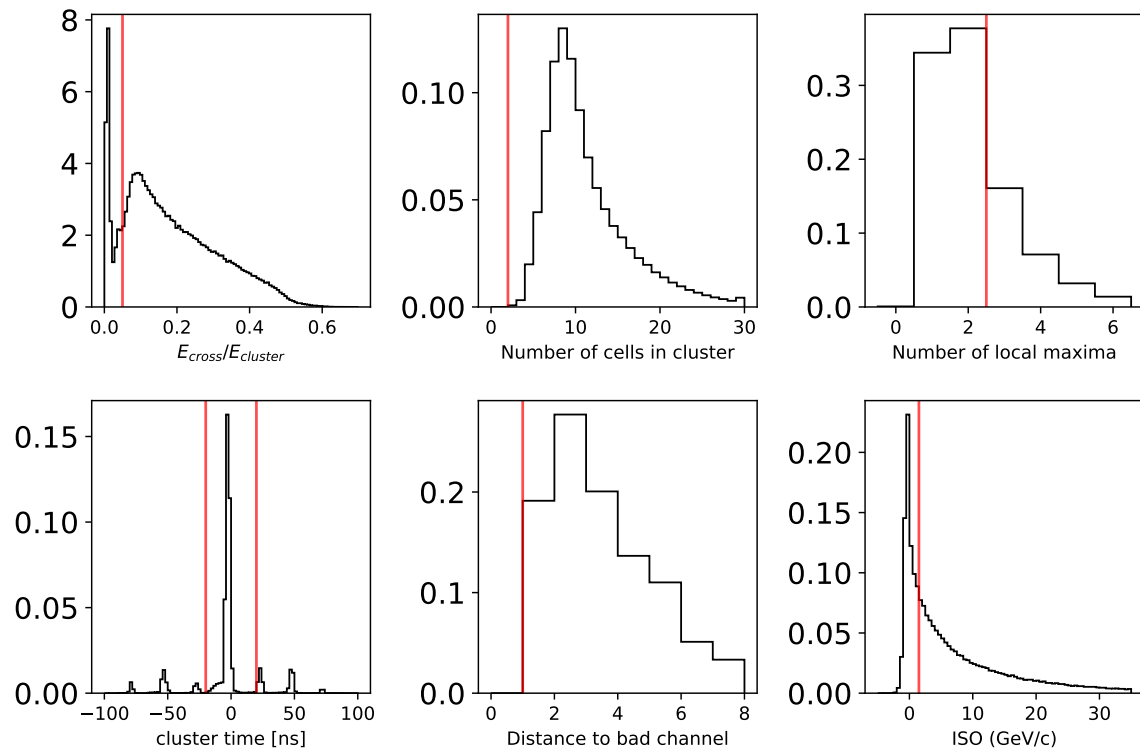


Figure 3.2: Distribution of variables used in the cluster selection in pp data. The red vertical lines represent the cuts used. The cluster cuts get applied sequentially, i.e. the clusters cut with a given variable do not appear in the next.

### 3.6 Photon Identification

Above  $\pi^0$   $p_T \approx 6$  GeV/ $c$ , photons from  $\pi^0$  decays start merging into a single cluster in the EMCal. To identify clusters produced by single photons and reject clusters produced by two photons from a meson decay, we use variables that encode the shape of the calorimeter shower. Single photons have a circular shower, while merged photons produce an elliptical shower in the calorimeter. The shape of the electromagnetic shower as seen in the cells of the EMCal was shown previously in section 2.21.

We use the  $\sigma_{\text{long}}^2$  shower shape variable in order to determine if the shower is circular or elliptical as seen in figure 3.3 with a left cartoon having a circular shower shape for a single photon and the right cartoon having a more elliptical shower shape for decay photons. The shower shape variable is defined as the weighted root-mean-square of the shower energy along the major ellipse axis, defined according to Ref. [64] as:

$$\sigma_{\text{long}}^2 = \frac{s_{\eta\eta} + s_{\varphi\varphi}}{2} + \sqrt{\frac{(s_{\eta\eta} - s_{\varphi\varphi})^2}{4} + s_{\eta\varphi}^2}, \quad (3.4)$$

where  $s_{\varphi\varphi}, s_{\eta\eta}, s_{\eta\varphi}$  are the elements of the covariance matrix which represents the energy distribution along the  $\eta$  and  $\varphi$  directions. The matrix elements are calculated using

$$s_{ab} = \sum_i \frac{w_i a_i b_i}{w_{\text{tot}}} - \sum_i \frac{w_i a_i}{w_{\text{tot}}} \sum_i \frac{w_i b_i}{w_{\text{tot}}} \quad (3.5)$$

where  $a_i$  and  $b_i$  are the cell indices in  $(\eta, \varphi)$  coordinates 2.21. The  $(w_i)$  are weights which depend on the cell energies logarithmically, i.e  $w_i = \text{Maximum}(0, w_{\text{max}} + \ln(E_{\text{cell},i}/E))$ .  $w_{\text{tot}}$  and  $E$  are both defined as sums of the  $w_i$  and  $E_{\text{cell},i}$ , respectively ( $w_{\text{tot}} = \sum_i w_i$  and  $E = \sum_i E_{\text{cell},i}$ ). Following a previous work [75], the cutoff ( $w_{\text{max}}$ ) was chosen such that that

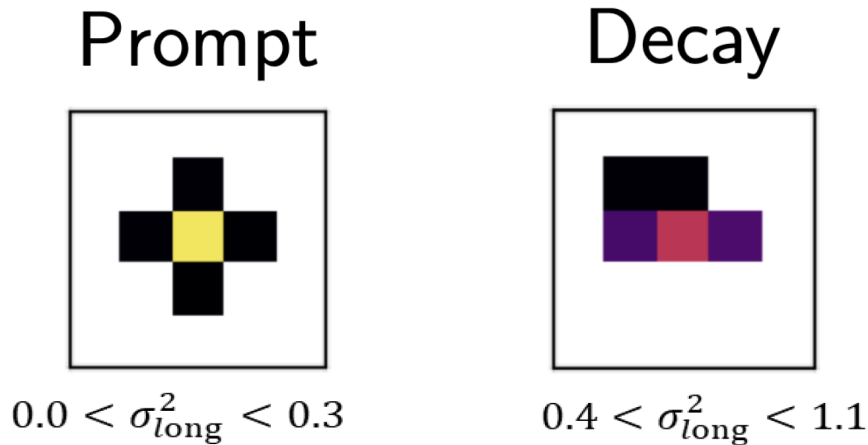


Figure 3.3: Two shower shape distributions - single photon (left) and decay photons (right)

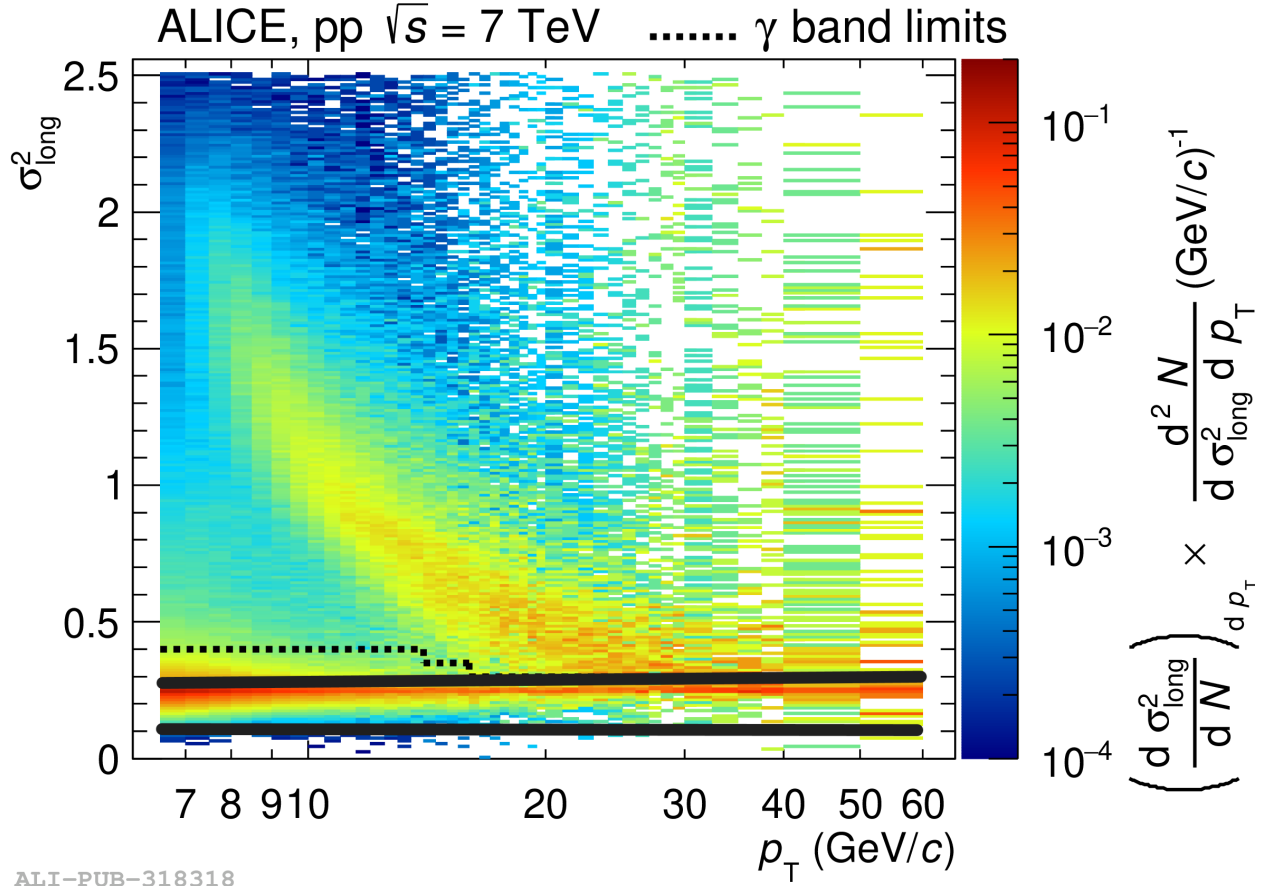


Figure 3.4: Shower shape parameter  $\sigma_{long}^2$  vs cluster  $p_T$  as measured by ALICE for 7 TeV pp data. The solid black lines indicate bounds of the shower shape used in this thesis:  $0.1 < \sigma_{long}^2 < 0.3$ . Image from [74]

cells that contain less than  $e^{-4.5} = 1.1\%$  of the total cluster energy would not be considered in the  $\sigma_{long}^2$  calculation.

We have determined that clusters within in the narrow, peaked region of of the  $\sigma_{long}^2$  distribution are single photons, and thus, we require a shower shape selection of  $0.1 < \sigma_{long}^2 < 0.3$ . Figure 3.4 shows the distribution of the shower shape variable vs  $p_T$  as measured by ALICE during a 2019 photon measurement at  $\sqrt{s} = 7$  TeV. The horizontal solid black lines represent upper and lower bounds of the shower shape cut used in this thesis:  $0.1 < \sigma_{long}^2 < 0.3$ .

## 3.7 Isolation

Direct photons are produced surrounded by small hadronic activity because the parton and the subsequent hadron should be on the opposite of the photon, while fragmentation photons are found within a jet at leading order in perturbative QCD. Direct and fragmentation components have no physical meaning beyond leading order, and cannot be factorized; the sum of their cross sections is the physical observable. However, in order to limit fragmentation photons and select photons produced in the initial hard scattering, we use an isolation requirement. The isolation requirement also suppresses the background from decays of neutral mesons.

We construct an isolation variable only using charged particle tracks in order to avoid biases due to the correlation between the isolation cuts and the  $\pi^0$  decay opening angle. This allows us to use the full EMCAL acceptance, albeit at the expense of a worse purity. It will be shown below that correcting for the purity results in a spectrum in full agreement with that arising from a charged+neutral isolation cut.

The isolation variable for this analysis is defined as the scalar sum of the transverse momentum of charged particles within an angular radius around the cluster direction,  $R = \sqrt{(\Delta\varphi)^2 + (\Delta\eta)^2} = 0.4$  (with  $\Delta\varphi$  measured in radians). A cartoon showing the cone around the photon is shown in figure 3.5. The arrows at the vertex of the cone are tracks whose  $p_T$  will be summed to obtain the raw isolation defined by equation 3.6.

$$\text{ISO}^{\text{raw}} = \sum_{\text{track} \in \Delta R < 0.4} p_T^{\text{track}} \quad (3.6)$$

The charged particles used as input for the isolation calculation are with  $0.15 < p_T < 10$  GeV/c,  $|\eta| < 0.8$  and pass the selection described in the tracking section of [65].

The isolation variable defined in Equation 3.6 ( $\text{ISO}^{\text{raw}}$  in figure 3.7) is susceptible to background from the charged particles from the underlying event, which is defined and explained in more detail in the following section (sec 3.7.1). In order to remove underlying event effects, we apply an underlying event subtraction on an event-by-event bases. The underlying event (UE) estimate and subtraction is performed in the same manner as in [65]. A summary of the process along with performance figures is provided in the follow subsections.

### 3.7.1 Underlying Event estimation

The UE is defined as the particles not associated with the hard-scattering of the collision. We utilize the FASTJET jet area/median method to discriminate between the soft and hard components of an event [76], which uses the median of the distribution of transverse momentum densities of all jets in an event.

The estimation of the UE density uses non-leading jets  $J'$  reconstructed by the  $k_T$ -algorithm, which clusters the softest particles first, with distance parameter  $R = 0.4$ . The transverse momentum density of each jet is the momentum of the jet divided by the area of the jet. The area of the jet is calculated using the sum of the Voronoi cells of each particle

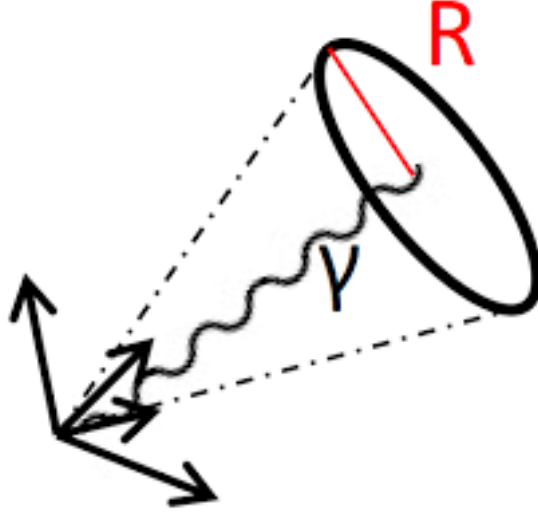


Figure 3.5: The isolation cone of radius  $R$  around the photon  $\gamma$ . The tracks within the cone are summed up according to equation 3.6.

within the jet. A Voronoi cell is the region for each particle, that consists of all points in the same plane that are closer to that particle than to any other. The estimated UE density is defined as:

$$\rho = \text{med} \left\{ \frac{\sum_{i \in J'_k} p_{T,i}}{\sum_{i \in J'_k} A_i} \right\} \quad (3.7)$$

where  $p_{T,i}$  is the transverse momentum, and  $A_i$  the Voronoi area, the area of a Voronoi cell<sup>3</sup> of the particle  $i$  within the jet ( $J'_k$ ) reconstructed for purpose of UE estimation.

Figure 3.6 shows the median charged-particle density,  $\rho$ , distribution obtained in pp and p-Pb data in minimum bias events and in events that pass the selection in Section 3.4 and thus have a high- $p_T$  cluster. The distribution in minimum-bias events decreases approximately exponentially. The distribution in photon-triggered events is different and follows an asymmetric Gaussian distribution that peaks at approximately 1.0 GeV/ $c$  and 2.5 GeV/ $c$  for pp and p-Pb collisions, respectively.

The mean and standard deviation for each distribution is shown in Table 3.6. The difference in UE-density in p-Pb, compared to pp, is expected due to the increased number of nucleon-nucleon collisions.

The average  $\rho$  for photon-triggered events reported in Table 3.6 is consistent with an independent estimate used in a previous isolated photon cross section measurement in p-Pb, based on the “ $\eta$ -band” method, that uses the same dataset and cluster selection [71].

<sup>3</sup>The method used is the following fastjet::VoronoiAreaSpec [http://www.fastjet.fr/repo/doxygen-2.4.5/classfastjet\\_1\\_1VoronoiAreaSpec.html](http://www.fastjet.fr/repo/doxygen-2.4.5/classfastjet_1_1VoronoiAreaSpec.html)

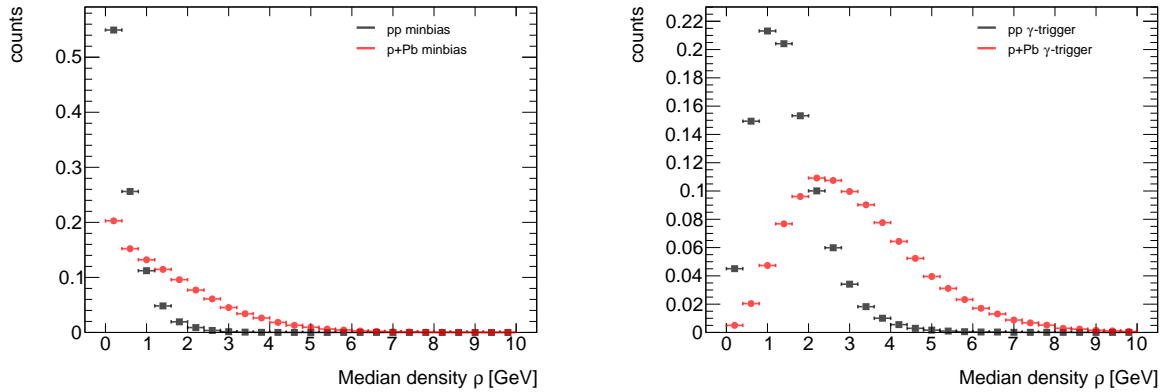


Figure 3.6: Distribution of the median charged-particle transverse momentum density,  $\rho$ , in pp and p–Pb data, for a minimum-bias selection (left panel) and in photon-triggered events (right panel).

Table 3.6: Median transverse momentum density mean and standard deviation in minimum-bias and and photon-triggered events in pp and p–Pb data. The statistical uncertainty in these numbers is negligible.

	pp minbias	pp $\gamma$ -trigger	p–Pb minbias	p–Pb $\gamma$ -trigger
$\langle\rho\rangle$	0.49 GeV/c	1.51 GeV/c	1.56 GeV/c	3.19 GeV/c
$\sigma_\rho$	0.47 GeV/c	0.85 GeV/c	1.32 GeV/c	1.60 GeV/c

### 3.7.2 UE correction to isolation variable

For each event and cluster, we subtract the underlying event using the measured charged-particle density  $\rho$  that is calculated event-by-event as described in Section 3.7.1:

$$\text{ISO} = \text{ISO}^{\text{raw}} - \rho \times \pi(0.4)^2. \quad (3.8)$$

with  $\text{ISO}^{\text{raw}}$  given in equation 3.6. The average subtraction for an isolation cone of  $R = 0.4$  is about 1.6 GeV/c and 0.8 GeV/c for p–Pb and pp collisions, with a standard deviation of 0.9 GeV/c and 0.4 GeV/c, respectively.

Figure 3.7 shows the isolation distribution before and after underlying event subtraction for p–Pb and pp collisions. The distributions have a positive tail that decreases exponentially, as this observable effectively measures multi-jet production. The difference between the p–Pb and pp distribution at low ISO values is due to larger number of nucleon-nucleon collisions in p–Pb collisions. The underlying event subtraction slightly modifies the isolation distribution, and a negative tail arises from a over-subtraction of the underlying event due to region-to-region fluctuations. The over-subtraction is a small effect as seen by rapidly falling tails in both pp and p–Pb.



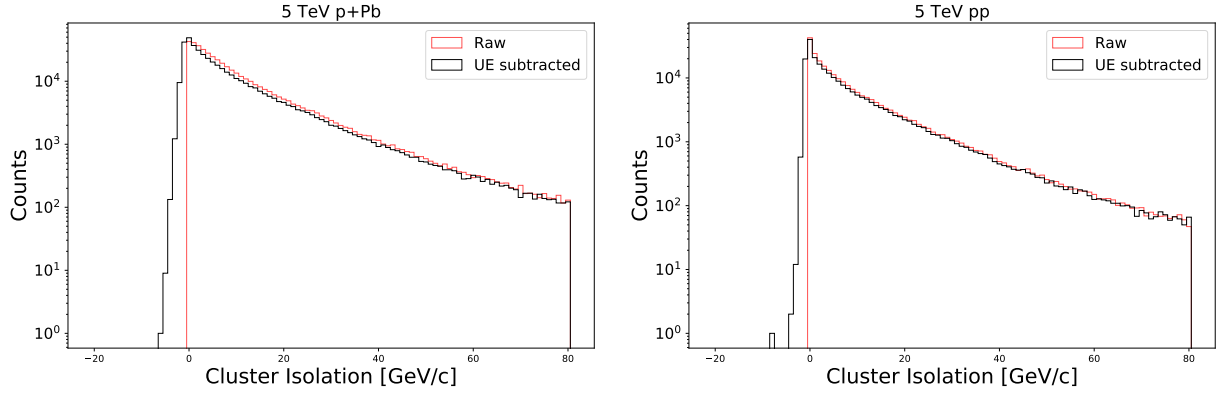


Figure 3.7: Cluster isolation before and after underlying event subtraction in p–Pb (left panel) and pp (right panel) collisions.

Figure 3.8 shows the distribution of cluster isolation energy after UE subtraction for photon-jet and dijet simulations of p–Pb data (see Table 3.4). The dijet simulation shows a prominent exponential tail at large ISO values, and the photon-jet simulation shows a Gaussian-like shape with a tail. In both cases, the negative tail falls rather sharply as expected due to the same reasons mentioned previously; region-to-region fluctuations in the UE do not come from the hard processes.

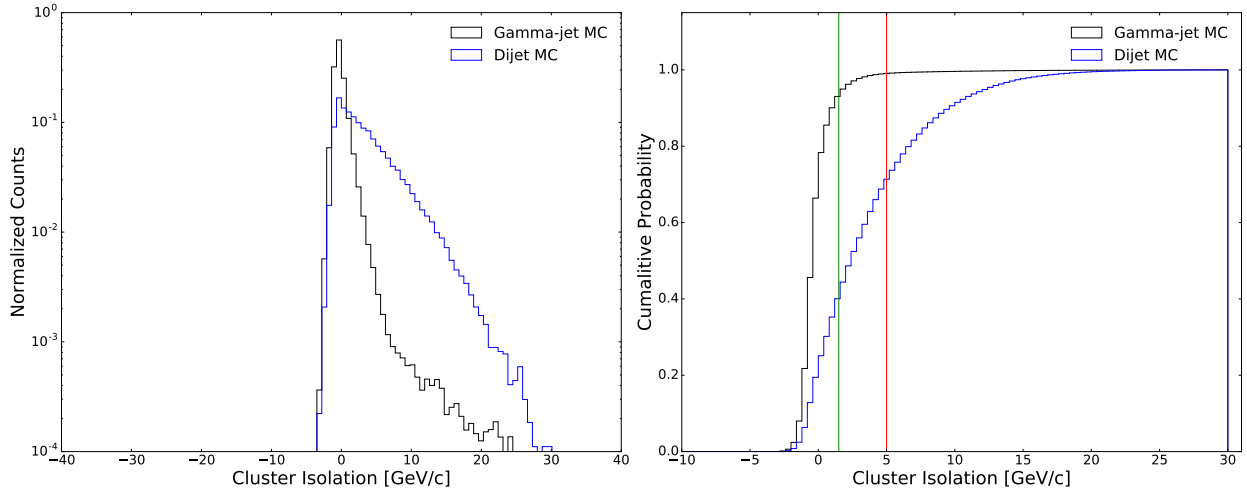


Figure 3.8: Isolation distribution of clusters that pass our selection in p–Pb photon-jet and dijet simulations, and corresponding cumulative distribution. Two vertical lines at  $\text{ISO} = 1.5 \text{ GeV}/c$  (green) and  $\text{ISO} = 5.0 \text{ GeV}/c$  are shown in the right panel for reference.

Since the purity measurement uses a two variable template fit, we define a sideband, which

is the region in the isolation distribution where we do not expect many signal photons. This region is dominated by background photons, so it used to define the background template. For the background template, we require  $\text{ISO} > 5 \text{ GeV}/c$ ; photons produced in the dijet simulation dominate this region compared to photons produced in the gamma-jet simulation, as seen in figure 3.8. The cumulative distributions (Figure 3.8, right panel) show that a  $\text{ISO} < 1.5 \text{ GeV}/c$  selection keeps about 90% of the signal and rejects about 60% of the background. The relatively loose photon isolation criteria reduces the dependence of the results on the details of the simulation of the detector noise, tracking resolution, and the underlying event.

## 3.8 Purity Measurement

The main background present in our  $\gamma^{\text{iso}}$  selection is photons from neutral meson decay. In high  $p_{\text{T}}$  jets, these decays can become collinear and deposit their energy in a single EMCal cluster. While the cluster and isolation cuts help reduce the bulk of neutral meson background, multi-jet events that produce a  $\pi^0$  or  $\eta$  that carries most of the jet energy can pass the selection. The  $\pi^0$  production cross-section is much larger than the prompt photon cross-section, so even if such pions are relatively rare, they are not rare compared to photons [77]. Consequently, we have contamination in our signal for the  $p_{\text{T}}$  range of interest. In this section, we show measurements of the purity of our  $\gamma^{\text{iso}}$ -candidate sample (photons which pass all our cluster selection criteria), done with a template-fit method. The purity measurement and procedure from [65] are summarized here and the reference should be consulted for more details.

### 3.8.1 Template fit method

The purity of the isolated photon sample is determined with a two-component template fit. The distribution of the measured shower shape variable for  $\gamma^{\text{iso}}$ -candidate sample is fit to a linear combination of the signal distribution and the background distribution, often denoted as signal template and background template. The shape of the signal distribution is determined by a photon-jet simulation (see Table 3.4) and the shape of the background distribution is determined from data by looking at the shower shape distribution in the anti-isolated sideband region. Then, a correction is computed from a dijet simulation which should be simulating only background. The correction is applied as a weight on the background distribution. This will be explained in more details below.

The shape of the background distribution is estimated by using the sideband technique. Described above, the sideband region selects of clusters from isolated decay photons with clusters that are in the anti-isolated region but pass all other selection criteria. The signal and sideband regions defined using the isolation variable are illustrated in Figure 3.9.

For simplicity, the same sideband regions are used for pp and p-Pb data. The lower bound of the sideband region is defined as  $\text{ISO} = 5 \text{ GeV}/c$ , while the upper bound is chosen

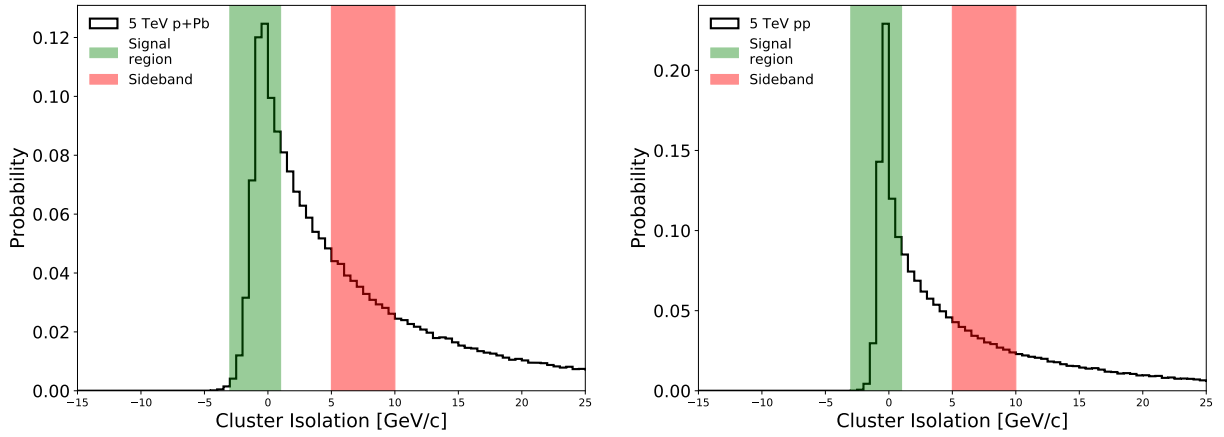


Figure 3.9: Isolation variable distribution of clusters with  $p_T$  between 12 and 16 GeV/ $c$  in p–Pb data (left panel) and pp data (right panel). The green shaded are represents the signal region (ISO < 1.5 GeV/ $c$ ); the red represent the sideband (5 < ISO < 10 GeV/ $c$ ) used to estimate the background template.

such that the sideband is as narrow as possible while still containing a comparable number of photons to those in the signal region.

Figure 3.10 summarizes the signal and background templates used in the template fit. The background shape in the  $\sigma_{\text{long}}^2$  variable shows a peak in the single-shower region and a “bump”, both due to photons from  $\pi^0$  decays. We can see that collinear decay photons still contaminate the single photon region even after the cluster cuts, hence the necessity of purity determination and correction.

The background template is corrected for the correlation between shower shape and isolation energy using weights obtained from a isolated and anti-isolated cluster ratio. These weights are then applied to the anti-isolated clusters in data using equation 3.9. If the MC correctly replicates the data, the Weights function properly corrects the anti-isolated decay photon  $\sigma_{\text{long}}^2$  distribution to the isolated decay photon  $\sigma_{\text{long}}^2$  distribution, which is our main background.

$$\begin{aligned} \text{Weights}(\sigma_{\text{long}}^2) &= \frac{\text{ISO}_{\text{MC}}(\sigma_{\text{long}}^2)}{\text{Anti-iso}_{\text{MC}}(\sigma_{\text{long}}^2)} \\ \text{Bkg}^{\text{corrected}}(\sigma_{\text{long}}^2) &= \text{Non-iso}_{\text{data}}(\sigma_{\text{long}}^2) \times \text{Weights}(\sigma_{\text{long}}^2) \end{aligned} \quad (3.9)$$

The purity calculated with the corrected background template is 8–13% lower than the purity calculated with the uncorrected background template; an example of both cases is shown in Figure 3.11. We can see that using the corrected background template greatly improves the quality of the fit. The evaluation of the systematic uncertainty associated with this correction is described in Section 3.8.2.

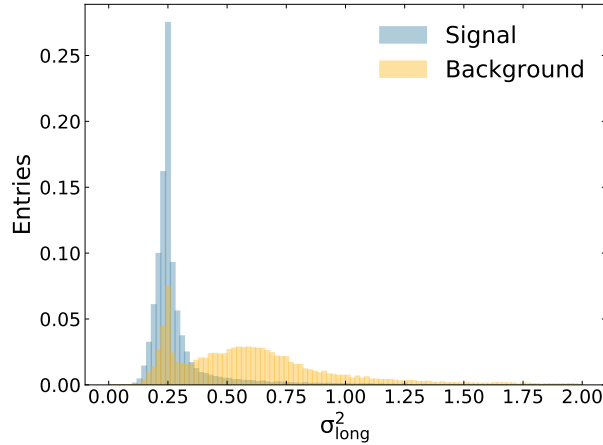


Figure 3.10: Normalized signal (blue) and background (yellow) distributions used as input for the template fit. These distributions correspond to clusters with  $p_T$  in the 15–20 GeV/ $c$  range.

The distribution of isolated clusters is fit with a linear combination of the signal and background templates, with the number of signal cluster as the only free parameter in the fit because the overall normalization,  $N$ , is fixed to the total number of isolated clusters:

$$N^{\text{observed}} = N_{\text{sig}} \times S + (N - N_{\text{sig}}) \times B, \quad (3.10)$$

where  $S$  and  $B$  are the normalized signal template and background template.

Figures 3.12 show template fit results for p–Pb and pp data as well as a distribution of the residuals for each fit. In all cases we see no systematic pattern in the residuals, and the reduced  $\chi^2$  ranges around 1. The purity measurements are presented in graphical form in Figure 3.13.

Since the shape of the purity distribution is sharply rising in the first three bins, there are bin edge effects. For example, two photon which have  $p_T$  of  $20 \pm \epsilon$  will have difference of almost 20% in terms of their purity correction based one being in the 15–20 GeV/ $c$  bin and the other in the 20–25 GeV/ $c$  bin. However, the purity correction of the two photons should be similar since they are very close to each in  $p_T$ . These are bin edge effects. To obtain smooth values of purity as a function of  $p_T$ , an error function is fitted to the purity for each system. When applying a purity correction, each cluster  $p_T$  is used as the input for error function, and resulting value is used as a weight while filling the cluster spectra. The error function fits to the purity are shown in figure 3.14 for both pp and p–Pb.

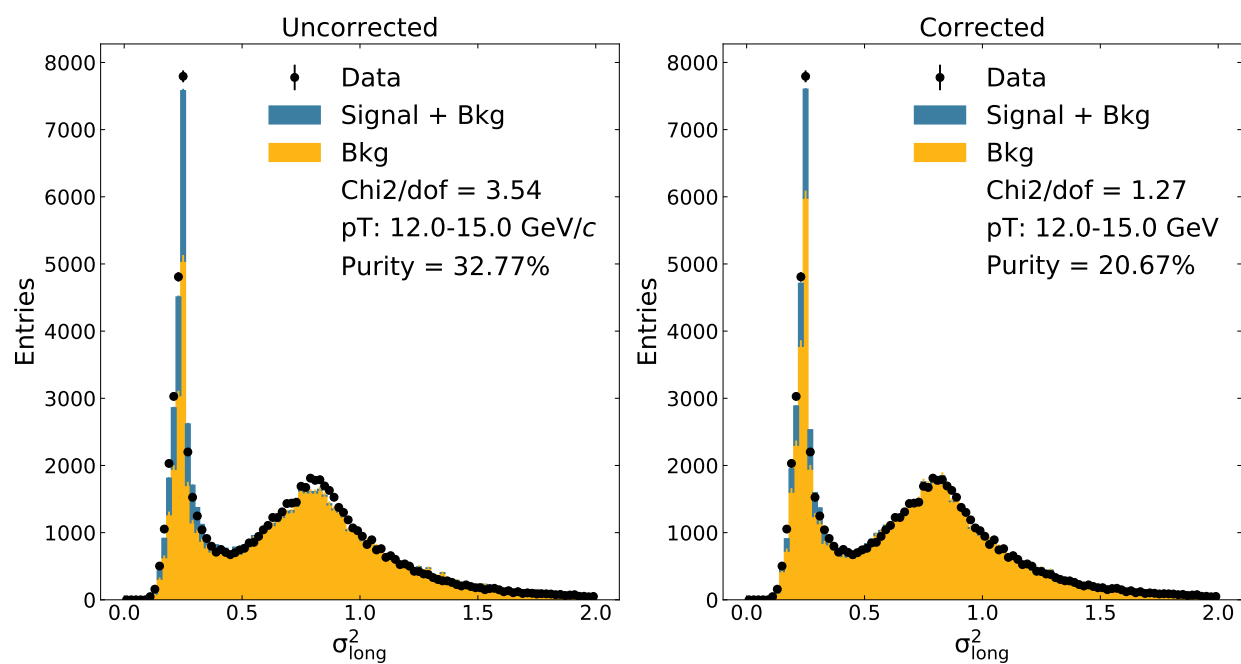


Figure 3.11: An example of the template fit with and without the background template correction in p–Pb for clusters with  $12 < p_{\text{T}} < 15$  GeV/ $c$ . The goodness of fit is better after the correction and the purity is significantly lower.

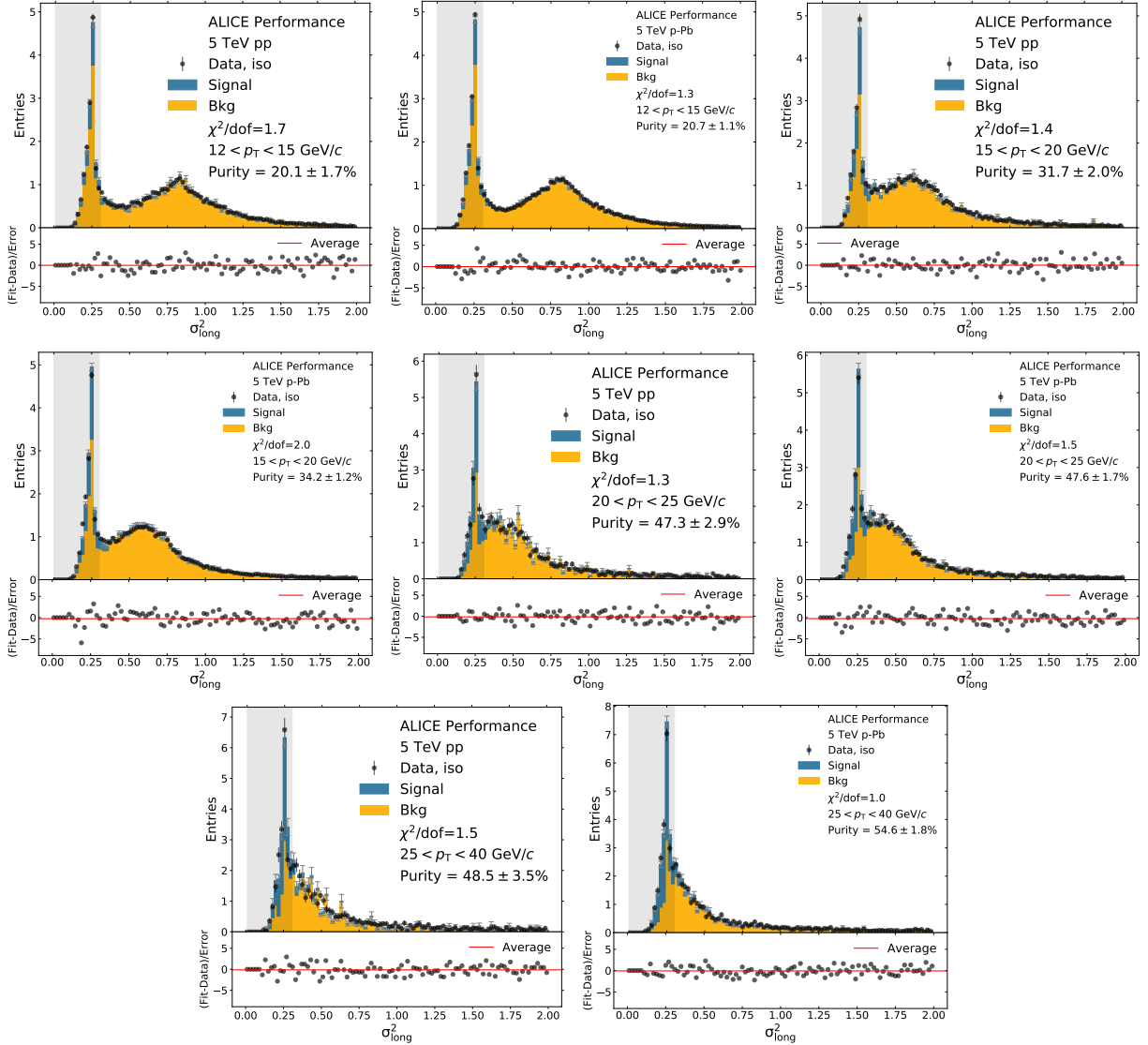


Figure 3.12: Template fit results in pp and p-Pb data. The stacked histograms (yellow for background, blue for signal) are the predicted counts given the best-fit value of the number of signal photons,  $N_{\text{sig}}$ . The hatched gray area represents the interval considered for the purity estimate. The bottom panels show the normalized residuals of the fit, considering the statistical uncertainty on the isolated cluster data and the background template added in quadrature.

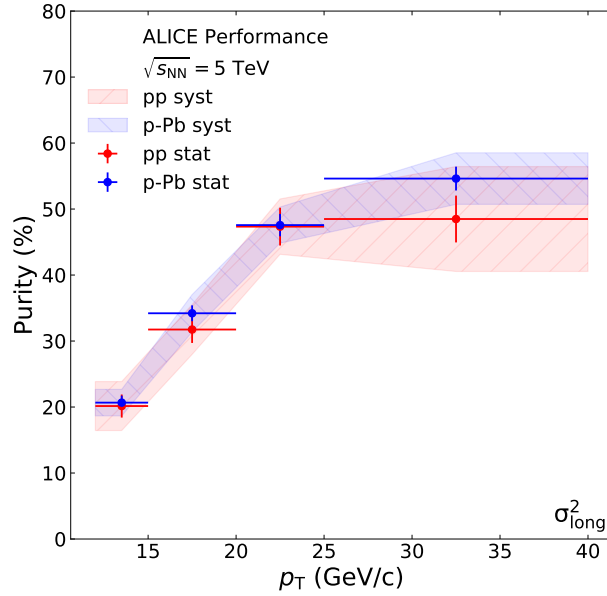


Figure 3.13: Purity of isolated-photon selection as a function of cluster  $p_T$ . The error bar represents statistical uncertainty only. The error band represents the systematic uncertainty only.

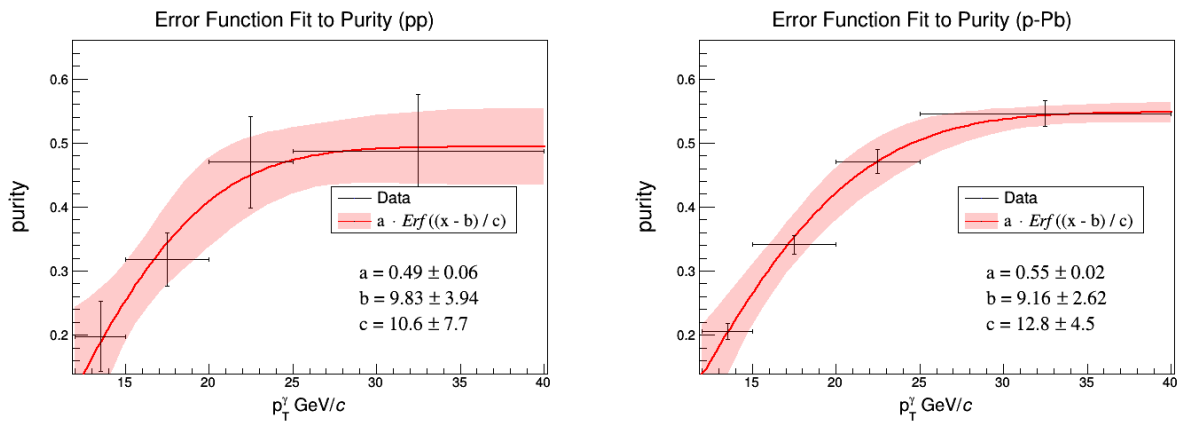


Figure 3.14: Purity of isolated-photon selection as a function of cluster  $p_T$  and the error function fit to the purity for pp (left) and p-Pb (right),

### 3.8.2 Systematic uncertainties of the purity measurement

There are two assumptions underlying the template fit procedure:

1. The signal template from simulations correctly represents the signal shape in real data
2. The shape of the corrected background estimated from the anti-isolated sideband reflects the shape of the background in the signal region

The dominant sources of systematic uncertainty on this measurement are as follows: the signal template, the sideband region selection, and the background template correction. The effects varying the cluster cuts on the purity are neglected as a source of systematic uncertainty as they are small compared to the dominant sources mentioned previously.

#### 3.8.2.1 Signal template

The systematic uncertainty on the purity due to the signal template is estimated by using a data-driven template fit. The fit range is restricted to the background-dominated region (0.4–1.5 for  $\sigma_{\text{long}}^2$ ), and only the background template is used to fit the isolated data. Since the background template alone is used to fit the data, any changes in the purity will be due to the lack of the signal template, giving an estimate of the magnitude of the signal template’s impact on the photon purity. This leaves the normalization as the only free parameter. The background normalization is fitted, and the difference between the integral of the isolated data and the integral of the background in the signal region is taken to be the signal. The results obtained with this method in pp and p–Pb (figure 3.15) have some systematic patterns and are observed in the residuals, which are attributed to the lack of MC-correction on the background template. As a conservative estimate, the full difference between the nominal results is taken as a systematic uncertainty in the signal template.

The effect of the cross-talk emulation was studied by calculating the purity with and without the cross-talk. The cross-talk emulation was Monte Carlo simulation correction because cross-talk has been observed in the EMCal super modules, but was not initially present in the simulations. The effect was compared to the purely data-driven template fit as described previously, and the uncertainty due to the cross-talk has been absorbed into the signal template uncertainty and propagated to the cross-section via the purity uncertainties.

We perform an additional check by smearing the signal template using a random number from a Gaussian with a fixed width and multiplying each cluster’s  $\sigma_{\text{long}}^2$  by the random number. This was done for various widths up to 10% and uncertainty was found to be smaller than the background-only fit. (See the appendix of [65] for more details).



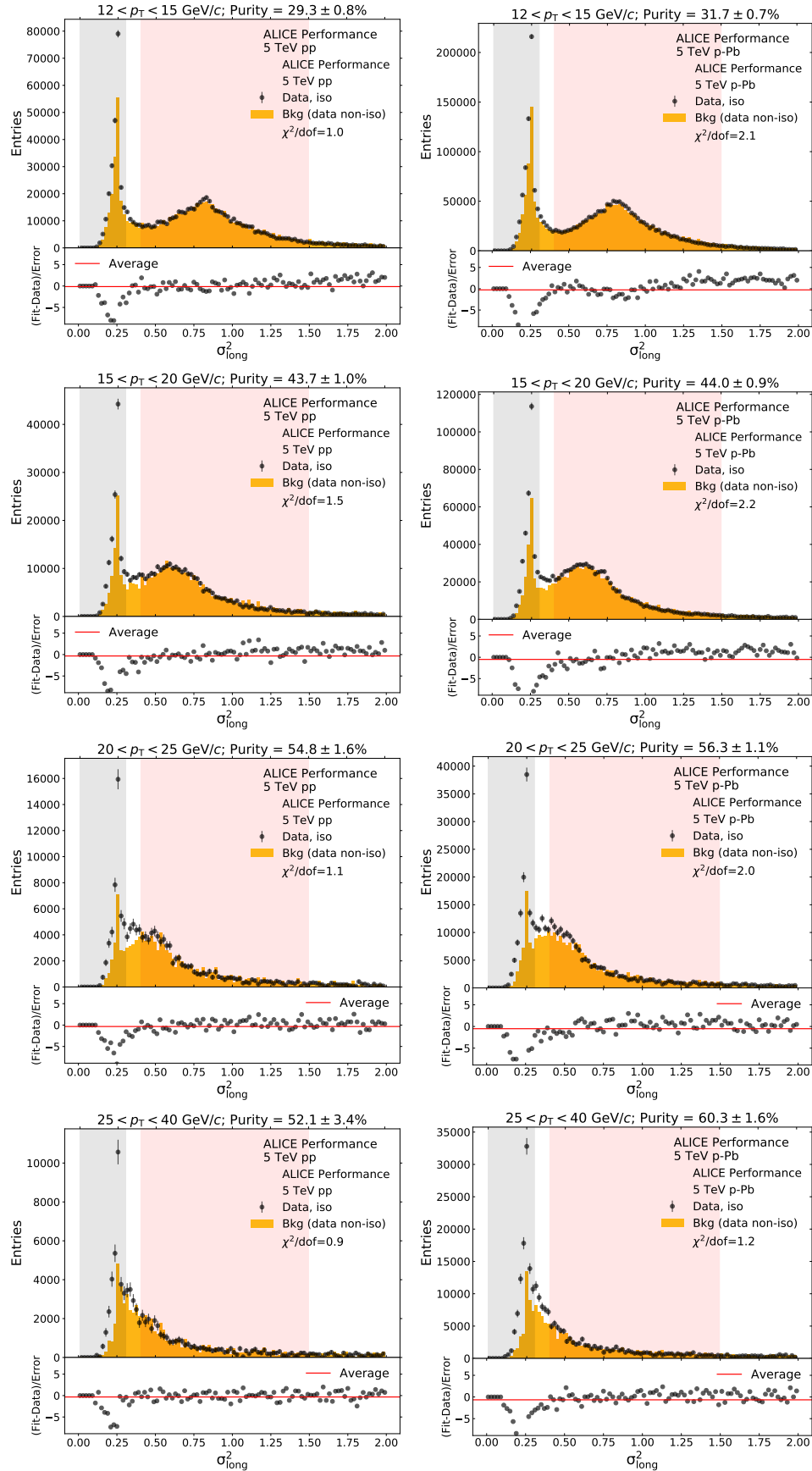


Figure 3.15: Template fit results of background-only template method for pp and p-Pb data

### 3.8.2.2 Sideband variation in the background template

In order to estimate the effect of varying the sideband in the background template on the purity, we use 2 GeV/ $c$  overlapping regions in the cluster isolation distribution to estimate various background shower-shape distributions. All the distributions are fitted using the template fit and  $\chi^2/\text{dof}$  and purity are calculated for each fit. The  $\chi^2/\text{dof}$  and purity are then plotted as a function of the anti-isolation region as shown in Figure 3.16. We look at the  $\chi^2/\text{dof}$  to determine the best anti-isolation regions which result in good fits; thus, we select the 5-10 GeV/ $c$  region in our sideband definition for the purity calculation. The systematic uncertainty due to choice of the sideband range is determined by using the max variation of purities calculated in the 5-10 GeV/ $c$  region and dividing by  $\sqrt{12}$ , the  $1\sigma$  for a uniform distribution. This is because for a uniform distribution the standard deviation is  $(b-a)/\sqrt{12}$  where  $b$  is minimum value and  $a$  is the maximum value in the distribution. This results in an uncertainty on the purity of 0.7–5.8%, depending on the collision system and cluster  $p_T$  range. This is not a percent uncertainty, but the value actual value of the uncertainty because the units of purity are percents.

### 3.8.2.3 Background template correction

The underlying assumption for the background template correction is that the correlation between isolation and shower shape can be corrected using the weights from the dijet simulation as described in equation 3.9. In order to check the validity of the dijet simulation, we use a double ratio technique based on ABCD method [71]. The double ratio, as described in equation 3.11 is ratio of the isolation to anti-isolation ratio in data compared to the simulation. Since there are prompt photons in the single photon region of the shower shape distribution ( $0.0 < \sigma_{\text{long}}^2 < 0.3$ ), the double ratio should deviate from unity. However, in the merged photon region, where the background dominates, the double ratio should be flat. We fit the double ratio in the merged photon region using a linear function fit.

$$\text{Double ratio} = \frac{\text{Iso}_{\text{data}}/\text{Anti-iso}_{\text{data}}}{\text{Iso}_{\text{MC}}/\text{Anti-iso}_{\text{MC}}} \quad (3.11)$$

Fits to the double ratio are shown in Figures 3.17 and 3.18, for pp and p-Pb data respectively. In order to remove co-variance effects between the slope and intercept, the fits had to intercept the weighted average of the double ratio value within the fit range at the center of the fit range, making it a single-parameter linear fit with only the slope as a free parameter. This allowed us to propagate the fit uncertainty on the slope to an uncertainty on the purity.

These linear fits to the double ratio were done in two fit ranges: 0.5–1.5 and 0.5–1.75 for  $\sigma_{\text{long}}^2$ . In all cases, we found that the slopes were consistent with 0 within the fit uncertainties and thus concluded that the dijet MC was consistent with the data. Additionally, the double ratio fits with the different fit ranges gave purities consistent with each other. In

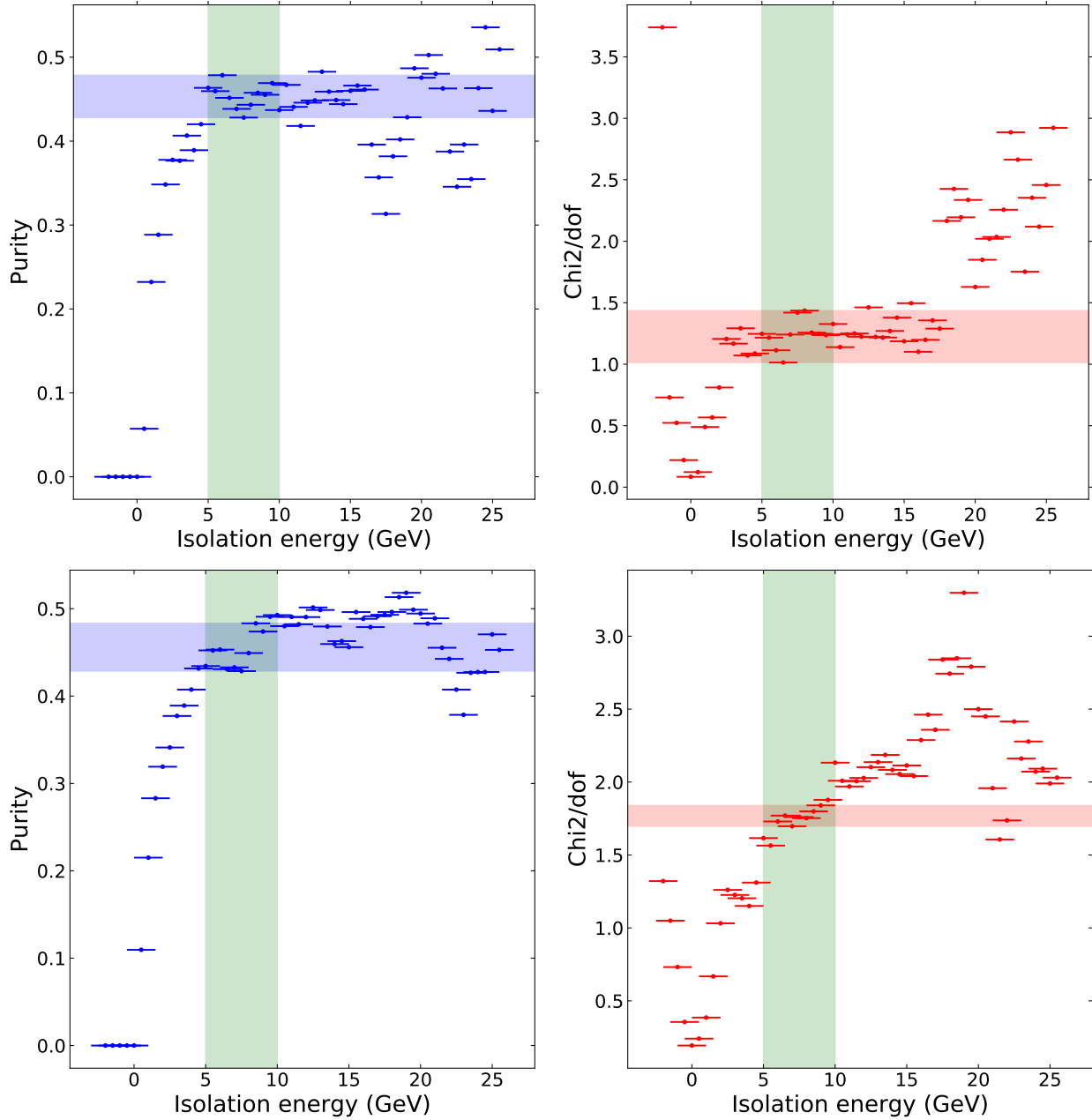


Figure 3.16: Template fit results (purity and  $\chi^2/\text{dof}$ ) as a function of anti-isolation region for clusters with  $15 < p_T < 20$  GeV/c in pp (top) and p-Pb (bottom). The green band shows the selected sideband region. The blue and red bands show the full extent of the purity within the selected sideband region.

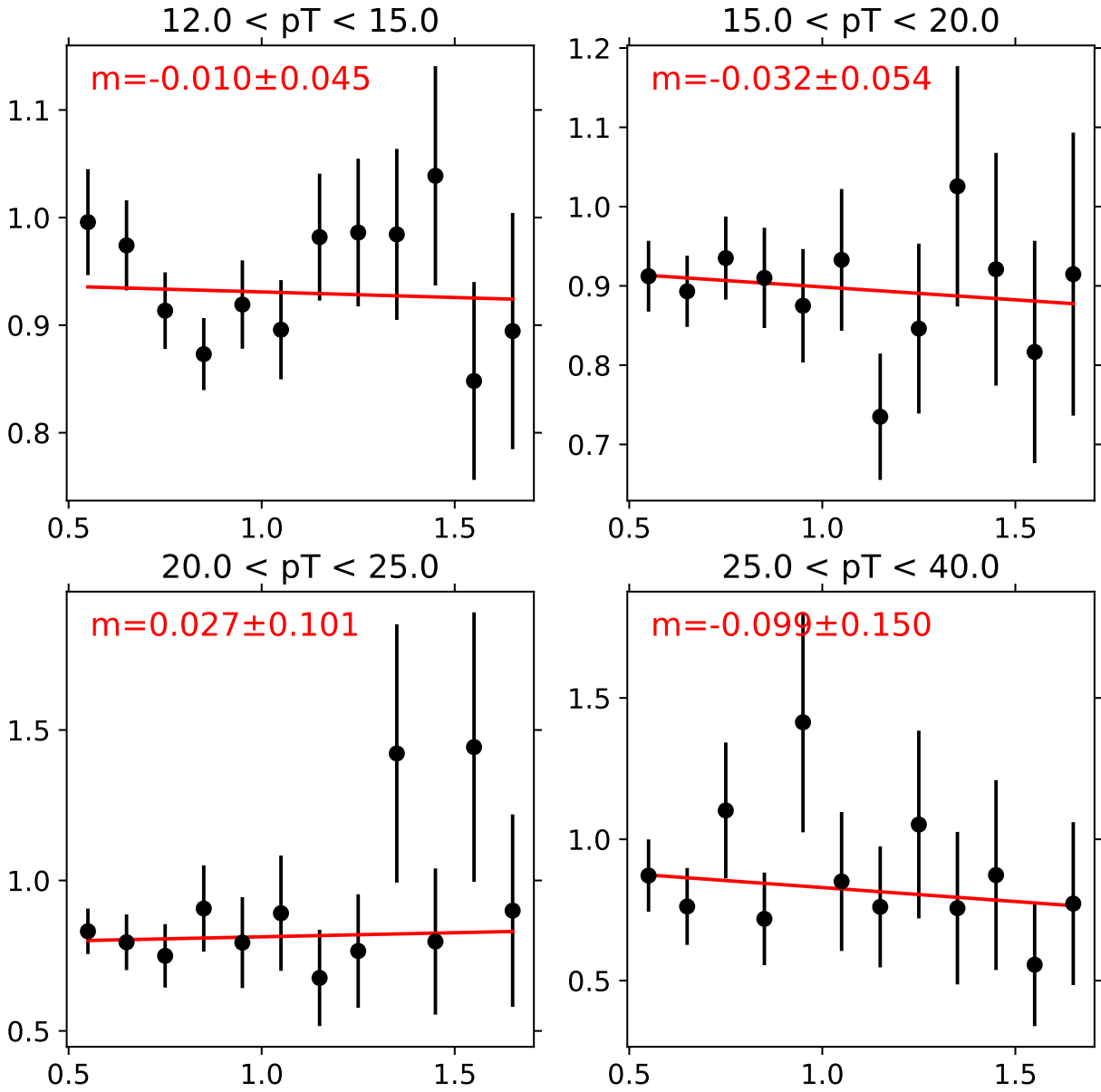


Figure 3.17: Linear fits for the double ratio (as described in Equation 3.11) for the  $\sigma_{\text{long}}^2$  variable in pp data. Included are the value and uncertainty of the fitted slope (in red).

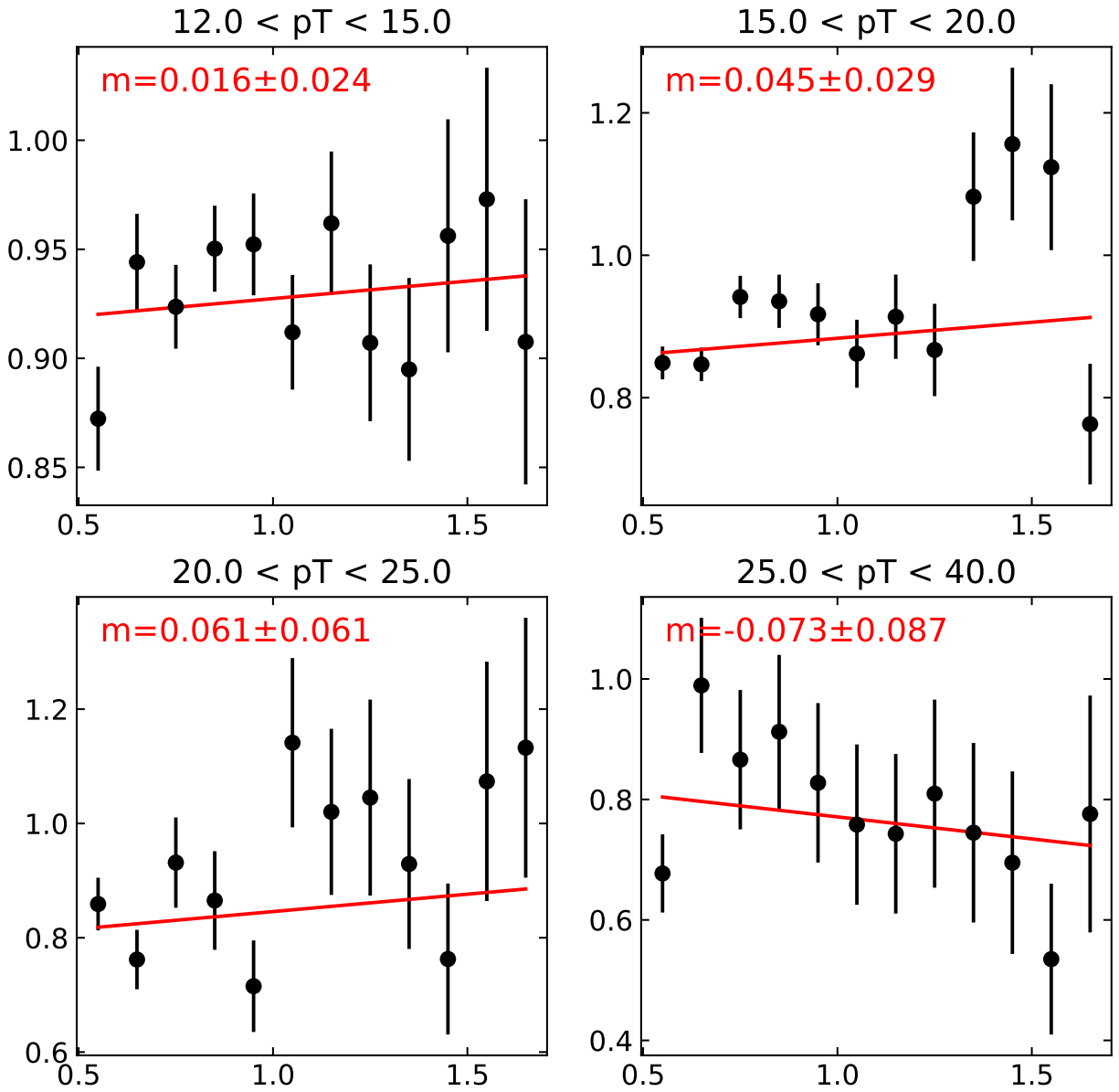


Figure 3.18: Linear fits for the double ratio (as described in Equation 3.11) for the  $\sigma_{\text{long}}^2$  variable in p-Pb data. Included are the value and uncertainty of the fitted slope (in red).

order to minimize the amount of extrapolation, we fit the largest reasonable ranges for each of the variables ( $0.5 < \sigma_{\text{long}}^2 < 1.75$ ).

The uncertainty on that double ratio fit was propagated to the purity uncertainty by changing the weights (3.9) applied to the background template relative to the error in the slope of the double ratio fit. The purity uncertainty due to the systematic uncertainty on the background correction was taken as the half the difference between the purity resulting from propagating the error on the double ratio fit by  $+\sigma$  and  $-\sigma$ . The resulting systematic uncertainty values are 1.2–3.4% (absolute) depending on cluster  $p_T$  and collision system.

### 3.8.3 Summary of systematic uncertainties of purity measurement

Tables 3.7 and 3.8 give the full estimates of the systematic uncertainties in both collision systems. Different source of systematic uncertainty dominates across  $p_T$  ranges or collision systems.

Table 3.7: Summary of the systematic uncertainties on the purity as measured with  $\sigma_{\text{long}}^2$  in p–Pb collisions. All values are in absolute percentage. “Stat.” refers to the statistical uncertainty; “Signal” refers to the signal template uncertainty; “Anti-iso” refers to the uncertainty due to the sideband selection; “Bkg” refers to the uncertainty due to the background template correction; “Total” is the sum of the previous three columns in quadrature.

$p_T(\text{GeV}/c)$	Purity (%)	Stat. (%)	Signal (%)	Anti-iso (%)	Bkg (%)	Total syst (%)
12.0-15.0	20.7	1.1	1.1	0.8	1.5	2.0
15.0-20.0	34.2	1.2	2.0	1.6	1.2	2.8
20.0-25.0	47.6	1.7	1.9	1.1	1.7	2.7
25.0-40.0	54.6	1.8	2.3	2.4	2.1	3.9

Table 3.8: Summary of the systematic uncertainties on the purity as measured with  $\sigma_{\text{long}}^2$  in pp collisions. All values are in absolute percentage. “Stat.” refers to the statistical uncertainty; “Signal” refers to the signal template uncertainty; “Anti-iso” refers to the uncertainty due to the sideband selection; “Bkg” refers to the uncertainty due to the background template correction; “Total” is the sum of the previous three columns in quadrature.

$p_T(\text{GeV}/c)$	Purity (%)	Stat. (%)	Signal (%)	Anti-iso (%)	Bkg (%)	Total syst (%)
12.0-15.0	20.6	1.7	2.0	1.2	2.5	3.4
15.0-20.0	32.3	2.0	2.5	1.5	2.1	3.6
20.0-25.0	45.6	3.0	0.8	3.0	2.6	4.0
25.0-40.0	49.3	3.3	5.9	4.0	3.2	7.8

### 3.9 Efficiency

The isolated photon efficiency. for isolated photons which pass all the selection criteria defined in the 3.5, is defined as the ratio of the number of reconstructed primary particles  $N_{\text{prim,rec}}$ , to the number of generated primary particles,  $N_{\text{prim,gen}}$ . The truth-to-reconstructed matching is done following the standard ALICE method where generated particles are assigned a label during generation and if the generated particles were successfully reconstructed in the detector, they label is match to them accordingly. Additionally, both the particle and its parent are required to be isolated photons, in order to avoid decay photons in the efficiency calculation.

The isolated reconstructed photons are selected in the same way as the photons in data (section 3.7. For generated photons, the isolation variable is the same as reconstructed photons, but the underlying event density is calculated using the perpendicular cones method. Cones are created in  $\eta, \varphi$ -space perpendicular to the photon  $(\eta, \varphi)$  coordinates. The underlying event estimation  $\sum_{UE} p_T$  to the isolation cone area  $A_{\text{cone}}$  as follows:

$$\left( \sum_{UE} p_T \right) = \frac{1}{A_{UE}} \sum_{UE} p_T \times A_{\text{cone}} \quad (3.12)$$

where, underlying event density ( $\rho_{\text{gen}}$ ) is given by  $\frac{1}{A_{UE}} \sum_{UE} p_T$ . This underlying event density is used for  $\rho$  in equation 3.8.

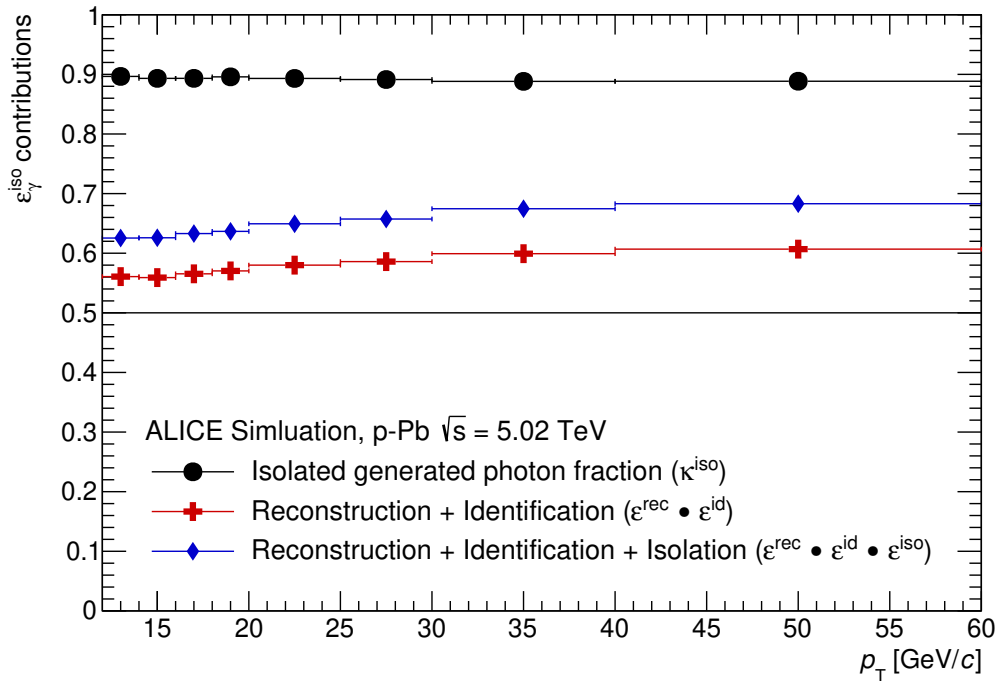
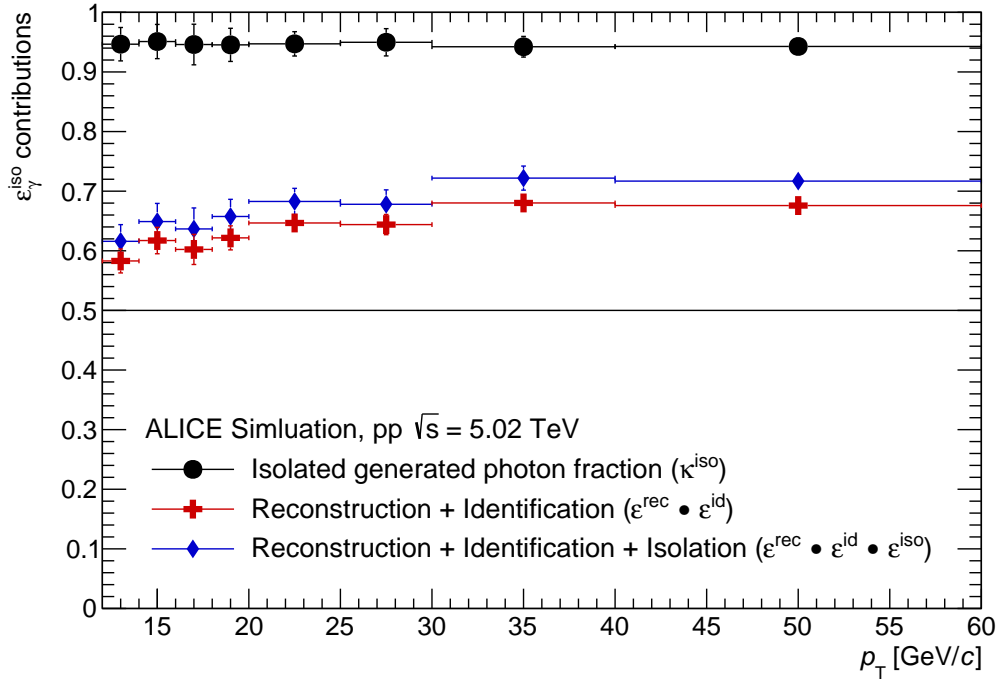
The total isolated photon efficiency is defined as:

$$\epsilon^{\gamma_{\text{iso}}} = \frac{dN_{\gamma_{\text{iso}}}^{\text{rec}}}{dp_T^{\text{rec}}} \bigg/ \frac{dN_{\gamma_{\text{iso}}}^{\text{gen}}}{dp_T^{\text{gen}}} \quad (3.13)$$

The numerator and denominator of Equation 3.13 are restricted for photons within the EMCal acceptance. Therefore, the correction factor accounts for both detector inefficiencies, and dead channels. Specifically, in order to determine whether a photon is a generated photon and not a reconstructed fake, we require that the at both detector and generator level, the particle has to be a photon and it's parent has to be a photon. Additionally, the particle need have a positive "mc\_truth\_status", meaning that it was generated particle, and not an accidental reconstruction. The efficiency and bin migration effects are calculated using these simulations: 17g6a1 for p-Pb and 18b10a for pp, which are both the  $\gamma$ -jet simulations.

The efficiency can be also be written as a product of the shower shape efficiency, the reconstruction efficiency, and the isolation efficiency. The shower shape and isolation efficiencies measure the percent of true isolated photons which we lose to the shower shape and isolation cuts, while the reconstruction efficiency is a measure of our detector's ability to identify true isolated photons and includes all the remaining cuts.

Figure 3.21 shows the over efficiency which is the product of the reconstruction, isolation and shower shape efficiencies for both pp and p-Pb. At this point, the efficiency is only a function of  $p_T^{\text{gen}}$ , but we need it to be a function of  $p_T^{\text{rec}}$  in order to connect the efficiency



ALI-SIMUL-508660

Figure 3.19: The isolated photon efficiency, along with the isolation, reconstruction and shower shape efficiencies for pp (top) and p-Pb(bottom).



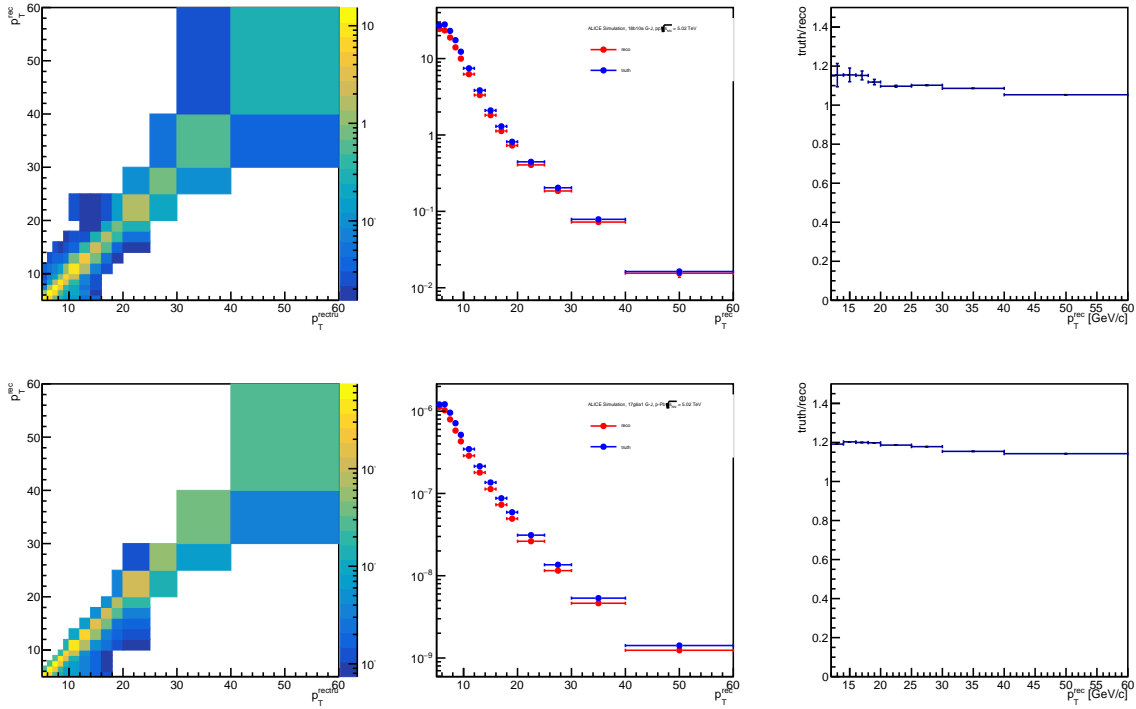


Figure 3.20: The photon  $p_T$  response matrix and the isolated photon bin migration pp (top) and p-Pb(bottom).

with  $p_T$  seen by the detector. Thus, this is corrected by calculating bin migration effects. The bin migration is calculated by making a response matrix with  $p_T^{gen}$  and  $p_T^{rec}$ , projecting the two  $p_T$  types on the respective axis, and taking a ratio as seen in figure 3.20.

Finally, we take the product of the bin migration with the efficiency in order to obtain the final correction factors for the cluster spectra. The values in figure 3.21 will be applied bin by bin in order to correct the raw data spectra.

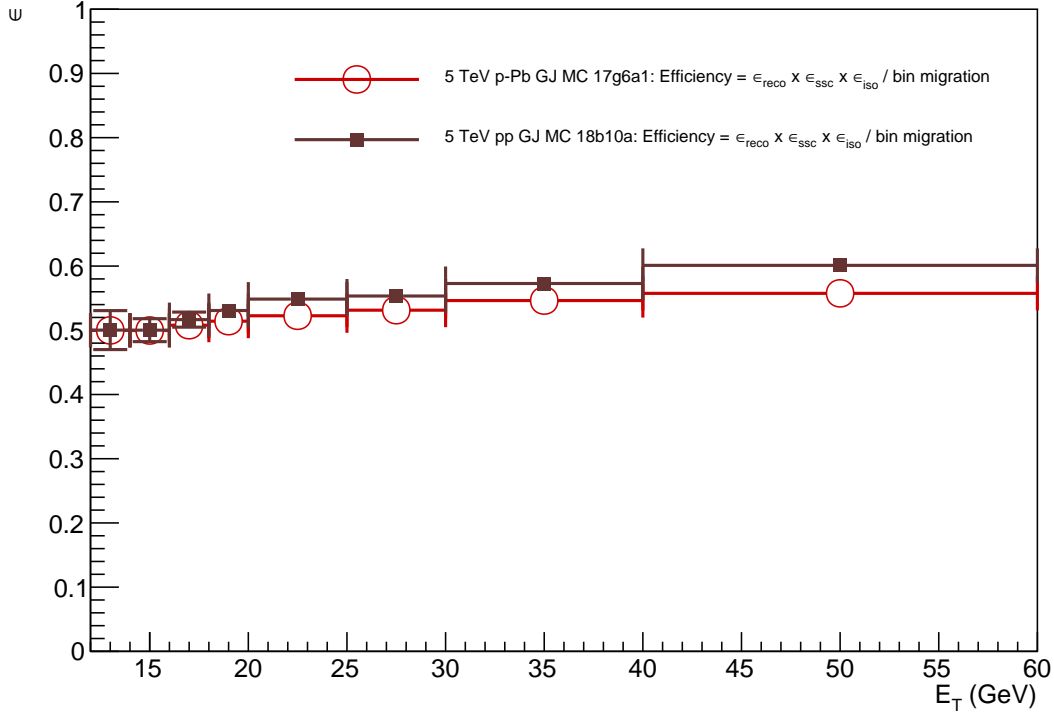


Figure 3.21: A comparison of the isolated photon efficiency between pp and p-Pb

### 3.10 Luminosity

As mentioned in section 3.1 the luminosity is calculated using the trigger rejection factors method [71]. The trigger rejection factor is defined as follows:

$$R_{trig}^{EGi} = \frac{1}{N_{ev}^{EGi}} \frac{dN_{clus}^{EGi}}{dp_T} \bigg/ \frac{1}{N_{ev}^{MB}} \frac{dN_{clus}^{MB}}{dp_T} \quad (3.14)$$

where EG*i* can be either EG1, EG2, or EG2calo (sec 2.2.5 and 2.2.1). The trigger rejection factor counts the fraction of minimum bias events which also satisfy the EMCAL trigger. Using the trigger rejection, and the number of events selected using that trigger and minimum bias cross section we can calculate the luminosity as given in equation 3.15

$$L_{int} = \frac{N_{ev}^{EGi} \times R_{trig}^{EGi}}{\sigma_{MB}} \quad (3.15)$$

Figure 3.22 shows the cluster spectra used in the numerator and denominator of equation 3.14. The peaks at 7 and 11 GeV in p-Pb and the peak at 5 GeV in pp are due to the

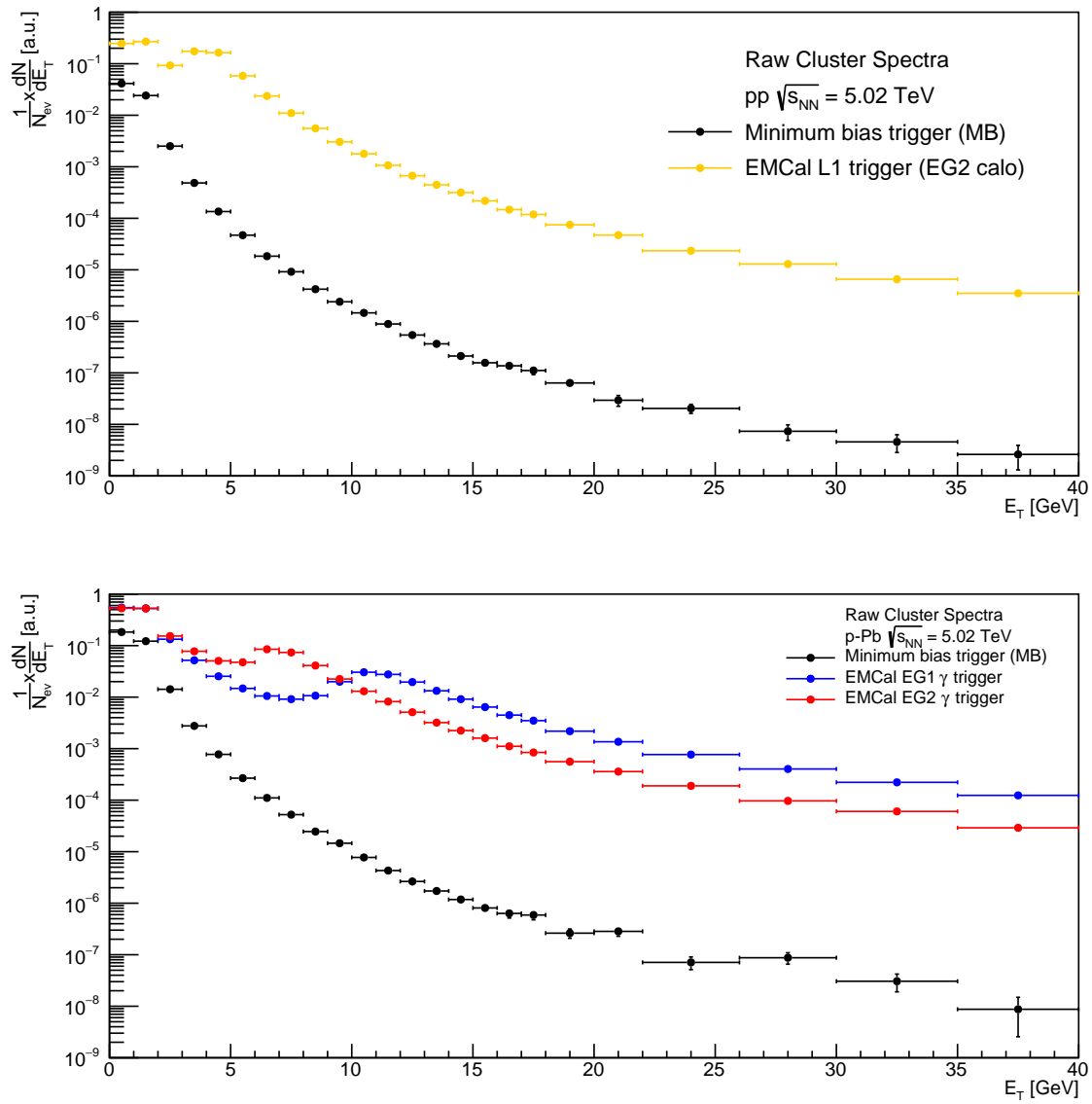


Figure 3.22: The EMCal triggered and minimum bias cluster spectra for pp (top) and p-Pb(bottom).

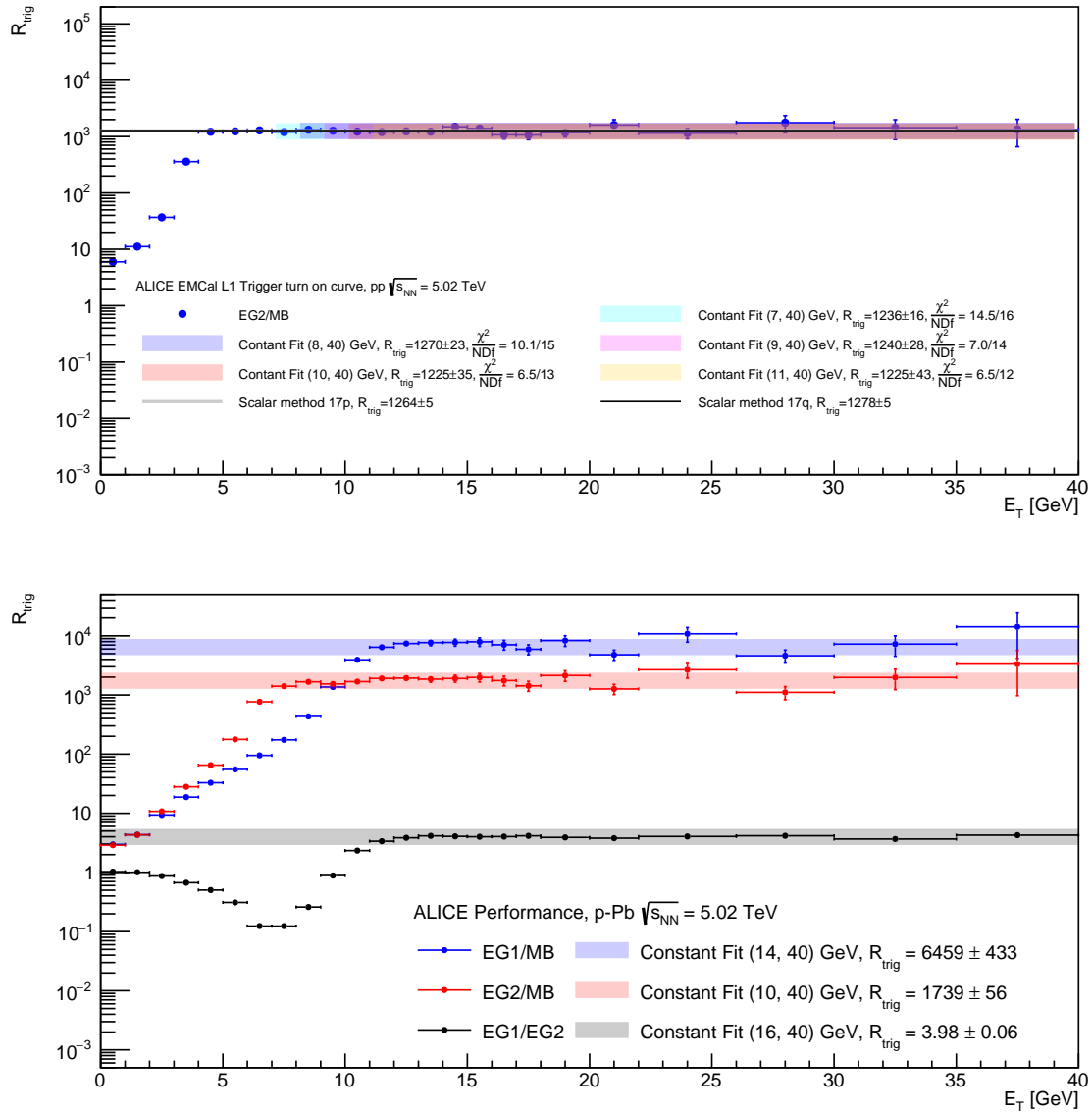


Figure 3.23: The turn on curves and trigger rejection factor fits for pp (top) and p-Pb(bottom). A zero degree polynomial fit is applied to calculate the trigger rejection factor. The fit ranges are provided on the figures next to respective turn on curve.

EMCal L1 trigger thresholds. The trigger thresholds for p–Pb are 7 and 11 GeV, while the trigger threshold for pp is 5 GeV.

In both pp and p–Pb, the statistical errors on the minimum bias triggered cluster spectra are significantly larger than the those on the EG triggered spectra. Additionally, we barely have sufficient statistics to reach 40 GeV using the minimum bias trigger. The trigger turn on curves are constructed from the ratio of EG triggered to minimum bias spectra, and shown in figure 3.23. Fits to the ratios well above the trigger thresholds are made in both pp and p–Pb to extract the trigger rejection factors; fit results are shown in the figure. In both systems, the fit uncertainties are dominated by the minimum bias spectra statistics. The trigger rejection factor from these fits, along with the number of events (from table 3.5), and the minimum bias cross section obtained from [66] for pp and [67] for p–Pb are used to calculate the luminosity.

Table 3.9: The integrated luminosity measured for each trigger.

Trigger	Rejection Factor	$N_{\text{ev}}$	$\sigma_{\text{MB}}(\text{b})$	Luminosity ( $\text{nb}^{-1}$ )
p–Pb EG1	$6917 \pm 245$	1,946,913	$2.11 \pm 0.055$	$6.3 \pm 0.3$
p–Pb EG2	$1739 \pm 56$	921633	$2.11 \pm 0.055$	$0.76 \pm 0.03$
pp EG2calo	$1278 \pm 28$	9,197,400	$5.09 \cdot 10^{-2} \pm 4.00 \cdot 10^{-5}$	$224 \pm 5$

The trigger rejection factor can also be calculated using the scalar method which counts the number of times a particular L1 trigger fired and compares the count to the number of times the minimum bias trigger fired for the same trigger cluster. In order to determine which method performed better, we scaled down the triggered cluster spectra using the trigger rejection factor and take a ratio with the minimum bias cluster spectra. Figure 3.24 shows both the scaled triggered cluster spectra and the ratio with the minimum bias cluster spectra. The ratio using the trigger rejection factor from the scalar method is closer to unity indicating that the trigger rejection factor from the scalar method gives us a better comparison with the minimum bias spectra. A summary of the trigger rejection factors and luminosity are listed in table 3.9.

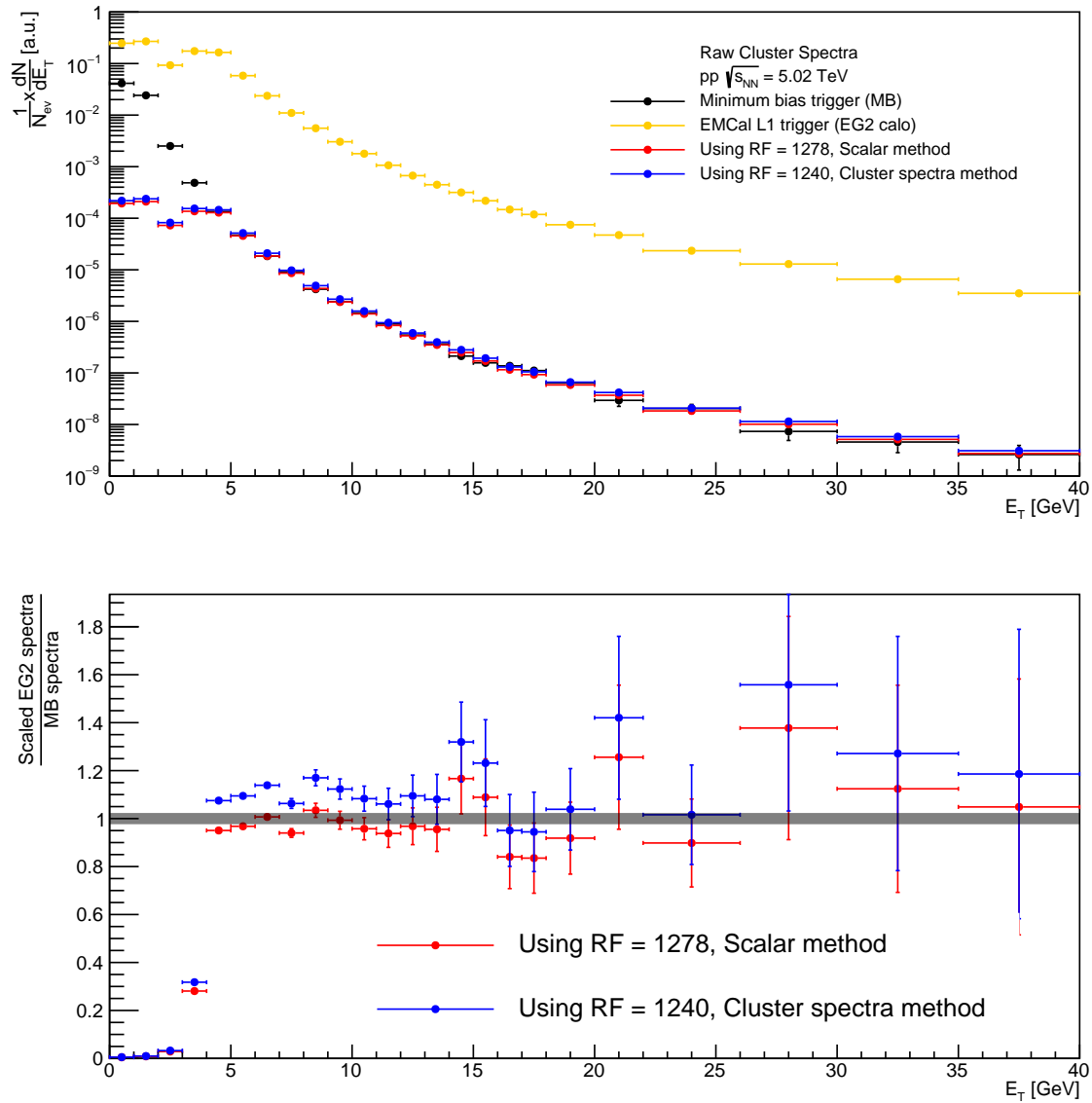


Figure 3.24: Top: The trigger spectra is scaled by the trigger rejection factor and compares to the minimum bias spectra. Bottom: ratio of the scaled triggered spectra and the minimum bias spectra

## 3.11 Data driven trigger acceptance correction

The basic unit of triggering in the ALICE EMCAL is known as FastORs which is comprised of 2 x 2 cells. A fraction of the FastORs had to be removed from the trigger electronics because the FastORs were either dead or contributed a large amount of electronic noise. Due to this, the trigger efficiency was lowered in some regions of the detector. Additionally, the effect was the dead and noisy FastORs were present in data, but had not been simulated in the Monte Carlo simulations used for this analysis. Due to the masked dead and noisy FastORs, there was an acceptance mismatch between data and reconstructed level output from the simulations. The cluster  $\eta$  and  $\varphi$  did not have similar trigger acceptances in data and simulation. Consequently, a correction was necessary for this trigger acceptance discrepancy. We developed a data driven correction for this purpose.

### 3.11.1 Correction procedure

As this is an acceptance issue, we compared cluster  $\eta$  and cluster  $\varphi$  distributions between data and simulation. We took a data/MC ratio which showed local maxima in regions which do not have FastOR holes in data. The local maxima are used to set a reference level to which other angles should be compared, A relative correction is then applied to data in the other regions to correct for the acceptance loss due to the FastOR holes. The process of obtaining the correction factors and applying them to cluster spectra was as follows:

1. Create histograms for cluster  $\eta$  distributions for data and MC
2. Take ratio of between the data and MC distributions (data/MC), and identify the local maxima
3. Use the local maxima to determine what the average value of the data/MC ratio between the maxima should be
4. Calculate the  $\eta$  correction factors for each bin by taking a ratio of the bin content with the average ( $\frac{\text{averagevaluefortheratio}}{\text{ratioineachbin}}$ )
5. Apply  $\eta$  correction as a weight when filling the cluster  $p_T$  spectra using the cluster  $\eta$  to select the appropriate correction value

For the  $\eta$  distributions, the clusters were required to pass all the cluster cuts mentioned in section 3.5.3. In cluster  $\eta$  distributions were normalized by the number of events. The event has to pass all the event cuts mentioned in section 3.4, and there was an added requirement that the event must have at least one cluster with  $p_T \geq 12$  GeV/ $c$ . The MC distributions are obtained by combining the output from all the different  $p_T^{\text{hard}}$ -bins. Higher  $p_T^{\text{hard}}$ -bins have more cluster with  $p_T \geq 12$  GeV/ $c$ , so the MC event count as well as the cluster  $\eta$  distributions were both weighted by using  $w_{p_T^{\text{hard}}}$ . The pp and p-Pb cluster  $\eta$  distributions for both data and MC are shown in figure 3.25.

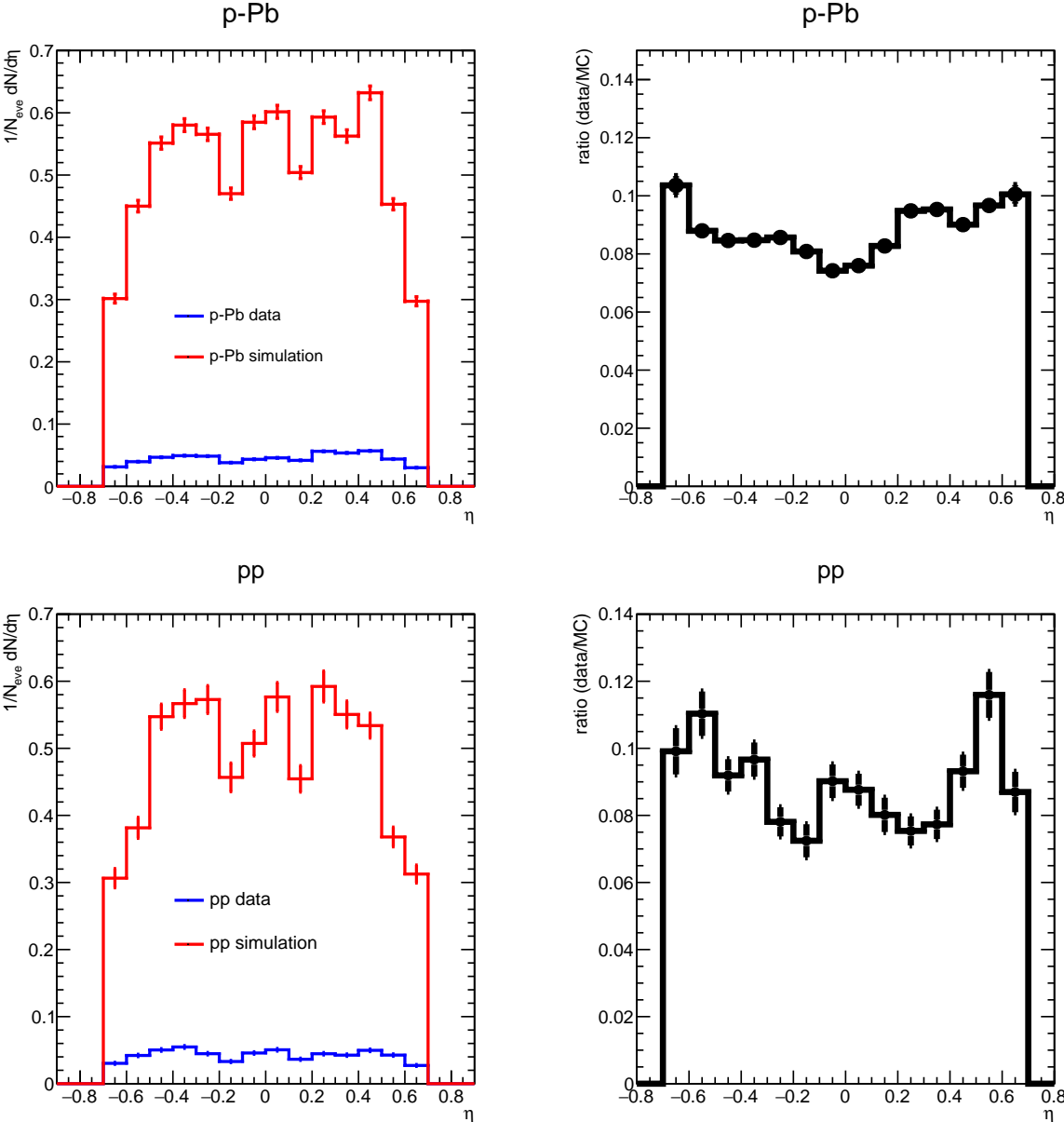


Figure 3.25: Cluster  $\eta$  distributions for data and MC along with the data/MC ratio for p-Pb(top) and pp(bottom).



Since the FastOR masking is period (as defined in sec 3.2) dependent, we studied the cluster  $\eta$  data/MC ratios for each period of the p–Pb dataset and for each run in the pp data set, since it consists of only period. We calculated data/MC ratios for each subsets and compared them with the data/MC for the full dataset. The ratios and comparisons are shown in figure 3.26. The shape of the ratio of individual p–Pb periods is comparable to each other and the collective p–Pb dataset. For pp, the shape of the ratio for most runs is in agreement with the full pp dataset; however, runs 282440 and 282365 seems to be outliers. Thus, runs 282440 and 282365 were removed from the analysis. The new set of pp runs, excluding runs 282440 and 282354, is labeled as "good pp". A qualitative calculation was also performed to determine how much the individual runs and periods deviated from the complete dataset by calculating the residuals for the run by run and period by period comparisons. The residuals are shown in figure 3.27. The residuals for pp show that runs 282440 and 282365 both deviate from the rest of the dataset as seen in regions with  $0.3 < \eta < 0.7$ .

In order to calculate the average, we selected the bins which are statistically significantly above the rest. However to avoid edge effects, the edge bins were not included. We corrected to the maximum because the purpose of this correction is to raise the data, which is affected by the FastOR holes, by using the simulations, which does not have holes in it. For p–Pb, the bins for the range  $0.2 < \eta < 0.6$  are used to calculate the average which is 0.094. For pp, the bins at  $0.5 < |\eta| < 0.6$  are used to an average of 0.113. The ratios and the averages for pp and p–Pb are shown in figure 3.28. Finally, to calculate the correction factors, each bin is compared to the average, and we took a correction factor determined to raise each bin's value to the average. The ratio, average/bin content, is used as the correction factor for the specific  $\eta$  bin. The correction factor are selected based on the cluster  $\eta$ , and applied as a weight to the cluster  $p_T$  when filling the cluster  $p_T$  histogram.

### 3.11.2 Systematic uncertainty for the trigger acceptance correction

The systematic uncertainty for the trigger acceptance correction is calculated by measuring the isolated photon cross sections with four other methods. The first two follow a similar approach to the  $\eta$  correction, where we use  $\varphi$  and 2D- $\eta\varphi$  correction instead. The second approach uses cluster and event masking where either the cluster or the event are thrown out of the sample in both data and MC using the FastOR masking map.

#### 3.11.2.1 Comparison with $\varphi$ and 2D- $\eta\varphi$

The trigger acceptance correction was initially applied as  $\eta$ -correction because the FastOR issue was originally discovered and considered to be an EMCAL supermodule by supermodule  $\eta$  problem. However, we were not limited to just using the  $\eta$  direction when applying the trigger acceptance correction. Since the FastOR holes affect the acceptance in both  $\eta$  and  $\varphi$ , we can use a  $\varphi$ -correction or a 2D- $\eta\varphi$ -correction as well. The procedure for the  $\varphi$  and 2D- $\eta\varphi$  is the same as used for the  $\eta$ -correction, described in 3.11.1, but instead of cluster  $\eta$ , we used

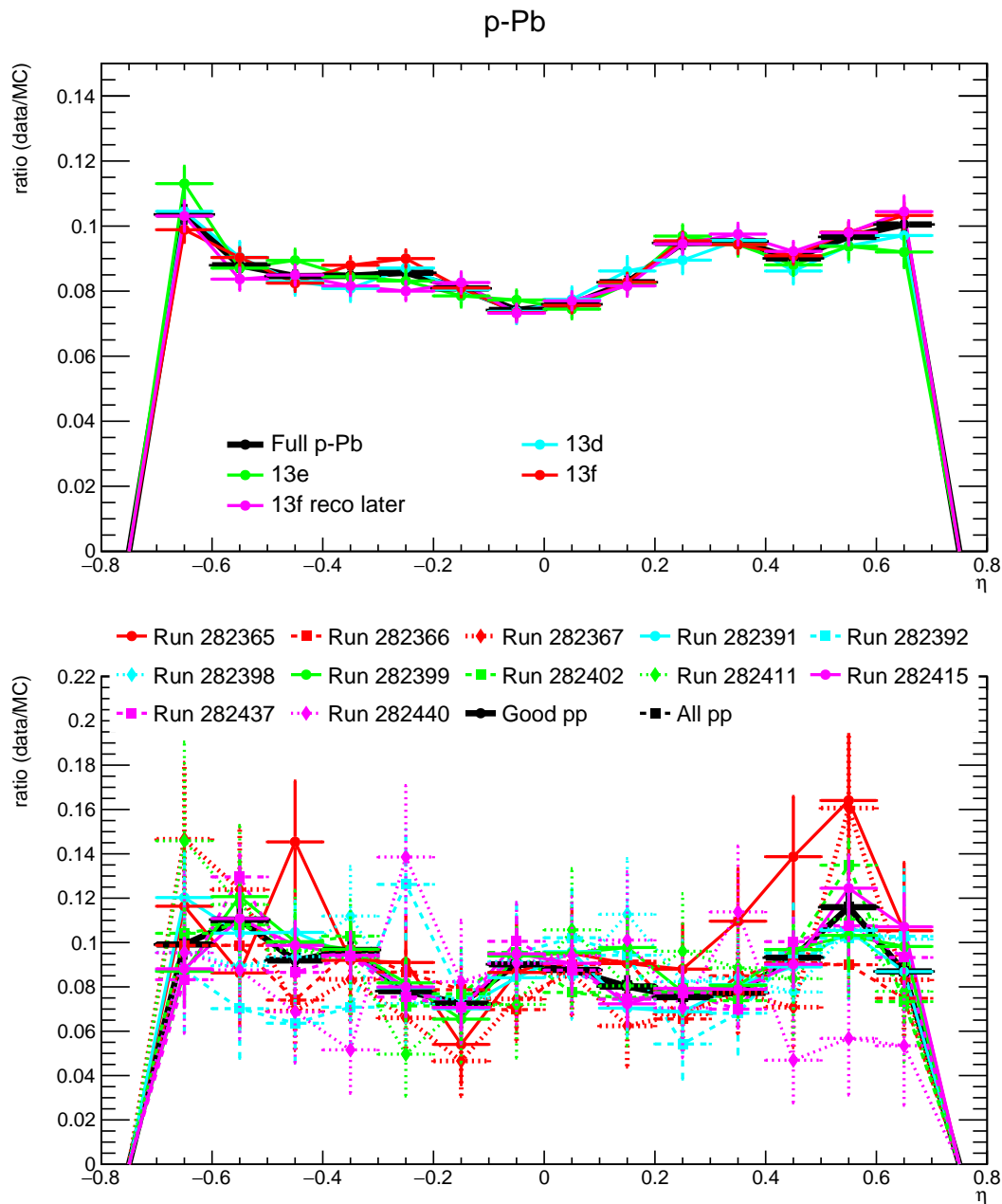


Figure 3.26: Cluster  $\eta$  data/MC ratios broken down by period for p-Pb(top) and by run for pp(bottom). The "Good pp" list does not include runs 282440 and 282365.

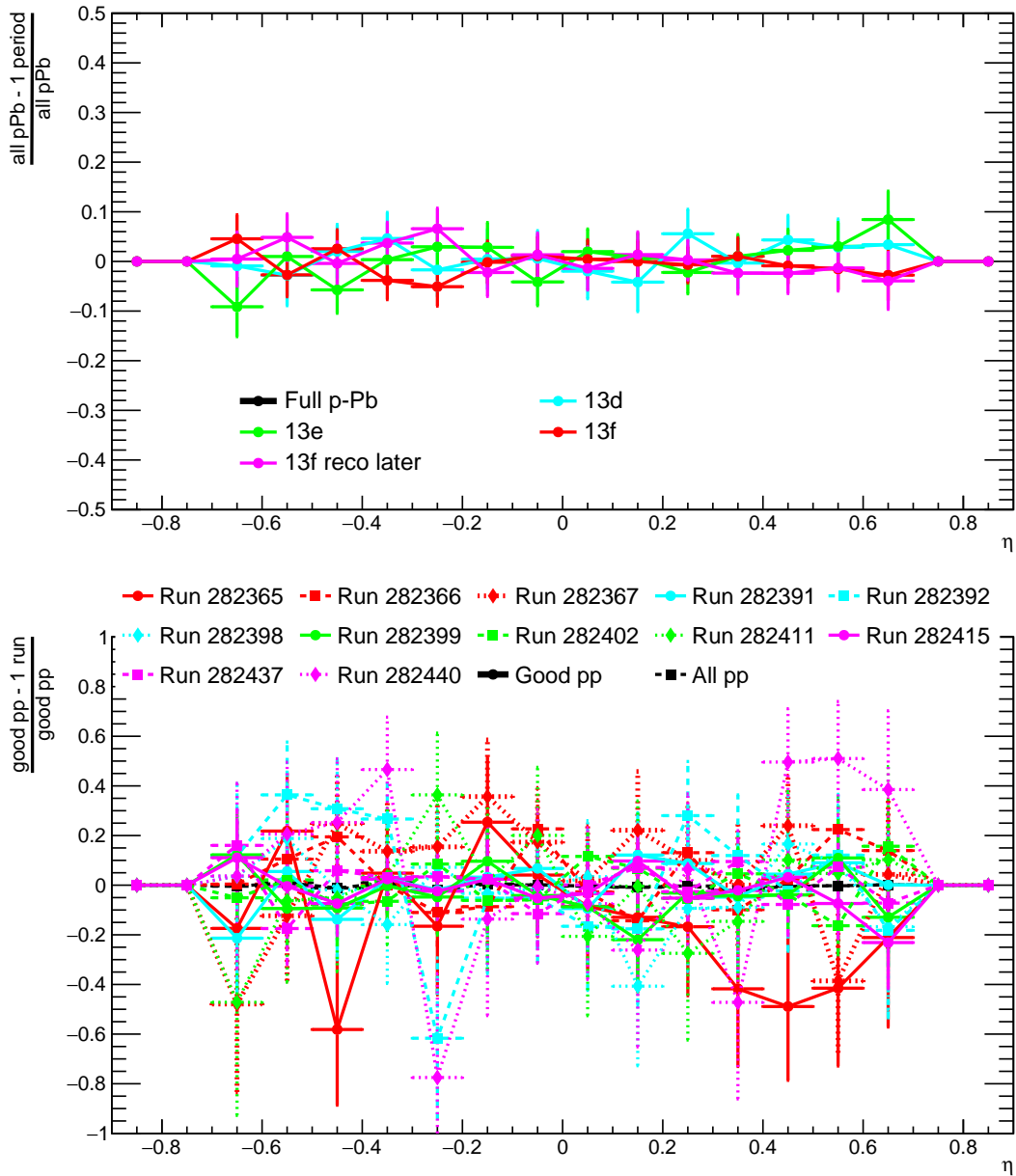


Figure 3.27: Residuals of the cluster  $\eta$  data/MC ratios broken down by period for p-Pb(top) and by run for pp(bottom) compared to the full dataset. The "Good pp" list does not include runs 282440 and 282365.

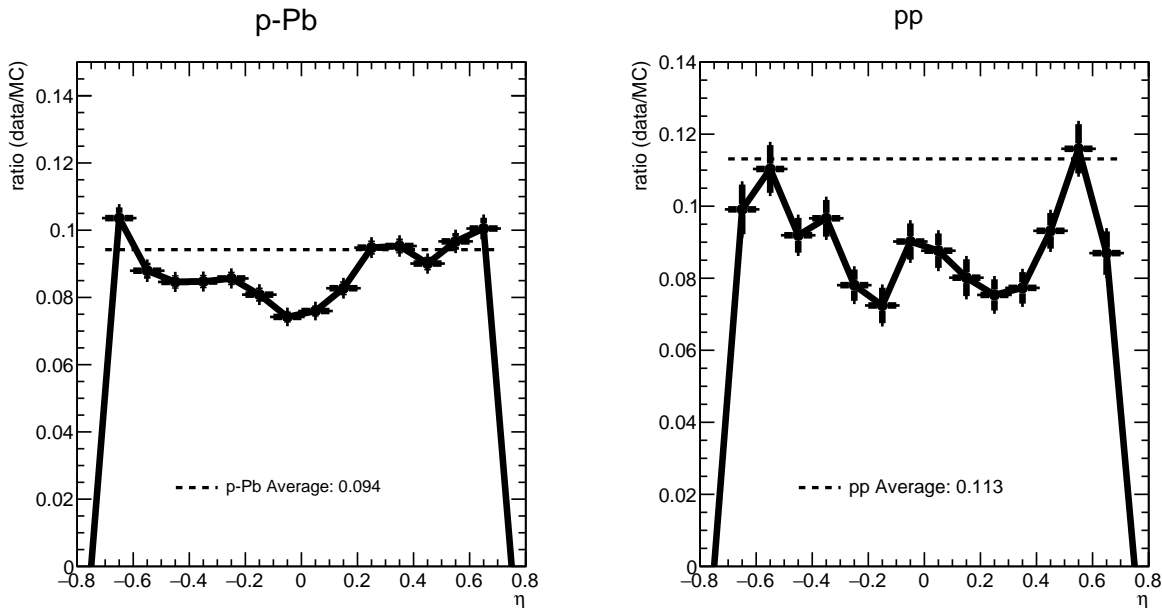


Figure 3.28: The data/MC ratio along with the average of the local maxima (dotted line) for pp and p-Pb.

the cluster  $\varphi$  or a 2D cluster  $\eta$  and cluster  $\varphi$  distributions. The ratios and averages for the  $\varphi$ -correction and the 2D- $\eta\varphi$  are in shown in figures 3.29 and 3.30, respectively. The binning is different between the p-Pb and pp because the orientation of the trigger region units is different between the p-Pb and pp data taking periods as explained previously in trigger part of section 2.2.5. We can see that local maxima in the 1D cluster  $\eta$  and  $\varphi$  ratio plots agrees with the maxima in the 2D- $\eta\varphi$  plot. For both the  $\varphi$ -correction and 2D- $\eta\varphi$ -correction, the maxima are chosen such that the counts in those bins are statically greater than the other bins. All the bins are then compared to the average to obtain the bin by bin correction factors. The isolated photon cross section is then calculated using either the  $\varphi$ -correction or the 2D- $\eta\varphi$ -correction. In order to compare with the effect of the  $\varphi$  and 2D- $\eta\varphi$ -correction with the  $\eta$ -correction, a ratio is taken of the cross sections with the different corrections. The ratio of  $\varphi$  and 2D- $\eta\varphi$ -correction to the  $\eta$ -correction is fitted with a constant fit. The constant fit values were 1.04 and 1.13 for  $\varphi$  and 2D- $\eta\varphi$ -corrections respectively, and the two corrections were consistent with the  $\eta$ -correction within statistical uncertainties.

### 3.11.2.2 FastOR masking

Further checks were performed using the masked FastOR map show in figure 3.31. Version 5 was used for the comparisons shown in this section. There were two approached used when applying the fastOR masking to the cross section calculation. In the first approach, all

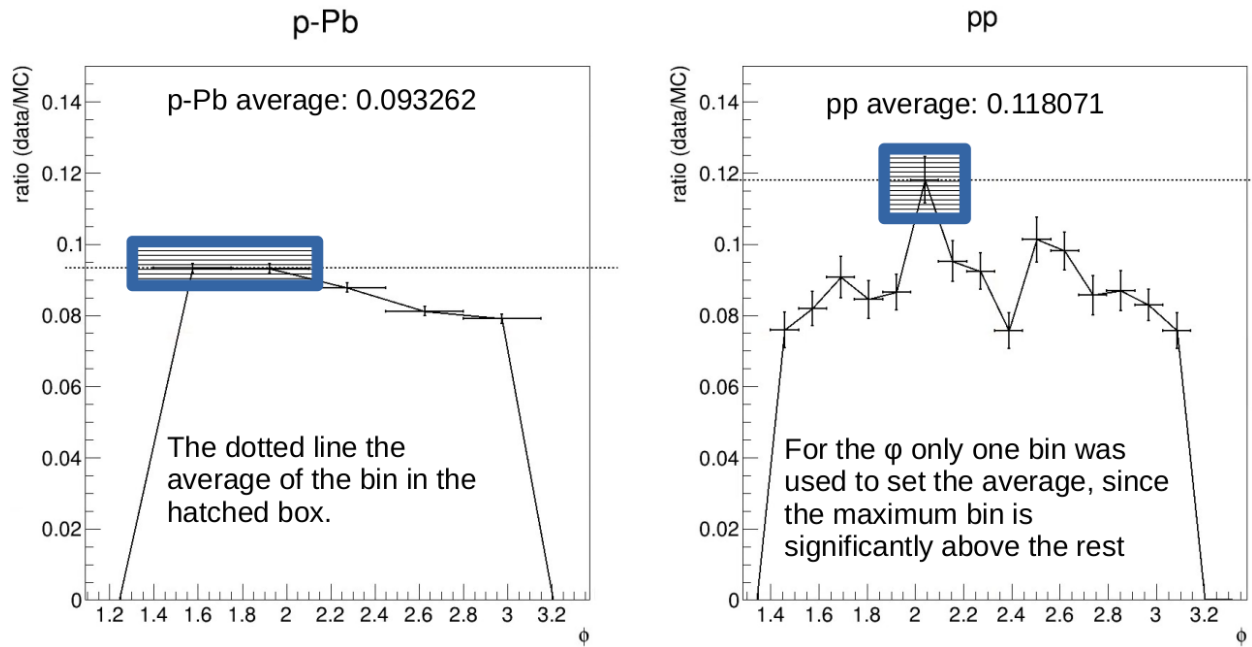


Figure 3.29: The data/MC ratio along with the average of the local maxima (dotted line) for pp and p-Pb.

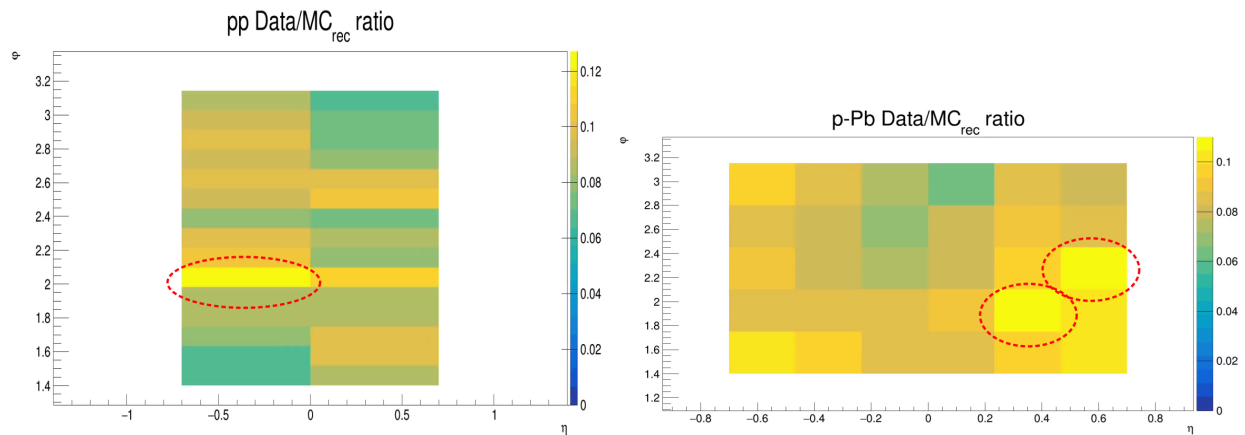


Figure 3.30: The data/MC ratio for the 2D- $\eta\phi$  distribution along with bins used to calculate the average(dotted oval) for pp and p-Pb.

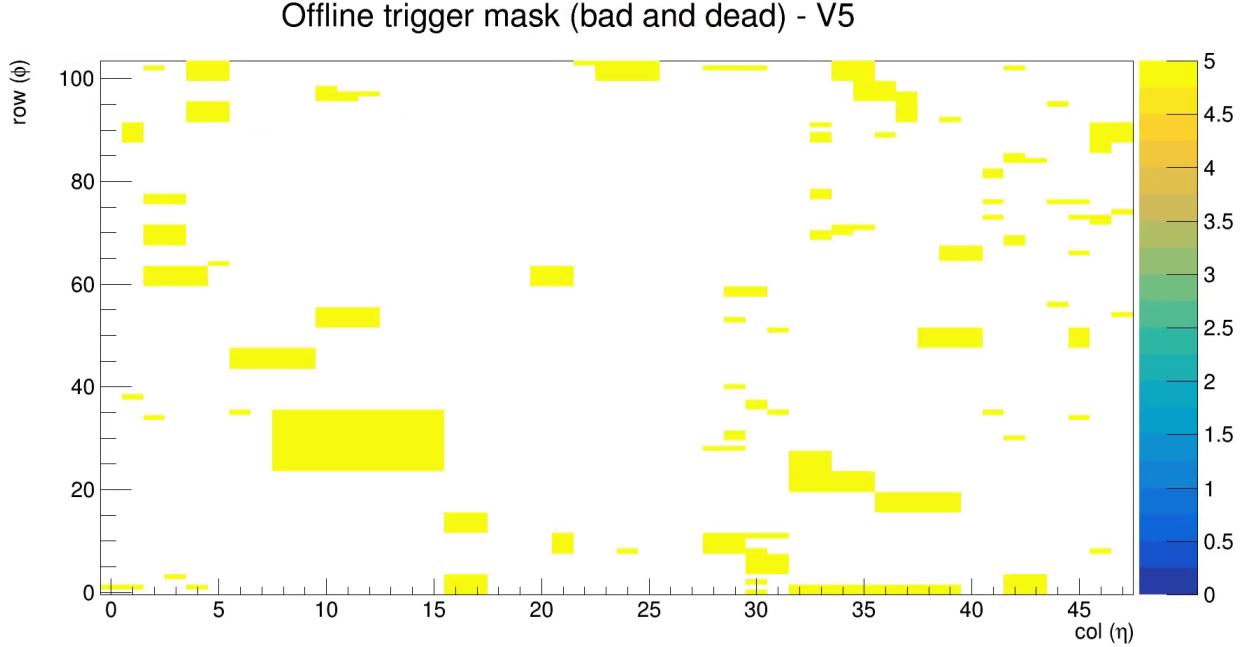


Figure 3.31: The map of the masked FastORs for the 17q 5.02 TeV pp period.

clusters were thrown out if a cluster was within the acceptance of the masked fastOR region. In the second approach, all events which has a photon in the acceptance of the masked fastOR region are rejected. These rejections are applied in both data for the photon yield and trigger rejection factor calculation, and in MC at reconstructed level for the efficiency calculation. When using the fastOR masking, we do not apply the  $\eta$ -correction to the data.

The resulting cross section are compare with the  $\eta$ -corrected cross section as in figure 3.32. The ratio is taken with respect to the  $\eta$  correction and fitted with a constant fit. As seen in the ratio plot in the bottom of figure 3.32, the ratios seem to flat and the points are consistent between different  $p_T$  bins agree with each other within statistical uncertainty.

### 3.11.2.3 Uniform distribution systematic uncertainty

Due to the lack of  $p_T$  dependence in the ratio, the distributions are assumed to be uniform. The upper bound is assigned to the 2D- $\eta\phi$ -correction (cyan) which has constant fit of 1.13 on the ratio, while the lower bound is assigned to the FastOR event mask (green) which has constant fit of 0.85 to the ratio. The systematic uncertainty is taken as the difference of the upper and lower bound fits divided by square root of 12, as this is the full extent of the possible variations. The resulting systematic uncertainty due to the  $\eta$ -correction in pp is 0.08. Since the mean of the four constant fits was 0.97, the relative systematic uncertainty for pp is 0.083.

To calculate the systematic uncertainty in p-Pb, we measured the isolated photon cross

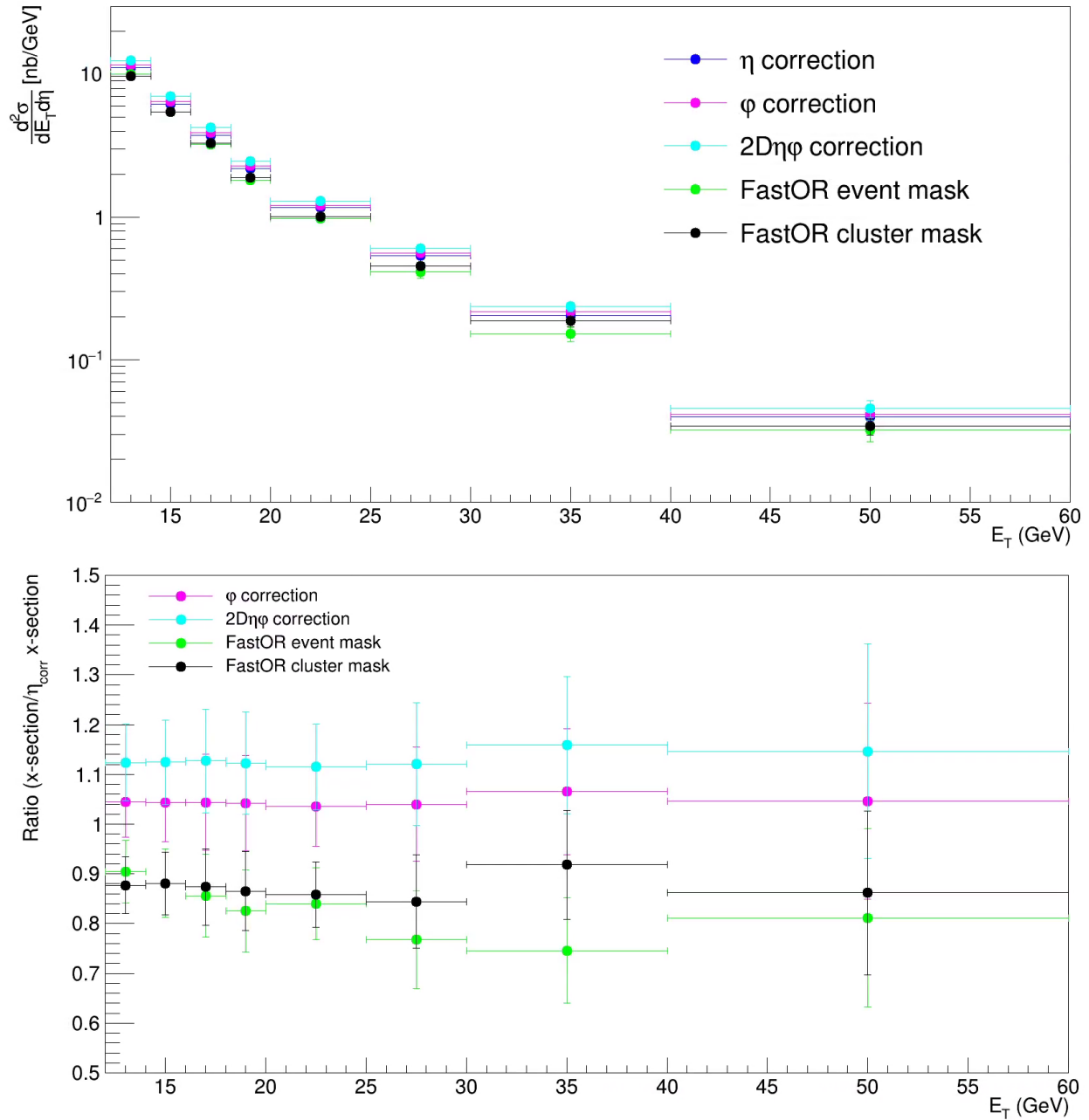


Figure 3.32: Comparison of the isolation photon cross section calculated five different ways:  $\eta$ ,  $\varphi$ , and  $2D\eta\varphi$ -corrections and fastOR masking cluster and event rejection (top). The ratio of the different ways compared with the  $\eta$ -correction method (bottom). Error bars only reflect the statistical uncertainty.

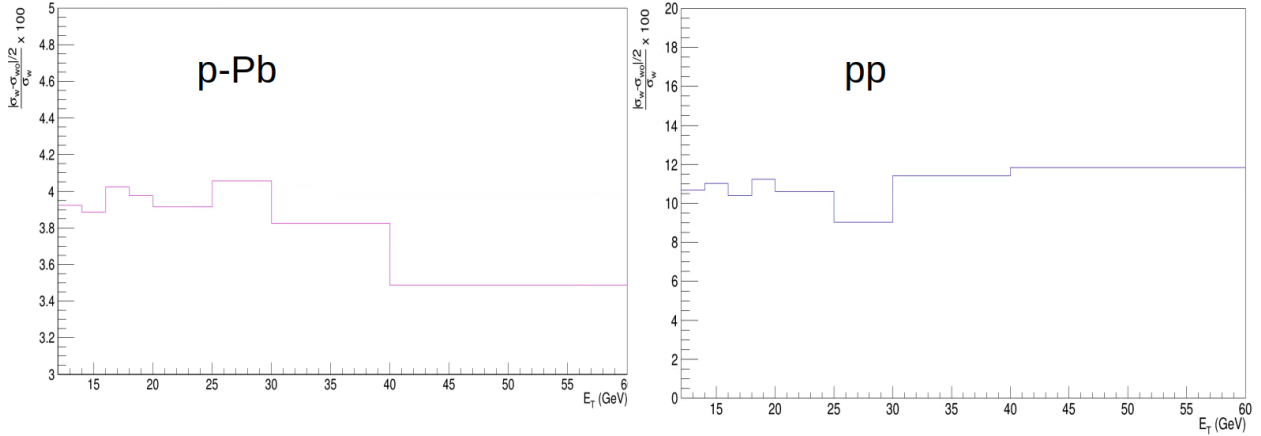


Figure 3.33: Relative change in the cross section as a result of turning the  $\eta$ -correction on and off in p-Pb(left) and pp(right).

section with and without  $\eta$ -correction enabled for both pp and p-Pb. Half the difference between the with and without  $\eta$ -corrected cross section was taken as a measure of the magnitude of the systematic uncertainty of the  $\eta$ -correction on the pp and p-Pb cross sections. The relative uncertainty on the cross sections with and without the  $\eta$  correction is shown in figure 3.33. The  $\eta$ -correction has larger effect on the pp compared to p-Pb, which is consistent with 3.28 where we saw that due to the depth of the holes in pp the correction will be larger in pp compare to p-Pb. Performing a constant to the ratio the pp and p-Pb distributions in figure 3.33 lets us know the magnitude of difference between pp and p-Pb due to the  $\eta$ -correction. The value of the fit, 3 in this case, is used to propagate the uniform distribution relative systematic uncertainty calculated for pp previously. Thus, the 8.3% relative uncertainty for pp would result in a 2.7% relative uncertainty for p-Pb. To summarize, the relative systematic uncertainty due to the data and Monte Carlo driven trigger acceptance correction on pp and p-Pb is 8.3% and 2.7% respectively.

## 3.12 Systematic uncertainties

The sources of systematic uncertainties of our  $\gamma^{\text{iso}}$  cross section measurement are the following:

- Purity

The uncertainty of the purity measurement is described in section 3.8.2. The resulting uncertainty is  $\pm 18\%$  for pp data and  $\pm 12\%$  for p-Pb data, relative. As described in Section 3.8.2, a large fraction of the purity total uncertainty is either statistical uncertainty or systematic uncertainties that arise due to limited data sample. Therefore, the purity uncertainty in pp and p-Pb data are largely uncorrelated. As a conservative



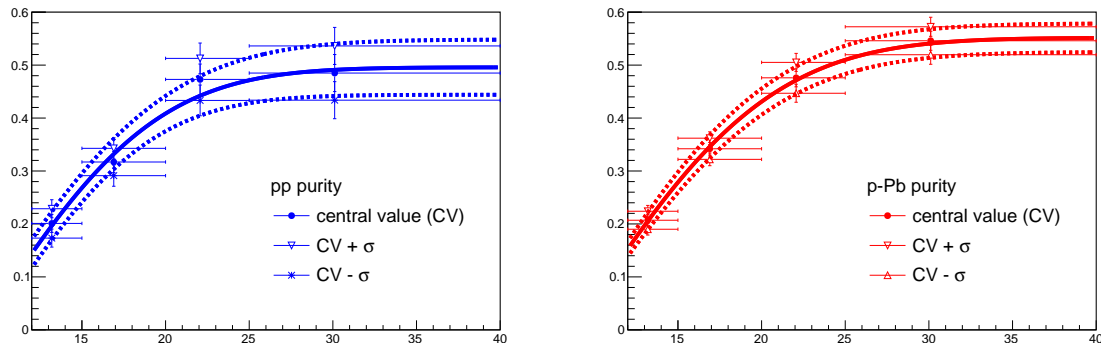


Figure 3.34: The purity fit functions for the purity central values as well as fits to adjusting the central values up or down one standard deviation systematic. The pp fits are shown on the top, while the p-Pb fits are shown on the bottom.

approach, we take them to be totally uncorrelated. The systematic uncertainty in the purity is propagated to the cross section by varying the central values by  $\pm\sigma$  as seen in figure 3.34. The new shifted purity values are used to fit an error function, and the error function fit for  $\pm\sigma$  purity is used to recompute the cross section. Finally, half the difference between the  $\pm\sigma$  cross section is taken as the systematic uncertainty.

The three sources of systematic uncertainty on the purity were initially considered to be independent, but they are in fact correlated. Both the signal template and the background template use the anti-isolation cut in order to calculate the systematic uncertainty, as described in section 3.8.2. In order to extract the correlation between the anti-isolation and the signal and background template fits, we looked at changes in the cross section if the purity was changed by one standard deviation for each component individually, instead of by the total. Then, the same procedure of fitting and calculating the cross sections described in the previous paragraph was used to see how the uncertainty from each component propagates to the cross section. The effect of each component of the purity systematic is seen in figure 3.35.

For pp, at  $E_T < 20\text{GeV}$ , there is a correlation between the background template and the anti-isolation selection while the signal template is anti-correlated with the anti-isolation selection. For  $E_T > 20\text{GeV}$ , the background template uncertainty is independent of  $E_T$  since a fit in that range has a slope consistent with zero within errors, while the signal template appears to be correlated with anti-isolation cut. For p-Pb, all three components seem to be correlated at  $E_T < 20\text{GeV}$ , but a correlation is hard to identify at  $E_T > 20\text{GeV}$ . Since both the signal template uncertainty and the background template uncertainty depend on the anti-isolation selection, the effect of changing the anti-isolation cut on the signal and background template uncertainties was studied, and is shown in figure 3.36. In figure 3.36a, the points in the range 20-25

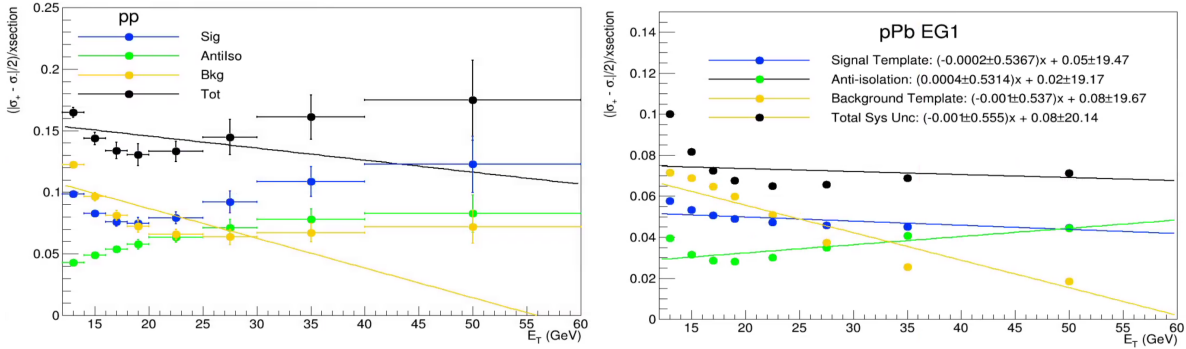


Figure 3.35: The systematic uncertainty due to each individual component of the purity systematic uncertainty propagated to the cross section for both pp(left) and p-Pb(right). The y-axis is the relative systematic uncertainty using half the difference in the cross section of changing the purity by  $\pm 1\sigma$ .

GeV and 25-40 GeV have a slopes close to zero within  $1.5\sigma$ . If the relative background template uncertainty were independent and uncorrelated with the anti-isolation selection, then all the fits would have a slope close to zero. Thus, the slopes close to zero can be used a reference to estimate the effect of the correlated error on the template uncertainty for photon  $p_T$  bins where the slope of the fit deviates from zero. Unfortunately, such a reference is only present in figure 3.36a, but is not present in the other three figures in figure 3.36.

Applying the new, reduced relative background template systematic uncertainty, the systematic uncertainty due to the background template decreased from 0.12 to 0.07 (figure 3.37).

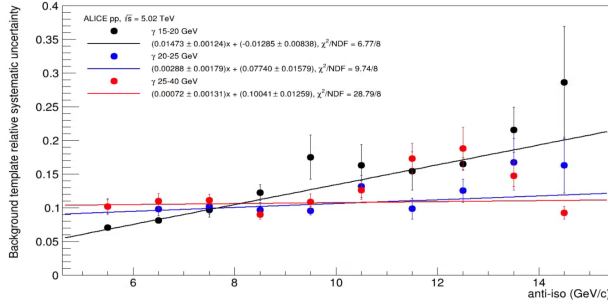
The total purity uncertainty ranged from 26-17% in pp and 12-8% in p-Pb, but after removing the correlation between the background template and the anti-isolation selection, the purity uncertainty for pp now ranges from 16-11%.

- Trigger acceptance ( $\eta$ ) correction:

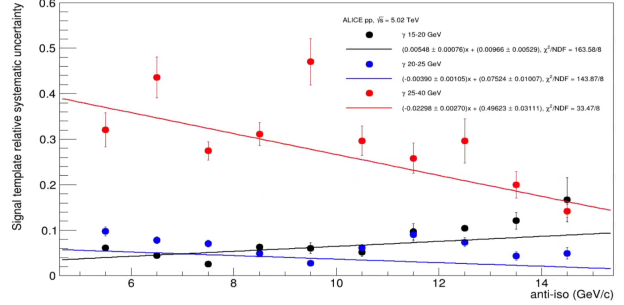
The uncertainty due to the trigger acceptance correction is described in Section 3.11.2. The resulting uncertainty on this a relative 8.3% for pp data and 2.7% for p-Pb data. As seen in Section 3.11.2, this systematic uncertainty is independent of cluster  $p_T$ ; thus, it is an uncorrelated point-to-point systematic uncertainty. For final results, this uncertainty will be shown as small box near one the axes.

- Underlying Event and isolation:

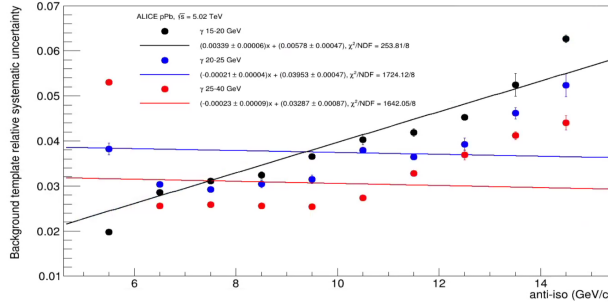
The underlying event measurement is used to determine the isolation variable. The impact of the underlying event on the cross section was assessed by varying  $\rho$  by a standard deviation, as given in table 3.6. Changing the underlying event changes the isolation variable based on equation 3.8, and changes on the cross section. The



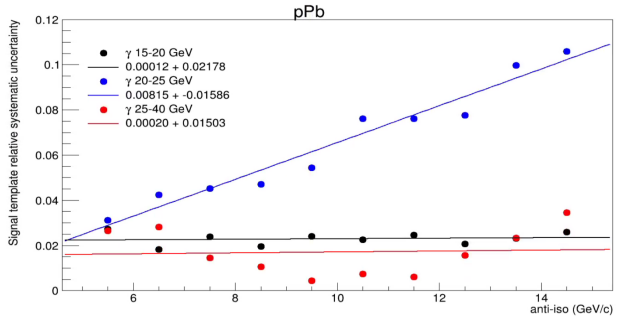
(a) pp: relative background template uncertainty vs anti-isolation



(b) pp: relative signal template uncertainty vs anti-isolation



(c) p-Pb: relative background template uncertainty vs anti-isolation

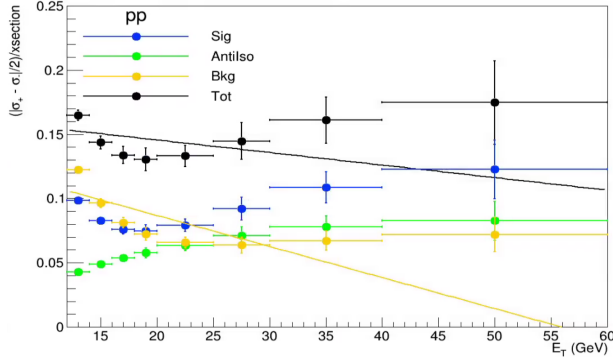


(d) p-Pb: relative signal template uncertainty vs anti-isolation

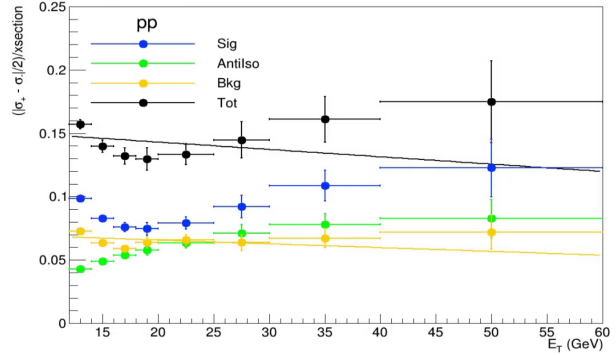
Figure 3.36: Changes to the relative signal and background template uncertainties as a function for the anti-isolation cut

isolation variable was changes to 1.0 GeV/c as the lower bound and 2.0 GeV/c as the upper bound. The lower and upper bounds were chosen such that they incorporate one standard deviation variation in the underlying event estimate. The systematic uncertainty on the cross section due to the isolation is  $< 2\%$  for pp and  $< 4\%$  for p-Pb.

- **Luminosity:**  
The integrated luminosity is measured using the trigger rejection factor, which are calculated by fitting a constant to the turn on curves. There is some variation in the trigger rejection factor due to the limited fit range as we run out of minimum bias photons at high  $p_T$ , and the variation in the starting point of the fit. This uncertainty is calculated by varying the fit ranges and observing the change in the cross section measurement due to the change in trigger rejection factor.
- **Shower shape:**  
The shower shape cut upper bound was varied from 0.3 to 0.26, 0.28, 0.33, and 0.35



(a) Same pp plot as figure 3.35, copied here for easy of comparison.



(b)

Figure 3.37: Looking at the effect of the purity systematic uncertainty components on the pp cross section with the background template and anti-isolation selection correlation present(left) and removed(right).

and cross section was calculated with the different upper bounds. The upper bound changes were implemented in purity, cluster spectra, and efficiency in order to calculate the cross section. Then, the mean and standard deviation were computed using the five cross-section measurements, and the standard deviation was used as the systematic uncertainty

- Photon energy scale, resolution and material budget:

The uncertainties due to photon energy scale, resolution, and material budget have been estimated for the isolated photon cross-section measurement with 7 TeV pp and 5 TeV p-Pb data and are less than 3% in the  $p_T$  range covered in this analysis [71, 74].

Table 3.10 presents a summary of all uncertainty estimates for our  $\gamma^{\text{iso}}$  cross-section measurement, while figure 3.38 provides the summary of uncertainties as a function of  $E_T$

Table 3.10: Summary of uncertainties in isolated photon cross section measurement in pp and p-Pb.

	pp	p-Pb
Statistical Uncertainty	6-15%	0.6-4.6%
Photon Purity	16-11%	12-8%
Trigger acceptance ( $\eta$ ) correction	8.3%	2.7%
Underlying Event	$\sim 2\%$	$\sim 4\%$
Luminosity	2.2%	6.4%
Shower shape cut	1-4%	1.4%
Photon Energy Scale	3.4%	3.4%
Photon Energy Resolution	3%	3%
Material budget	2.1%	2.1%

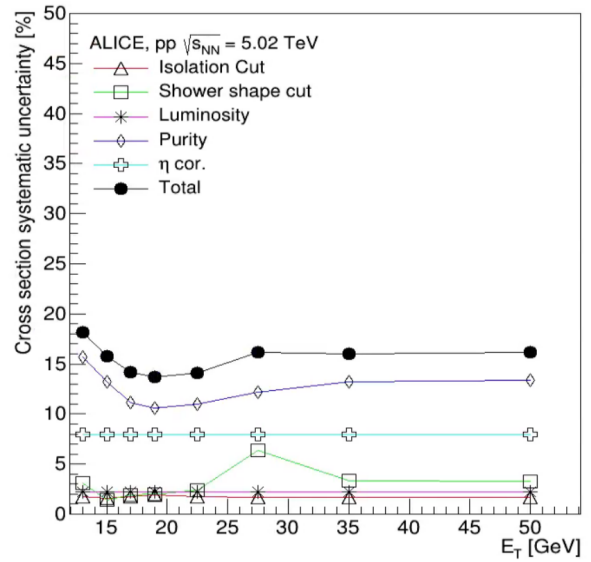
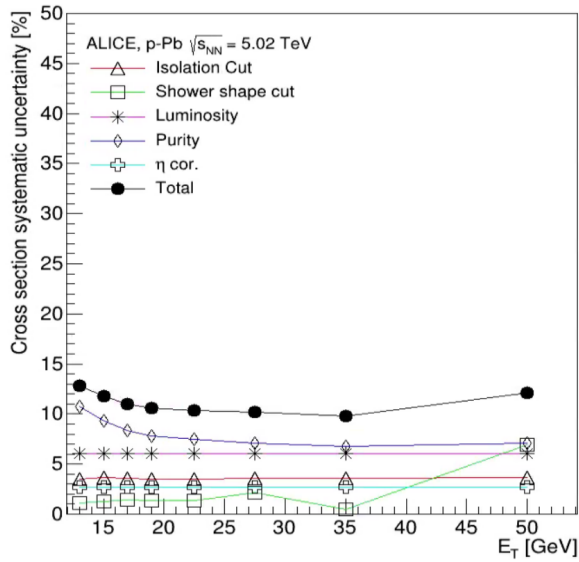


Figure 3.38: A look at the percent contribution of the major sources of systematic uncertainty on cross section as a function of  $E_T$  for pp and p-Pb.

# Chapter 4

## Results and Discussion

### 4.1 Isolated Photon Cross Section

The photon efficiency is applied as a bin-by-bin correction as described in section 3.9 to a purity weighted photon yield. The integrated luminosity is applied as scalar quantity identically to all bins in order to obtain the cross sections in figure 4.1.

The EG1 and EG2 cross sections were consolidated using the statistical errors and performing an inverse variance weighed mean calculated for the p–Pb cross section. The statistical uncertainties were summed in quadrature for the EG1 and EG2 cross section. The shape of the pp and p–Pb isolated photon cross section is comparable.

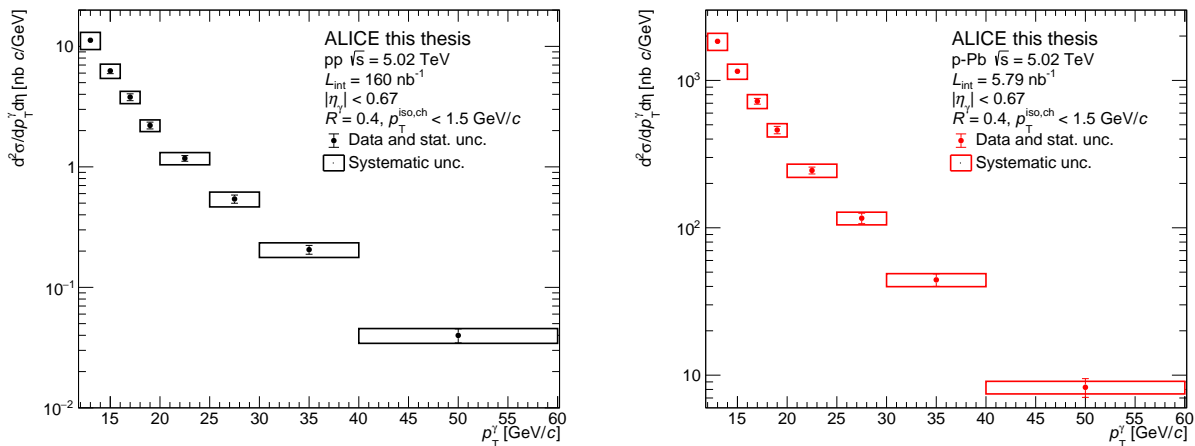


Figure 4.1: Isolated photon cross section for pp (left) and p–Pb(right).The boxes represent the systematic uncertainty while the error bars represent the statistical uncertainty. All points have a statistical uncertainty, but it might be hard to see to the log scale.

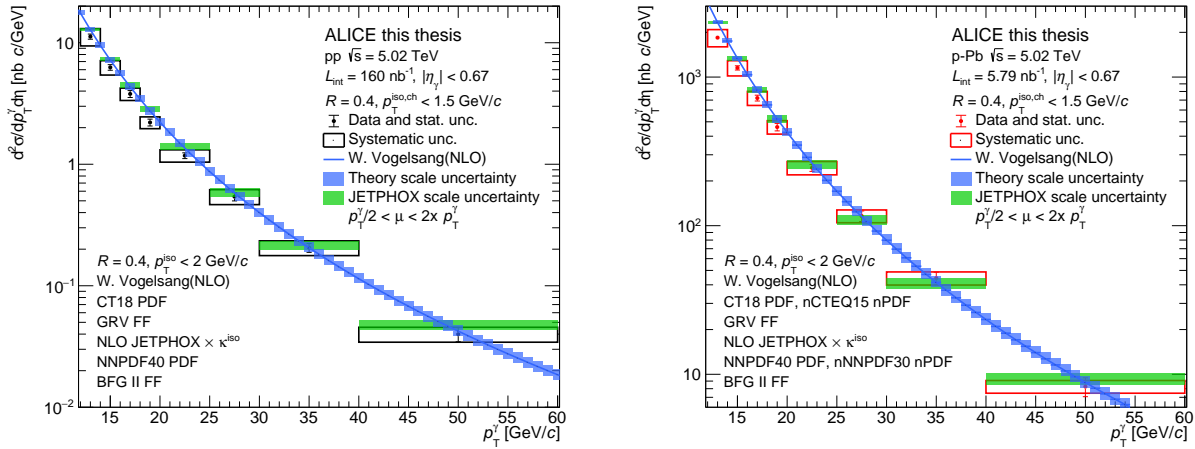


Figure 4.2: Isolated photon cross section for pp (left) and p–Pb(right) compared with NLO JETPHOX and calculations provided by Werner Vogelsang. The boxes represent the systematic uncertainty while the error bars represent the statistical uncertainty. All points have a statistical uncertainty, but it might be hard to see to the log scale.

## 4.2 Theory comparison

We compare the cross sections for pp and p–Pb to NLO JETPHOX [78] calculations. JETPHOX is a FORTRAN based computer package for NLO photon calculations. It is a general purpose Monte Carlo based cross section integrator, which calculates both single photon inclusive and photon-jet inclusive cross sections and related correlations [79, 78]. Experimental cuts such as kinematics and isolation can be implemented at the parton level. It is the only available software package which can compute direct and fragmentation photons at NLO using a Monte Carlo approach. Additionally, JETPHOX also allows the user to select various PDFs and nPDFs.

We also compare the isolated photon cross sections with theory calculations from Werner Vogelsang as seen in figure 4.2. The NLO JETPHOX predictions use NNPDF4.0 [80] and nNNPDF3.0 [81] as the PDF and nPDF respectively along with BFG II fragmentation function<sup>1</sup>. Vogelsang’s calculations use CT18 PDF and nCTEQ15 nPDF along with GRV fragmentation function. Both calculations agree with the data within the systematic uncertainties of the measurement.

<sup>1</sup>Fragmentation functions describe how color carrying partons transform into color neutral particles such as hadrons or photons. The probability of quarks and gluons fragmenting into photons cannot be computed using pQCD. The phenomenon is described using photon fragmentation functions  $D_{\gamma/q,g}(z, Q^2)$ , where  $z$  is the fraction of the parton momentum carried off by the fragmenting photon. The fragmentation functions are modelled at scale  $Q_0^2$ , and then evolved to higher scales of  $Q$  where experimental results can be used to constrain the theory, similar to the PDFs and nPDFs as mentioned in section 1.4.2.

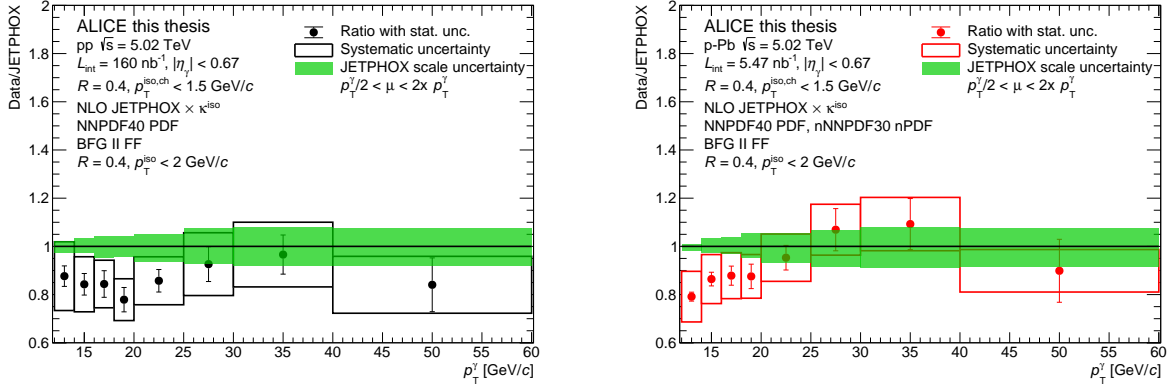


Figure 4.3: Isolated photon cross section data/JETPHOX ratio for pp (left) and p-Pb(right) compared with NLO JETPHOX and calculations provided by Werner Vogelsang. The boxes represent the systematic uncertainty while the error bars represent the statistical uncertainty. The green band is the scale uncertainty on JETPHOX

Additionally, we took a ratio with JETPHOX as seen in figure 4.3. JETPHOX seems to overestimate the photon production at low  $p_T$  since central values are systematically below unity. The overestimation of the photon production at low  $p_T$  is also seen in the NLO calculations by Vogelsang using CT18 PDF and nCTEQ15 nPDF. In figure 4.2, the blue lines from Vogelsang's NLO are above central values of the cross section and for the first two bins, they are above the systematic uncertainty boxes as well. The data seems to agree with JETPHOX within systematic uncertainties, except for the first two bins. The gluon nuclear modification for nNNPDF3.0 and nCTEQ15 agree within PDF uncertainties as seen in figure 4.4 in the  $x$  region of this measurement ( $\approx x$  between 0.005-0.02). Within the current uncertainties on the isolated photon cross sections, we cannot resolve the differences between the nPDFs.

### 4.3 The isolated photon nuclear modification factor ( $R_{pPb}$ )

Now that we have the cross sections, the final step is to compare the pp and p-Pb cross sections to obtain the nuclear modification factor,  $R_{pPb}$ . The  $R_{pPb}$  serves as a important baseline for understanding the effects of due to QGP using  $R_{PbPb}$ , as well as providing a sensitive measure of cold nuclear matter effects. The  $R_{pPb}$  is shown in figure 4.5.

A constant fit to the red points in figure 4.5 yields  $0.89 \pm 0.03$ . This is due to the fact the fit is dominated by the low  $p_T$  region with higher statistics. If we perform a fit in the plateau region ( $p_T > 20$  GeV/ $c$ ), then the fit result is  $1.02 \pm 0.03$ , which is consistent with



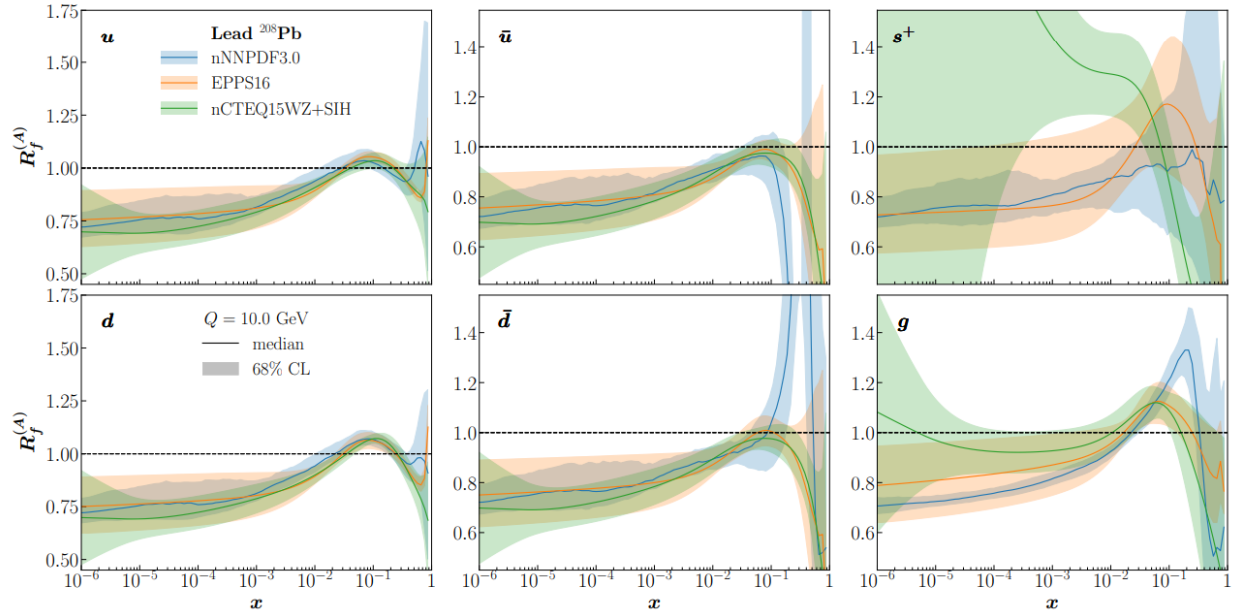


Figure 4.4: Comparisons of the nuclear modification factor between different nPDFs at  $Q = 10\text{GeV}$ : nNNPDF3.0, nCTEQ15, and EPPS16 in  $(x, Q^2)$  space

unity. The  $R_{p\text{Pb}}$  is in agreement with unity within one standard deviation for all the points except first one. Since we see no significant deviation from unity, we can conclude that there is no modification of prompt photon production in p–Pb collisions, within the statistical and systematic uncertainties shown.

The model in green [78] used JETPHOX isolated photon cross section shown in figure 4.3 to calculate an  $R_{p\text{Pb}}$ . The JETPHOX calculation used nNNPDF3.0 [81] which parameterized its fit function using new LHC data about inclusive electroweak boson, prompt photon, dijet, and prompt  $D^0$ -meson production.

The model in the azure [26] uses EPS09 as the nPDF. EPS09 uses a centrality dependent nuclear modification factor. The nuclear overlap function is calculated using a Wood-Saxon distribution. There is an assumption that the proton is point-like in a p–Pb collision, so the overlap function for pPb is the assumed to be the same as Pb only. The partonic cross section has both direct photon production along with fragmentation functions. EPS09 was the prequel to EPPS16. Thus, EPPS16 and EPS09 are similar nPDFs, but EPPS16 neutrino-nucleus DIS and LHC 2013 dijet data, which were not present for EPS09. However, the PDF uncertainty for EPS09 is smaller. The proton PDF was CTEQ6.6M [82] along with BBG for the fragmentation function. While the EPS09 model did break down the  $R_{p\text{Pb}}$  calculation in different centrality bins, for this comparison, we only use the minimum bias calculations. There is some tension between the JETPHOX calculations and EPS09 at low  $p_{\text{T}}$ . If we only consider the central values and statistical uncertainty, then the data seems to favor the

JETPHOX calculations at low  $p_T$  compared to EPS09. However due the large systematic uncertainty, we can only say that the measurement is consistent with the calculations within systematic uncertainties.

The model shown in magenta color [83] in figure 4.5 uses EPPS16 as the nPDF and is calculated with the following parameters: (i)  $|\eta| < 0.67$ , and (ii)  $E^{had} < 1.5$  in an isolation cone of 0.4, allowing as to make a direct comparison with the model. This model uses perturbative QCD (pQCD) parton model to compute the cross section for pp using CT14 for the PDFs. For the p-Pb case, cold nuclear matter effects are added by including a nuclear thickness function for a given impact parameter determined by the Wood-Saxon distribution. The nuclear modification factor used for Pb is parameterized from EPPS16 [29]. Within uncertainty, there is agreement with the model.

In conclusion, for the cross section comparisons to theory, we cannot resolve the differences between EPS09, EPPS16, and nNNPDF3.0 due to the uncertainties on the  $R_{pPb}$  since the nPDFs are very similar to each other (4.4) in kinematic range of this measurement. There is also agreement with unity within systematic uncertainties indicating that we do not see any modifications in the photon production due to cold nuclear matter effects.

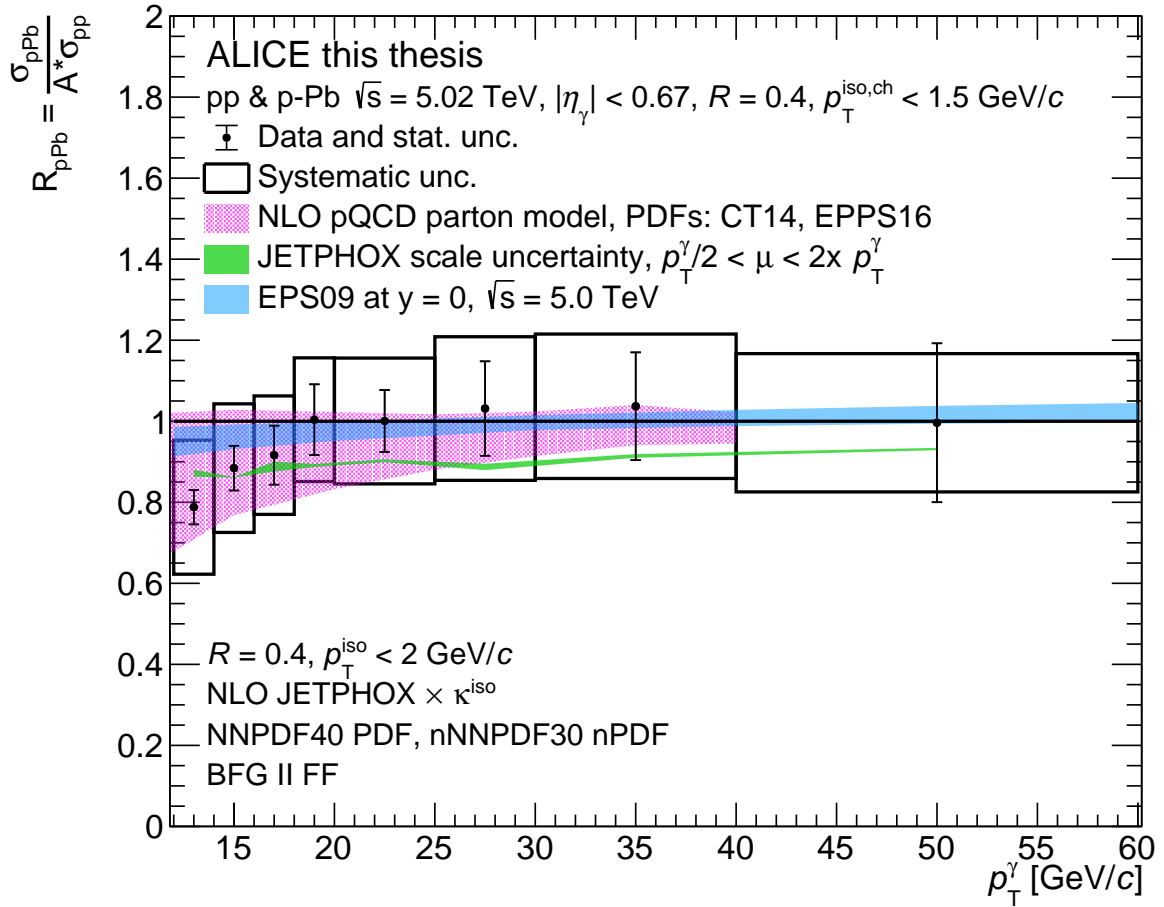


Figure 4.5: The  $R_{pPb}$  is shown using the ratio of pp cross section presented in this analysis and the p-Pb cross section presented in this analysis.

# Chapter 5

## Conclusions

We have reported a measurement of isolated photon cross section in  $\sqrt{s_{\text{NN}}} = 5.02$  TeV pp and p-Pb in ALICE. This is the first measurement of isolated photon cross section in pp and the nuclear modification factor,  $R_{p\text{Pb}}$ , at 5.02 TeV.

The new pp reference measurement allowed for a direct comparison with the p-Pb measurement without the need for any extrapolation of a reference result from other center of mass results or theory. The comparison to EPPS16, EPS09, and JETPHOX shows agreement with the measurement within statistical and systematic uncertainties showing that cold nuclear matter effects can appropriately describe photo-production between pp and p-Pb. If we only consider the central values and the statistical uncertainties, the data is best comparable to the NLO pQCD parton model. In the first bin, both the EPS09 and JETPHOX are not consistent with data. The JETPHOX is  $2\sigma$  statistical away from data, and EPS09 is  $3\sigma$  statistical away from data. The distance in standard deviations corresponds to p-values of 0.0455 and 0.0027 for JETPHOX and EP09, respectively. The JETPHOX calculation is also systematically below unity for all bins indicating that perhaps photon production is suppressed in nNNPDF3.0 compared to EPS09 and EPPS16, both of which are consistent with unity. However, within systematics uncertainty, we are unable to differentiate between the different PDFs and nPDFs.

The pp and p-Pb measurements will serve as a reference to the photon cross section measured in 5.02 TeV Pb-Pb collisions by ALICE. If there is any modification in the photon cross section measured in Pb-Pb, then any modifications larger than the 15-20% uncertainty cannot be attributed to cold nuclear matter effects. As mentioned in 1.5, besides the prompt photons from the hard scattering, there will also be the semi-hard pre-equilibrium and thermal photons emitted from the QGP. These pre-equilibrium and thermal photons could lead to larger photon cross section in same kinematic range used in this thesis in Pb-Pb compared to p-Pb.

Additionally, since photons do not interact strongly, they serve as control. Unlike hadrons, photons are not expected to be modified due to strong interactions. Thus, any modification in hadron production not seen in the photon production will serve to isolate the effect of strong interactions and QGP on the hadrons. There has even been evidence of

$\psi(2s)$  and  $J/\psi$  suppression in p-Pb[84, 85]. Hadron suppression is one of the signatures of QGP, so this photon measurement will also serve as a control for hadron suppression measurements in small systems. Any modifications hadron  $R_{pPb}$  outside the uncertainty range of 15-20% on the photon  $R_{pPb}$  could be attributed to strong interactions. Besides equation 3.2, the  $R_{pPb}$  can also be defined as

$$R_{pPb} \equiv \frac{1}{N_{coll}} \frac{(d^2 N^{pPb}/dp_T d\eta)}{(d^2 N^{pp}/dp_T d\eta)} \quad (5.1)$$

where  $N_{coll}$  is number of the binary collisions obtained from the Glauber model (previously defined in section 1.3.1.1), and  $d^2 N/dp_T d\eta$  is the differential photon yield. Unfortunately,  $N_{coll}$  is not well defined in x-A<sup>1</sup> collisions, and can be biased due to hard scattering processes [86]. This bias makes it difficult to disentangle final-state effects in  $R_{xA}$  collisions from effects due to Glauber model event activity. Since the photon yield is not expected to be modified in different collision systems, and photon yields can be used to measure  $N_{coll}$  experimentally as the ratio of the photon yields,

$$N_{coll}^{EXP} = \frac{N^{pPb}}{N^{pp}}, \quad (5.2)$$

which can be used instead of the Glauber model  $N_{coll}$  for  $R_{pPb}$  measurements using hadrons.

ALICE has also collected data on isolated photons in  $\sqrt{s_{NN}} = 8$  TeV, and 13 TeV pp. These measurements are currently on-going, but the isolated photon cross section measured at 5 TeV pp can be compared to photon cross sections at other  $\sqrt{s_{NN}}$  in order to study if there is any  $\sqrt{s_{NN}}$  dependence on the photon production. Similar comparison can be performed in p-Pb collisions between 5 TeV and 8 TeV. A preliminary look at the comparison of the different isolated photon cross sections at various collision energies can be seen in figure 5.1. All the cross section measurements are compared to JETPHOX. It is difficult to draw any strong conclusions, but it could be said that at low  $p_T$  JETPHOX seems to overestimate data. Almost all of the yellow bars are closer to the upper bound of the systematic uncertainty. Due to size of the systematic uncertainties, the only conclusion is that the various cross sections agree with JETPHOX within the systematic uncertainties. The cross sections at various collisions energy can be directly compared using  $x_T = \frac{2 \cdot p_T}{\sqrt{s_{NN}}}$ , which acts as a proxy for the momentum fraction,  $x$ . Once the on-going measurements are finished, direct comparison using  $x_T$  will provide information regarding any correlation between isolated photon cross sections and collision energies.

Finally, there are two on-going effort to better understand the structure of nucleons and nuclei. First, the LHC run 3 has recently start and many detectors and subsystems in ALICE were upgraded. With more statistics and improved photon measurements, it maybe be possible to different between the different nPDFs. Secondly, the Electron Ion Collider [87] is currently being developed to make precision measurements of the collisions

---

<sup>1</sup>x can be a proton or a deuteron, while A is a heavy-ion nuclei

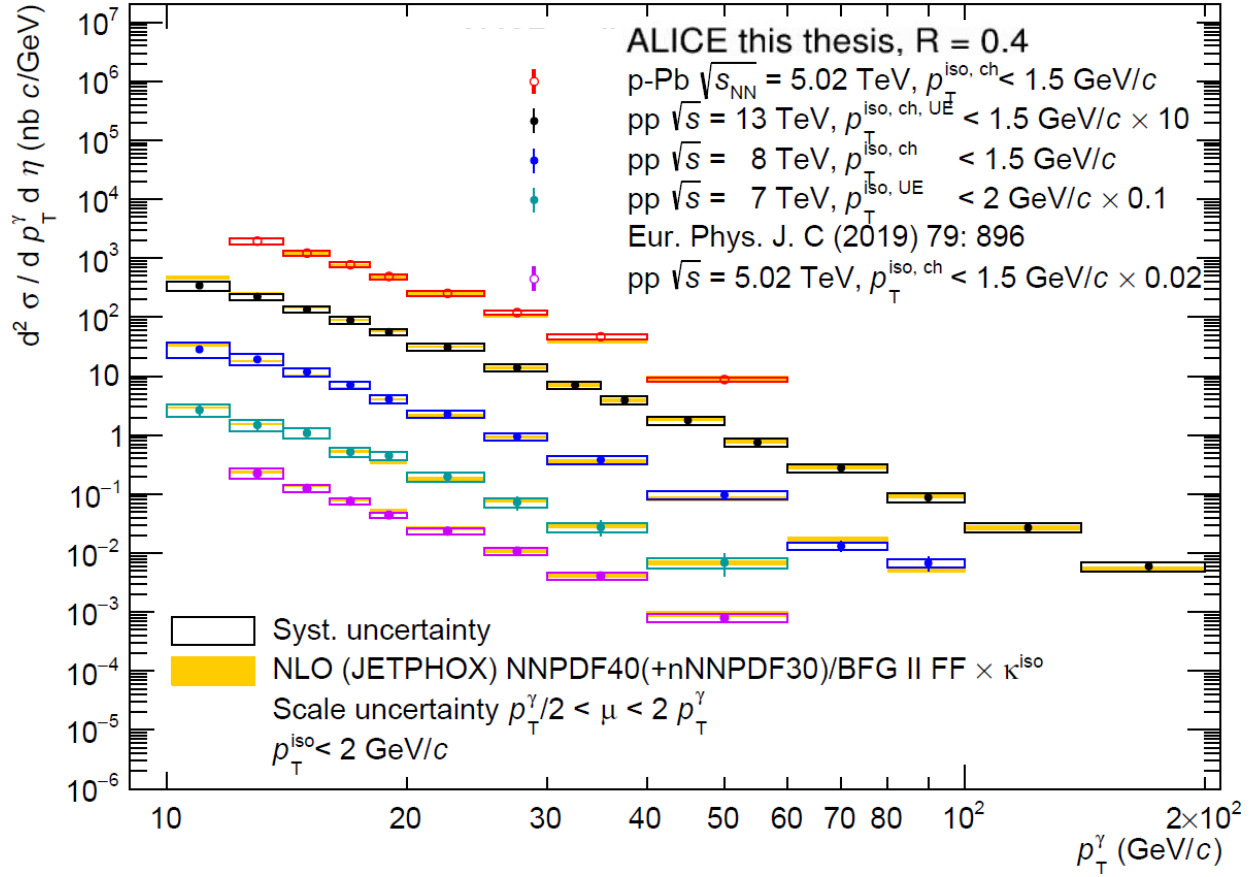


Figure 5.1: A comparison of isolated photon cross sections in  $\sqrt{s_{\text{NN}}} = 5.02, 7, 8,$  and  $13$  TeV pp and  $5.02$  TeV p–Pb. Note that the isolation criteria have some differences between the different measurements. The cross sections are compared with JETPHOX. The figure was provided by Gustavo Conesa Balbastre, and created using ALICE preliminary cross-section measurements in  $8$  TeV pp by Florian Jonas and  $13$  TeV pp by Ran Xu.

of electrons with polarized protons and ions over a large mass range to study Quantum Chromodynamics. Deep inelastic scattering, where a high energy electron will be used to probe both proton and nucleus structure, will provide a cleaner collision environment as there will not be hadronic remnants from the electron. Measurements with much higher statistical precision are expected, and more rigorous comparisons to theoretical predictions will be possible.

# Bibliography

- [1] M. Thomson. *Modern particle physics*. New York: Cambridge University Press, 2013. ISBN: 978-1-107-03426-6. DOI: 10.1017/CB09781139525367.
- [2] E. Drexler. *Elementary particle interactions in the standard Model*. Apr. 2014. URL: [https://commons.wikimedia.org/wiki/File:Elementary\\_particle\\_interactions\\_in\\_the\\_Standard\\_Model.png](https://commons.wikimedia.org/wiki/File:Elementary_particle_interactions_in_the_Standard_Model.png).
- [3] MissMJ and Cush. *Standard model of elementary particles*. Sept. 2019. URL: [https://upload.wikimedia.org/wikipedia/commons/thumb/0/00/Standard\\_Model\\_of\\_Elementary\\_Particles.svg/1390px-Standard\\_Model\\_of\\_Elementary\\_Particles.svg.png](https://upload.wikimedia.org/wikipedia/commons/thumb/0/00/Standard_Model_of_Elementary_Particles.svg/1390px-Standard_Model_of_Elementary_Particles.svg.png).
- [4] UA1 collaboration. “Experimental observation of isolated large transverse energy electrons with associated missing energy at  $s=540$  GeV”. In: *Physics Letters B* 122.1 (1983), pp. 103–116. ISSN: 0370-2693. DOI: [https://doi.org/10.1016/0370-2693\(83\)91177-2](https://doi.org/10.1016/0370-2693(83)91177-2). URL: <https://www.sciencedirect.com/science/article/pii/0370269383911772>.
- [5] UA2 Collaboration. “Observation of single isolated electrons of high transverse momentum in events with missing transverse energy at the CERN pp collider”. In: *Physics Letters B* 122.5 (1983), pp. 476–485. ISSN: 0370-2693. DOI: [https://doi.org/10.1016/0370-2693\(83\)91605-2](https://doi.org/10.1016/0370-2693(83)91605-2). URL: <https://www.sciencedirect.com/science/article/pii/0370269383916052>.
- [6] P. Bagnaia et al. “Evidence for  $Z^0 \rightarrow e^+e^-$  at the CERN  $\bar{p}p$  Collider”. In: *Phys. Lett. B* 129 (1983), pp. 130–140. DOI: 10.1016/0370-2693(83)90744-X.
- [7] ATLAS Collaboration. “Observation of a new particle in the search for the Standard Model Higgs boson with the ATLAS detector at the LHC”. In: *Physics Letters B* 716.1 (2012), pp. 1–29. ISSN: 0370-2693. DOI: <https://doi.org/10.1016/j.physletb.2012.08.020>. URL: <https://www.sciencedirect.com/science/article/pii/S037026931200857X>.
- [8] CMS Collaboration. “Observation of a new boson at a mass of 125 GeV with the CMS experiment at the LHC”. In: *Physics Letters B* 716.1 (2012), pp. 30–61. ISSN: 0370-2693. DOI: <https://doi.org/10.1016/j.physletb.2012.08.021>. URL: <https://www.sciencedirect.com/science/article/pii/S0370269312008581>.

- [9] D. J. Gross et al. “Ultraviolet Behavior of Non-Abelian Gauge Theories”. In: *Phys. Rev. Lett.* 30 (26 June 1973), pp. 1343–1346. DOI: 10.1103/PhysRevLett.30.1343. URL: <https://link.aps.org/doi/10.1103/PhysRevLett.30.1343>.
- [10] H. D. Politzer. “Reliable Perturbative Results for Strong Interactions?” In: *Phys. Rev. Lett.* 30 (26 June 1973), pp. 1346–1349. DOI: 10.1103/PhysRevLett.30.1346. URL: <https://link.aps.org/doi/10.1103/PhysRevLett.30.1346>.
- [11] P.A. Zyla et al. “Review of Particle Physics”. In: *PTEP* 2020.8 (2020), p. 083C01. DOI: 10.1093/ptep/ptaa104.
- [12] J. Lindon. “Particle Collider Probes of Dark Energy, Dark Matter and Generic Beyond Standard Model Signatures in Events With an Energetic Jet and Large Missing Transverse Momentum Using the ATLAS Detector at the LHC”. Presented 30 Oct 2020. 2020. URL: <https://cds.cern.ch/record/2746537>.
- [13] A. Bettini. *Introduction to Elementary Particle Physics*. Cambridge University Press, 2008. DOI: 10.1017/CB09780511809019.
- [14] B. V. Jacak et al. “The Exploration of Hot Nuclear Matter”. In: *Science* 337.6092 (2012), pp. 310–314. DOI: 10.1126/science.1215901. eprint: <https://www.science.org/doi/pdf/10.1126/science.1215901>. URL: <https://www.science.org/doi/abs/10.1126/science.1215901>.
- [15] Particle Data Group at Lawrence Berkeley National Lab. *History of the Universe Poster*. 2014. URL: <https://particleadventure.org/history-universe.html>.
- [16] W. Busza et al. “Heavy Ion Collisions: The Big Picture, and the Big Questions”. In: *Ann. Rev. Nucl. Part. Sci.* 68 (2018), pp. 339–376. DOI: 10.1146/annurev-nucl-101917-020852. arXiv: 1802.04801 [hep-ph].
- [17] P. Romatschke et al. “Viscosity Information from Relativistic Nuclear Collisions: How Perfect is the Fluid Observed at RHIC?” In: *Phys. Rev. Lett.* 99 (17 Oct. 2007), p. 172301. DOI: 10.1103/PhysRevLett.99.172301. URL: <https://link.aps.org/doi/10.1103/PhysRevLett.99.172301>.
- [18] M. L. Miller et al. “Glauber Modeling in High-Energy Nuclear Collisions”. In: *Annual Review of Nuclear and Particle Science* 57.1 (2007), pp. 205–243. DOI: 10.1146/annurev.nucl.57.090506.123020. eprint: <https://doi.org/10.1146/annurev.nucl.57.090506.123020>. URL: <https://doi.org/10.1146/annurev.nucl.57.090506.123020>.
- [19] R. Nouicer. “New state of nuclear matter: Nearly perfect fluid of quarks and gluons in heavy-ion collisions at RHIC energies”. In: *The European Physical Journal Plus* 131.70 (2016). DOI: 10.1140/epjp/i2016-16070-2. eprint: <https://doi.org/10.1140/epjp/i2016-16070-2>. URL: <https://doi.org/10.1140/epjp/i2016-16070-2>.



- [20] PHENIX Collaboration. “Formation of dense partonic matter in relativistic nucleus–nucleus collisions at RHIC: Experimental evaluation by the PHENIX Collaboration,” in: *Nuclear Physics A* 757.1 (2005), pp. 184–283. ISSN: 0375-9474. DOI: <https://doi.org/10.1016/j.nuclphysa.2005.03.086>. URL: <https://www.sciencedirect.com/science/article/pii/S0375947405005300>.
- [21] STAR Collaboration. “Experimental and theoretical challenges in the search for the quark–gluon plasma: The STAR Collaboration’s critical assessment of the evidence from RHIC collisions”. In: *Nuclear Physics A* 757.1 (2005), pp. 102–183. ISSN: 0375-9474. DOI: <https://doi.org/10.1016/j.nuclphysa.2005.03.085>. URL: <https://www.sciencedirect.com/science/article/pii/S0375947405005294>.
- [22] M. Arneodo. “Nuclear effects in structure functions”. In: *Physics Reports* 240.5 (1994), pp. 301–393. ISSN: 0370-1573. DOI: [https://doi.org/10.1016/0370-1573\(94\)90048-5](https://doi.org/10.1016/0370-1573(94)90048-5). URL: <https://www.sciencedirect.com/science/article/pii/0370157394900485>.
- [23] EMC collaboration. “The ratio of the nucleon structure functions  $F_2^N$  for iron and deuterium”. In: *Physics Letters B* 123.3 (1983), pp. 275–278. ISSN: 0370-2693. DOI: [https://doi.org/10.1016/0370-2693\(83\)90437-9](https://doi.org/10.1016/0370-2693(83)90437-9). URL: <https://www.sciencedirect.com/science/article/pii/0370269383904379>.
- [24] N. Armesto. “Nuclear shadowing”. In: *Journal of Physics G: Nuclear and Particle Physics* 32.11 (Sept. 2006), R367. DOI: 10.1088/0954-3899/32/11/R01. URL: <https://dx.doi.org/10.1088/0954-3899/32/11/R01>.
- [25] D. F. Geesaman et al. “The Nuclear EMC Effect”. In: *Annual Review of Nuclear and Particle Science* 45.1 (1995), pp. 337–390. DOI: 10.1146/annurev.ns.45.120195.002005. eprint: <https://doi.org/10.1146/annurev.ns.45.120195.002005>. URL: <https://doi.org/10.1146/annurev.ns.45.120195.002005>.
- [26] I. Helenius et al. “Centrality dependence of inclusive prompt photon production in d+Au, Au+Au, p+Pb, and Pb+Pb collisions”. In: *Journal of High Energy Physics* C77.30 (2013). DOI: 10.1007/JHEP05(2013)030. arXiv: 1302.5580 [hep-ph].
- [27] M. Hirai et al. “Determination of nuclear parton distributions”. In: *Phys. Rev. D* 64 (3 June 2001), p. 034003. DOI: 10.1103/PhysRevD.64.034003. URL: <https://link.aps.org/doi/10.1103/PhysRevD.64.034003>.
- [28] . “nCTEQ15: Global analysis of nuclear parton distributions with uncertainties in the CTEQ framework”. In: *Phys. Rev. D* 93 (8 Apr. 2016), p. 085037. DOI: 10.1103/PhysRevD.93.085037. URL: <https://link.aps.org/doi/10.1103/PhysRevD.93.085037>.
- [29] K. J. Eskola et al. “EPPS16: nuclear parton distributions with LHC data”. In: *The European Physical Journal C* 77 (8 Apr. 2017), p. 163. DOI: 10.1140/epjc/s10052-017-4725-9. URL: <https://doi.org/10.1140/epjc/s10052-017-4725-9>.

- [30] A. Monnai. “Direct photons in hydrodynamic modeling of relativistic nuclear collisions”. In: *International Journal of Modern Physics A* 93 (8 Apr. 2022), p. 085037. DOI: 10.1103/PhysRevD.93.085037. URL: <https://link.aps.org/doi/10.1103/PhysRevD.93.085037>.
- [31] G. David. “Direct real photons in relativistic heavy ion collisions”. In: *Reports on Progress in Physics* 83.4 (8 Feb. 2020), p. 046301. DOI: 10.1088/1361-6633/ab6f57. URL: <https://dx.doi.org/10.1088/1361-6633/ab6f57>.
- [32] J. J. Ethier et al. “Parton Distributions in Nucleons and Nuclei”. In: *Annual Review of Nuclear and Particle Science* 70.1 (8 Apr. 2020), pp. 43–76. DOI: 10.1146/annurev-nucl-011720-042725. eprint: <https://doi.org/10.1146/annurev-nucl-011720-042725>. URL: <https://doi.org/10.1146/annurev-nucl-011720-042725>.
- [33] C. Loizides. “Experimental overview on small collision systems at the LHC”. In: *Nuclear Physics A* 956 (8 Apr. 2016). The XXV International Conference on Ultrarelativistic Nucleus-Nucleus Collisions: Quark Matter 2015, pp. 200–207. ISSN: 0375-9474. DOI: <https://doi.org/10.1016/j.nuclphysa.2016.04.022>. URL: <https://www.sciencedirect.com/science/article/pii/S0375947416300732>.
- [34] . *CERN accelerating science*. Apr. 2023. DOI: 10.1103/PhysRevD.93.085037. URL: <https://home.cern/resources/faqs/facts-and-figures-about-lhc>.
- [35] R. Bruce et al. “Performance and luminosity models for heavy-ion operation at the CERN Large Hadron Collider”. In: *The European Physical Journal Plus* 745.136 (8 Apr. 2021), p. 085037. DOI: <https://doi.org/10.1140/epjp/s13360-021-01685-5>. arXiv: 2107.09560 [hep-ph]. URL: <https://home.cern/resources/faqs/facts-and-figures-about-lhc>.
- [36] E. Mobs. “The CERN accelerator complex - August 2018. Complexe des accélérateurs du CERN - Août 2018”. In: *CERN* 93 (8 Apr. 2018). General Photo, p. 085037. DOI: 10.1103/PhysRevD.93.085037. URL: <https://cds.cern.ch/record/2636343>.
- [37] J. Wenninger. “Machine Protection and Operation for LHC”. In: *CERN* 93 (8 Apr. 2016). Comments: 25 pages, contribution to the 2014 Joint International Accelerator School: Beam Loss and Accelerator Protection, Newport Beach, CA, USA , 5-14 Nov 2014, pp. 377–401. DOI: 10.5170/CERN-2016-002.377. arXiv: 1608.03113. URL: <https://cds.cern.ch/record/2207176>.
- [38] ATLAS Collaboration. “The ATLAS Experiment at the CERN Large Hadron Collider”. In: *JINST* 3 (8 Apr. 2008). Also published by CERN Geneva in 2010, S08003. DOI: 10.1088/1748-0221/3/08/S08003. URL: <https://cds.cern.ch/record/1129811>.
- [39] ALICE Collaboration. “The ALICE experiment at the CERN LHC”. In: *Journal of Instrumentation* 3.08 (8 Aug. 2008), S08002. DOI: 10.1088/1748-0221/3/08/S08002. URL: <https://doi.org/10.1088/1748-0221/3/08/S08002>.

- [40] CMS Collaboration. “The CMS experiment at the CERN LHC. The Compact Muon Solenoid experiment”. In: *JINST* 3 (8 Apr. 2008). Also published by CERN Geneva in 2010, S08004. DOI: 10.1088/1748-0221/3/08/S08004. URL: <https://cds.cern.ch/record/1129810>.
- [41] LHCb Collaboration. “The LHCb Detector at the LHC”. In: *JINST* 3 (8 Apr. 2008). Also published by CERN Geneva in 2010, S08005. DOI: 10.1088/1748-0221/3/08/S08005. URL: <https://cds.cern.ch/record/1129809>.
- [42] A. Tauro. “ALICE Schematics”. General Photo. Apr. 2017. DOI: 10.1103/PhysRevD.93.085037. URL: <https://cds.cern.ch/record/2263642>.
- [43] . “Distributed simulation and visualization of the ALICE detector magnetic field”. In: *Computer Physics Communications* 271 (8 Apr. 2022), p. 108206. ISSN: 0010-4655. DOI: <https://doi.org/10.1016/j.cpc.2021.108206>. URL: <https://www.sciencedirect.com/science/article/pii/S0010465521003180>.
- [44] A. Peck. “Photoproduction of c mesons in ultra-peripheral Pb+Pb collisions at  $\sqrt{s_{NN}} = 5.02$  TeV at the LHC”. PhD thesis. July 2020, p. 108206. DOI: 10.13140/RG.2.2.35949.87524. URL: <https://www.sciencedirect.com/science/article/pii/S0010465521003180>.
- [45] ALICE Collaboration. “Performance of the ALICE experiment at the CERN LHC”. In: *International Journal of Modern Physics A* 29.24 (8 Apr. 2014), p. 1430044. ISSN: 0010-4655. DOI: 10.1142/S0217751X14300440. eprint: <https://doi.org/10.1142/S0217751X14300440>. URL: <https://doi.org/10.1142/S0217751X14300440>.
- [46] P. Antonioli et al. *Upgrade of the ALICE Readout amp; Trigger System*. Tech. rep. Presently we require a LHCC-TDR reference number.a later stage we will fill the required information. Apr. 2013, p. 108206. DOI: <https://doi.org/10.1016/j.cpc.2021.108206>. URL: <https://cds.cern.ch/record/1603472>.
- [47] D. Evans et al. “The ALICE central trigger system”. In: *14th IEEE-NPSS Real Time Conference, 2005*. Vol. 271. CERN, Apr. 2005, 5 pp.-. DOI: 10.1109/RTC.2005.1547458. URL: <https://www.sciencedirect.com/science/article/pii/S0010465521003180>.
- [48] B. O. Villalobos et al. “The ALICE Central Trigger Processor”. In: *Computer Physics Communications* 271 (8 Apr. 2005), p. 108206. ISSN: 0010-4655. DOI: 10.5170/CERN-2005-011.284. URL: <https://cds.cern.ch/record/921038>.
- [49] J. Lehrbach et al. for the ALICE Collaboration. “ALICE HLT Cluster operation during ALICE Run 2”. In: *Journal of Physics: Conference Series* 898.8 (8 Oct. 2017), p. 082027. ISSN: 0010-4655. DOI: 10.1088/1742-6596/898/8/082027. URL: <https://dx.doi.org/10.1088/1742-6596/898/8/082027>.
- [50] M. Krzewicki et al. for the ALICE Collaboration. “ALICE HLT Run 2 performance overview.” In: *Computer Physics Communications* 898.3 (8 Oct. 2017), p. 032056. ISSN: 0010-4655. DOI: 10.1088/1742-6596/898/3/032056. URL: <https://dx.doi.org/10.1088/1742-6596/898/3/032056>.

- [51] J.-Y. Grossiord. “The V0 detector is two disks of counters in both sides of the interaction point.” ALICE Collection. Apr. 2006. DOI: <https://doi.org/10.1016/j.cpc.2021.108206>. URL: <https://cds.cern.ch/record/1045976>.
- [52] . “One of the eight sectors of the V0A trigger hodoscope.” ALICE Collection. Apr. 2005. DOI: <https://doi.org/10.1016/j.cpc.2021.108206>. URL: <https://cds.cern.ch/record/975945>.
- [53] ALICE Collaboration. *ALICE forward detectors: FMD, TO and VO: Technical Design Report*. Vol. 271. Technical design report. ALICE. Submitted on 10 Sep 2004. Geneva: CERN, Apr. 2004, p. 108206. DOI: <https://doi.org/10.1016/j.cpc.2021.108206>. URL: <http://cds.cern.ch/record/781854>.
- [54] A. Maire et al. “ALICE sub-detectors highlighted (LHC runs 1+2 runs 3+4)”. General Photo. Apr. 2017. DOI: <https://doi.org/10.1016/j.cpc.2021.108206>. URL: <https://cds.cern.ch/record/2302924>.
- [55] ALICE collaboration. “Particle identification performance at ALICE”. In: *arXiv: Nuclear Experiment 271* (8 Apr. 2017). ALICE Collection., p. 108206. ISSN: 0010-4655. DOI: [10.48550/arXiv.1709.00288](https://doi.org/10.48550/arXiv.1709.00288). arXiv: 1709.00288 [nucl-ex]. URL: <https://doi.org/10.48550/arXiv.1709.00288>.
- [56] M. Brice. “Integration of the ALICE experiment’s inner tracker”. ALICE Collection. Apr. 2007. DOI: <https://doi.org/10.1016/j.cpc.2021.108206>. URL: <https://cds.cern.ch/record/1111433>.
- [57] A. Saba. “Module of the Silicon Drift Detector of ALICE”. ALICE Collection. Apr. 2006. DOI: <https://doi.org/10.1016/j.cpc.2021.108206>. URL: <https://cds.cern.ch/record/1046800>.
- [58] A. Van den Brink et al. “Conductive Cooling of SDD and SSD Front-End Chips for ALICE”. In: *Computer Physics Communications 271* (8 Apr. 2001). ALICE Collection., p. 108206. ISSN: 0010-4655. DOI: [10.5170/CERN-2001-005.368](https://doi.org/10.5170/CERN-2001-005.368). URL: <https://cds.cern.ch/record/521854>.
- [59] G. Durk. “Alice Silicon Strip Detector”. ALICE Collection. Apr. 2007. DOI: <https://doi.org/10.1016/j.cpc.2021.108206>. URL: <https://cds.cern.ch/record/1044755>.
- [60] . “Alice Silicon Strip Detector, chip”. ALICE Collection. Apr. 1999. DOI: <https://doi.org/10.1016/j.cpc.2021.108206>. URL: <https://cds.cern.ch/record/1044831>.
- [61] A. P. De Haas et al. “Very low mass microcables for the ALICE silicon strip detector. Very Low-Mass Microcables for the ALICE SSD Detector”. In: *Computer Physics Communications 271* (8 Apr. 1999). ALICE Collection., p. 108206. ISSN: 0010-4655. DOI: [10.5170/CERN-1999-009.143](https://doi.org/10.5170/CERN-1999-009.143). URL: <http://cds.cern.ch/record/426351>.

- [62] W. Yu for the ALICE collaboration. “Particle identification of the ALICE TPC via  $dE/dx$ ”. In: *Nuclear Instruments and Methods in Physics Research Section A: Accelerators, Spectrometers, Detectors and Associated Equipment* 706 (8 Apr. 2013). ALICE Collection., pp. 55–58. ISSN: 0168-9002. DOI: <https://doi.org/10.1016/j.nima.2012.05.022>. URL: <https://www.sciencedirect.com/science/article/pii/S0168900212005098>.
- [63] J. Alme et. al. “The ALICE TPC, a large 3-dimensional tracking device with fast read-out for ultra-high multiplicity events”. In: *Nuclear Instruments and Methods in Physics Research Section A: Accelerators, Spectrometers, Detectors and Associated Equipment* 622.1 (8 Apr. 2010). ALICE Collection., pp. 316–367. ISSN: 0168-9002. DOI: <https://doi.org/10.1016/j.nima.2010.04.042>. URL: <https://www.sciencedirect.com/science/article/pii/S0168900210008910>.
- [64] ALICE Collaboration. *Performance of the ALICE Electromagnetic Calorimeter*. Tech. rep. 129 pages, 104 captioned figures, 16 tables, submitted to JINST, figures at <http://alice-publications.web.cern.ch/node/8398>. Geneva: CERN, Apr. 2022, p. 108206. DOI: <https://doi.org/10.1016/j.cpc.2021.108206>. arXiv: 2209.04216. URL: <https://cds.cern.ch/record/2825648>.
- [65] M. Arriata et al. “Measurement of isolated photon-hadron correlations in 5 TeV pp and p-Pb <https://alice-notes.web.cern.ch/node/938>.” In: *Computer Physics Communications* 271 (8 Apr. ANA-938). ALICE Collection., p. 108206. ISSN: 0010-4655. DOI: <https://doi.org/10.1016/j.cpc.2021.108206>. URL: <https://cds.cern.ch/record/1044831>.
- [66] ALICE Collaboration. “ALICE 2017 luminosity determination for pp collisions at  $\sqrt{s} = 5$  TeV”. In: *Computer Physics Communications* 271 (8 Nov. 2018). ALICE Collection., p. 108206. ISSN: 0010-4655. DOI: <https://doi.org/10.1016/j.cpc.2021.108206>. URL: <https://cds.cern.ch/record/2648933>.
- [67] ALICE Collaboration. “Public Note – Centrality determination in heavy ion collisions. <https://alice-notes.web.cern.ch/node/711>”. In: *Computer Physics Communications* 271 (8 Apr. 2019). ALICE Collection., p. 108206. ISSN: 0010-4655. DOI: <https://doi.org/10.1016/j.cpc.2021.108206>. URL: <https://cds.cern.ch/record/1044831>.
- [68] ALICE Collaboration. “Production of  $\pi^0$  and  $\eta$  mesons up to high transverse momentum in pp collisions at 2.76 TeV”. In: *Eur. Phys. J C* 77.5 (8 May 2017). ALICE Collection., p. 108206. ISSN: 1434-6052. DOI: [10.1140/epjc/s10052-017-4890-x](https://doi.org/10.1140/epjc/s10052-017-4890-x). URL: <http://dx.doi.org/10.1140/epjc/s10052-017-4890-x>.
- [69] C. Bierlich et al. *A comprehensive guide to the physics and usage of PYTHIA 8.3*. ALICE Collection. Apr. 2022. DOI: <https://doi.org/10.1016/j.cpc.2021.108206>. arXiv: 2203.11601 [hep-ph]. URL: <https://cds.cern.ch/record/1044831>.

- [70] S. Roesler et al. “The Monte Carlo event generator DPMJET-III”. In: vol. 271. ALICE Collection. CERN, Dec. 2000, pp. 1033–1038. DOI: 10.1007/978-3-642-18211-2\_166. arXiv: hep-ph/0012252. URL: <https://cds.cern.ch/record/1044831>.
- [71] E. Masson. “Measurement of isolated photons in p–Pb collisions at 5.02 TeV with the EMCAL detector in ALICE. <https://alice-notes.web.cern.ch/system/files/notes/analysis/741/>”. In: *Computer Physics Communications* 271 (8 Apr. ALICE-ANA-2018-4677). ALICE Collection., p. 108206. ISSN: 0010-4655. DOI: <https://doi.org/10.1016/j.cpc.2021.108206>. URL: <https://cds.cern.ch/record/1044831>.
- [72] G. C. Balbastre. “Study and emulation of cell energy cross-talk in EMCAL”. In: *Computer Physics Communications* 271 (8 Apr. ANA-837, 2018). ALICE Collection., p. 108206. ISSN: 0010-4655. DOI: <https://doi.org/10.1016/j.cpc.2021.108206>. URL: <https://cds.cern.ch/record/1044831>.
- [73] ALICE Collaboration. “Measurement of isolated photon-hadron correlations in  $\sqrt{s_{NN}} = 5.02$  TeV *pp* and *p*-Pb collisions”. In: *Phys. Rev. C* 102 (4 Oct. 2020). ALICE Collection., p. 044908. ISSN: 0010-4655. DOI: 10.1103/PhysRevC.102.044908. URL: <https://link.aps.org/doi/10.1103/PhysRevC.102.044908>.
- [74] ALICE Collaboration. “Measurement of the inclusive isolated photon production cross section in *pp* collisions at  $\sqrt{s} = 7$  TeV”. In: *Eur. Phys. J.* 79.896 (8 Apr. 2019). ALICE Collection., p. 108206. ISSN: 0010-4655. DOI: 10.1140/epja/i2016-16268-9. arXiv: 1906.01371 [nucl-ex]. URL: <https://cds.cern.ch/record/1044831>.
- [75] ALICE Collaboration. “Direct photon production at low transverse momentum in proton-proton collisions at  $\sqrt{s} = 2.76$  and 8 TeV”. In: *Computer Physics Communications* 271 (8 Apr. arXiv:1803.09857, 2018). ALICE Collection., p. 108206. ISSN: 0010-4655. DOI: <https://doi.org/10.1016/j.cpc.2021.108206>. arXiv: 1803.09857 [nucl-ex]. URL: <https://cds.cern.ch/record/1044831>.
- [76] M. Cacciari et al. “On the characterisation of the underlying event”. In: *JHEP* 04 (8 Apr. 2010). ALICE Collection., p. 065. ISSN: 0010-4655. DOI: 10.1007/JHEP04(2010)065. arXiv: 0912.4926 [hep-ph]. URL: <https://cds.cern.ch/record/1044831>.
- [77] F. Arleo et al. “Hard probes in heavy-ion collisions at the LHC: Photon physics in heavy ion collisions at the LHC”. In: *arXiv:hep-ph/0311131* 271 (8 Apr. 2004). ALICE Collection., p. 108206. ISSN: 0010-4655. DOI: <https://doi.org/10.1016/j.cpc.2021.108206>. arXiv: hep-ph/0311131 [hep-ph]. URL: <https://cds.cern.ch/record/1044831>.
- [78] P. Aurenche et al. *JETPHOX*. ALICE Collection. Apr. 1999. DOI: <https://doi.org/10.1016/j.cpc.2021.108206>. URL: [https://lapth.cnrs.fr/PHOX\\_FAMILY/jetphox.html](https://lapth.cnrs.fr/PHOX_FAMILY/jetphox.html).

- [79] P. Aurenche et al. “Recent critical study of photon production in hadronic collisions”. In: *Phys. Rev. D* 73 (9 May 2006). ALICE Collection., p. 094007. ISSN: 0010-4655. DOI: 10.1103/PhysRevD.73.094007. URL: <https://link.aps.org/doi/10.1103/PhysRevD.73.094007>.
- [80] The NNPDF collaboration. “The path to proton structure at 1% accuracy.” In: *Eur. Phys. J. C* 82.428 (8 Apr. 2022). ALICE Collection., p. 108206. ISSN: 0010-4655. DOI: 10.1140/epjc/s10052-022-10328-7. URL: <https://doi.org/10.1140/epjc/s10052-022-10328-7>.
- [81] R. A. Khalek et al. *NNPDF3.0: Evidence for a modified partonic structure in heavy nuclei*. ALICE Collection. Apr. 2022. DOI: <https://doi.org/10.1016/j.cpc.2021.108206>. arXiv: 2201.12363 [hep-ph]. URL: <https://cds.cern.ch/record/1044831>.
- [82] P. M. Nadolsky et al. “Implications of CTEQ global analysis for collider observables”. In: *Phys. Rev. D* 78 (1 July 2008). ALICE Collection., p. 013004. ISSN: 0010-4655. DOI: 10.1103/PhysRevD.78.013004. URL: <https://link.aps.org/doi/10.1103/PhysRevD.78.013004>.
- [83] M. Xie et al. “ $\gamma$ -hadron spectra in  $p + \text{Pb}$  collisions at  $\sqrt{s_{NN}} = 5.02 \text{ TeV}$ ”. In: *Phys. Rev. C* 103 (3 Mar. 2021). ALICE Collection., p. 034911. ISSN: 0010-4655. DOI: 10.1103/PhysRevC.103.034911. URL: <https://link.aps.org/doi/10.1103/PhysRevC.103.034911>.
- [84] ALICE collaboration. “Suppression of  $\psi(2S)$  production in p–Pb collisions at  $\sqrt{s_{NN}} = 5.02 \text{ TeV}$ ”. In: *J. High Energ. Phys* 271.73 (8 Apr. 2014). ALICE Collection., p. 108206. ISSN: 0010-4655. DOI: 10.1007/JHEP12(2014)073. URL: [https://doi.org/10.1007/JHEP12\(2014\)073](https://doi.org/10.1007/JHEP12(2014)073).
- [85] ALICE collaboration. “Centrality dependence of inclusive  $J/\psi$  production in p–Pb collisions at  $\sqrt{s_{NN}} = 5.02 \text{ TeV}$ ”. In: *J. High Energ. Phys* 271.127 (8 Apr. 2015). ALICE Collection., p. 108206. ISSN: 0010-4655. DOI: 10.1007/JHEP11(2015)127. URL: [https://doi.org/10.1007/JHEP11\(2015\)127](https://doi.org/10.1007/JHEP11(2015)127).
- [86] PHENIX Collaboration. *Disentangling centrality bias and final-state effects in the production of high- $p_T$   $\pi^0$  using direct  $\gamma$  in d+Au collisions at  $\sqrt{s_{NN}} = 200 \text{ GeV}$* . ALICE Collection. Apr. 2023. DOI: 10.48550/arXiv.2303.12899. arXiv: 2303.12899 [nucl-ex]. URL: <https://doi.org/10.48550/arXiv.2303.12899>.
- [87] A. Accardi et al. *Electron Ion Collider: The Next QCD Frontier - Understanding the glue that binds us all*. ALICE Collection. Apr. 2014. DOI: <https://doi.org/10.1016/j.cpc.2021.108206>. arXiv: {1212.1701} [nucl-ex]. URL: <https://cds.cern.ch/record/1044831>.